OPTICAL CHARACTERISATION OF RARE-EARTH DOPED FLUORIDE AND PHOSPHATE GLASS MICROSPHERE RESONATORS

By

Danny O'Shea

SUBMITTED IN PARTIAL FULFILLMENT OF THE
REQUIREMENTS FOR THE DEGREE OF
MASTER OF SCIENCE
AT
NATIONAL UNIVERSITY OF IRELAND,
UNIVERSITY COLLEGE CORK
IRELAND
AUGUST 2007

Department Head, Prof. John McInerney
Supervisor, Dr. Síle Nic Chormaic

To the O'Shea families and Martha.

Table of Contents

Acknowledgements

The work in this thesis would not be possible without the great efforts of Dr. Síle Nic Chormaic, my supervisor, Jonathan Ward, my work colleague, and the other members of the Quantum Optics Group - Dr. Brian Shortt, Michael Morrissey, Kieran Deasy, and Thejesh Bandi. I am indebted to their suggestions, encouragement, and most importantly, their humour. The warm atmosphere in our group over my two years in the Tyndall National Institute, have made it a fine environment in which to develop and realise ideas. The relative freedom to choose our own course of research afforded to us by Síle, helped me develop a degree of independence. My level of scientific education as well as personal knowledge of my abilities have truly benefitted from this experience. Despite having a busy schedule running the group, Síle was always available, either in person or email, to answer any problems I needed help with. She is also responsible for identifying my next work, which will be for my PhD, in the Glass Fiber Quantum Optics Group in Mainz, Germany, with Prof. Dr. Arno Rauschenbeutel.

There were a number of fruitful trips throughout my thesis work. During my time in the Q&NLO summer school in Denmark, I met many very intelligent and friendly students. Dr. Renzoni and his two students in University College London made me feel very welcome when I visited his laboratory in 2006. The CLEO 2007 conference in Baltimore, USA, led to friendship with Scott Lewis, who kindly visited Martha, my partner, and I in June. We look forward to reciprocating the visit some time in the near future.

Looking back at my first draft of our first paper, I am a little astounded by the contrast in my writing style compared to later papers. I will forever be grateful to Síle and Brian for teaching me the skill of technical writing. Martha kindly spent a number of days reading over the manuscript and making corrections. Síle also spent many long hours making corrections and improvements to the thesis; too numerous

to be counted. Any remaining errors are, of course, my own fault.

I wish to express my gratitude to a number of people around the various institutions in Cork. A special thanks must go to Dr. Anthony Grant in the Cork Institute of Technology (CIT) for taking time out to teach me how to use their electron microscope. The Department Head of my previous department in CIT, Dr. Liam McDonnell, showed an interest in my progress and offered useful advice for which I thank him. This appreciation is extended to all the technicians and staff of the department. Halfway through my work, Síle and I transferred to the Physics Department in University College Cork (UCC). Here I had the opportunity of co-supervising an undergraduate physics laboratory; it can be more difficult than it seems, but rewarding nonetheless. During my time in UCC, several of us, under the guidance of Síle, set up the Cork Chapter of the Optical Society of America; this also took some effort and persistence. The staff and students in CIT, UCC and the Tyndall National Institute, the place where my work was undertaken, were always a pleasure to talk with, both during and after work. Of course, I am grateful to my parents for their support and for making every effort in ensuring my studies went as smoothly as possible. Our collaborators in France, Patrice Féron and Michel Mortier, provided us with the bulk doped glass and absorption measurements, which are studied in this thesis. Last, but not least, I thank Prof. Roger Whatmore, Tyndall CEO, for selecting me for the Tyndall bursary in 2007.

I am also very happy to acknowledge the financial help of IRCSET through the Embark Initiative who provided me with a scholarship over 2005-2007.

Kenmare, Ireland — Danny O'Shea
2 August, 2007

List of Publications

[1] J. Ward, D. G. O'Shea, B. J. Short, M. J. Morrissey, K. Deasy and S. G. Nic Chormaic, "Heat-and-pull rig for fiber taper fabrication," *Rev. Sci. Instrum.*, **77**, 083105, (2006).

[2] B. J. Shortt, J. Ward, D. O'Shea and S. Nic Chormaic, "Spectral characterisation of erbium-doped microspherical lasers," *Proc. SPIE*, **6187**, 618708, (2006).

[3] J. Ward, D. O'Shea, B. Shortt, and S. Nic Chormaic, "Optical Bistability in Er-Yb co-doped phosphate glass microspheres at room temperature," *J. Appl. Phys.*, **102**, 023104, (2007).

[4] D. G. O'Shea, J. M. Ward, B. J. Shortt, M. Mortier, P. Féron and S. Nic Chormaic, "Upconversion channels in Er:ZBLALiP: a multi-color microspherical light source," *Eur. Phys. J. Appl. Phys.*, **40**, 181, (2007).

[5] D. G. O'Shea, J. M. Ward, B. J. Shortt, and S. Nic Chormaic, "An All-Fiber Coupled Multicolor Microspherical Light Source," *IEEE Photon. Technol. Lett.*, **19**, 1720 (2007).

Abstract

The unique ability of microresonators to confine tens of Watts of power in micron-sized structures for long periods of time has prompted applications ranging from optical processing of data to more fundamental studies, such as cavity quantum electrodynamics. Rare-earth ions embedded in glasses serve as solid state laser sources for applications in telecommunications, nuclear fusion, environmental sensors, and even quantum information. This combination of active medium and resonant cavity has opened new areas of research focusing on the characterisation of doped microspheres. The aim of this research was the investigation of the emission characteristics of a singly-doped fluorozirconate glass microsphere, made from ZBLALiP, and a co-doped phosphate glass microsphere, made from IOG-2.

The technique used for microsphere and taper fabrication is outlined. A rig for fabricating adiabatic tapered optical fibres is also described and the profile of the resulting fibres is characterised. Light is coupled from these fibres into the microspheres, whereupon it propagates in cavity modes and excites the active medium. Bulk samples normally operate with excitation densities of only a few tens of kW/cm^2. Excitation densities as high as 200 MW/cm^2 circulate in the doped microspheres, thereby making it possible to investigate interesting new behaviour in the glasses under study.

In ZBLALiP we observe a total of thirteen discrete fluorescence emissions from 320 nm to 850 nm and a lasing emission at 1.5 μm. Results from the literature normally show a limited number of emissions at green, red and - possibly - blue wavelengths. A spectroscopic study of the absorption and fluorescence properties is given, and the processes responsible for the generation of the observed wavelengths are outlined.

To the best of our knowledge, this thesis presents the first systematic study of optical bistability in any doped microspherical laser glass. In comparison to other bistable glasses and crystals, IOG-2 microspheres have large contrast between the two bistable states and require very low switching powers. In addition, their small size and room temperature operation, in contrast to other glasses that require cryogenic cooling, make them interesting for miniature devices.

Finally, details of the construction and performance of a homemade, fibre-coupled, external cavity diode laser are given.

Glossary of Acronyms

CW	Continuous Wave
ECDL	External Cavity Diode Laser
EDFA	Erbium Doped Fibre Amplifier
ESA	Excited State Absorption
ETU	Energy Transfer Upconversion
FSR	Free Spectral Range
GSA	Ground State Absorption
JO	Judd-Ofelt
LL	Light in - light out
OB	Optical Bistability
OSA	Optical Spectrum Analyser
PA	Photon Avalanche
SEM	Scanning Electron Microscope
SMF	Single Mode Fibre
TIR	Total Internal Reflection

WDM	Wavelength Division Multiplexer
WGM	Whispering Gallery Mode
ZBNA	ZrF4-BaF2-NaF-AlF3
ZBLALiP	ZrF4-BaF2-LaF3-AlF3-LiF-PbF2
ZBLAN	ZrF4-BaF2-LaF3-AlF3-NaF

List of Figures

List of Tables

Introduction

Optical glasses are a huge driving force behind technological progress in our society. One of mankind's most challenging programmes to control nuclear fusion, through a process known as inertial confinement fusion, relies on neodymium doped glass lasers to heat and compress deuterium/tritium fuel pellets. Such lasers use either silicate or phosphate glasses to deliver TeraWatts of power. In the other extreme, clinical dentistry has found more prosaic applications for erbium doped YAG lasers in the preparation of tooth enamel, delivering sub-mW powers [1]. One of the great successes of solid-state and semiconductor technology has been the development of miniature, i.e. micron-sized, light structures for use in integrated circuits and telecommunications. Such light structures have reached a high degree of sophistication, e.g. operating at GHz and offering ultra-narrow linewidths - with many relying on nonlinear processes - and come in numerous designs, e.g. microcavities [2], VCSELs (Vertical Cavity Surface Emitting Lasers), and photonic crystal fibres [3].

Microcavities have a particularly unique combination of properties which have been the subject of intensive research and rapid developments in the last decade. Braginsky and Ilchenko [4] realised at an early stage that the strong temporal (up to 10^{-6} s) and spatial confinement (10^{-11} cm^{-3}) of the cavity mode, and the small

device size (typically < 200 μm diameter), could meet the technical needs of all-optical computers. Earlier work by Garret *et al.* [5] in the 60's had shown stimulated emission from CaF_2 doped Sm^{2+} millimetre sized spheres when pumped with a xenon flashtube. Subsequent work began to exploit the combined advantages of using a high quality microcavity and different rare earth dopants in a wide variety of glasses.

1987 was a fortuitous year for these whispering gallery mode (WGM) resonators. Braginsky and Ilchenko [4] provided the first demonstration of an ultra-high quality (Q) factor ($> 10^7$) in a passive, micron-sized silica resonator, and Baer [6] demonstrated the first laser action in a solid-state resonator by using Nd:YAG spheres with a diameter of 5 mm and a lasing threshold of 100 mW.[1] Today, some twenty years later, the Q factor of silica resonators has risen from 10^6 up to 10^{10}. The Q factor determines the ability of a cavity to build up very high circulating fields. In fact, Savchenkov and co-workers have recently described [7] how they achieved exceptional Q factors ($> 10^{11}$) in a CaF_2 crystal microtoroid, using an annealing and polishing technique. This is far in excess of so-called super Fabry-Pérot cavities which can have Q factors of up to 1.9×10^6 [2] at optical wavelengths.[2] Current day resonators are a factor of ten smaller in both diameter ($\sim$50 μm) and threshold power ($\leqslant$100 μW) and, hence, we term these resonators "microcavities". More specifically, in the case of the work presented in this thesis, microspheres are the resonator of choice.

The strong confinement of the cavity mode ensures immense enhancements of the light field - an important requirement for the observation of nonlinear processes. For

[1] In a general sense, the quality factor is defined as the energy stored in the cavity at a particular wavelength divided by the loss rate at this wavelength.

[2] A record high finesse of 4.6×10^9 was demonstrated in a Fabry-Pŕot cavity but operated in the microwave region, while the work in this thesis focusses on optical wavelengths. Due to its operation at this wavelength, the quality factor (4.2×10^{10}) is still less than Ilchenko's microtoroid.

example, in the case of a typical doped microsphere with a Q factor of 10^6, for 1 mW light coupled in, the cavity mode power can be amplified by a factor of 10^4 to 10 W. In passive cavities, with much higher Q factors, the mode can reach up to kW's of power. Early work on nonlinear processes in liquid microdroplets by Lin *et. al* [8] demonstrated stimulated Raman scattering. Stimulated Brilluoin scattering was shown by Zhang and Chang [9]. Others had also shown very low threshold powers for dispersive bistability in microspheres, which had the effect of overwhelming any observable Kerr nonlinearity at room temperature. Later, Treussart *et al.* [10] produced measurements for Kerr nonlinearity in a silica microsphere at 2 K. Following the development of ultra-high Q resonators, along with fibre taper coupling techniques, several studies realised low threshold, high efficiency stimulated Raman emission [11], parametric oscillations [12], and cascaded Raman lasing [13] in silica microspheres and microtoroids, as well as a measurement of the Kerr nonlinearity at room temperature [14].

Optical bistability (OB) in a sodium vapour was first reported by Gibbs in 1976 [15] and, since then, numerous other materials exhibiting the phenomenon have been studied, including Yb^{3+} doped glasses and crystals, and semiconductors [16]-[22]. A device with this attribute must have a nonlinear process and a feedback mechanism that causes the output signal to operate in either of two stable output states that are dependent on the history of the input signal. The mechanisms responsible for nonlinearity in doped glasses and crystals are varied, with many requiring cryogenic temperatures (typically < 40 K) to maintain the necessary low atomic decay rates in Yb^{3+} dimer and monomer systems [17]. Alternative and more easily achievable mechanisms include photon avalanche and thermal avalanche [16, 19], suggesting that

a wider range of materials can exhibit OB at room temperature and above. However, no evidence of OB through these mechanisms in this temperature range has yet been observed. Bistable sensitised luminescence in Er^{3+}:Yb^{3+}:$CsCdBr_3$ was shown by Redmond and Rand [17], and, subsequently, by Ródenas *et al.* [18] in a Nd^{3+}:Yb^{3+} co-doped crystal. They also described *chromatic* or *wavelength* switching in addition to the more traditional *intensity* switching, though both mechanisms required temperatures well below room temperature. To date, OB has also been predicted and observed in Yb^{3+} doped oxide crystals, Cr-doped $LiSrGaF_6$ and $LiSrAlF_6$ crystals [19], Sm^{3+} doped glass microspheres [20], and Tm^{3+}:Yb^{3+} co-doped glass [21]. The latter system exhibited multiple hysteresis loops in the fluorescence intensity at room temperature. The experimental realisation of a doped glass/crystal microsphere exhibiting bistability has been limited to a single paper on the effect in a Sm^{3+} doped glass [20].

This work is focused on the development and analysis of bistable fluorescent and lasing emissions from Er^{3+}:Yb^{3+}-doped phosphate glass microspheres. Dispersive bistability is often seen as a hindrance for many applications involving passive cavities, such as filtering, as it causes microcavity line broadening and bistable wavelength response [11]. These effects are generally well understood. It is, however, not known how bistable microspheres behave when doped. This aspect of doped microspheres is shown to have beneficial qualities for applications such as optical switching and temperature sensing devices. In particular, cavity temperatures as high as 742 K, just below the glass transition temperature, can arise without any structural damage.

Heavy metal fluoride glasses, such as the commonly used ZBLAN glass, were developed by the Poulain brothers in 1974 as an ultra-low-loss material transmitting

from the UV ($\sim$ 250 nm) to the mid-IR (8 μm) with 0.001 dB/km loss at 2.6 μm. The name ZBLAN arises from its constituent elements: ZrF_4 BaF_2 LaF_3 AlF_3 NaF. When dealing with wavelengths in the mid and near IR, applications such as dentistry, remote IR spectroscopy, and industrial quality control can benefit from this large, high-transmission window. In contrast, silica fibres can only transmit from the UV ($\sim$ 250 nm) to the near IR ($\sim$ 2 μm). Unfortunately, ZBLAN glass has suffered from difficulties in glass fibre manufacturing due to crystallisation (see [23] for an overview of fluorozirconate glasses). An alternative material, ZBLALiP, was mooted as possibly having better shaping properties for fabricating fibres and microspheres [24]. In this work, we build on this argument and show additional benefits of ZBLALiP in terms of very efficient upconversion fluorescence emissions in the 320-850 nm range. We have performed a comprehensive Judd-Ofelt analysis in order to understand the glass behaviour when doped with erbium.

The layout of this thesis is as follows:

A general introduction to the optical properties of microspheres is presented in Chapter 1. This provides a groundwork for the rest of the thesis. Parameters such as resonance positions, quality factor limitations, mode volume, and electric field profiles are summarised. The fabrication of the doped microspheres used in this work is also discussed. There is a brief introduction to the topic of optical spectroscopy of laser glasses, which is later used in Chapters 3 and 4. Several topics are covered: the difference between glasses and crystals, selection rules for radiative transitions, Einstein A and B coefficients, excitation mechanisms in ions with multi-phonon decay, and finally thermal issues.

The two different microsphere-coupling schemes that we considered are discussed

in Chapter 2: angle-polished fibres and tapered fibres. The latter scheme was chosen as the most appealing on the basis of its reported ability to provide the most efficient excitation of resonant modes in microspheres [25]. The spatial extent of the evanescent field in the fibre is outlined, after which fibre taper fabrication with a CO_2 laser and the characterisation of such fibres is discussed.

In Chapter 3 the methods outlined in Chapter 1 are used to analyse the fluorescence emissions and absorption data from Er^{3+}:ZBLALiP. The glass is shown to have high upconversion rates yielding strong upconversion fluorescence.

Experimental results of optical bistability in Er^{3+}:Yb^{3+} phosphate glass microspheres are given in Chapter 4. The results are explained in terms of dispersive bistability. Thermal issues related to phosphate glass are shown to give rise to nonlinear behaviour in the intensity and wavelength output. Full confirmation of the dispersive bistability effect requires using a narrow linewidth 980 nm laser to probe the individual cavity resonances. For this purpose, an external cavity diode laser has been built, the details of which are given in Chapter 5.

Finally, the main achievements of the research work are summarised in Chapter 6. Thermally induced bistability can potentially display add-drop filtering capability. ZBLALiP microspheres may serve as laser sources at visible wavelengths, 1.5 μm, and possibly at 2.6 μm, if ultra low-loss fluorozirconate glass technology can be further exploited.

Chapter 1

Optical Properties of Doped Microcavities

1.1 Introduction

Some insight into electromagnetic resonances in a microsphere is presented in this Chapter. In this chapter I provide some insight into electromagnetic resonances existing in a microsphere. Efficient coupling to a microsphere requires that the propagation modes of light in the coupling element match the WGMs within the sphere. Several factors can affect the quality factor including material losses and coupling losses. The total unloaded quality factor, i.e. without any coupling device, and the modal confinement are calculated under realistic experimental conditions. Finally, the concepts and different types of analyses of laser glass spectroscopy that will be used later in the work are introduced. I conclude the chapter by introducing concepts and different types of analyses in laser glass spectroscopy that will be used later in the thesis.

1.2 Whispering Gallery Modes

Whispering gallery modes can occur in a symmetrical structure when a wave undergoes total internal reflection (TIR). In the geometrical-optic model, if a ray strikes the glass-air interface of a spherical cavity such that the angle of incidence is greater than the critical angle, TIR will occur (c.f. Fig. 1.1(a)). The ray is reflected and, due to the symmetry of the cavity, strikes the glass-air interface again at the same angle. In the case of large microspheres, i.e. radius $\gg$ wavelength of trapped light ($a \gg \lambda$), the light ray will be trapped by this mechanism and can propagate continuously around the inside wall giving rise to a standing wave, hence the concept of resonant modes. The integer number of these wavelengths around a single revolution can be denoted by the equatorial mode number, l.

The momentum, p, of a photon is $p = \hbar k = 2\pi\hbar/\lambda$, where $\hbar$ is Planck's constant divided by 2π, and k is the wavenumber inside the sphere. The angular momentum, $\hbar l$, of the photon when it strikes the surface with near glancing incidence is $\hbar l = 2\pi a n_s \hbar/\lambda$, where n_s is the refractive index of the sphere. The integer l is the angular momentum of the photon of unit $\hbar$ and is pointing into the page with reference to Fig. 1.1(a). An important variable describing the resonance condition is the size parameter, $x_{nl} = 2\pi a/\lambda$. Figure 1.1(b) shows the spherical coordinate system which is used to model the WGMs in the next section.

1.3 Electromagnetic Description of Modes

A mathematically realistic description of the electromagnetic field patterns in a microsphere begins with the solution of the Helmholtz equation in spherical coordinates

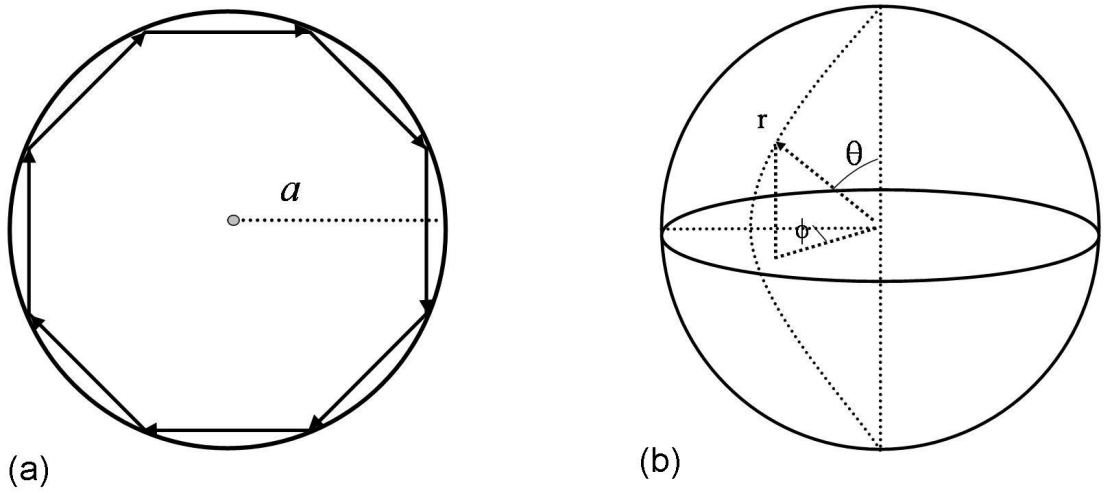

Figure 1.1: WGM in a microsphere. (a) Ray propagation around the sphere by TIR; (b) Spherical coordinate system.

(see [26] for example). The solution is obtainable from the scalar wave equation

$$\nabla^2\Psi(r) + n_s^2 k^2 \Psi(r) = 0, \tag{1.1}$$

by assuming a constant polarisation. There are four solutions to Eqn. 1.1 corresponding to the transverse electric (TE) and transverse magnetic (TM) components of the sphere's electric and magnetic fields. Spherical Bessel (Hankel) functions describe the radial fields inside (outside) the sphere, and these are given by

$$\begin{aligned}
\overrightarrow{E}^{TE}(r,\theta,\phi) &= \begin{cases} j_l(n_s kr)\overrightarrow{X}_{lm}(\theta,\phi) & r \le a \\ j_l(n_s kr)h_l^{(1)}(kr)/h_l^{(1)}(ka)\overrightarrow{X}_{lm}(\theta,\phi) & r > a \end{cases} \\
\overrightarrow{B}^{TE}(r,\theta,\phi) &= -\frac{1}{k}\nabla \times \overrightarrow{E}(r,\theta,\phi) \\
\overrightarrow{B}^{TM}(r,\theta,\phi) &= \begin{cases} j_l(n_s kr)\overrightarrow{X}_{lm}(\theta,\phi) & r \le a \\ j_l(n_s kr)h_{(l)}^{1}(kr)/h_{(l)}^{(1)}(ka)\overrightarrow{X}_{lm}(\theta,\phi) & r > a \end{cases} \\
\overrightarrow{E}^{TM}(r,\theta,\phi) &= -\frac{1}{\varepsilon(\overrightarrow{r})k}\nabla \times \overrightarrow{B}(r,\theta,\phi),
\end{aligned} \tag{1.2}$$

where $j_l(h_l^{(1)})$ are spherical Bessel functions (Hankel functions of the first kind) of order l and $\overrightarrow{X}_{lm} = [l(l+1)]^{-1/2}\overrightarrow{L}Y_{lm}$ and Y_{lm} are vector spherical harmonic functions with $\overrightarrow{L} = \overrightarrow{r}\times(-i\nabla)$. These functions ($X_{lm}$ and Y_{lm}) describe the sinusoidal nature of the field corresponding to reflections of the ray off the sphere surface.

The three mode numbers, n, l, and m, are used to characterise the radial, the equatorial, and the polar components of the electromagnetic field. Mode number n ($n = 1, 2, 3, \ldots$) gives the number of maxima in the radial electromagnetic field distribution. The fundamental ($n = 1$) TM radial mode is depicted in Fig. 1.2(a) and two radial modes are depicted in Fig. 1.2(b). The second mode number, m ($m = -l, -l+1, \ldots, 0, \ldots, l-1, l$), describes the number of maxima in the sinusoidal variation in field intensity in the equatorial or latitudinal direction. Finally, the mode number l describes the field intensity distribution in the polar or longitudinal direction, and can take values $l = 0, 1, 2, \ldots$ with the number of maxima present in the polar field distribution given by $l - |m| + 1$.

For a perfect sphere (zero ellipticity), modes with the same l but different m values have a $2l + 1$ degeneracy, and, therefore, the mode numbers n and l are sufficient to describe the WGM. In reality, some ellipticity exists in the sphere and this removes the degeneracy. For minimal mode volumes one wants n to be small and $m \approx l$, as shown in Fig. 1.3. The spheres used in the present studies have a diameter in the range 50 - 200 μm with $< 5\%$ ellipticity. Figure 1.3 shows a cross-section of the field for different values of m and l. We see that the mode volume is lowest for the fundamental mode and increases for more complicated mode structures. In the ray optics picture, the fundamental mode represents a ray with the smallest reflection angle, the lowest diffraction losses, the lowest mode volume, and the highest Q factor.

The fundamental mode in Fig. 1.3(a) is located on the equatorial plane of the sphere. Although modes with $l-|m|>0$ travel with greater inclinations with respect to the equator, they still have the same resonant wavelength as the fundamental mode, since the curvature of the sphere precisely compensates the greater incline. The path length for $l-|m|>0$ modes in Fig. 1.3(a) to Fig. 1.3(d) are all equal, i.e. they are degenerate. Therefore, the equatorial mode number, m, is superfluous when describing the resonance wavelength.

1.4 Resonance Positions

The continuity of the tangential components of the electric and magnetic fields at the sphere surface (see Eqn. 1.2) must satisfy a characteristic equation,

$$n_s^{-2b}\frac{[n_s ka j_l(n_s ka)]'}{j_l(n_s ka)} = \frac{\left[n_s ka h_l^{(1)}(ka)\right]'}{h_l^{(1)}(ka)}, \tag{1.3}$$

where b is the polarisation (equal to 1 for TM modes and 0 for TE modes). The prime denotes differentiation with respect to the argument. The position and width of the resonances are obtained by numerically solving this characteristic equation. The solution yields discrete values of frequency at which resonances are possible. In practice, the locations of these resonances are found by scanning a tuneable diode laser over the free spectral range of the sphere.

The solution to Eqn. 1.3 requires a significant amount of computational time as the resonances have sharp Lorentzian line-shapes. Schiller [27] has used an asymptotic formula to yield an approximation for the resonance frequency in terms of the size

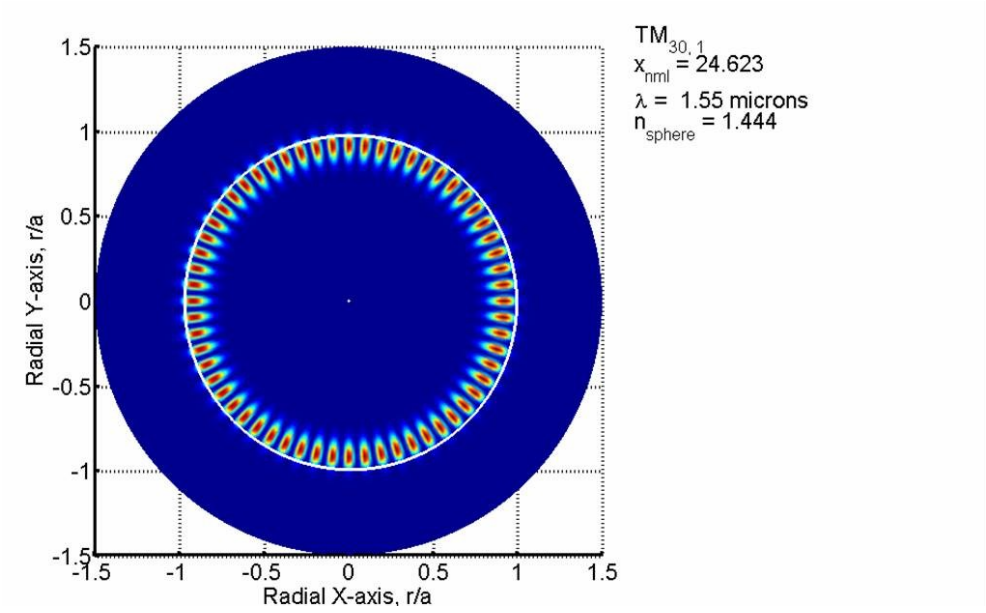

(a)

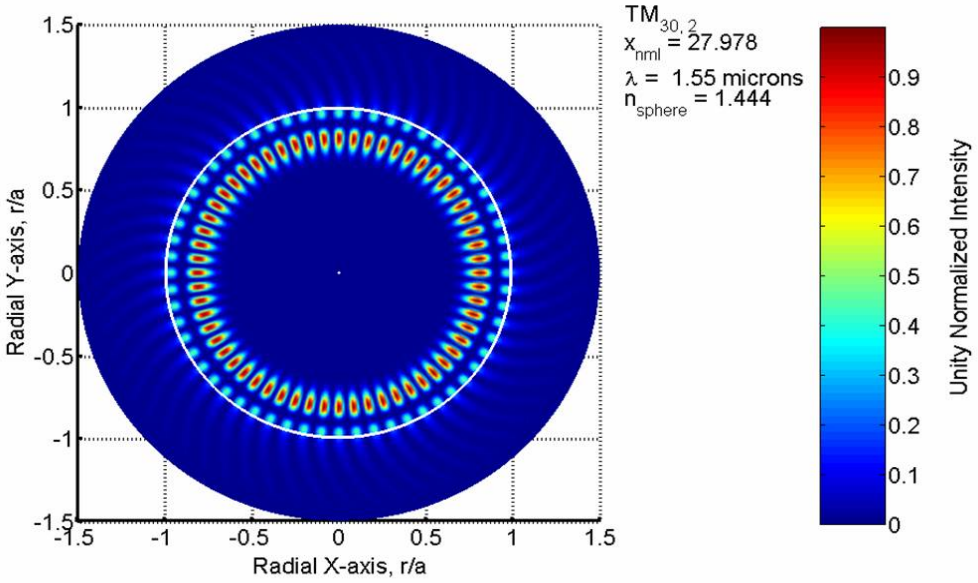

(b)

Figure 1.2: Calculated intensity distribution of the TM mode in the equatorial plane (a) for $n = 1$ and $l = 30$ with $x = 24.623$ (b) and for $n = 2$ and $l = 30$ with $x = 27.978$. The wavelength is 1.55 μm, and the sphere radius and intensity are normalised to unity in both cases.

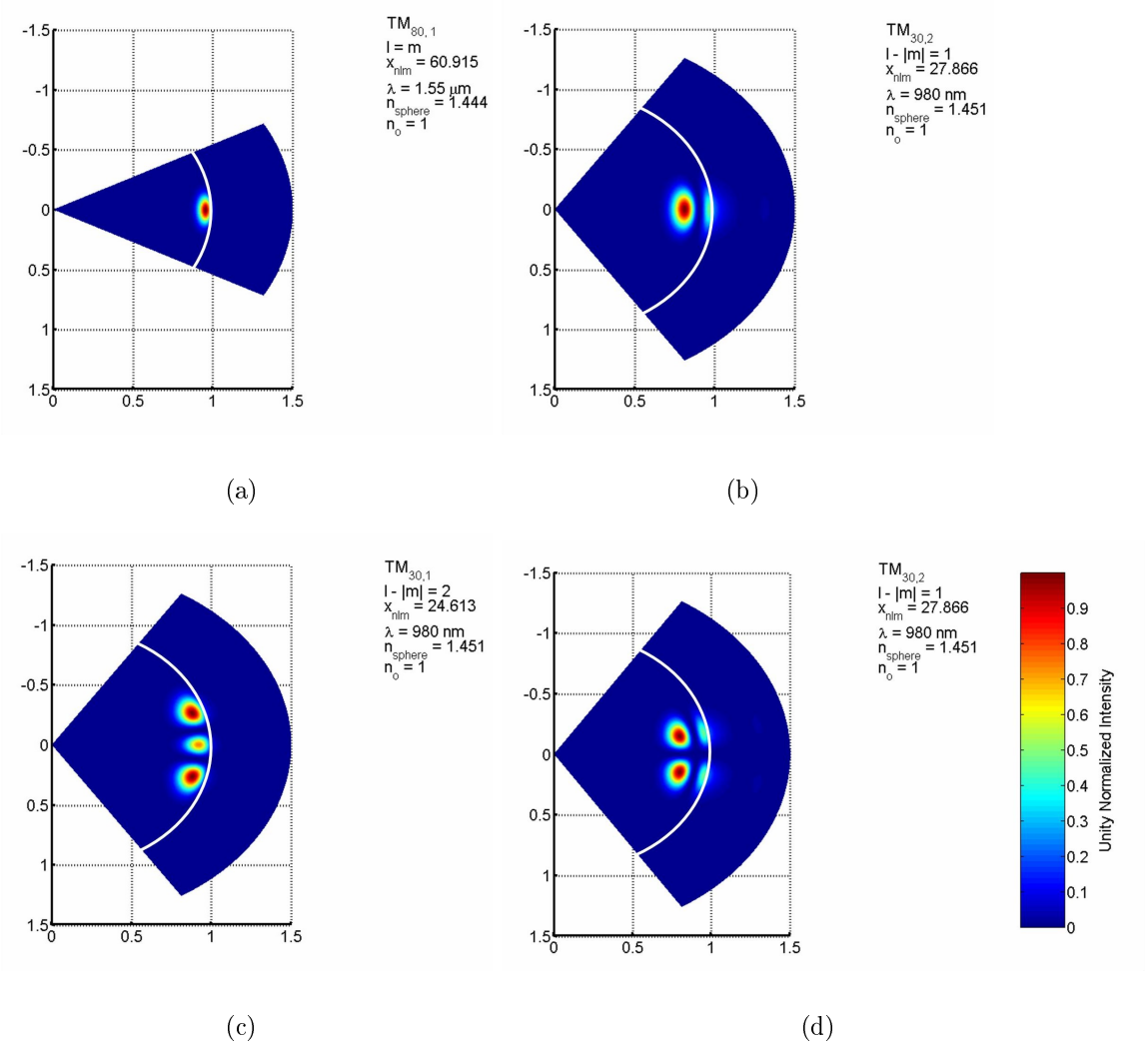

Figure 1.3: Azimuthal intensity distribution for TM modes with (a) $n = 1, l - |m| = 1$, (b) $n = 2, l - |m| = 1$, (c) $n = 1, l - |m| = 2$, (d) $n = 2, l - |m| = 1$. The wavelength is 980 μm, and the sphere radius is normalised to unity.

parameter, x_{nl}, up to order $\alpha = 8$ such that

$$x_{nl} = \frac{\nu}{m} - \frac{\zeta_t}{m}\left(\frac{\nu}{2}\right)^{1/3} + \sum_{\alpha=0}^{8} \frac{d_\alpha(m,\zeta_t)}{\nu^{\alpha/3}(m^2-1)^{\alpha/2}}, \tag{1.4}$$

where $\nu = l + 1/2$, $m = n_s/n_a$, n_a is the refractive index of the surrounding medium, and t is the t^{th} zero of the Airy function, ζ. The coefficients of the expansion are given by the polarisation dependent term $d_\alpha(m,\zeta_t)$.

Identification of these resonances is achieved by measuring the separations of the resonance frequencies $x_{nl} - x_{nl-1}$. The widths of the resonances, $\Gamma_l^{(n)}$, are given at FWHM as [28]:

$$\Gamma_{nl} = 2\left[N x^2 n_l(x)^2\right]^{-1}, \tag{1.5}$$

where n_l is the spherical Neumann function, and

$$N = \begin{cases} n_s^2 - 1, & \text{for TE modes} \\ (n_s^2-1)[\mu^2 + (\mu^2/n_s^2 - 1)], & \text{for TM modes,} \end{cases} \tag{1.6}$$

where $\mu = \nu/x$ with x evaluated at x_{nl}.

1.5 Cavity Quality Factor

Microcavities have exhibited the highest quality factors among all types of resonators. A value of $> 10^{11}$ was reported for a microtoroid at 1559 nm in 2007 [7]. The quality factor is the primary performance characteristic measure of microspheres and is defined in terms of the resonators ability to store energy. In its most simple expression, the Q factor of a resonant system is given as:

$$Q = 2\pi(\text{Energy Stored})/(\text{Power Dissipated per cycle}). \tag{1.7}$$

The Q factor is dictated by the length of time for which a photon can be stored within the cavity and is limited by several other factors apart from the WGM losses. In fact, WGM losses have an appreciable effect only for radii less than about 7 μm [29].

The losses within a microsphere resonator arise due to both internal and external mechanisms. The internal losses result from WGM losses and material losses from the cavity such as surface scattering, water absorption and bulk absorption of the material.

Coupling losses, $Q_{coupling}$, depend on the coupling technique and on the ability to achieve good phase matching between the coupler and the microsphere. We typically use 1-2 μm diameter taper fibres for coupling due to their near ideal performance [25]. These fibres are fabricated by heating and stretching a strand of single mode fibre down to a diameter of 1 μm. An evanescent field forms in this region which is then coupled into an adjacent microsphere. The coupling Q factor is governed by the overlap of the evanescent fields of the fibre taper and the sphere (c.f. page 28 for more details) [30]. The interaction strength between the cavity mode and fibre mode govern $Q_{coupling}$.[1]

It has been found [31] that the Q factor shows an initial rapid decay within the first two to three minutes of fabrication of microspheres. This is due to one or two monolayers of water forming on the surface. Ideally, fabrication should be performed in a vacuum environment. The formula for losses due to water absorption [32] is

$$Q_w \approx \sqrt{\frac{2a\pi}{8\lambda n_s^3}}\frac{1}{\delta\alpha_w}, \tag{1.8}$$

where $\delta \approx 0.2$ nm is the thickness of the monolayers of water, and α_w is the absorption

[1] $Q_{coupling}$ is maximised when the mode matching is optimised in terms of the spatial modes and the propagation constants of the microsphere and fibre taper.

coefficient of water. There is an $a^{1/2}$ dependency, but the wavelength has an inverse square root dependency.

Bulk losses do not exhibit a sphere size dependency. The absorption coefficient of silica, α_s, has a minimum at 1550 nm corresponding to a peak in Q at this value, while for fluorozirconate glass this minimum is at 2.6 μm. We use the form of the equation given in [33], for bulk losses:

$$Q_{bulk} = \frac{2\pi n_s}{\alpha_s \lambda} \tag{1.9}$$

where $\alpha_s \approx (0.7\,\mu\text{m}^4/\lambda^4) + 1.1\times10^{-3}\exp(4.6\,\mu\text{m}/\lambda) + 4\times10^{12}\exp(-56\,\mu\text{m}/\lambda))$dB/km. Bulk losses are dominant for large spheres at 633 nm. (*NB* The Q arising from other loss mechanisms are much higher than Q_{bulk}).

Surface scattering is due to surface roughness and absorption arising from impurities within the cavity. Our passive silica microspheres are produced by melting the tip of a silica fibre and our doped microspheres are fabricated from a powder glass sample (c.f. Section 2.2). While production of the microspheres results in near atomic smoothness owing to surface tension during melting, it has been shown that these minute irregularities not only degrade the Q factor for small spheres, but also cause light to be backscattered into degenerate counter-propagating modes [34]. For silica spheres, it is imperative that the fibre be cleaned with acetone and, sometimes, with other chemicals before production. An accurate model describing the surface scattering Q factor, Q_{ss}, has yet to be found, but observations have found a $(a\lambda)^{1/2}$ relationship [33]. This model is of the form

$$Q_{ss} = \frac{K_{TE}}{1 + K_{TE}} \frac{3\lambda^3 a}{8 n_s \pi^2 B^2 \sigma^2}, \tag{1.10}$$

where K_{TE} is the suppression coefficient defined as the ratio of complete scattered

power to the power scattered into a TE mode scattering angle defined in [33], B is the statistical correlation length, and σ is the average standard deviation of the surface roughness. The TE and TM mode suppression coefficients are 2.8 and 9.6 respectively. The parameters B and σ have been measured [32] to be 5 nm and 1.7 nm respectively.

The size dependence of Q_{ss} for a wavelength of 980 nm is plotted in Fig. 1.4. Apart from sphere size, the choice of pump wavelength will dictate the observed Q. For example, at a wavelength of 633 nm, surface scattering becomes dominant for radii of less than about 20 μm until whispering gallery losses begin to dominate at about 7 μm (not shown). Longer wavelengths do not share this dependence on surface scattering, which is due to the role of the absorption coefficient of water, α_w. This coefficient is only 0.363 m^{-1} at 633 nm and rapidly increases to 799 m^{-1} at 1550 nm. This plays a crucial role in selecting a suitable wavelength and sphere diameter in order to achieve large Qs. The Er^{3+} and Yb^{3+} ions in the glasses under study here have a large absorption coefficient at 980 nm compared to other wavelengths (except C-band wavelengths), thus making ion absorption a dominating factor when choosing the optimal pump wavelength. Unlike the passive microspheres, our doped microspheres are transported from France to our lab in a petri dish, which undoubtedly increases the surface roughness. The importance of the surface roughness for our spheres is shown in Fig. 1.4(b) where we have reasonably assumed degraded surface parameters compared to silica microspheres. The B value is taken as 7 nm and σ is taken as 15 nm. We find a loaded Q factor of 1×10^7 at 780 nm for our ZBLALiP microspheres which corresponds reasonably with the unloaded Q factor in Fig. 1.4(b). We can assume surface scattering losses are the largest loss mechanism.

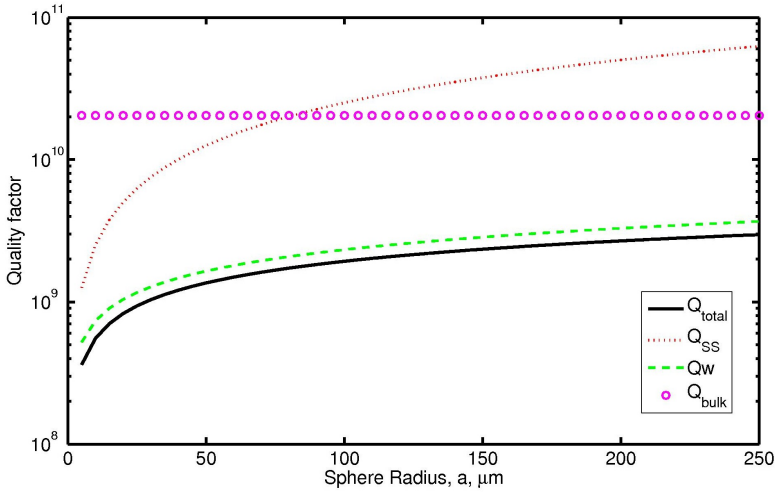

(a) Silica glass

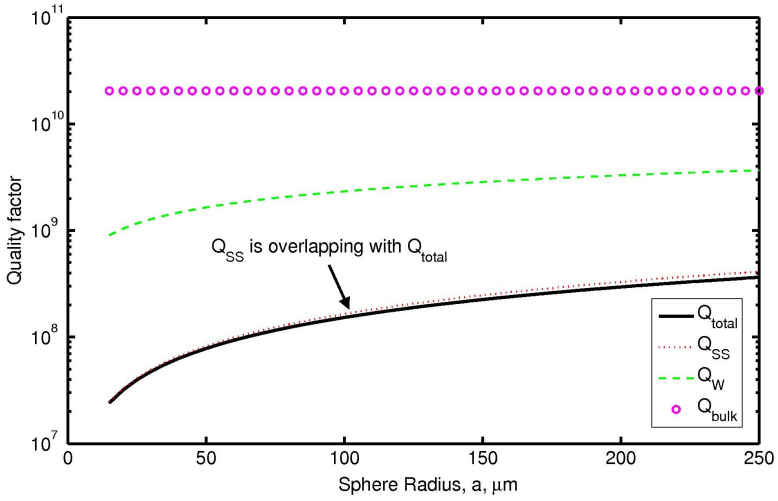

(b) ZBLALiP glass

Figure 1.4: Total quality factor and individual quality factors as a function of sphere diameter at a wavelength of 980 nm. Water absorption limits the Q in silica. In (b), the statistical correlation length, B, and the average standard deviation of the surface roughness, σ, are increased by a factor of about three to simulate the estimated poorer surface quality in our doped microspheres ($B = 7$ nm and $\sigma = 15$ nm). Coupling losses with a tapered fibre have been neglected.

An issue closely related to Q factor is finesse, $\mathcal{F}$, defined as the free spectral range (FSR) divided by the bandwidth of the resonances, or equivalently,

$$\mathcal{F} = \frac{\lambda Q}{2\pi n_s a}. \tag{1.11}$$

To date, the highest reported finesse is 10^7 at an optical wavelength, recorded by Savchenkov *et al.* in 2007 in a CaF_2 microtoroid [7]. As a comparison, the highest reported finesse in a super Fabry-Pérot cavity is 10^5 at optical wavelengths [2].

Each of these individual contributions to the cavity loss can be combined together to give a system Q factor as

$$\begin{aligned} Q_{total}^{-1} &= Q_{wgm}^{-1} + Q_{material}^{-1} + Q_{coupling}^{-1} \\ Q_{material}^{-1} &= Q_{ss}^{-1} + Q_{water}^{-1} + Q_{bulk}^{-1}, \end{aligned} \tag{1.12}$$

where Q_{wgm} is the whispering gallery Q, and $Q_{material}$ is the material Q.

1.6 Mode Volume

The degree of modal confinement in a sphere can be determined by integrating the volume as shown in Fig. 1.3, and, optionally, choosing a $1/e^2$ boundary for the intensity distribution. It is a non-trivial exercise to determine the volume based on the set of formulae in Eqn. 1.2. Despite that, it can be shown that mode volumes can be as small as 1000-4000 μm^3, depending on microsphere size and wavelength. Such tightly propagating modes around the microsphere can easily develop very high excitation densities ($\sim 10^3$ Vm^{-1}) as mentioned earlier. This is very important for studying nonlinear processes and microlaser operation.

The effective mode volume, V_{eff}, is defined as the integral of the square of the

field (Eqn. 1.2) over a quantisation volume, V_Q, and is given by [35]

$$V_{eff} = \int_{V_Q} \epsilon(r,\theta,\psi) E(r,\theta,\psi)^2 dV, \tag{1.13}$$

where the quantisation volume includes both real internal microsphere fields and the imaginary evanescent fields, and

$$\epsilon = \begin{cases} n_s^2, & r \leq a \\ 1, & r > a. \end{cases} \tag{1.14}$$

It can be shown that both TE modes and TM modes have different mode volumes due to slight differences in the configuration of the fields in the cavity (c.f. Fig. 1.5). TE modes are found deeper inside the sphere and, therefore, occupy a smaller volume (and an associated higher Q factor), as given by [36]

$$\begin{aligned} V_{TE} &\approx 1.02(2a)^{11/6}(\lambda/n_s)^{7/6} \\ V_{TM} &\approx 1.08(2a)^{11/6}(\lambda/n_s)^{7/6}. \end{aligned} \tag{1.15}$$

There is also an alternative definition of mode volume for nonlinear processes [37]

$$V_{eff} \approx \frac{\left(\int_{V_Q} E(r,\theta,\psi)^2 dV\right)^2}{\int_{V_Q} E(r,\theta,\psi)^4 dV} \tag{1.16}$$

$$\approx 3.4\pi^{3/2}(\lambda/2\pi n_s)^3 l^{11/6}\sqrt{l-m+1}, \tag{1.17}$$

where $l \approx 2\pi a n_s/\lambda$. In the case of both Eqns. 1.15 and 1.17, the volume scales as $a^{11/6}$. However, as can be seen from Fig. 1.5, which presents the quantum and nonlinear mode volumes, there are some differences in the definitions.

Another issue to note is the difference in mode volume between the pump wavelength for Er^{3+} (980 nm) and the lasing wavelength (1.5 μm): the volume scales almost linearly with wavelength. Therefore, the gain region in the 1.5 μm mode is some 1.7 times larger than the excitation region.

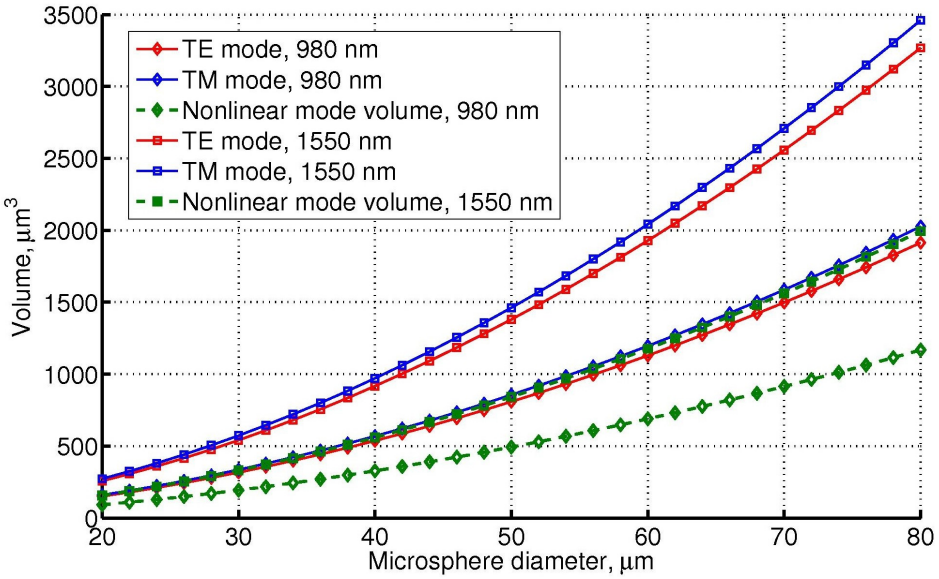

Figure 1.5: Mode volume for a doped microsphere with $n_s = 1.5$ for $\lambda = 1550$ nm (squares) and 980 nm (diamonds). The TE modes have a slightly smaller mode volume. In contrast, the nonlinear mode volume (green markers) is at variance with the quantum mode volumes (red and blue markers).

1.7 Spectroscopy of Rare Earth Ions

The lanthanides, or rare earths as they are referred to in this thesis, have unique spectroscopic properties arising from their electronic configuration. The material sciences have an intense interest in the properties of glasses, crystals, and ceramics doped with these ions (e.g. Ce^{3+}, Nd^{3+}, Sm^{3+}, Ho^{3+}, Er^{3+}, Tm^{3+}, and Yb^{3+}). All transitions occur with 4f electrons deep within the ion, shielded by optically passive outer electrons in the filled 5s and 5d shells. This shielding "protects" the transitions from interactions with fields in the lattice environment. Evaluation of the glass behaviour must include aspects of the spectroscopic properties, such as Judd-Ofelt parameters, McCumber analysis, and cavity effects.

This work is concerned with Er^{3+} doped fluoride and phosphate glasses, which exhibit large homogeneous and inhomogeneous broadening of the levels compared to doped crystals. The inhomogeneous broadening arises from an overlap of Stark levels arising from the location of individual lattice sites for the rare earth ions, despite the aforementioned shielding. The homogeneous broadening arises because phonons affect all ions by smearing out the transitions and energies of emitted photons with approximately the same magnitude as inhomogeneous broadening.

1.8 Selection Rules for Er^{3+}

In principle, there should be no emissions from Er^{3+} due to the selection rules; all transitions have the same parity and are, therefore, not allowed. Judd-Ofelt theory reveals, however, that certain transitions are in fact weakly allowed when the 4f electrons are mixed with the 5d electrons. These 5d electrons have opposite parity

to the 4f electrons. If transitions in the 4f levels were allowed by selection rules, the lifetimes would typically be less than a few nanoseconds. Since the transitions in the 4f levels are only weakly allowed, the lifetimes can range from hundreds of microseconds to milliseconds for metastable levels.

The parameters describing the strength of these transitions are the electric dipole oscillator strength and, to a lesser extent, the magnetic dipole oscillator strength. It is important to note that higher order interactions are also possible. The selection rules for electric dipole transitions in their most rigorous form are in Table 1.1 [38]. The notation in the table is used to designate energy levels in the form $^{2S+1}L_J$, e.g., $^4I_{15/2}$ for the ground level in Er^{3+} has $S = 3/2$, $L = 6$, and $J = 15/2$. The symbol J is taken to mean the total angular momentum unless stated otherwise.

Table 1.1: Rigorous selection rules for electric dipole transitions.

Spin quantum number	$\Delta S = 0$
Orbital angular momentum	$\Delta L = \pm 1$
Total Angular Momentum	$\Delta J = 0, \pm 1, J = 0 \nrightarrow 0$

Absorption measurements over a wide spectral range - from UV to near IR - form the basis for theoretical calculations. The McCumber theory is a powerful, and yet simple, tool that equates the absorption cross-section to the emission cross-section based on absorption measurements. Conceptually, the absorption cross-section is the area of the ion that will absorb a photon passing through it. In a similar vein, the emission cross-section is the area of the ion that will emit a photon. Therefore, the cross-section can be interpreted as a probability of absorbing or emitting a photon.

1.9 Radiative Emission Rates

In the previous section we mentioned a number of techniques for studying laser behaviour, i.e. Judd-Ofelt theory and McCumber theory. Before proceeding, we describe three processes by which light can interact with matter: absorption, spontaneous emission, and stimulated emission. These interactions are ascribed with three Einstein Coefficients: $B_{J',J}$, $B_{J,J'}$, and $A_{J,J'}$ respectively. For the two level system in Fig. 1.6, these interactions are related through the equation

$$N_{J'}B_{J',J} = N_J(B_{J,J'}g(\lambda) + A_{J,J'}), \tag{1.18}$$

where N is the population of the upper (J) or lower (J') levels, and $g(\lambda)$ is a lineshape function describing the emission probability of a photon with wavelength λ. This lineshape function is given by Planck's Law.

In reality, levels J and J' are composed of Stark-split levels, populated according to Boltzmann's equation. Figure 1.7 shows the population distribution for the lasing transition in Er^{3+}. The upper Stark-split level in $^4I_{13/2}$ is only 32% of the lower Stark-split level. This means that the Einstein coefficients need to be taken as the sum of each coefficient over all the transitions from each Stark level M [38]. For the spontaneous emission rate $A_{J,J'}$, this becomes

$$A_{J,J'} = \frac{1}{2D'+1}\sum_{M_J,M_{J'}} A'_{J,J'}(M_J, M_{J'}), \tag{1.19}$$

where D' is the degeneracy of level J'. Later in this thesis we will apply this theory to Er^{3+} doped ZBLALiP.

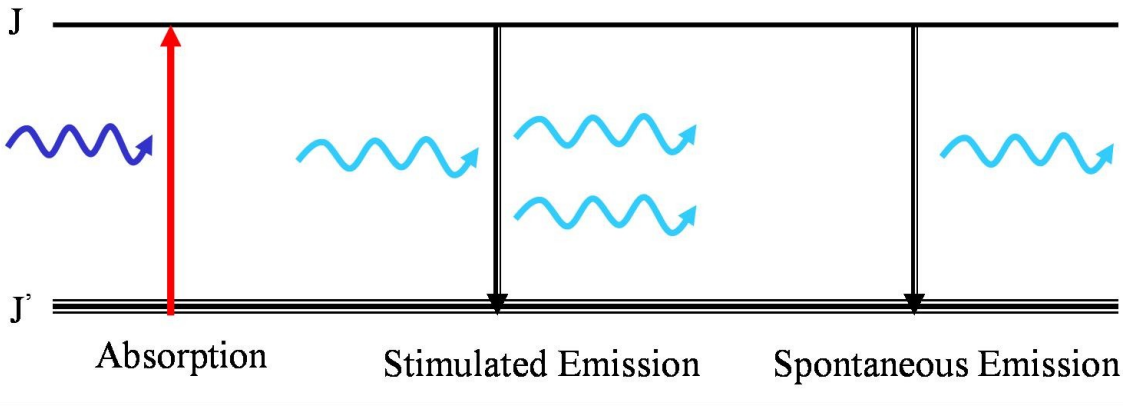

Figure 1.6: Fundamental light-matter interactions in a two level system. The notation J and J' designate the upper and lower energy levels respectively.

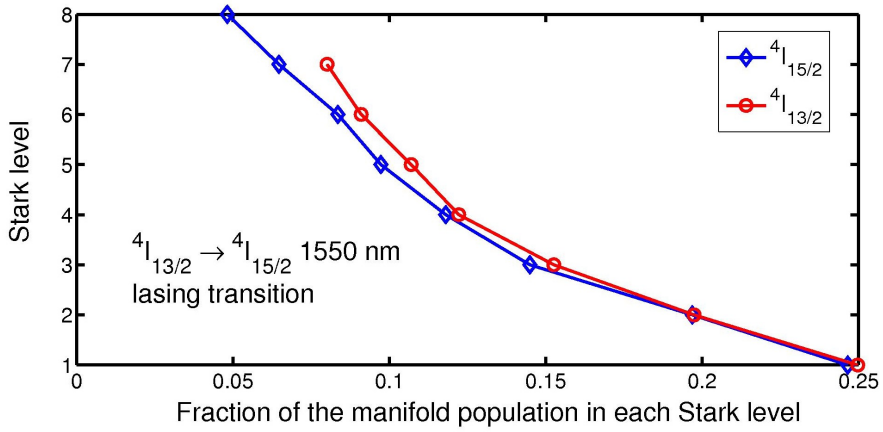

Figure 1.7: Population of each of the Stark levels for the 1.5 μm lasing transition ($^4I_{13/2} \rightarrow {}^4I_{15/2}$) in Er^{3+}.

1.10 Material Loss Mechanisms in Lasers

In Section 1.5 several cavity loss mechanisms that degrade the Q factor were mentioned. In this section we consider a number of material loss mechanisms inside the laser cavity that affect the lasing quantum efficiency. The efficiency in a downconversion laser, $\eta = dP_{out}/dP_{in}$, is governed by the energy conservation rule $E_{signal} < E_{pump}$, assuming that all the incident photons are absorbed.[2]

For most doped glasses, there will be some combination of interionic processes, such as excited state absorption (ESA), energy transfer upconversion (ETU), and co-operative upconversion competing with the 1.5 μm lasing emission. Upconversion is where an electron in an ion can be excited to successively higher energy levels either by (i) repeated excitation by pump photons or photons emitted from other ions (i.e. radiation trapping), or by (ii) dipole-dipole interactions with one or more excited ions a few Å apart. Case (i) usually dominates over case (ii) when the dopant concentration is not excessive and clustering/nucleation is absent. A good overview of upconversion processes is given in reference [39].

Phonon energies are significantly large compared to the energy gap between levels such that multi-phonon decay to lower levels cannot be ignored. This effect causes heating of the glass, and is especially prominent in Er^{3+}:Yb^{3+} co-doped phosphate glasses due to the high phonon energy up to 1300 cm^{-1}. Fluoride glass has much lower phonon energies of 600 cm^{-1} maximum. The thermo-optic effect and thermal expansion of the cavity can cause thermal lensing which can seriously degrade the cavity power build-up and cause the lasing wavelength to shift. The lensing effect,

[2]The quantum efficiency is the fraction of incident photons contributing to lasing. The quantum defect is the ratio of the energies between the pump and lasing photons.

which is negative for both fluoride and phosphate glasses, results from an unequal refractive index variation across the pump beam's Gaussian profile. Mode propagation becomes distorted in the presence of this lensing. These issues have varying degrees of importance in the two glasses of study and will be elucidated in later chapters.

Chapter 2

Fabrication of and Coupling to Microspheres

2.1 Introduction

In this chapter we expand on the brief introduction to tapered fibre coupling to microspheres in Chapter 1. After giving a description of the microsphere fabrication and coupling details, the procedure for fabricating and characterising tapered fibres - our coupling element of choice - is outlined. In terms of coupling, the taper mode must be overlapped both spatially and spectrally with the microsphere mode. The evanescent wave component of the light field is used for this purpose, and we present how one can ensure that the coupling technique satisfies the mode-matching requirements when a taper fibre is used as the coupling component. Spatial mode matching requires good taper-microsphere alignment, and spectral mode matching is achieved by matching the propagation constant of the taper with that of the microsphere.

2.2 Microsphere Fabrication

All the doped microspheres used for this thesis work are made in the Laboratoire d'Optronique of ENSSAT, Lannion using a microwave plasma torch. The torch is shown schematically in Fig. 2.1 and uses a mixture of argon and oxygen or nitrogen. The plasma is generated using a microwave supply with an oscillator frequency of 2.4 GHz and a maximum power of 2 kW [40]. Fluoride or phosphate glass is first crushed into a powder and is then slowly fed into the flame by hand. The glass is melted on passing through the plasma flame and surface tension gives the spheres their spherical form. After passing through, the free spheres solidify and are collected in a dish several tens of cm beneath the torch. The diameter of the spheres produced varies between 10 μm and 200 μm and is largely dependent on powder size. The system can be optimised for different glass materials by changing the ratio of the gases feeding the plasma discharge.

The quality of the resulting microspheres is reliant on the black-art of carefully selecting a suitable gas flow rate for the melting point of the glasses. Evidently, the most important factor in determining the Q factor is the surface roughness, which must be somewhat higher than that for silica microspheres fabricated from the end of a tapered fibre using a CO_2 laser, as outlined below. We have assumed that nucleation of the dopant ions is not a problem.

Silica microspheres were fabricated by placing the end of a tapered fibre into the beam of a 20 W Synard CO_2 laser. Silica is highly absorbing at the lasing wavelength of 10.2 μm and melts into a spherical shape under surface tension. The scanning electron microscope image in Fig. 2.2 shows the internal "fetal-like" structure obtained with clearly defined core and cladding regions. As glass is a poor reflector

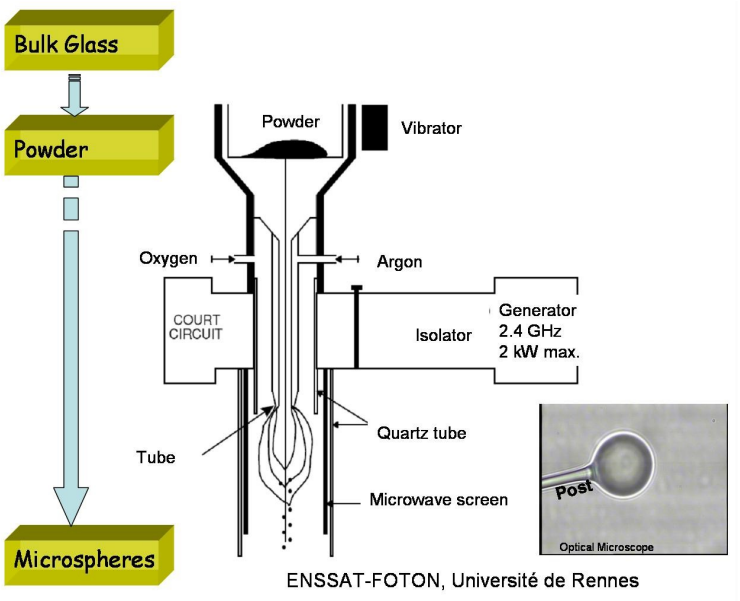

Figure 2.1: Microsphere fabrication with a microwave plasma chamber. A bulk sample is first ground into a powder and then injected through a quartz tube to a flame, where microspheres form under surface tension. The microsphere can later be mounted on the end of an optical fibre for manipulation (see bottom right image).

of secondary electrons, they penetrate deep into the glass while very few electrons originate from the glass surface. The structure reveals that a WGM will propagate in the cladding material which forms the microsphere surface. This affects the Q factor in so much as absorption losses in this cladding material are higher than in the silica core. In future work it may be possible to exploit the low absorption loss of silica by first removing the cladding through etching with HF acid and then fabricating a microsphere with the CO_2 laser.

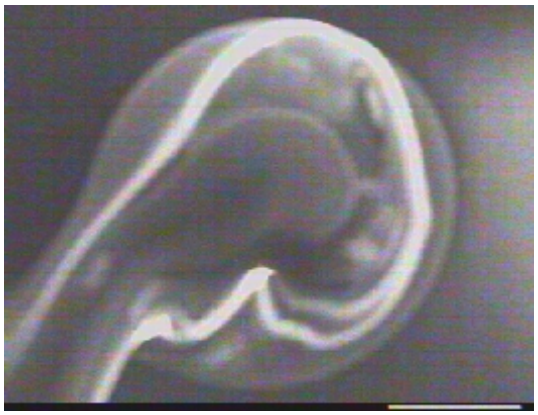

Figure 2.2: Scanning Electron Microscope image of a silica microsphere fabricated by melting the end of a tapered optical fibre. The electrons penetrate into the microsphere, revealing the fibre core in the centre and cladding in the outer region, where the WGM should propagate.

2.3 Introduction to Coupling

Techniques for evanescent coupling of light into microspherical cavities include prism couplers [41], optical fibre half-block couplers [42], angle-polished fibres [43], and fibre tapers [40]. Fibre tapers have proven to be the most attractive device for achieving near loss-less coupling of light into microspherical cavities and exciting the fundamental resonant mode [25, 40]. The overlap of the taper and microsphere evanescent fields defines the strength of this coupling [30]. The attainment of small taper diameters, typically in the range of 1 to 4 μm, is critical to maximise this coupling. Recent discussions on the form of the evanescent field have shown the spatial extent of the radial component of the field to greatly increase for diameters less than 2 μm [44, 45]. It has also been reported that efficient coupling of light into sub-millimetre sized silica microspheres is possible for taper diameters up to 4.5 μm [46].

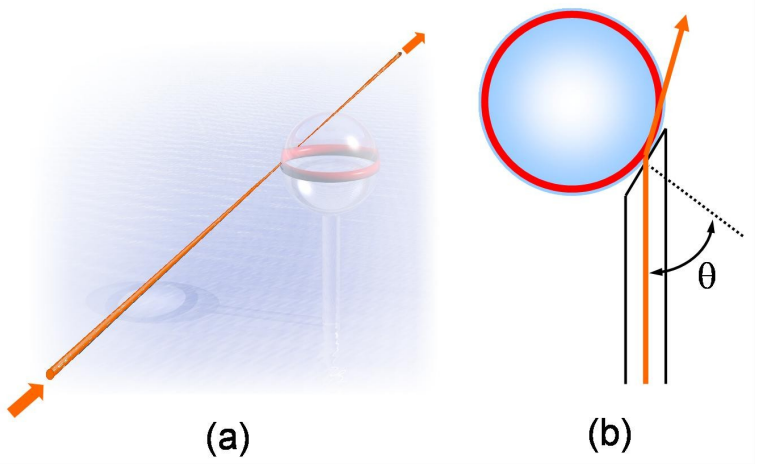

Figure 2.3: Schematic of (a) tapered fibre-microsphere and (b) angle-polished fibre-microsphere coupling schemes.

We start by briefly summarising two of the most commonly used coupling schemes nowadays: angle-polished fibres and tapered fibres. The advantages and disadvantages of both schemes are discussed with reference to phase matching constraints and maximal coupling efficiencies. The schematic in Fig. 2.3 explains the basic concept behind the two techniques.

2.3.1 Angle-Polished Fibres

We initially investigated these couplers as a robust method of coupling. The device is a hybrid of the more traditional prism and taper couplers [43]. The fabrication consists of polishing the end of a single mode fibre to an angle sufficient to obtain efficient coupling into the sphere. By placing the sphere at the polished surface, TIR conditions will be met. Likewise, this is the case with prism coupling. Therefore, the phase matching condition is controlled by the polish angle, $\theta = \arcsin(n_{sphere}/n_{fibre})$.

The effective index of the resonant mode in the sphere is found from $n_{sphere} = l n_s / x_l^{(n)}$ where n_s is the refractive index of the sphere material, for example silica, as determined from the Sellmeier dispersion formula, and l is the polar mode number. The effective index of the fibre is assumed to be β/k, where β is the propagation constant for the sphere material and k is the free space propagation constant, and is evaluated from Eqn. 2.1 for the fundamental HE_{11} mode. Figure 2.4 shows the required polish angle as a function of sphere radius for $n = 1$ and $n = 2$ modes at a wavelength of 980 nm. For decreasing sphere sizes the phase matching condition becomes more selective with almost a 1° angle to 1 μm diameter correspondence.

Among the advantages of angle-polished fibres are their robustness and small package size. Further advantages of angle-polished fibres are the ease of alignment of the sphere and fibre as the interaction region is larger, and good coupling efficiencies of up to 60% [43]. One disadvantage of using fibre tapers is the competing requirement of small diameter to maximise the evanescent field, against a suitably large diameter for good phase matching. For example, a silica fibre diameter of 6 μm is required to phase match an Er^{3+}:ZBLAN sphere with a diameter of 100 μm [40]. The fraction of the field in the core of the fibre is 100% for this diameter taper.

2.3.2 Tapered Fibres

In order to effectively couple light into a microsphere, the angular momentum and propagation constant of the pump beam must match that of the WGMs within the sphere, in such a way that there is phase matching at the point of closest contact. We decided on tapered fibres as opposed to angle-polished fibres to achieve this. Light is coupled between the microsphere and fibre via evanescent wave coupling.

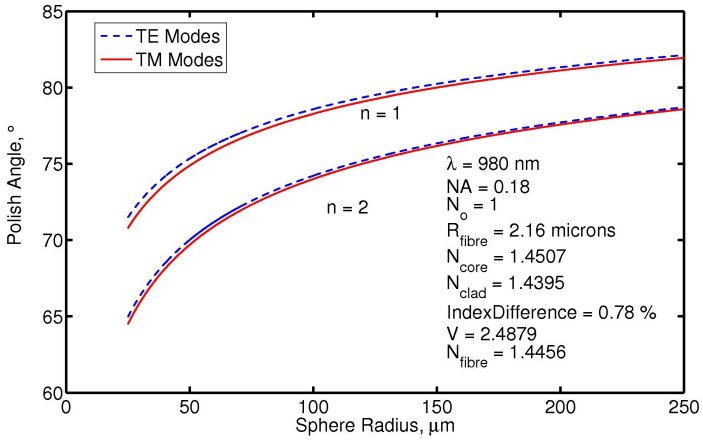

Figure 2.4: Calculated polish angle as a function of sphere radius for a wavelength of 980 nm for the fundamental $n = 1$ mode, and the $n = 2$ mode.

The technique involves overlapping the sphere with the evanescent field of the fibre while maintaining good phase matching. In contrast to angle-polished fibres, tapered fibres can achieve greater than 99% coupling efficiency when operating at their critical coupling position [25].

2.4 Mode Propagation Constants

The transcendental equation for the propagation constant of a fibre is given by [47]

$$\left[\frac{J_n'(ha)}{haJ_n(ha)} + \frac{K_n'(qa)}{qaK_n(qa)}\right]\left[\frac{n_{core}^2 J_n'(ha)}{haJ_n(ha)}\right] = \left[\frac{n\beta}{k}\right]^2 \left[(qa)^{-2} + (ha)^{-2}\right]^2, \qquad (2.1)$$

for HE_{nm} and EH_{nm} modes, where $J_n(K_n)$ is a Bessel function (modified Hankel function of the second kind) of order n, k is the free space propagation constant, n_{core} is the index of the core, n_{clad} is the index of the cladding, $h^2 = n_{core}^2 k^2 - \beta^2$ is the radial

propagation constant in the core, $q^2 = n_{clad}^2 k^2 - \beta^2$ is the radial propagation constant in the cladding, and the prime denotes differentiation with respect to the argument. Eqn. 2.1 is solved numerically for the fundamental HE_{11} fibre mode for specific taper diameters. The propagation constant of the sphere is $\beta = kl/x_{nlm}$, where x_{nlm} is the microsphere size parameter determined from Eqn. 1.4.[1] Similar equations for TE and TM modes can be obtained [47], and are plotted in Fig. 2.5(a). A summary of waveguiding properties of tapered fibres is given in [44] and [47]. The taper and sphere are phase matched when the difference between propagation constants is zero. This is represented in Fig. 2.5(b) for a silica microsphere at 980 nm.

2.5 Tapered Fibre Fields

If efficient coupling is to be achieved using tapers or half-tapers, it is imperative that the taper be only a few microns in diameter. Taper coupling provides a simple and potentially compact method of exciting the sphere. We fabricate low-loss 3-4 μm diameter tapers using a 25 W CO_2 Synrad laser, and 1-2 μm diameter tapers using either a ceramic fibre heater or a flame. Fibre taper coupling efficiencies of more than 99% have been reported [25], indicating excellent phase matching between the taper and microsphere.

As with the microsphere, the field inside the fibre is described by a Bessel function, and the field outside the fibre is described by a Hankel function. For fields inside the

[1] All calculations, both with the microsphere and tapered fibre, should be done with the effective index, n_{eff} and not simply n_{sphere} or n_{core}. However, it is sometimes acceptable to approximate n_{eff} for convenience.

fibre, the exact electric field equations in cylindrical coordinates are [44]

$$\begin{aligned} e_r &= -\frac{a_1 J_0(2ahR) + a_2 J_2(2ahR)}{J_1(2ah)} f_1(\phi) \\ e_\phi &= -\frac{a_1 J_0(2ahR) - a_2 J_2(2ahR)}{J_1(2ah)} g_1(\phi) \\ e_z &= -\frac{i2ah}{a\beta} \frac{J_1(2ahR)}{J_1(2ah)} f_1(\phi). \end{aligned} \tag{2.2}$$

The fields outside the fibre are given by:

$$\begin{aligned} e_r &= -\frac{2ah}{2aq} \frac{a_1 K_0(2aqR) - a_2 K_2(2aqR)}{K_1(2aq)} f_1(\phi) \\ e_\phi &= -\frac{2ah}{W} \frac{a_1 K_0(2aqR) + a_2 K_2(2aqR)}{K_1(2aq)} g_1(\phi) \\ e_z &= -\frac{i2ah}{a\beta} \frac{K_1(2aqR)}{K_1(2aq)} f_1(\phi). \end{aligned} \tag{2.3}$$

The linear polarisation is given by $f_1(\phi)$ and $g_1(\phi)$, which are sine and cosine functions around the fibre respectively. The other variables are not defined here, but the interested reader can refer to [44] for details.

Another representation of these equations that has much importance for taper-microsphere coupling, as well as atom-light interactions, is the Poynting vector. The Poynting vector gives the power density across the fibre and outside the fibre in the evanescent region, i.e. the mode pattern. In the limit of a weakly guiding approximation, the Poynting vector is given by $\overrightarrow{S}(r) = \frac{1}{2}\overrightarrow{E} \times \overrightarrow{H}$, and is proportional to the square of the Bessel or Hankel function [44]. Figure 2.6 shows this calculation for a fibre of radius 0.6 μm and light of wavelength 1.5 μm. An important feature in this plot is the sharp discontinuity at the fibre surface, which only becomes appreciable for diameters below roughly 2 μm. At this radius of 0.6 μm, about 18% of the power is in the evanescent region, while for a radius of 1.5 μm there is only about 1% of the power in the evanescent region.

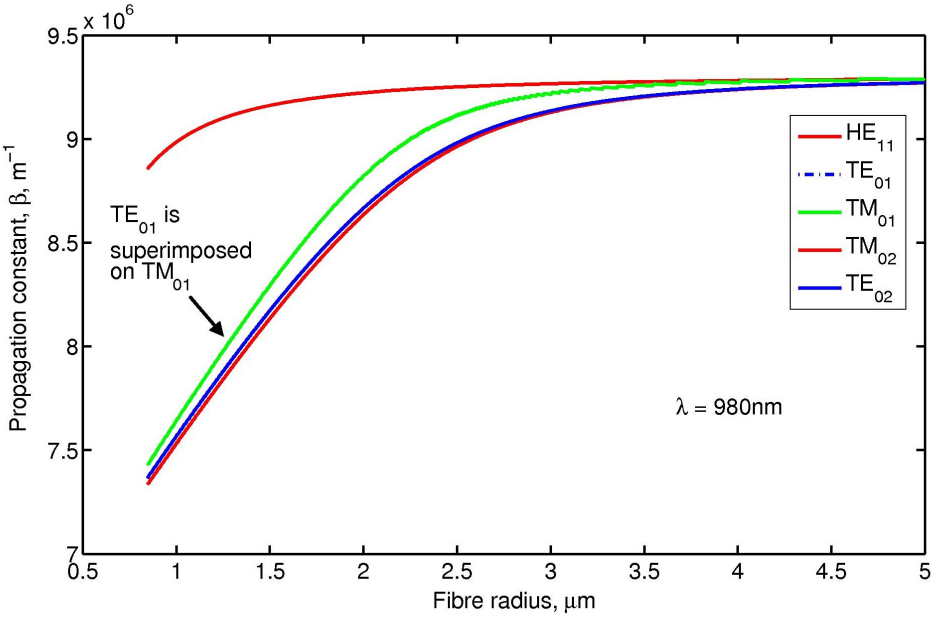

(a) Propagation constant at 980 nm.

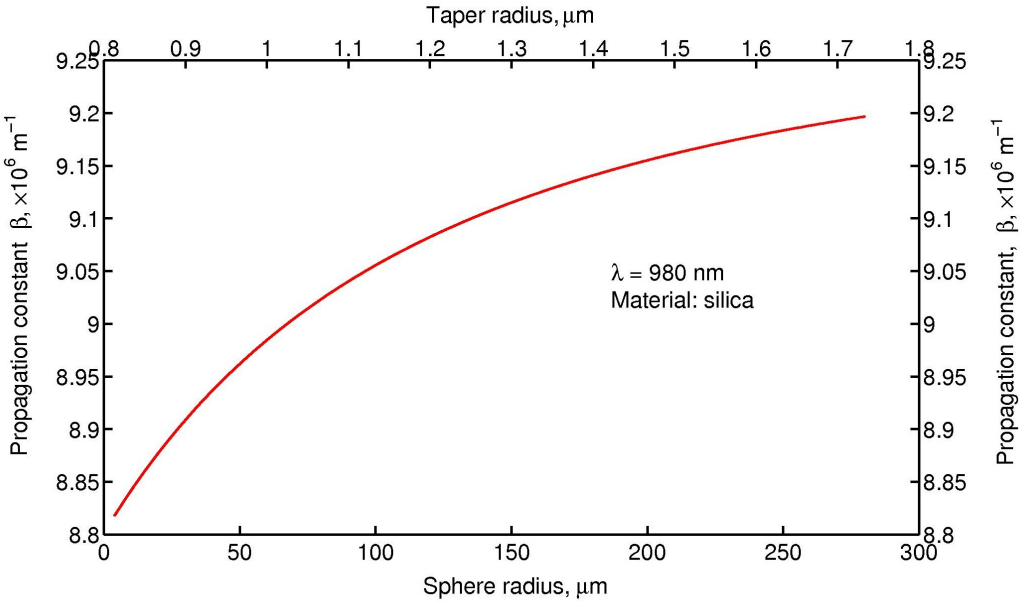

(b) Phase matching condition at 980 nm for a silica microsphere.

Figure 2.5: (a) Propagation constant for the fundamental HE_{11} mode at 980 nm, and (b) phase matching condition at 980 nm in a silica microsphere.

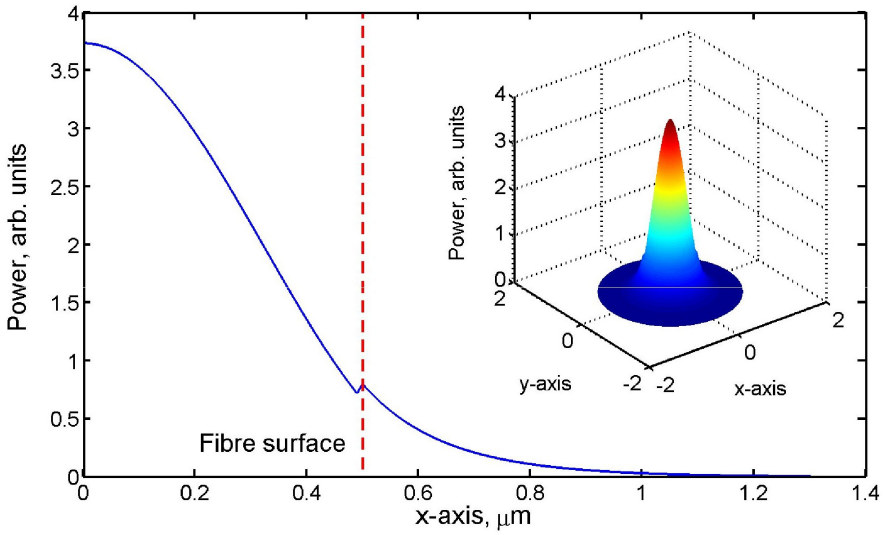

Figure 2.6: Poynting vector for a 0.5 μm radius fibre taper for light with a wavelength of 1.5 μm. The boundary of the fibre wall shows a discontinuity in the vector field causing a large power density. The evanescent field is quasi linearly polarised.

2.6 Fabrication and Characterisation of Tapered Fibres[2]

This section describes how we designed a reproducible method of fabricating adiabatic tapers with 3-4 μm diameter. The method is based on a heat-and-pull rig, whereby a CO_2 laser is continuously scanned across a length of fibre that is being pulled synchronously. Our system relies on a CO_2-compatible mirror mounted on a geared stepper motor in order to scan the laser beam across the taper region. We show that this system offers a reliable alternative to more traditional rigs incorporating galvanometer scanners. Transmission losses are routinely between 0.1 and 0.3 dB,

[2]**The following sections have appeared in "Heat-and-pull rig for fiber taper fabrication," *Rev. Sci. Instrum.*, 77, 083105, (2006).**

indicating the satisfactory production of adiabatic tapers. The operation of the rig is described in detail, and an analysis on the produced tapers is provided. The flexibility of the rig is demonstrated by fabricating prolate dielectric microresonators (so-called "bottle" resonators) using a micro-tapering technique. Such a rig is of interest to a range of fields that require tapered fibre fabrication, such as microcavity-taper coupling, optical fibre sensing, and the fabrication of fused biconical tapered couplers. It should be noted at the outset that fibre tapers fabricated using this rig were only used in early experiments. The experiments in Chapters 3 and 4 relied on 1 μm diameter fibre tapers fabricated using either a butane torch or ceramic heaters.

2.6.1 Introduction

The four most widely exploited means of achieving micron-sized tapers are by flame [25, 48, 49], CO_2 laser heating [50], micro-furnace [51, 52], and, to a lesser extent, fusion splicer [40]. While subwavelength diameters have been shown to be achievable with the flame method, it presents significant technical challenges [49]. Firstly, the gas flow rate must be precisely regulated in order to maintain a suitable temperature. Secondly, the purity of the gas supply becomes increasingly important for smaller taper diameters due to contamination concerns. Air currents in the vicinity of the flame also pose a problem by causing areas of uneven heating, thereby limiting the option of scanning the flame across a length of fibre.[3] Despite being able to produce sub-micron tapers with the micro-furnace method, the fibres cannot be controllably structured to produce different taper profiles. We have also found that such tapers are not adiabatic, and the micro-furnace itself degrades substantially after fabricating

[3]The alternative is to scan the taper over the stationary flame. This has the added advantage of producing long taper waists.

a few dozen tapered fibres.

As an alternative, CO_2 lasers present a largely stable and easily controllable method of heating a fibre. Air currents or other deleterious environmental effects bear no consequence on the power output or the ability to scan the beam across the fibre with a mirror scanner. It is possible to precisely control the length of fibre to be heated (i.e. the hot-zone), thereby yielding any desired taper profile [53]. The physical process of heating a fibre with a laser beam involves the fibre absorbing radiation and heating from the inside, whereas for a flame the process involves heating the surface of the fibre. There is an inverse square relationship between radius and heating for a CO_2 laser heat source, while for a flame heat source there is simply an inverse relationship between heating and radius. This ultimately places a stricter limit on the minimum taper diameter attainable for a given CO_2 laser power as compared with a flame heat source [54]. Previous reported attempts of producing tapers using the CO_2 laser technique have achieved a diameter of 4.6 μm with a CO_2 laser power of 13 W, and FWHM spot size of 820 μm using a galvanometer mirror scanner [50]. Here, we describe a reliable method of fabricating low-loss 3-4 μm diameter tapers as well as the possibility of fabricating bottle-resonators using a micro-tapering technique with a 25 W CO_2 laser.

Our fabrication method relies on the use of a geared stepper motor to scan the laser beam rather than the more traditional galvanometer. Implementation of our rig is trivial, requiring only interconnection of the stepper motor with the controller circuit. In contrast, Galvanometer scanners require PD (proportional-derivative) or PID (proportional-integral-derivative) control, which can be awkward to tune correctly. From a mechanical perspective, the stepper motor has a more robust design

and better torque, which negates any effects induced by the inertia of the mirror attached to the shaft of the motor. Additionally, the stepper motor represents a significant cost saving since the cost of a scanning galvanometer system is typically in excess of US $1990 [55], while the cost of a Radionics hybrid stepper motor, gear box, and controller circuit is approximately US $210 [56]. The following subsections describe the procedure and requirements for pulling adiabatic fibre tapers [53, 57] with typical losses in the range of 0.1 to 0.3 dB at 980 nm, and prolate resonators.

2.6.2 Experiment

A schematic of the laser-scanning rig for taper fabrication is shown in Fig. 2.7. Custom designed software automates all the instrument control and data acquisition through serial and USB interfaces, thereby ensuring ease of parameter adjustment and reproducibility. A 12.5 cm focal length ZnSe lens focuses the laser beam onto the fibre with a FWHM spot size of approximately 500 μm, 5.5 cm in front of the scanning mirror. The stepper motor used in conjunction with a 500:1 gear box in half-step mode has a resolution of 1.8×10^{-3} degrees per half-step, which corresponds to a hot-spot translation of around 1.7 μm per half-step on the fibre. The hot-spot refers to the point on the fibre which is being heated by the laser beam at any instant. A $1''$ gold mirror and holder are vertically mounted on the shaft of the gear box. The CO_2 laser beam is incident on the centre of the mirror at an angle of 45° and is directed onto the fibre. A Thurlby Thander TG250 function generator, connected to the stepper motor controller circuit, cyclically scans the mirror through a sweep angle of approximately 10°, thereby scanning the laser beam across the fibre. Alternatively, we can use customised limit switches to control the sweep angle of the mirror. Another

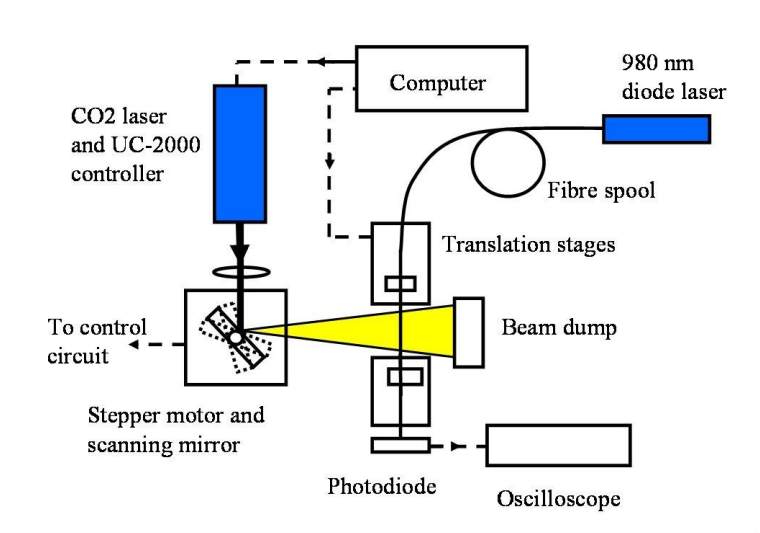

Figure 2.7: Schematic of the taper fabrication rig. Dashed lines indicate control lines or data transfer.

function generator, connected to the stepper motor controller circuit, provides the clocking pulses, which dictate the speed at which the mirror scans the laser beam. The discrete nature of the stepper motor step-size is smeared out by the size of the beam at the focus. Two motorised translation stages (Standa Ltd., Lithuania) pull the ends of the fibre taper (SM980 single mode fibre from Fibercore) with a resolution of 1 μm. As the taper is being drawn, the transmission loss of a 980 nm diode laser through the fibre is monitored with a Thorlabs Si-photodiode (DET-series) connected to a digital storage oscilloscope. The computer provides an analog voltage signal to the UC-2000 laser controller.

Since the taper profile closely follows an exponential profile, we use this relationship to predict suitable scan lengths, L, and pull lengths, z, for any desired taper waist radius, $r(z)$,

$$r(z) = r_o \exp(-z/L), \tag{2.4}$$

where r_o is the initial fibre radius before tapering [53]. There is some flexibility in choosing z and L. Scan lengths ranging from 5 to 15 mm and pull lengths ranging from 12 to 40 mm were examined, and all yielded low transmission losses and taper diameters of 3-4 μm. We found that Eqn. 2.4 always gives an accurate prediction of the waist diameter. The pull speed is less flexible, and a value of 80-110 μm per second provided the best results. Several preparatory steps are essential in ensuring finished taper quality. Firstly, the fibre is liberally cleaned with acetone to remove inorganic substances. It is imperative that the laser beam and fibre be horizontal to within a few tens of microns so that the focus of the beam covers the fibre precisely throughout the scan. The fibre must also be slightly taut before attempting this alignment. Failure to optimise the alignment before starting fabrication results in sagging and possible vibrations of the fibre, which tends to distort taper profiles, leading to high transmission losses. The polarisation of the laser beam is set vertical to the fibre so that the absorption coefficient is maximised [54].

The taper profile was measured under a Nikon MM-66 microscope with a resolution of 2-4 μm and is shown in Fig. 2.8. Surface roughness on the taper is not noticeable as evidenced by the inset SEM image.

2.6.3 Results and Discussion

As a rule, tapers can only be produced with low losses if their profile follows the adiabaticity criterion [57]. This criterion requires the taper profile to be such that the change in taper angle is small enough to prevent light propagation being either coupled from the fundamental mode, HE_{11}, to higher order parasitic modes in the fibre or being lost as radiation. The criterion can be stated as $|dr/dz| \leq \rho(z)[\beta_1(z) - \beta_2(z)]/2\pi$,

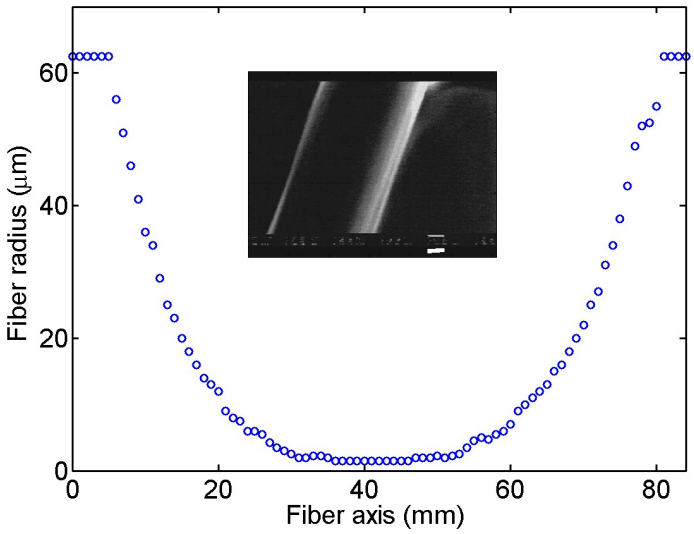

Figure 2.8: Taper profile for a 3 μm diameter taper. The pull length is 40 mm, the scan length is 7 mm, and the initial taper diameter is 125 μm. The inset shows an SEM image of a section of the taper with a diameter of 5.9 μm. The inset bar in the lower right is 1.0 μm.

where $|dr/dz|$ defines the local taper angle, $\Omega(z)$, by the trigonometric expression $\Omega(z) = \arctan|dr/dz|$. The other variables are $\rho(z)$, the local core radius, $\beta_1(z)$ and $\beta_2(z)$, the local propagation constants of the fundamental mode and the next closest mode respectively, and z is along the fibre axis [53, 57]. The transcendental equation for the propagation constants has been solved numerically as a function of local taper diameter. Figure 2.9 shows a plot of this criterion and of the core taper angle of a typical adiabatic taper as produced by the above described method. The taper curve is based on an optimum exponential fit of the measurements in Fig. 2.8 and has the form as described by Eqn. 2.4.

When the angle of the delineation curve is less than approximately ten times the

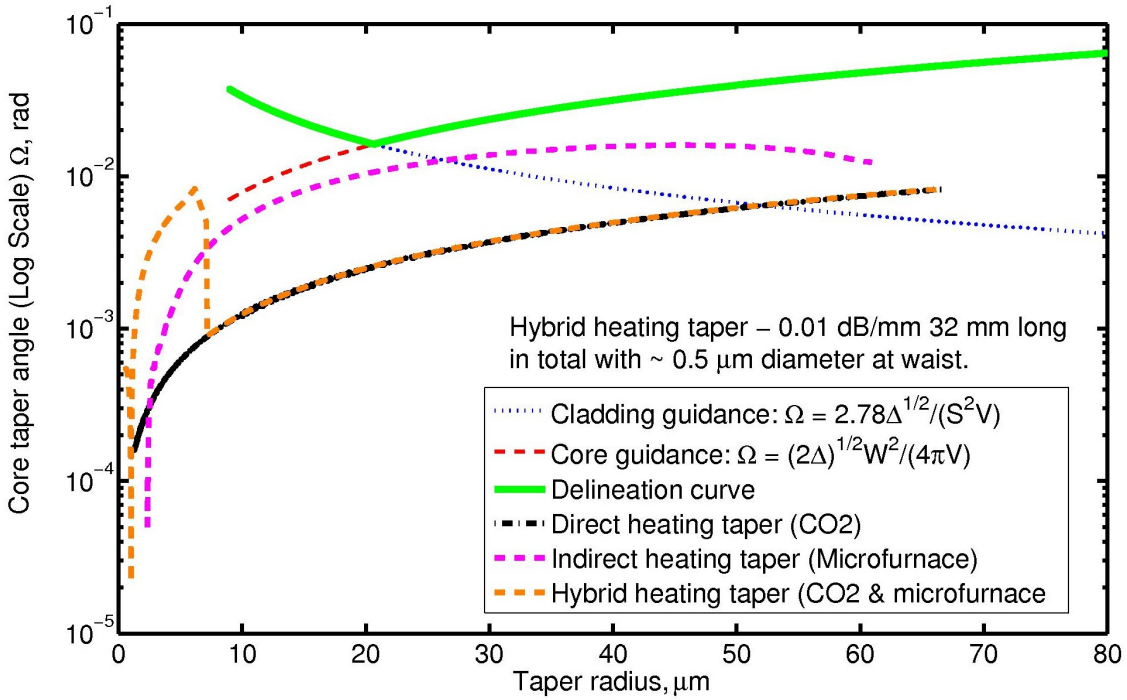

Figure 2.9: Approximated length-scale delineation curves for three taper fabrication techniques - direct CO_2 heating, indirect micro-furnace heating, and a 2-step process employing both techniques. The green trace represents the delineation between guidance and non-guidance of light.

taper angle, the light in the propagating mode will be lost to parasitic modes. While the fibre has only a single propagating mode in the untapered region, the taper itself contains multiple modes since the light is cladding-air guided. For a taper waist radius, r_a, of 1.5 μm, the core guidance parameter $V = kr_a\sqrt{n_{core}^2 - n_{clad}^2} \approx 9.669 > 2.405$ at a wavelength of 980 nm, indicating the taper is multimoded [45]. The refractive index of the core, n_{core}, is actually the effective index of the fundamental mode determined from $\beta_1(z)/k$, where k is the free space wavenumber, and the refractive index of the air cladding, n_{clad}, is 1. Once the taper is adiabatic, and below a diameter of about 0.8 μm at a wavelength of 980 nm, light only propagates in the fundamental mode.

The delineation curve in Fig. 2.9 is read from right to left when considering a decreasing taper diameter. Starting from the untapered region on the right, the initial taper transition consists of a core, where the light propagates, and a cladding, where the refractive index difference is $\Delta = (n_{core} - n_{clad})/n_{clad} = 7.8 \times 10^{-3}$. An approximation for the core guidance curve is given in [57], and is based on the assumption of an infinite cladding diameter. Gradually, the diameter and core guidance parameter decrease until the core effectively disappears and the propagating light becomes cladding-air guided. At the taper waist, there is a large index difference of about 0.42 between the cladding and surrounding air causing the core guidance parameter to gradually increase; this is shown as an increase in the angle of the delineation curve. Similarly, for the cladding guidance curve an approximation is given in [57], and is based on the assumption that the core diameter is vanishing. Figure 2.8 shows a typical taper angle decreasing when approaching the taper waist. Both core and cladding contribute to distinct regions in the delineation curve. The taper clearly meets the

adiabaticity criterion since the angle of the taper transitions is sufficiently below the delineation curve. Using a shorter wavelength diode laser would proportionately shift the delineation curve to the left and this would increase the taper-delineation curve separation, consequently giving lower losses.

2.6.4 Micro-furnace Tapering

Subwavelength diameters of below 100 nm have been achieved with the micro-furnace method [58]. A 20 W CO_2 laser heats a small Sapphire tube (8-10 mm long, 2 mm outer diameter, and 0.8 mm inner diameter) that surrounds the fibre rather than directly heating the fibre with the laser. Alignment of the beam focus with the taper is not as stringent as compared to the direct laser heating method. A limitation of this method is that microstructuring of the fibre profile cannot be achieved. Different taper shapes may not be easily produced since the hot-zone cannot be precisely varied and is typically several millimetres in length, and a very short hot-zone is vital for the micro-tapering step when producing bottle resonators. Furthermore, high losses of several dB have thus far been observed with the micro-furnace method because the taper transitions are non-adiabatic as shown in the delineation curve in Fig. 2.9. This is detrimental when coupling to the fundamental mode of a microresonator.

2.6.5 Fabrication of Prolate Microresonators

In recent years, interest in the use of microspherical resonators in cavity QED experiments has increased [10]. The use of such microcavities in these experiments requires the possibility of tuning the resonance frequency of the microcavity to an atomic line. In principle, there are two main methods of achieving this: strain tuning

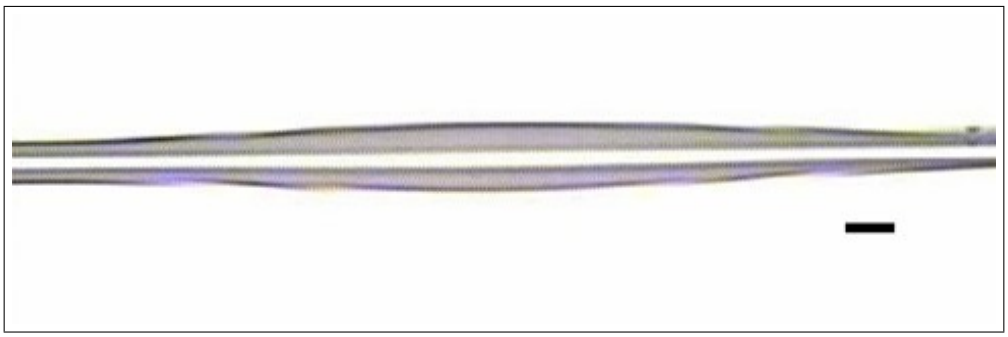

Figure 2.10: Optical micrograph of a bottle resonator with a diameter of 12 μm and a length of 300 μm. The bar is 10 μm.

and temperature tuning. Strain tuning can be used to sweep the resonant frequency through the cavity FSR, whereas temperature tuning is limited to a fraction of the FSR [59]. Temperature tuning is unsuitable as a stand-alone method, and the fabrication of microspheres suitable for the strain tuning apparatus is difficult. A new type of prolate microcavity that offers potentially greater flexibility in tuning the microcavity resonance frequency has recently been described theoretically in the literature [60, 52]. Strain tuning of these bottle resonators may tune the frequency over several FSR, while temperature tuning over a single FSR may only require a few tens of Kelvin. Another appealing feature compared with typical spherical microcavities is the stronger evanescent field at the bottle resonator surface due to the smaller resonator dimensions.

The bottle resonator in Fig. 2.10 is produced with similar dimensions to the one described in the theoretical work of Louyer *et al.* [60] and Sumetsky [52]. The resonator has a midsection diameter of 12 μm and a length of approximately 300 μm. Shorter bottle resonators are limited by the size of the hot-spot. Kakarantzas *et al.* [61] describe a bottle resonator 160 μm long with a diameter of 16 μm. The

fabrication begins with tapering of the fibre down to a waist diameter of 10-20 μm as described already. Each micro-tapered section on either side of the resonator is produced by pulling the taper at a speed of 10 μm per second for a length of about 0.2 mm while keeping the hot-spot stationary. The discrete rotation of the stepper motor shaft allows the scanning mirror to direct the beam onto exact locations, where micro-tapering is to take place.

2.6.6 Conclusions

In this chapter, we have described the fabrication methods used for our passive and active microspheres. Most work in this thesis deals with active spheres fabricated from Er doped fluoride or phosphate glasses. In addition, we have devised a simple procedure for producing fibre tapers as coupling elements into the microspheres. This method routinely produces 3-4 μm diameter tapers using commercial single-mode SM980 fibre. A stepper motor and gear box can be used to scan the laser beam across the fibre with sufficient precision as an inexpensive alternative to the more traditional galvanometer scanners reported for flame systems. Transmission losses of 0.3 ± 0.2 dB at a wavelength of 980 nm are within acceptable limits of other tapering rigs described in the literature [62]. We verify our optical microscope measurements of the taper diameter with SEM imaging. This rig is of interest for applications involving microresonator coupling. The rig can also be used to produce long period gratings [61] and fused biconical taper couplers [62]. Apart from the cost savings of such a laser-scanning rig, we have shown its flexibility for producing bottle resonators. This technique involves micro-tapering a fibre over a distance of about 0.2 mm and at a very slow speed. The dimensions of this new type of resonator can be precisely

controlled. The discrete step-size of the stepper motor can be used to control the length of the resonator with a resolution of approximately 1.7 μm per half-step given the current rig configuration. The diameter of the bottle resonators can be as small as 3-4 μm. Installation and operation of our laser-scanning rig requires a minimum amount of skill compared with most other tapering methods. Smaller diameter tapers and shorter bottle resonators would, no doubt, be possible by first expanding the CO_2 beam before focusing it through the 12.5 cm lens, thereby yielding a higher power density by virtue of the smaller size of the laser beam at the focus. Even though the micro-furnace tapering method can achieve any reasonable diameter required for microcavity coupling, the tapers are not adiabatic and the CO_2 technique is still required for bottle resonator fabrication.

Chapter 3

Efficient Upconversions in Heavy Metal Fluoride Glass: Er^{3+} doped ZBLALiP

3.1 Introduction[1]

Results on the realisation of a multicolour microspherical glass light source fabricated from the erbium doped fluoride glass ZBLALiP are presented in this chapter. Whispering gallery mode lasing and upconversion processes give rise to laser and fluorescent emissions at multiple wavelengths from the ultraviolet to the infrared. Thirteen discrete emissions ranging from 320 in the ultraviolet to 850 nm in the infrared have been observed in the upconversion spectrum. The absorption and fluorescence properties, and infrared lasing are studied, and the processes responsible for the generation of the observed wavelengths are outlined. We report, to the best of our knowledge, the first observation of 320 nm upconversion emission following 980 nm pumping of Er^{3+}.

[1]**This chapter has appeared in "Upconversion channels in Er:ZBLALiP: a multi-color microspherical light source,"** ***Eur. Phys. J. Appl. Phys.*****, 40, 181, (2007).**

In recent years, much effort has been devoted to the exploitation of upconversion mechanisms in rare-earth ion doped materials to yield a range of wavelengths from near infrared to ultraviolet. The spectral properties of the resulting fluorescence and/or lasing emissions depends on the choice of dopant and the host matrix in which it is embedded. In particular, microspheres fabricated from rare-earth ion doped materials have been shown to operate as miniature laser devices [40, 24]. The close proximity of numerous energy levels in triply-ionised rare earth ions is advantageous for obtaining fluorescent and lasing emissions through various upconversion mechanisms, such as excited state absorption (ESA), energy transfer upconversion (ETU), and photon avalanche (PA) [63]. This combination of active medium and resonant cavity has resulted in much research focusing on the characterisation of doped microspheres.

The interest in heavy metal fluoride glasses (HMFG) is due to the ultra-low absorption losses compared to the more traditional silica glass shown in Fig. 3.1. Fluorozirconate glasses are ideal for producing upconversion emissions due to their lower phonon energy (600 cm^{-1} max.) compared with silica (1190 cm^{-1} max.), for example. The figure shows losses of around 0.001 dB/km at 2.6 μm, whereas for silica, the losses are an order of magnitude greater. Unfortunately, ZBLAN usually suffers from recrystallisation problems when drawn into long fibres suitable for telecommunications.

The vast majority of work on activated glasses found in the literature deal with bulk samples, waveguides, and to a lesser extent, microcavities. The suitability of fluoride glasses as rare-earth host materials has long been known [64], as their low

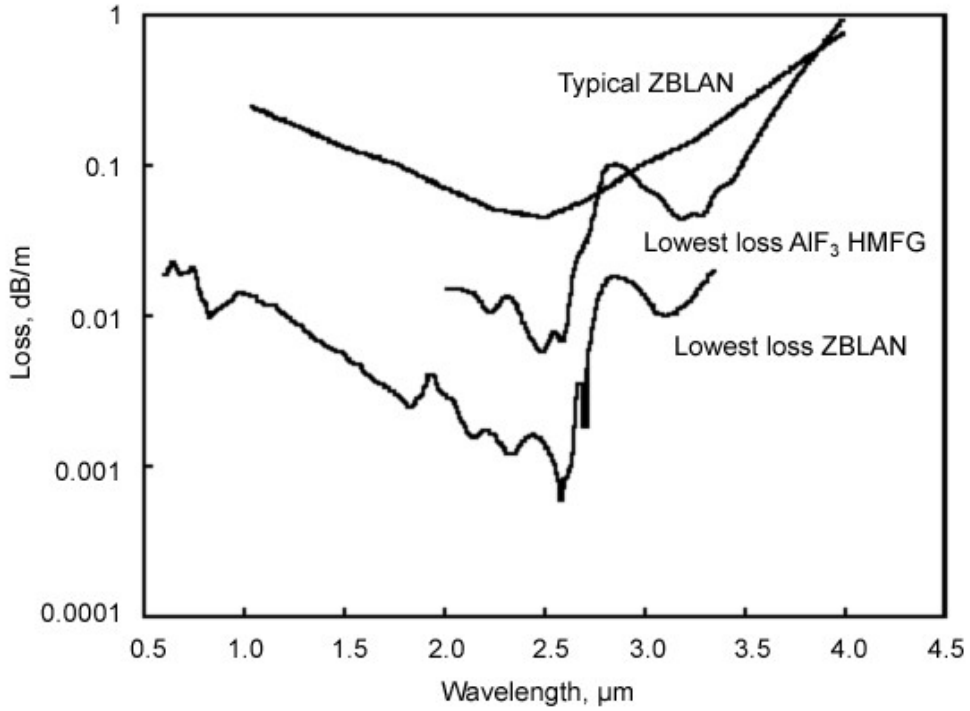

Figure 3.1: The theoretical absorption loss of ZBLAN is compared to that of experimentally realised fibres from the visible to the near infra-red [23]. The attenuation in silica is higher by a factor of about 10 or more.

phonon energies determine multiphonon relaxation rates, and, ultimately, the efficiency of upconversion processes. Preliminary work on the material and IR lasing properties of Er^{3+}:ZBLALiP was presented in [24]. Here, this work is extended to a more systematic study of the upconversion processes involved in 980 nm pumping of Er^{3+}:ZBLALiP microspheres.

3.2 ZBLALiP Material Properties

We start by briefly introducing the material properties of ZBLALiP. A detailed study of some fundamental material properties of Er^{3+} doped ZBLALiP (ZrF_4-BaF_2-LaF_3-AlF_3-LiF-PbF_2) glass has been presented in an earlier paper [24]. That work described the improved stability of ZBLALiP with respect to similar fluorozirconate glasses and its suitability as a host for rare-earth ions. Additional material properties are presented here, including the absorption spectrum for a 5.8 mm thick bulk sample of 0.2 mol% Er^{3+}:ZBLALiP (c.f. Fig. 3.2). Twelve absorption bands are indicated in Fig. 3.2(a) and represent the transitions from the ground state $^4I_{15/2} \longrightarrow A_N$ with $A_1 = {}^2G_{9/2} + {}^2K_{15/2} + {}^2G_{7/2}$, $A_2 = {}^4G_{11/2}$, $A_3 = {}^2H_{9/2}$, $A_4 = {}^4F_{3/2}$, $A_5 = {}^4F_{5/2}$, $A_6 = {}^4F_{7/2}$, $A_7 = {}^2H_{11/2}$, $A_8 = {}^4S_{3/2}$, $A_9 = {}^4F_{9/2}$, $A_{10} = {}^4I_{9/2}$, $A_{11} = {}^4I_{11/2}$, and $A_{12} = {}^4I_{13/2}$. We use the same glass sample as described in [24]. Figure 3.2(b) shows the absorption in the C-band. The measured energy levels for Er^{3+} is shown in Fig. 3.3 and are discussed further in Section 3.5.

An important parameter, especially in relation to phase matching, is the spectral variation of the refractive index in the material. We will assume that ZBLALiP has a similar behaviour to ZBLAN and use a Cauchy formula to estimate the wavelength dependence such that the refractive index is [38]

$$n_s(\lambda) = A\lambda^{-4} + B\lambda^{-2} + C + D\lambda^2 + E\lambda^4, \tag{3.1}$$

where the coefficients are $A = 1.35123 \times 10^{-5}\mu\text{m}^4, B = 2.94780 \times 10^{-3}\mu\text{m}^2, C = 1.48965 D = -1.30933 \times 10^{-3}\mu\text{m}^{-2}$, and $E = -3.23335 \times 10^{-6}\mu\text{m}^{-4}$.

When lead is added to ZBLAN - as is the case with the P component in ZBLALiP - the refractive index is linearly increased across the whole spectrum. Figure 3.4 was

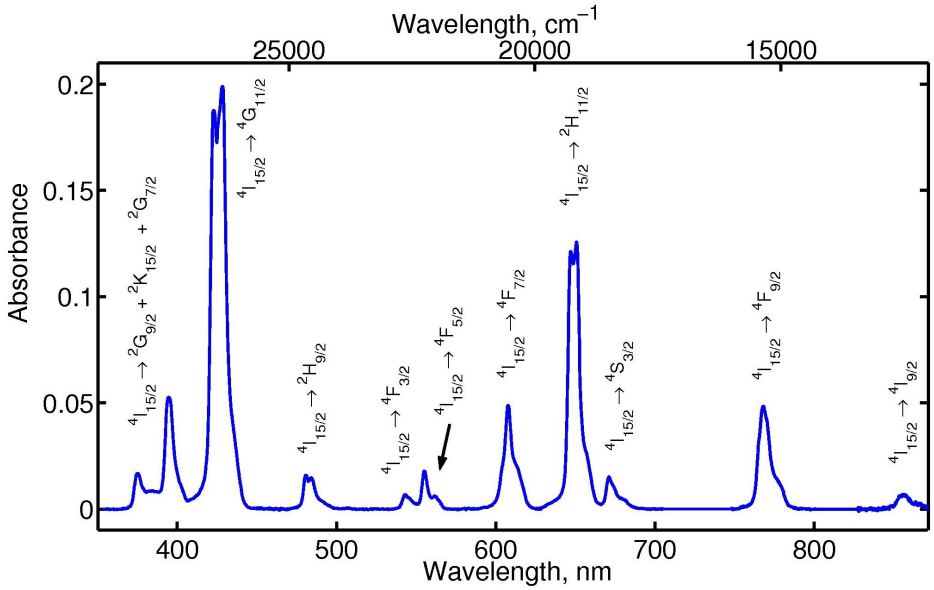

(a) UV to visible absorption spectrum of ZBLALiP bulk glass.

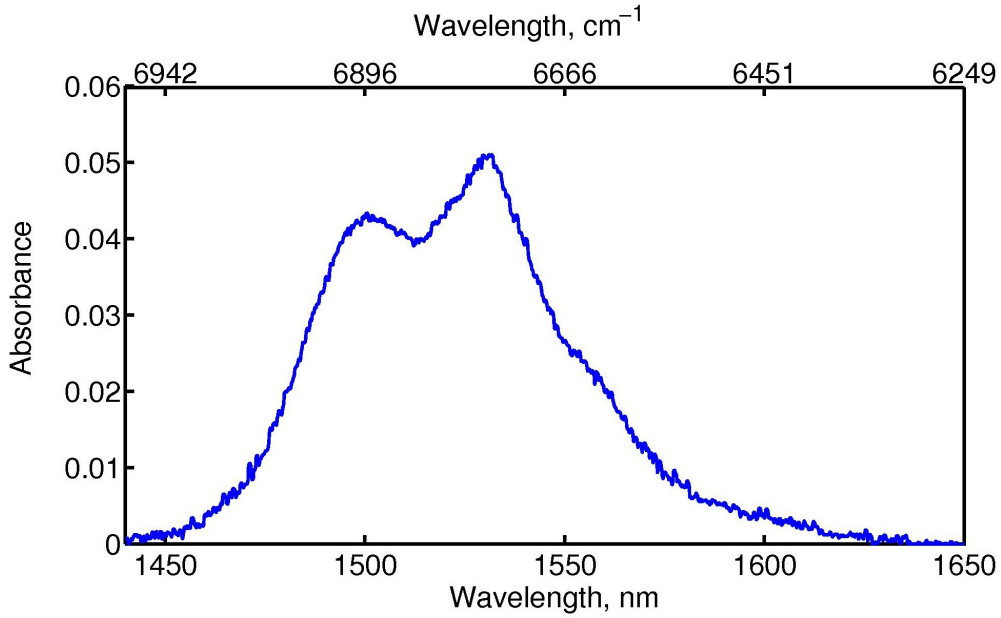

(b) C-band absorption spectrum of ZBLALiP bulk glass.

Figure 3.2: Absorption spectra for 0.2 mol% Er^{3+} doped ZBLALiP bulk glass at optical and IR wavelengths.

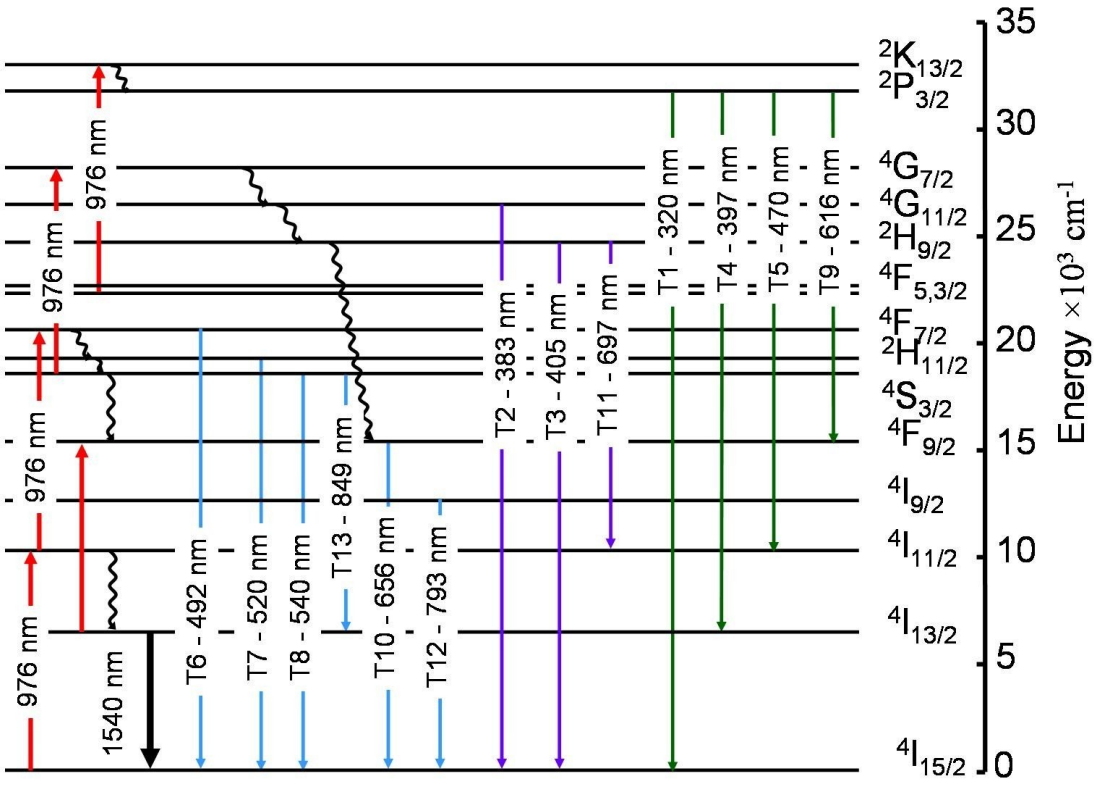

Figure 3.3: Er^{3+} energy level diagram with radiative (solid lines) and non-radiative transitions for a 976 nm pump. The thick, black line at 1540 nm indicates the C-band lasing transition.

generated from Eqn. 3.1 and the measurement of the refractive index for ZBLALiP at 1.5 μm, 1.49, was used as an offset from the pure ZBLAN graph. It can be seen that the UV and violet parts of the spectrum have a rapidly increasing refractive index, which complicates phase matching at multiple wavelengths. This complication is in addition to the spectral variation of phase matching when the simplified assumption of a constant refractive index is taken.

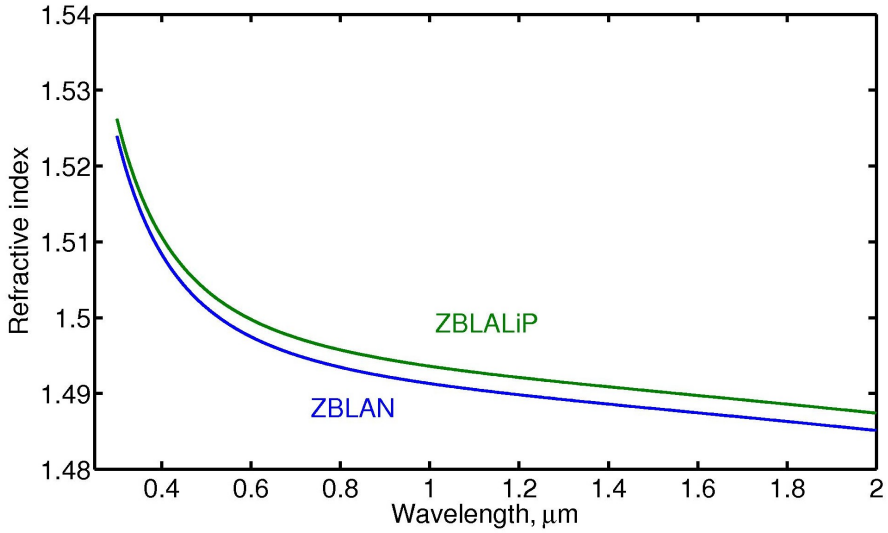

Figure 3.4: Theoretical refractive index variation as a function of wavelength in ZBLALiP.

3.3 Experimental Details

The Er^{3+}:ZBLALiP microspheres studied for this work contain erbium at a concentration of 0.2 mol%, which equates to 4×10^{19} Er^{3+} ions/cm^3. It should be noted that, at this concentration, energy transfer (ET) is not expected to play a major role, and, as such, excited state absorption (ESA) is the dominant mechanism in the upconversion process [65]. Nevertheless, due to the non-trivial problem of distinguishing the two mechanisms, some authors have suggested that ET may play a role even when the dopant concentration is below the critical value of about 1 mol% [66]-[68]. This may be true if ion clustering is present.

In our work, the C-band lasing characteristics and upconversion spectrum are investigated at room temperature using a single mode 980 nm diode laser pump

(Avanex, 1998 PLM) with a spectral width of about 1 nm under CW pumping conditions. Figure 3.5 is a schematic of the experimental setup. Up to 15 mW of power from the diode laser (DL) is coupled into a tapered fibre. A fibre coupled isolator (Agiltron, 980 nm), with 1 dB insertion loss, is placed after the DL to prevent back-reflection from other optical components down the line. We monitor the DL power during the microsphere-taper alignment using the 10% line on a 10:90% coupler (Fibercom, EFAG0306207) connected to a power meter (Thorlabs). Typically, 10-15% of the pump light is coupled into the microsphere.[2] A fibred variable attenuator (VA - OZ optics, BB-100-11-980-61-125-S-40-3S3S-1-1) controls the power. The emissions are collected in two ways: the scattered fluorescence emissions are collected using a free-space probe connected to a CCD spectrometer (Ocean Optics, CCD 2000) located about 1 mm from the microsphere: and the C-band lasing is collected from the output port of the tapered fibre connected to an optical spectrum analyser (OSA - Anritsu, MS9710B). Some residual power from the pump is measurable in the C-band, even though the pump wavelength is about 550 nm away from the lasing wavelength at 1.5 μm. A 980/1550 nm WDM is used to provide further isolation, thereby ensuring that the detected pump power in the C-band remains below around 100 pW, depending on the bandwidth setting on the OSA.

The tapered fibre is fabricated in order to efficiently couple the pump into the microsphere and efficiently collect the infrared lasing spectrum. A 1550 nm SMF-28 fibre was adiabatically tapered to a diameter of 1 μm using a butane flame following a similar technique as described in Section 2.6. The transmission loss of these tapers

[2]This measurement is rather crude as it excludes any estimation of the light scattered from the taper-sphere coupling junction. A more accurate method would involve measuring the nonresonant transmitted light before and after contact with the microsphere using a narrow linewidth laser.

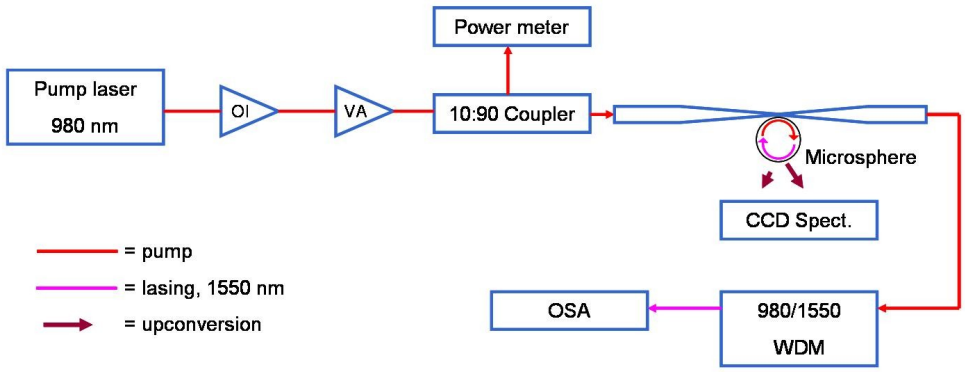

Figure 3.5: The experimental setup schematically represents how the microsphere is excited with a 980 nm diode laser (DL) and the emissions are collected. The fluorescence is collected on a CCD spectrometer, and the lasing emission is collected in an optical spectrum analyser (OSA). Legend: OI - optical isolator, VA - variable attenuator, WDM - wavelength division multiplexer.

is typically less than 0.1 dB/cm. Optimum mechanical alignment of the taper and microsphere is achieved by moving the microsphere to different locations along the taper until the microsphere emission spectrum about 1.5 μm is maximised on the OSA. This coupling efficiency is, in part, due to the broad spectral nature of the pump laser relative to the whispering gallery mode resonances of the microsphere, and can be improved by the use of a narrow linewidth pump source [46]. Only when the taper and microsphere are critically coupled is $\sim 100\%$ coupling expected. A typical emission spectrum is presented in Fig. 3.6 and the inset shows the characteristic WGM bands about the sphere equator.

The taper-microsphere coupling is performed under a Zeiss Stemi 2000-C microscope using either a CCD camera (JAI, CV-S3200) or the eyepieces. Due to vibrations in the microscope support arm, it is difficult to use a $\times 50$ magnification objective.

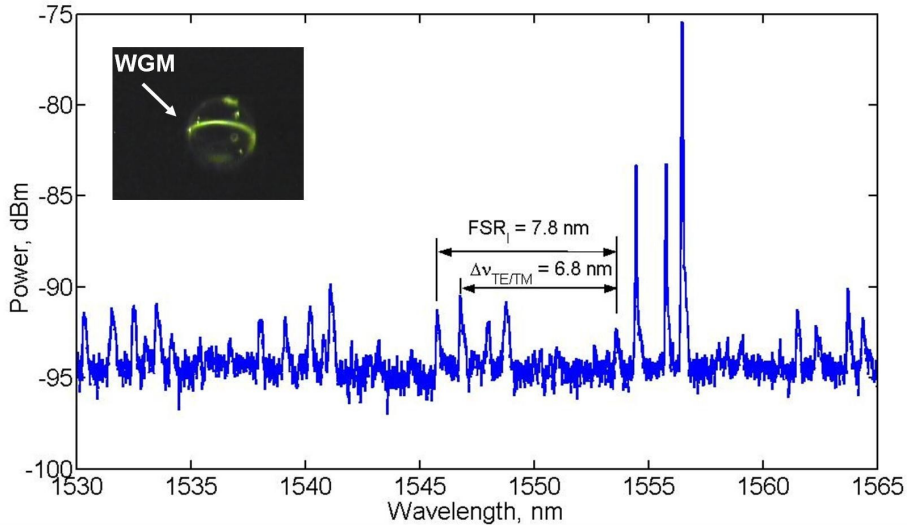

Figure 3.6: 66 μm diameter microsphere lasing spectrum about 1.5 μm showing whispering gallery mode structure. Inset: microsphere and fibre taper with a green WGM. The FSR is 7.8 nm.

Alternatively, we can mount the taper-microsphere coupling rig on a Nikon MM-66 microscope, which offers greater mechanical stability and fine control over x-y movements of the microscope table. This setup allows us to use a $\times 100$ magnification objective, if needed, without any noticeable vibrations.

3.4 McCumber Analysis

The emission cross-section, σ_{ems}, for Er^{3+}:ZBLALiP around 1.5 μm can be determined from the absorption spectrum in Fig. 3.2. Before proceeding with the analysis, the absorption cross-section, σ_{abs}, for each of the levels must be evaluated using the following expression [67]

$$\sigma_{abs}(\lambda) = \frac{-\ln(A)}{l N_{Er}}, \tag{3.2}$$

where A is the absorbance, l is the sample thickness, and N_{Er} is the Er^{3+} concentration of 3.76×10^{19} cm^{-3} (c.f. Fig. 3.3 for the energy level diagram). Using McCumber theory, under the assumption of a strongly phonon coupled system [69], the emission cross-section is given by

$$\sigma_{ems}(\lambda) = \sigma_{abs}(\lambda)\frac{Z_L}{Z_U}\exp\left(-\frac{hc}{\lambda k_B T}\right), \tag{3.3}$$

where Z_L (Z_U) is the partition function of the lower (upper) state given by a summation of continuous levels $\sum \exp \Delta E_i/k_B T$, where ΔE_i is the energy difference between the Stark split sublevels and the lowest energy level in the lower (upper) manifold, h is Planck's constant, c is the speed of light, k_B is Boltzmann's constant, and T is the temperature in Kelvin. From Eqn. 3.3, the bulk sample of Er^{3+}:ZBLALiP has a peak emission cross-section of 4.6×10^{-21} cm^2 in the C-band, which compares well with 4.9×10^{-21} cm^2 measured for fluoroindate glasses [70] and 4.6×10^{-21} cm^2 measured in ZBLAN [71].

Figure 3.7 presents the absorption and emission cross-section measurement for 0.2 mol% Er^{3+}:ZBLALiP in the C-band and pump band. The cross-sections effectively give the probability that an ion will absorb or emit a photon over a particular spectral region. By a simple extension of this definition, the spectral gain coefficient, $G(\lambda)$, can be determined in terms of the fraction of the ion population, p_{Er}, in the metastable level, $^4I_{13/2}$, using the formula

$$G(\lambda) = N_{Er}\left[p_{Er}\sigma_{ems}(\lambda) - (1 - p_{Er})\sigma_{abs}(\lambda)\right]. \tag{3.4}$$

Figure 3.8 shows that emissions from $^4I_{13/2}$ at shorter wavelengths become possible as the population inversion increases. For example, an emission at 1560 nm becomes

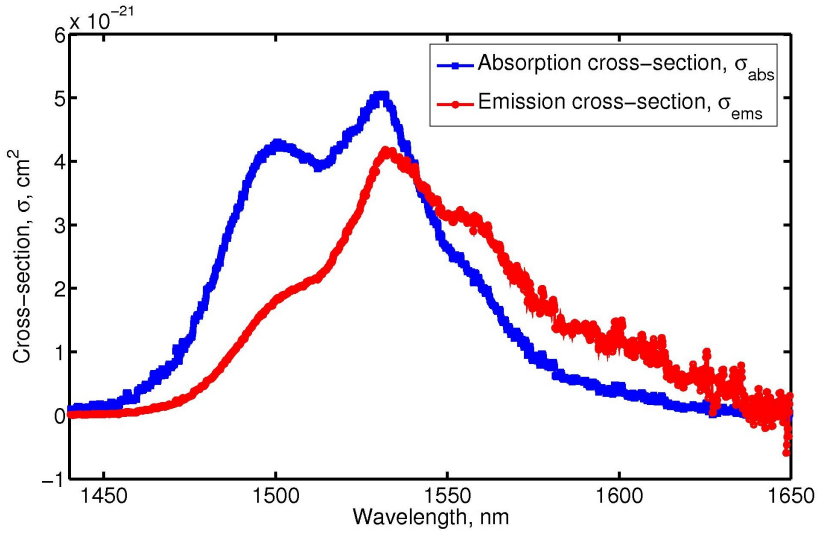

(a) C-band

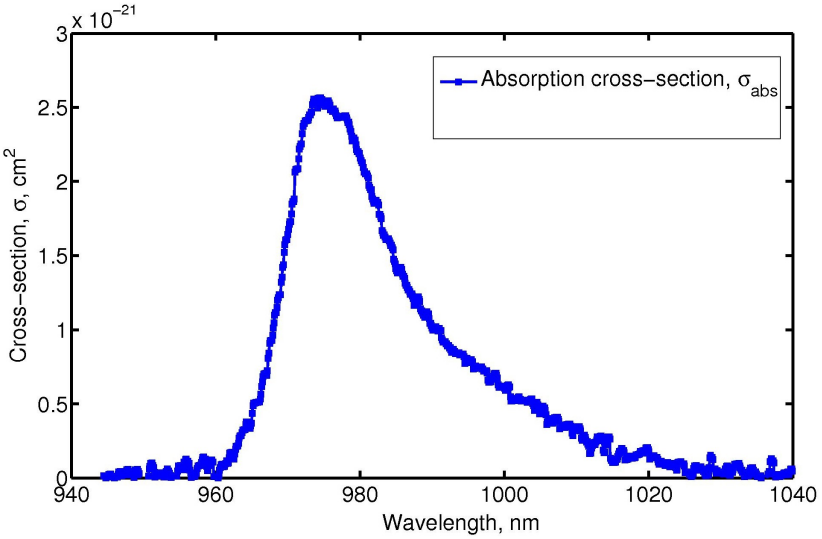

(b) Pump band

Figure 3.7: Absorption and emission cross-sections for 0.2 mol% Er^{3+} doped bulk ZBLALiP.

favourable only when the gain coefficient is positive at that wavelength, which corresponds to a fraction $p_{Er} \geq 40\%$. This does not mean, however, that lasing will occur because the lasing threshold at a particular wavelength is dependent on the Q factor of the cavity mode. Note also, the degree of population inversion is governed by the pump power.

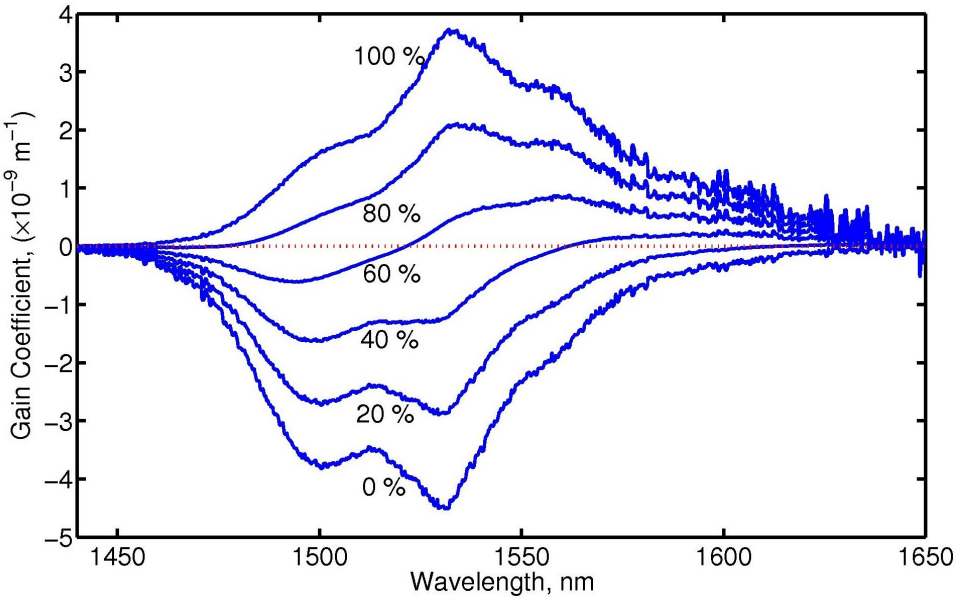

Figure 3.8: Gain coefficient for different population inversions between the metastable ${}^4I_{13/2}$ and the ground level ${}^4I_{15/2}$. The percentages correspond to different amounts of population inversion.

3.5 Judd-Ofelt Analysis

The absorption cross-sections can reveal several important material properties. The process of analysing this data has been described in numerous papers, and is known

as Judd-Ofelt (JO) analysis [72]-[74]. The JO intensity parameters, Ω_t, (t = 2, 4, 6), are derived from the electric-dipole contributions of the measured line strengths by a least-squares-fitting approach to minimise the rms deviation with the calculated line strength. Throughout this work we use the JO intensity parameters, $\Omega = 3.12 \pm 0.15 \times 10^{-20}$ cm^2, $\Omega = 1.49 \pm 0.07 \times 10^{-20}$ cm^2, and $\Omega = 1.15 \pm 0.03 \times 10^{-20}$ cm^2, as previously calculated in [24], since we use the same glass sample to fabricate our microspheres. These three parameters dictate all the material properties determined in this section. A spectroscopic quality factor can be defined as Ω_4/Ω_6, yielding a value of 1.30 for the quoted intensity parameters. A higher number makes miniaturisation of devices easier while improving their performance. Table 3.5 compares Er^{3+}:ZBLALiP to other erbium-doped glasses. The three parameters in ZBLALiP are quite similar to the other fluorozirconate glasses, as expected. In contrast, the Ω_2 value is appreciably smaller than in most other glasses, such as silicate, phosphate, and tellurite.

Table 3.1: Comparison of Judd-Ofelt parameters for fluoride and other glasses doped with Er^{3+}.

	$\Omega_2 \times 10^{-20}$cm^2	$\Omega_4 \times 10^{-20}$cm^2	$\Omega_6 \times 10^{-20}$cm^2	Ref.
ZBLALiP	3.12±0.15	1.49±0.07	1.15±0.03	[24]
ZBLAN	2.37±0.15	1.24±0.23	0.73±0.16	[72]
ZBLAN	2.912	1.464	1.184	[38]
Al/Silicate	5.59	1.42	0.87	[75]
Phosphate	4.67	1.37	0.77	[75]
Tellurite	5.34	1.75	0.94	[75]

A larger Ω_2 indicates greater asymmetry of the host glass, while a larger Ω_6 has

a dominant influence on the electric dipole line strength, S_{ed}, of the lasing transition $^4I_{13/2} \rightarrow ^4 I_{15/2}$, as shown in the expression

$$S^{ed}\left[^4I_{13/2} \rightarrow ^4 I_{15/2}\right] = 0.0195\Omega_2 + 0.1173\Omega_4 + 1.4316\Omega_6. \tag{3.5}$$

Equation 3.5 can be expressed more generally as

$$S^{ed} = \sum_{t=2,4,6} \Omega_t |\langle (S,L)J||U^t||(S',L'J'\rangle|^2, \tag{3.6}$$

where $|\langle (S,L)J||U^t||(S',L'J'\rangle|^2$ are the double reduced matrix elements of the unit tensor operator, U, and are assumed to be independent of the host material [73]. Therefore, we have taken the matrix elements from references [73, 74, 70] for our calculations, and these are reproduced in Table 3.5 for convenience.[3] The magnetic dipole line strengths are calculated from

$$S^{md} = \frac{1}{4m^2c^2} |\langle (S,L)J||L+2S||(S',L')J'\rangle|^2, \tag{3.7}$$

where $|\langle (S,L)J||L+2S||(S',L')J'\rangle|^2$ are the double reduced matrix elements of the $L+2S$ operator, where L is the total orbital angular momentum and S is the total spin.

The data yielded from Eqns. 3.2, 3.6, and 3.7 combined with the JO intensity parameters, are used to calculate important radiative properties, such as the spontaneous radiative transition rates, electric dipole line strengths, branching ratios, and radiative lifetimes.

[3] There are few complete tables of reduced matrix elements in the literature for transitions up to 35×10^3 cm^{-1} because researchers normally only observe emissions from transitions below 28×10^3 cm^{-1}. In addition, it is difficult and time-consuming to perform these calculations for U. Just prior to completing my thesis, I became aware of a thesis by Casprary [38] that gives a full table of matrix elements for transitions up to 97×10^3 cm^{-1} with Er^{3+} and other dopants in ZBLAN.

The total spontaneous radiative transition rate between level J and a lower level J' is given by

$$A_{JJ'} = A^{ed}_{JJ'} + A^{md}_{JJ'} = \frac{64\pi^4}{3h\lambda^3(2J+1)}\left(\chi_{ed}S^{ed} + \chi_{md}S^{md}\right), \tag{3.8}$$

where λ is the mean wavelength of the absorption, $\chi_{ed} = p(p^2+2)^2/9$ is the local field correction factor for electric dipole transitions, and $\chi_{md} = p^3$ is the local field correction factor for magnetic dipole transitions. In this work, $A_{JJ'}$ is calculated using the values given by Carnall *et al.* [74] for LaF_3 ($A'_{JJ'}$) corrected for the refractive index difference using the relation $A_{JJ'} = (p/p')^3 A'_{JJ'}$, where $p'(p)$ is the refractive index of LaF_3 (ZBLALiP). The refractive index for ZBLALiP is 1.49 at 1.5 μm, while that for LaF_3 is 1.57. Using the relation given in Eqn. 3.1, we can approximate the refractive index at other wavelengths also.

The radiative lifetime, τ_R, of transitions between levels J and J' is related to the inverse of $A_{JJ'}$ by

$$\tau_R = \frac{1}{\sum_{J'} A_{JJ'}}, \tag{3.9}$$

and the branching ratio, β, between J and J' is simply the ratio of $A_{JJ'}$ for the initial level to the sum of $A_{JJ'}$ for all the lower levels given by

$$\beta = A_{JJ'}\tau_R. \tag{3.10}$$

Table 3.5 shows the radiative probabilities, electric dipole line strengths, branching ratios, and radiative lifetimes for the transitions. Several levels have high branching ratios for transitions to the ground level and intermediate levels, many of which have been observed in the emission spectrum shown in Fig. 3.9.

Table 3.2: Predicted radiative transition probabilities, $A_{JJ'}$, electric dipole line strengths, $A^{ed}_{JJ'}$, branching ratios, β, and radiative lifetimes, τ_R, of Er^{3+}:ZBLALiP. The wavelength λ_{calc} is the baricenter of the absorption bands.

Table 3.2

Transition	Label	λ_{calc} (nm)	$\left[U^{(2)}\right]^2$	$\left[U^{(4)}\right]^2$	$\left[U^{(6)}\right]^2$	$A^{ed}_{JJ'}$ (s^{-1})	$A^{md}_{JJ'}$ (s^{-1})	S^{ed} $(\times 10^{-20}$ $cm^3)$	β	τ_R(ms)
$^4I_{13/2} \rightarrow {}^4I_{15/2}$		1519	0.0195	0.1173	1.4316	78	32	18.8	1.00	9.10
$^4I_{11/2} \rightarrow {}^4I_{15/2}$		975	0.0282	0.0003	0.3953	98		5.4	0.84	8.57
$\rightarrow {}^4I_{13/2}$		2727	0.0210	0.1100	1.0400	12	7	1.43	0.16	
$^4I_{9/2} \rightarrow {}^4I_{15/2}$	T12	799	0.0000	0.1733	0.0099	106		2.7	0.77	7.18
$\rightarrow {}^4I_{13/2}$		1668	0.0003	0.0081	0.6400	32		7.5	0.22	
$\rightarrow {}^4I_{11/2}$		4663	0.0030	0.0674	0.1271	1	1	2.6	0.01	
$^4F_{9/2} \rightarrow {}^4I_{15/2}$	T10	656	0.0000	0.5354	0.4618	928		13.3	0.89	0.96
$\rightarrow {}^4I_{13/2}$		1025	0.0096	0.1576	0.0870	67		3.6	0.06	
$\rightarrow {}^4I_{11/2}$		1966	0.0671	0.0088	1.2611	44	5	16.7	0.05	
$\rightarrow {}^4I_{9/2}$		3623	0.0960	0.0061	0.0120	1	2	3.2	0.00	
$^4S_{3/2} \rightarrow {}^4I_{15/2}$	T8	540	0.0000	0.0000	0.2211	700		2.5	0.66	0.95
$\rightarrow {}^4I_{13/2}$	T13	849	0.0000	0.0000	0.3481	294		4.0	0.28	
$\rightarrow {}^4I_{11/2}$		1212	0.0000	0.0037	0.0789	24		1.0	0.02	
$\rightarrow {}^4I_{9/2}$		1688	0.0000	0.0729	0.2560	36		4.0	0.04	
$^2H_{11/2} \rightarrow {}^4I_{15/2}$	T7	520	0.7056	0.4109	0.0870	3453		29.1	0.96	0.27
$\rightarrow {}^4I_{13/2}$		792	0.0230	0.0611	0.0527	75	54	2.2	0.02	
$\rightarrow {}^4I_{11/2}$		1115	0.0357	0.1382	0.0371	43	81	3.6	0.02	
$\rightarrow {}^4I_{9/2}$		1507	0.2077	0.0662	0.2858	53	0	10.8	0.00	
$\rightarrow {}^4F_{9/2}$		2579	0.3629	0.0224	0.0022	11	0	11.7	0.00	
$^4F_{7/2} \rightarrow {}^4I_{15/2}$	T6	487	0.0000	0.1467	0.6273	1964		9.4	0.78	0.40
$\rightarrow {}^4I_{13/2}$		727	0.0000	0.3371	0.0001	316		5.0	0.13	
$\rightarrow {}^4I_{11/2}$		983	0.0035	0.2648	0.1515	147		5.8	0.06	
$\rightarrow {}^4I_{9/2}$		1245	0.0163	0.0954	0.4277	86		6.8	0.03	
$\rightarrow {}^4F_{9/2}$		1947	0.0121	0.0342	0.0151	4		1.1	0.00	

Continued on next page

Table 3.2: Predicted radiative transition probabilities, $A_{JJ'}$, electric dipole line strengths, $A^{ed}_{JJ'}$, branching ratios, β, and radiative lifetimes, τ_R, of Er^{3+}:ZBLALiP. The wavelength λ_{calc} is the baricenter of the absorption bands.

Table 3.2

Transition	Label	λ_{calc} (nm)	$\left[U^{(2)}\right]^2$	$\left[U^{(4)}\right]^2$	$\left[U^{(6)}\right]^2$	$A^{ed}_{JJ'}$ (s^{-1})	$A^{md}_{JJ'}$ (s^{-1})	S^{ed} ($\times 10^{-20}$ cm^3)	β	τ_R(ms)
						Continued from previous page				
$^4F_{5/2} \rightarrow ^4 I_{15/2}$		450	0.0000	0.0000	0.2237	873		2.6	1.00	1.15
$^4F_{3/2} \rightarrow ^4 I_{15/2}$		443	0.0000	0.0000	0.1204	690		1.4	1.00	1.44
$^2H_{9/2} \rightarrow ^4 I_{15/2}$	T3	406	0.0000	0.0190	0.2255	850		2.9	0.34	0.40
$\rightarrow ^4 I_{13/2}$		556	0.0780	0.1194	0.3535	953		8.3	0.38	
$\rightarrow ^4 I_{11/2}$	T11	697	0.0428	0.0824	0.1128	226	31	3.9	0.10	
$\rightarrow ^4 I_{9/2}$		823	0.0147	0.0062	0.0043	21	1	0.6	0.01	
$\rightarrow ^4 F_{9/2}$		1079	0.0055	0.0314	0.0369	184	36	1.1	0.09	
$\rightarrow ^2 H_{11/2}$		1854	0.0308	0.1828	0.0671	152	1	4.5	0.06	
$\rightarrow ^4 F_{7/2}$		2485	0.1058	0.0488	0.0240	61	1	4.3	0.02	
$^4G_{11/2} \rightarrow ^4 I_{15/2}$	T2	378	0.9178	0.5271	0.1197	11752		37.9	0.83	0.07
$\rightarrow ^4 I_{13/2}$		505	0.1011	0.2642	0.2550	1300	38	10.0	0.10	
$\rightarrow ^4 I_{11/2}$		618	0.0002	0.4930	0.0144	527	0	7.5	0.04	
$\rightarrow ^4 I_{9/2}$		724	0.0645	0.0117	0.0467	120	1	2.7	0.01	
$\rightarrow ^4 F_{9/2}$		905	0.4436	0.0388	0.0104	328	3	14.5	0.02	
$\rightarrow ^2 H_{11/2}$		1394	0.0006	0.1600	0.1100		10	3.7	0.00	
$^2G_{9/2} \rightarrow ^4 I_{15/2}$		365	0.0000	0.2416	0.1235	2034		5.0	1.00	0.49
$^2G_{7/2} \rightarrow ^4 I_{15/2}$		358	0.0000	0.0174	0.1163	839		1.6	1.00	1.13
$^2P_{3/2} \rightarrow ^4 I_{15/2}$	T1	320	0.0000	0.0000	0.0260	403		0.3	0.12	0.31
$\rightarrow ^4 I_{13/2}$	T4	397	0.0000	0.0000	0.1600	1242		1.8	0.38	
$\rightarrow ^4 I_{11/2}$	T5	470	0.0000	0.1300	0.0250	936		2.2	0.29	
$\rightarrow ^4 I_{9/2}$		524	0.0000	0.0440	0.0092	230		0.8	0.07	
$\rightarrow ^4 F_{9/2}$	T9	616	0.0000	0.0560	0.0045	164		0.9	0.05	
$\rightarrow ^4 S_{3/2}$		763	0.0847	0.0000	0.0000	259		2.6	0.09	
$^2K_{13/2} \rightarrow ^4 I_{15/2}$		302	0.0032	0.0029	0.0152	167		0.3	1.00	5.99

3.6 Upconversion Fluorescence and 1.5 μm Lasing

Figure 3.3 shows an energy level diagram for Er^{3+} indicating the radiative and non-radiative transitions that are responsible for the thirteen emissions observed in Fig. 3.9. The upconversion spectrum is recorded coincidentally to the C-band lasing spectrum (c.f. Fig. 3.6). Thirteen discrete peaks have been noted in the scattering spectrum and are numbered from T1-T13 along with their centre wavelengths. Approximately 700 μW of 980 nm pump light was coupled into the microsphere. The total power of the scattered light outcoupled to the spectrometer is a few nW for the green transitions (T7 and T8).

The limited resolution of the spectrometer used to study the upconversion, combined with the smaller microsphere FSR at shorter wavelengths, means that the whispering gallery mode structure is only visible for emissions at wavelengths longer than about 800 nm. The mode structure for the 849 nm (T13) emission is distinguishable in the inset of Fig. 3.9.

Our results demonstrate a broad range of emission from 320 nm to 849 nm in addition to the C-band lasing. We suggest that the combination of high cavity quality factor - typically 1×10^7, measured at 780 nm - and low whispering gallery mode volume - approximately 1,000-2,000 μm^3 - serves to significantly enhance the probability of excited state absorption by enhancing the pump field strength ($\sim 10^3$ V/m per photon) within the microsphere. This is reflected in the fact that a large number of the observed transitions are likely the result of 3-photon and 4-photon absorption events for what is a relatively modest pump power (sub mW) coupled into the microsphere.

Even though it is energetically possible for several emissions to originate from the

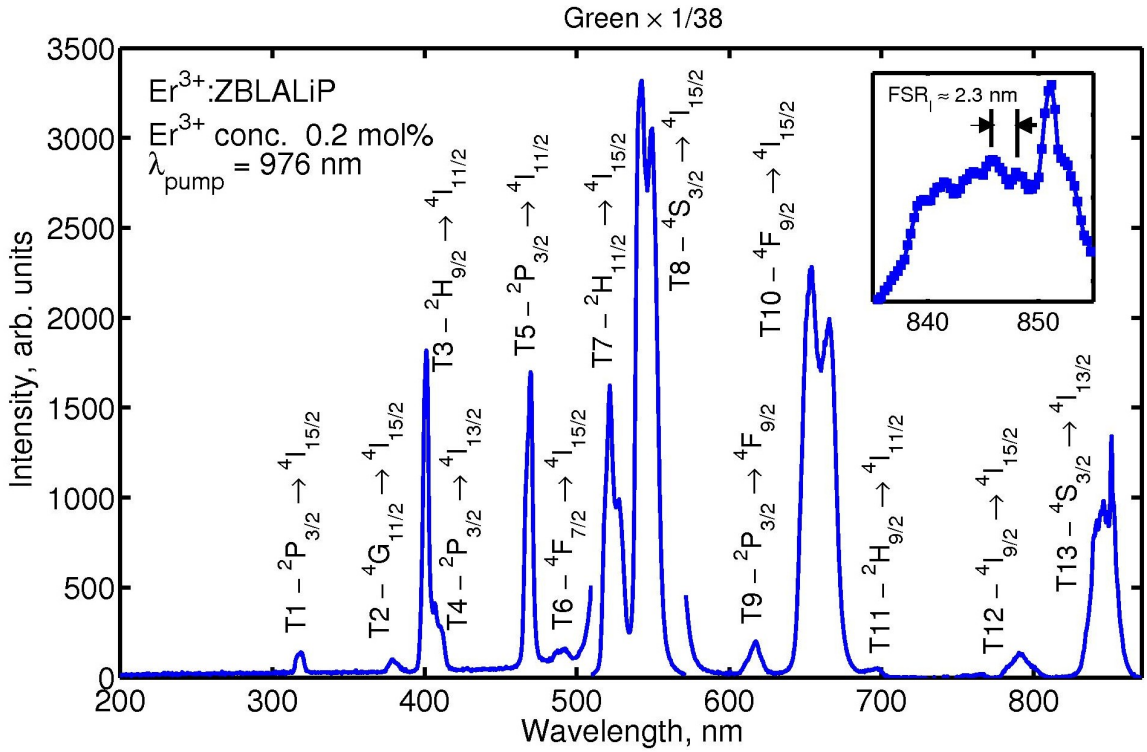

Figure 3.9: Observed Er^{3+}:ZBLALiP microsphere upconversion spectrum for 976 nm pumping. Inset: whispering gallery mode structure about T13 with a FSR of 2.3 nm.

same level, the branching ratios predicted in the JO theory can help determine the most likely emissions from a particular level. For example, it is energetically possible for both the 383 nm and 616 nm emissions to originate from radiative decay from the $^4G_{11/2}$ level to lower levels. However, the ratio of the measured emission intensities, 1:3, disagrees substantially from the calculated ratios, 1:22, thereby indicating that both emissions cannot arise from the $^4G_{11/2}$ level.

In fact, the 618 nm emission is due to the $^2P_{3/2} \rightarrow ^4F_{9/2}$ decay. In this way, we can

use a combination of the energy gaps between the energy levels and the calculated branching ratios to determine what levels are involved in the radiative emissions.

Four emissions in Fig. 3.9 (618 nm, 470 nm, 403 nm and 320 nm) are attributed to the transitions $^2P_{3/2} \rightarrow^4 F_{9/2}$ (β= 0.05), $^2P_{3/2} \rightarrow^4 I_{11/2}$ (β= 0.29), $^2P_{3/2} \rightarrow^4 I_{13/2}$ (β= 0.39), and $^2P_{3/2} \rightarrow^4 I_{15/2}$ (β = 0.12) respectively. The branching ratio calculations predict the ratio of emission intensities for each of the levels to be 1 (616 nm):5.8 (470 nm):7.8 (403 nm), which is in reasonable agreement with the measured ratios of 1:5.3:6.6. We have excluded the emission intensity of the 320 nm emission from this comparison, because fluorozirconate glasses have very substantial absorption losses in the UV region [76].

The $^4F_{3,5/2}$ levels in Er^{3+}:ZBLALiP have unusually long radiative lifetimes of 1.45 ms and 1.15 ms compared to other glasses, such as Er^{3+} doped fluoroindate glass, which has a lifetime of 0.50 ms [77]. As can be seen from the energy level diagram, this is critically important for the UV and violet emissions from the $^2P_{3/2}$ level because it facilitates the third ESA, $^4F_{3,5/2} \rightarrow^2 K_{13/2}$, by maintaining a large $^4F_{3,5/2}$ population. This is in sharp contrast to Er^{3+} doped fluoroindate glass, where nonradiative decay rapidly depletes the $^4F_{3,5/2}$ population, effectively preventing any further ESA.

The emission line centred at 320 nm (T1) is most likely a 4-photon process populating the $^2P_{3/2}$ state, which in turn radiatively relaxes to the $^4I_{15/2}$ ground state. Three pump photons populate the $^2G_{7/2}$ state. The $^2G_{7/2}$-$^2P_{3/2}$ energy gap of $\sim$ 3600 cm^{-1}, combined with a phonon energy of 600 cm^{-1}, is such that the $^2P_{3/2}$ state is unlikely to be populated by thermalisation, and, as such, we suggest that the absorption of a fourth pump photon is necessary to explain T1. This transition has previously been reported in Er-doped glass, but was identified as a 3-photon process following

pumping at 637 nm [77]. The same authors also reported emissions corresponding to the transitions T4, T5, and T8. Transition T1 has also been reported [78] in a Er^{3+}:Yb^{3+} co-doped material, although, in that case, the excitation process involved successive energy transfers from Yb^{3+}. It should be noted that this is very different from our work, which involves a single dopant, does not rely on a sensitiser ion, and ETU probably does not play a major role due to the low dopant concentration.

The transitions $^2P_{3/2} \rightarrow^4 I_{13/2}$ (T4) and $^2P_{3/2} \rightarrow^4 I_{11/2}$ (T5) are also thought to involve 4-photon excitations. Transitions T1, T4, and T5 have previously been observed following pumping at 545 nm [79]. Transitions T7, T8, T10, and T13 have been reported following 980 nm pumping [80]. The ultraviolet line at 383 nm (T2) and the 492 nm emission (T6) have been reported under 973 nm excitation [81].

The Er^{3+} emission at 700 nm has been attributed to the transition $^4F_{7/2} \rightarrow^4 I_{13/2}$ following absorption of three pump photons at 1480 nm in reference [82]. We presume this assignment was on the basis of the 3-photon resonance $^4F_{7/2} \rightarrow^4 I_{15/2}$. We have also observed emission about 700 nm (T11) but propose it to follow the transition $^2H_{9/2} \rightarrow^4 I_{11/2}$, based on the observed intensity ratio compared with the branching ratios calculated from JO theory. Finally, we have observed emissions centred at 618 nm (T8) and 667 nm (T10). We are currently unaware of other reports on such emissions from Er^{3+}.

3.7 Radiative and Multi-phonon Decay

Fluorozirconate glass, with its low phonon energies, has a comparatively high probability of radiative decay to lower levels. This probability is dependent on the energy gap, δE, between levels J and the lower level J'. For most energy levels, multi-phonon

decay is dominant, except for the case of the nine radiating levels identified in the energy level diagram. The rate of multi-phonon decay, A_{mp}, scales exponentially with the number of phonons, P, required to bridge the energy gap, ΔE. In general, this rate is an increasing function of temperature, governed by Bose-Einstein statistics, and is given by [38]

$$A_{mp}(T) = C \exp(-\alpha \left[\Delta E - 2.6\hbar\omega_{max}\right]) \left[1 - \exp(-\hbar\omega_{max}/k_B T)\right]^{-P}, \qquad (3.11)$$

where $P = \Delta E/\hbar\omega_{max}$, $\hbar\omega_{max}$ is the maximum phonon energy, which is assumed to be the same as in ZBLAN, i.e. 600 cm^{-1}, and C and α are material dependent constants.[4] Using Eqn. 3.11 and the radiative transition rates calculated in Table 3.5, the fraction of the ion population undergoing radiative decay can be determined. Figure 3.10 shows the estimated fraction for each of the 13 observed emissions plus two weaker emissions at 556 nm and 520 nm.

The figure bears considerable resemblance to the fluorescence spectrum in terms of the relative amplitude of the emissions resulting from each ESA. The two other emissions at 556 nm ($^2H_{9/2} \rightarrow^4 I_{13/2}$) and 520 nm ($^2P_{3/2} \rightarrow^4 I_{9/2}$) predicted by the JO theory, are overwhelmed by the strong green emissions in Fig. 3.10 and are not observed as a result; consider, for example, the *missing* transition between $^4F_{9/2}$ and $^4I_{11/2}$ in the energy level diagram corresponding to a weak 520 nm emission.

The dominance of the IR lasing transition is confirmed in Fig. 3.10. Even though the fraction of ions contributing to radiative upconversion emissions is at least a factor of ten smaller than the metastable $^4I_{13/2}$ level, the calculation predicts they should still be observable for energies up to 32×10^3 cm^{-1}, in support of the measurements in Fig.

[4]The model can only serve as an approximation as it excludes any mention of the spectral nature of the phonons and the Stark energy levels.

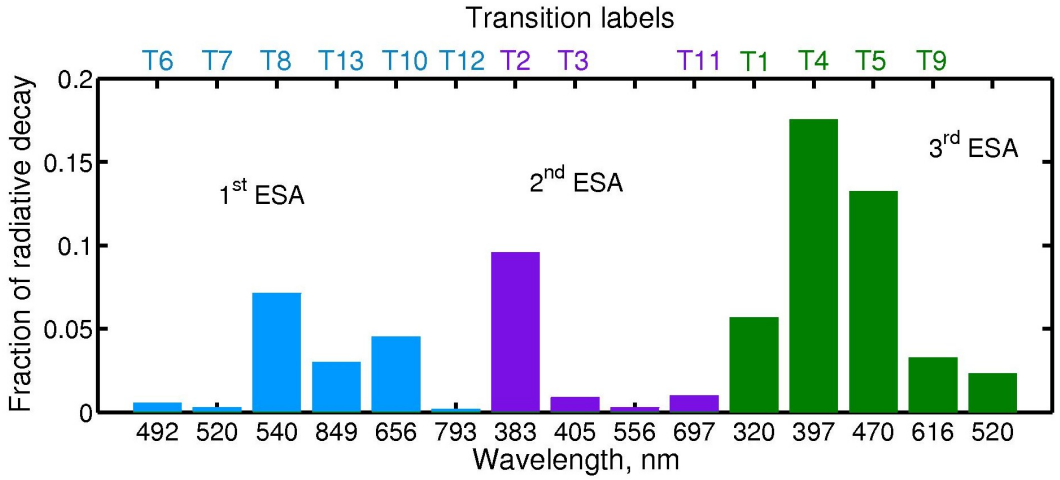

Figure 3.10: Calculated fraction of radiative decay, $A/\sum A$, for the observed emissions. The parameters C and α are 1.99×10^5 s^{-1} and 2.11×10^{-3} cm respectively, taken for ZBLAN at 300 K [38]. The fraction for $^4I_{13/2} \rightarrow ^4 I_{15/2}$ at 1.5 μm is 0.93 (not shown).

3.9. The low value for $^2H_{11/2}$ at 520 nm is counter-balanced by rapid thermalisation of the level by $^4S_{3/2}$ at 540 nm.

3.8 Power-law Upconversions

Further understanding of the upconversion (and downconversion) dynamics can be obtained by studying the intensity dependence of the fluorescence at a particular wavelength. The intensity of an upconversion fluorescence is related to the sequential absorption of q pump photons. Two possible outcomes can arise: (i) In the vast majority of glasses, the relationship between the pumping and emission intensities, I, tends to show a $I_{signal} \propto I_{pump}^q$ relationship where upconversion rates are insignificant, and (ii) in some cases, the presence of strong upconversion modifies the power law so

that fluorescence slopes less than q are observed. Measurements of this dependence for the case of six upconversion emissions are presented in Fig. 3.11, where the signal intensity was determined for increasing powers as an LL (light in - light out) logarithmic plot.

Case (ii) is sometimes regarded as undesirable as it hinders the identification of the levels from which emissions originate. The rate equation analysis performed in [83] describes how to relate the slope of the fluorescence emission LL plot from arbitrary energy levels to the possible upconversion mechanisms. Given the low dopant concentration of 0.2 mol% Er^{3+} in our glass sample, ETU can be assumed to be negligible, and the dominant mechanism is ESA.[5]

Figure 3.11 shows linear slopes on a log-log scale with values ranging from 0.78 to 1.10. Strong upconversion rates explain the departure from the power law prediction [83]. For slopes close to 1, which is due to the $I^{i/q}$ dependence of level i, the influence of upconversion is large, with ESA being the dominant upconversion mechanism. The predominant decay route is to the next lowest level, and the fraction of pump power absorbed is large. The data for T2 at 383 nm is comparable with the background noise, which results in a large error in the slope of 0.78 ± 0.15.

The proceeding sections have shown qualitatively that Er^{3+}:ZBLALiP has a high upconversion rate, which indicates that the power law relationship relaxes to $I_{signal} \propto I^1_{pump}$ and less, for levels that are populated through multi-phonon relaxations. Furthermore, this power dependence relies on whether ETU or ESA is dominant [83].

[5]ETU processes cannot be strictly rejected because of the possibility of clustering of ions. Such effects have a sixth power dependence on the inter-ion separation (c.f. Section 4.3.1 for a more thorough discussion of ETU in IOG-2 glass). In the case where only ETU is present, the fluorescence slope changes from I^q_{pump} to I^1_{pump} for lower pump powers. For isolated ions, the fluorescence slope will be linear for all pump powers.

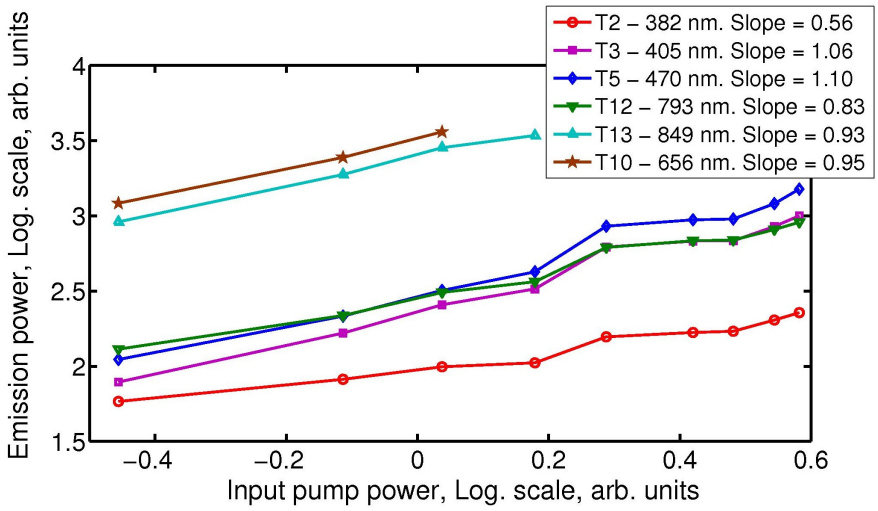

Figure 3.11: Light in-Light out logarithmic graph for the fluorescence emissions. All emissions show a slope of approximately 1. Note the lines are an aid for the eye.

The issue governing the observed fluorescence is an interplay between the linear decay and upconversion; for increasing pump power, the upconversion rate changes from I^q_{pump} to I^1_{pump}, while the GSA rate changes from I^1_{pump} to $< I^1_{pump}$.

3.9 Microsphere Characterisation

3.9.1 Eccentricity

Successful excitation of the ${}^4I_{13/2} \rightarrow {}^4 I_{15/2}$ transition results in whispering gallery mode lasing resonances within the microsphere, as shown in Fig. 3.6. The figure shows a typical lasing spectrum, in addition to four other modes, obtained for a 70 μm diameter sphere. As already outlined in Section 1.3, the number n gives the number of radial modes, and modes with increasing value of n have lower l and

longer resonance wavelength. In a perfect sphere, with $l = |m|$, these polar modes are degenerate. For practical microspheres this degeneracy is lifted because there will be some small degree of eccentricity; the microsphere will be either slightly prolate or oblate. The wavelength separation between the modes is proportional to the degree of deformation, and is given by $\Delta\lambda \approx (-\lambda^2/2\pi)(\Delta a)/(a^2)$. The microsphere eccentricity is determined from

$$\varepsilon = \left(\frac{\Delta\omega_{ecc}}{\Delta\omega_{nml}}\right)\left(\frac{l^2}{|m|} - \frac{1}{2}\right), \tag{3.12}$$

where l and m are the angular mode numbers, and ω_{nml} is the angular frequency of the mode. This is calculated to be $\sim 2.1\%$ for the corresponding azimuthal mode splitting, $\Delta\omega_{ecc}$, of ~ 11 GHz. Analysis of the lasing peaks enables us to measure the free spectral range, ν_{FSR}, between successive mode groups with a difference in angular mode number l of 1, to be ~ 7.8 nm (0.97 THz). Theoretically, we can determine the diameter of the sphere from $D = c/\pi n_s \nu_{FSR}$, where c is the speed of light in a vacuum, and n_s is the refractive index of the material. Using $n_s = 1.49$ at 1.5 μm, we find that the FSR = 7.8 nm indicates a microsphere diameter of 66 μm, which is reasonably close to the (70 ± 2) μm determined using an optical microscope. The peak power of the lasing peaks presented here is ~ 30 nW, although we have also observed lasing in a single mode with a peak value of ~ 500 nW. The spacing between TE and TM modes (ν_{TETM}) of 6.8 nm agrees well with the calculated value of 6.4 nm.

A rough estimate of the quality factor at the signal wavelength, Q_{signal}, can be obtained by determining the ratio of resonance wavelength at 1.5 μm to peak FWHM, yielding a value typically higher than 5×10^4, limited by the spectral resolution of the OSA. Even with an accurate measurement of Q_{signal} this cannot be regarded as

representing the Q of the cavity. This is obvious when you consider that the definition of Q relies on the energy stored in the mode, which, in the case of a doped cavity, is proportional to the dopant concentration. At the lasing threshold, the Q_{signal} value approaches infinity! The next section describes how to measure the cavity Q value at a pump wavelength of 780 nm.

3.9.2 Quality Factor Measurement

The Q factor was measured using a commercial, tuneable narrow linewidth (Sacher Lasertechnik, Tiger TEC-300-0780-0750, $\sim$ 100 kHz linewidth with 750 mW power) laser at 780 nm and saturable absorption spectroscopy of Rb atoms. Figure 3.12 shows the experimental setup. Several hundred mW is passed through the polarising beam splitter to the Rb cell, and the remainder ($\sim$ 100 mW) is sent to a GRIN lens fibre coupler (OZ Optics, LPC-03-780-5/125-S-0.72-2.6GR-25-X-3-1.5). The light coupled into the fibre is evanescently coupled into a microsphere and the light transmitted past the taper-microsphere coupling junction is detected on a photodiode (PD2). The light sent through the Rb cell only saturates the Rb atoms on the reflected pass after which another photodiode (PD1) detects the absorption peaks for both ^{85}Rb and ^{87}Rb isotopes. A function generator scans the laser frequency via the piezo element in the external cavity of the laser. It is important to ensure the optical table is vibrationally isolated because the microsphere cavity resonance becomes very unstable otherwise.

The isotope ^{87}Rb has crossover peaks for $F = 2 \rightarrow F = 3'$ and $F = 1 \rightarrow F = 3'$, separated by 78.5 MHz. One can also measure the crossover peaks for ^{85}Rb which are $F = 2 \rightarrow F' = 4$ and $F = 3 \rightarrow F' = 4$, separated by 31.5 MHz. These peaks provide the frequency scale on the x-axis of the oscilloscope. A single cavity resonance dip

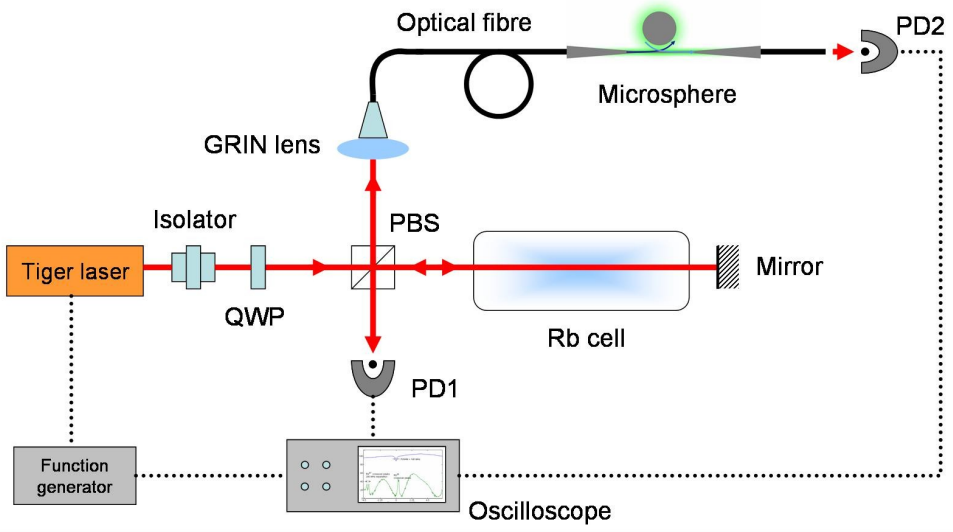

Figure 3.12: Experimental setup to perform Q factor measurement. Legend - PBS: polarising beam splitter, QWP: quarter wave plate, PD: photodiode. The black dotted line indicates electronic data/control signals.

is shown in the upper trace of Fig. 3.13 with a linewidth of 39 MHz at FWHM, corresponding to a Q factor of 1×10^7 at 780 nm. Up to 17% of the light is coupled into the microsphere when in the on-resonance position.

3.10 Conclusions

In conclusion, a multiwavelength microsphere light source is demonstrated with possible microphotonic applications. The Er^{3+} transitions involved in the thirteen upconversion emissions have been identified with the aid of JO analysis. This device could find many uses as a miniature multicolour light source with, for example, application to evanescent wave sensing based on excitation of transitions in target molecules adsorbed on to the microsphere surface. Our results for the violet emissions

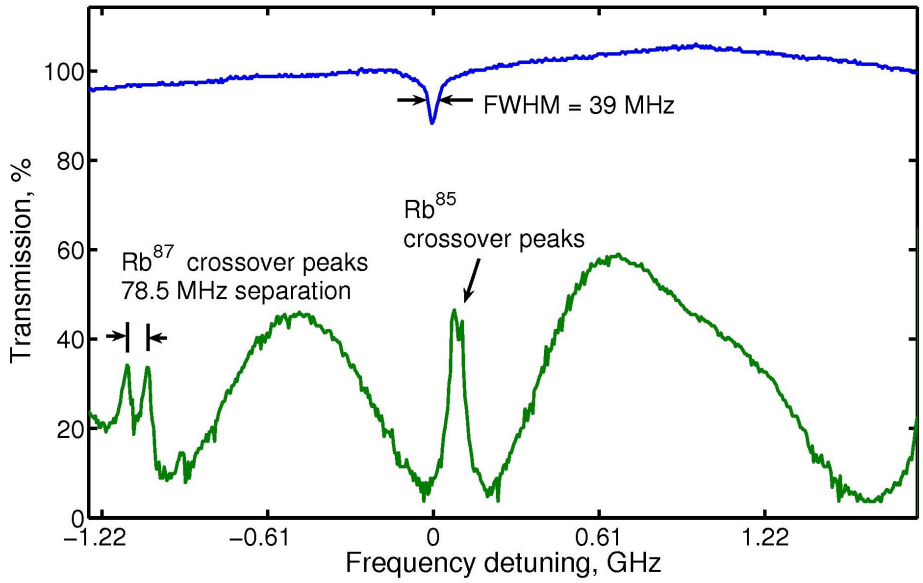

Figure 3.13: Quality factor measurement. The upper trace represents the transmission past the taper-sphere coupling junction. The lower trace is the Rb saturation absorption measurement used to calibrate the x-axis in terms of frequency.

in Er^{3+}:ZBLALiP indicate an attractive alternative to Er^{3+}:ZBLAN for information-storage applications, where even very small powers are sufficient for data retrieval operations [77]. Future work will need to focus on improving the outcoupling efficiency of the device using waveguide technology for integrated optics [84].

Chapter 4

Thermally Induced Optical Bistability in Er^{3+}:Yb^{3+} Co-doped Phosphate Glass

4.1 Introduction[1]

The presence of optical bistability in doped glasses and crystals holds promise for telecommunications and optical computing applications. A miniature bistable laser source would be ideal for microchip integration, especially if it can be mounted with a waveguide such as a stripline pedestal anti-resonant reflecting optical waveguide (SPARROW) [85].

We experimentally demonstrate optical bistability in Er^{3+}:Yb^{3+} phosphate glass microspheres at 295 K. Bistability is associated with both Er^{3+} fluorescence and lasing behaviour, and wavelength/chromatic behaviour. The chromatic switching results from an intrinsic mechanism exploiting the thermal coupling of closely-spaced energy levels, and occurs simultaneously with the intensity switching. A contrast ratio, as

[1]**This chapter has appeared in "Optical Bistability in Er-Yb co-doped phosphate glass microspheres at room temperature," *J. Appl. Phys.*, 102, 023104, (2007).**

measured as the ratio between upper and lower switching positions, of 2.8 has been obtained for chromatic switching. The intensity switching shows ratios of 2.9 and 4.6 for the two green fluorescence emissions at 520 nm and 550 nm respectively, 3.1 for the red fluorescence emission at 660 nm, and 4.7 for the IR lasing at 1.5 μm. The influences of the host matrix on lasing and fluorescence mechanisms are highlighted.

A system is said to exhibit bistability when there are two possible output states for the same input state and the choice of output state depends on the history of the input.

4.2 Er^{3+}:Yb^{3+} Co-doping of Phosphate Glass

In our work, an Er^{3+}:Yb^{3+} co-doped phosphate glass (Schott IOG-2) was used to demonstrate chromatic and intensity optical bistability (OB) simultaneously. The glass is doped with 2 wt% Er_2O_3 (1.7×10^{20} ions/cm^3) and co-doped with 3 wt% Yb_2O_3 (2.5×10^{20} ions/cm^3). The concept of an Er^{3+}:Yb^{3+} co-doped glass laser was demonstrated [86] in 1965 as a means of optimising the Er^{3+} emission cross-section, while simultaneously ensuring an optimum Yb^{3+} absorption cross-section. This overlap alleviates the difficulty of trying to directly pump the narrow Er^{3+} absorption band [87]. Phosphate glass has been investigated as a host matrix for rare-earth ions due to its favourable properties, such as: (i) the possibility of obtaining large dopant concentrations (up to 1.8×10^{21} ions/cm^3 for Yb^{3+}, and $\sim 10^{19}$ ions/cm^3 for Er^{3+}) compared to silicate, borate, and fluoride glasses, (ii) its large absorption band in the near-infrared region, (iii) its large emission cross-section at 1.5 μm, and (iv) the low back energy transfer from Er^{3+} ions to Yb^{3+} ions [88]-[90].

The energy level diagram is shown in Fig. 4.1. The spectral characteristics are also

especially beneficial for C-band lasing; the intermediate lasing level, $^4I_{11/2}$, has a high non-radiative relaxation rate (< 1 μs lifetime, maximum phonon energy of 1300 cm^{-1}) to the $^4I_{13/2}$ level compared with silica (maximum phonon energy of 1190 cm^{-1}), and the long lifetime of the $^4I_{13/2}$ level of about 8.45 ms facilitates population inversion and high gain [91]. The larger phonon energy of phosphate glass has a negative effect on the upconversion efficiency compared to fluoride glass (with a maximum phonon energy of 600 cm^{-1}). This, however, is partially counter-balanced by the large dopant concentrations and wide absorption cross-section of the Yb^{3+} sensitiser. In addition, phosphate glass has better optomechanical properties compared to other glasses used for OB, such as $CsCdBr_3$.[2]

Here, we present experimental OB results on lasing around 1.5 μm and propose suitable upconversion mechanisms for the observed three colour emission bands.

4.3 Experimental Details

We study lasing and upconversion fluorescent emissions following CW pumping with a tunable 980 nm laser diode (spectral width ~ 1 nm) identical to the one described in Section 3.3. IOG-2 glass, with a low glass transition temperature of around 648 K [92], is ideal for producing microspheres with diameters of between 30-70 μm using a microwave plasma torch [93] as described in Chapter 1. A detailed description of the experimental setup is identical to that in Chapter 3, except for the fact that a different active material is used for the microspheres. Microsphere coupling is again done with a 1 μm diameter, 1550 nm SMF-28 fibre. The lasing emissions around 1.5 μm are

[2]It must be noted here that $CsCdBr_3$, and other materials, are of interest for their ability to show intrinsic bistability, in contrast to the extrinsic, self-induced bistability described in the present work.

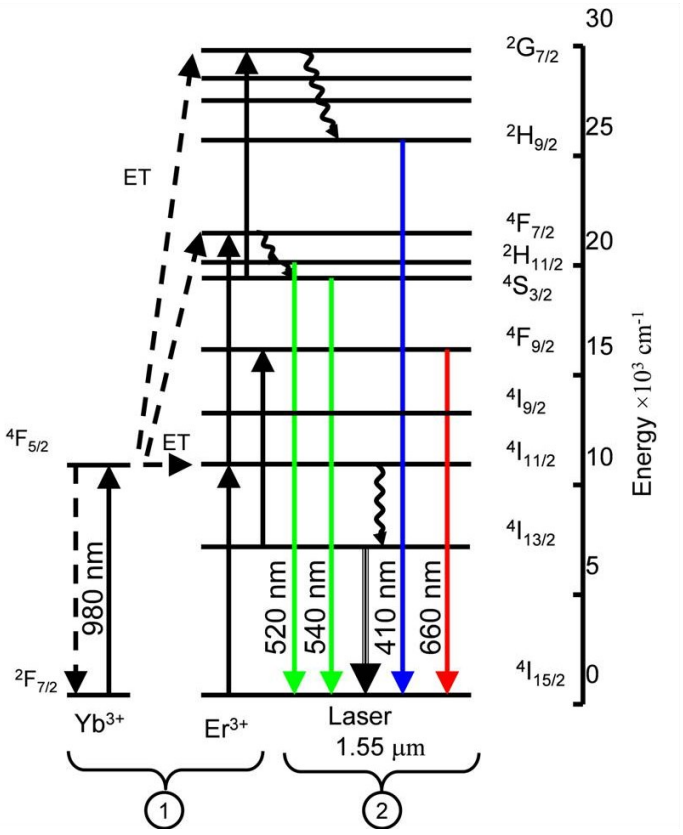

Figure 4.1: Energy level diagram and fluorescence mechanisms with radiative (solid lines) and non-radiative transitions (wiggly lines).

monitored by connecting one end of the fibre taper to an OSA. All upconversion fluorescence spectra were acquired by free space coupling into an Ocean Optics 2000 CCD spectrometer.

4.3.1 Lasing and Fluorescence in IOG-2

In our first experiments, the 980 nm pump power was set to a constant value of about 10 mW. There is a clear difference in the visible emission spectra (c.f. Fig. 4.2) obtained for the two sphere depending on the presence of 1.5 μm lasing. We

note three distinct emission bands corresponding to erbium transitions at 520 nm ($^2H_{11/2} \rightarrow^4 I_{15/2}$), 550 nm ($^4S_{3/2} \rightarrow^4 I_{15/2}$), and 660 nm ($^4F_{9/2} \rightarrow^4 I_{15/2}$). The red emission is stronger than red emissions produced in other singly doped glasses investigated in our laboratory, such as Er^{3+}:ZBLALiP and Er^{3+}:ZBNA, due to the much larger Yb^{3+} absorption cross-section compared to Er^{3+}.

Note that, on occasion, we have also observed a very weak, but distinct fourth emission band in the UV corresponding to an erbium transition at 405 nm ($^2H_{9/2} \rightarrow^4 I_{15/2}$). Figure 4.2(b) shows a fluorescence spectrum representing the violet to red upconversions for a fixed pump power of 8 mW and a 35 μm sphere. Such violet emissions are only observed in spheres that do not lase around 1.5 μm due to a competition between processes involved .

The ESA from $^4I_{13/2}$ feeding the $^4F_{9/2}$ level depletes the intermediate $^4I_{11/2}$ level and the metastable $^4I_{13/2}$ level, thereby placing the 1.5 μm emission in competition with the red emission and the other upconversion processes. This process is shown in the energy level diagram in Fig. 4.1. We find that the power of the red emission is, typically, twice as high in microspheres that exhibit no lasing (due to excessive inhomogeneities in the cavity) compared to those that do exhibit lasing.

For ions excited to the $^2F_{5/2}$ level in Yb^{3+}, IOG-2 has a quantum defect, $\eta_{defect} = \lambda_{pump}/\lambda_{signal}$, of about 60%, resulting in the remaining 40% being dissipated in the host matrix as heat. This statement can be taken further by noting that energy transfer from Yb^{3+} to Er^{3+} depends on three parameters: the energy migration rate among the Yb^{3+} ions (which depends on the inter-ion separation as discussed later in this section), the back transfer rate from Er^{3+} to Yb^{3+}, and the multiphonon relaxation rate from $^4I_{11/2}$ to $^4I_{13/2}$ in Er^{3+}. The overall laser efficiency, η_{laser}, is

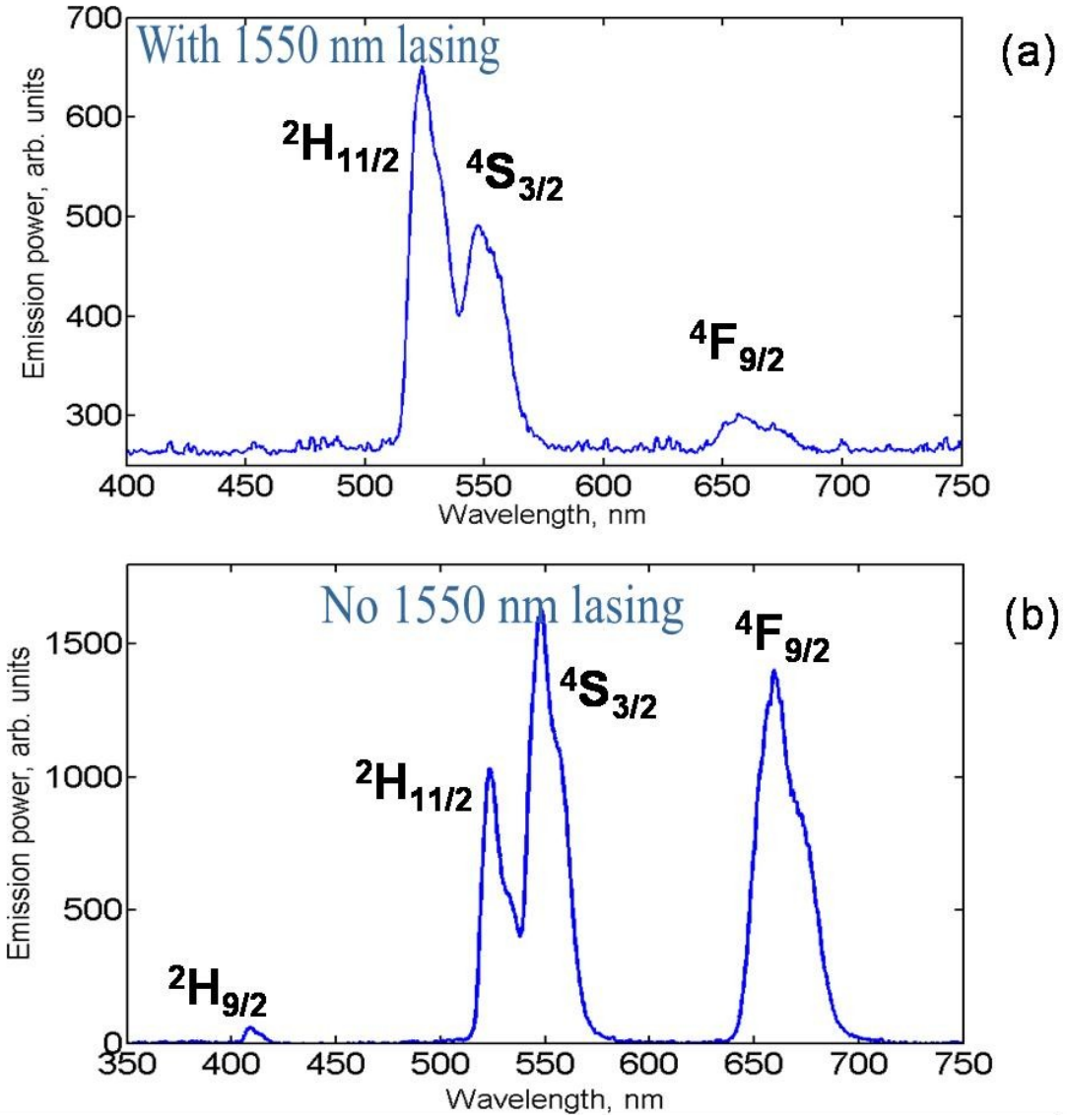

Figure 4.2: Upconversion fluorescence spectrum for two different IOG-2 microspheres. Strong red fluorescence is dependent on whether lasing is present in the microsphere. The figure in (a) shows that a larger proportion of the population is involved in the C-band lasing compared to (b), where upconversion is strong and lasing is absent. An additional weak violet emission from a 35 μm diameter microsphere is shown, for a pump power of 8 mW. The violet emission has been scaled up by a factor of five for clarity.

therefore a combination of the intrinsic quantum efficiency, $\eta_{quantum} = \tau/\tau_R$ (the ratio between the calculated and measured radiative rates), and the efficiency of the energy transfer, η_{ET}, [94]

$$\eta_{laser} = \eta_{quantum}\eta_{ET}, \tag{4.1}$$

where $\eta_{ET} = (\tau_{Yb} - \tau_f)/\tau_{Yb}$, τ_{Yb} is the lifetime of the $^2F_{5/2}$ excited state when there is no ET ($\sim$ 1.3 ms), and τ_f is the lifetime of the same level with ET. In practical systems with high dopant concentrations, the laser slope efficiency can approach the quantum efficiency.

The $^2H_{11/2}$ level and the $^4S_{3/2}$ level can be considered to be in quasi-thermal equilibrium since the energy gap is ≈ 740 cm^{-1} and is comparable to the maximum phonon energy of 1300 cm^{-1} for phosphate glass [91]. As such, only one phonon is required to bridge the energy difference between the two green levels, thereby populating the $^2H_{11/2}$ level at room temperature. The thermalisation of the $^2H_{11/2}$ level by the $^4S_{3/2}$ level has a temperature dependent effect on the ratio of the radiative emissions from these two levels as well as on the excited state lifetimes [95]. The multi-phonon emission rate between these levels at a temperature, T, is

$$K_{mp}(T) = K_{mp}(0)\left[1 - \exp\left(-\frac{\hbar\omega}{k_B T}\right)\right]^{-\varphi}, \tag{4.2}$$

where k_B is Boltzmann's constant, ω is the phonon frequency, and φ is the number of phonons required to bridge the energy gap, ΔE, between the levels and is given by $\Delta E/\hbar\omega$, where $\hbar\omega$ is the phonon energy [96]. For phosphate glass, this multiphonon emission rate is $K_{mp}(295K) \approx 10^{11}$ s^{-1}, which is significantly higher than the value of 10^3 s^{-1} for radiative emissions [96]. The energy difference between the $^4S_{3/2}$ level and the next lowest level, $^4F_{9/2}$, requires three phonons, therefore making this level far less likely to be populated from the $^4S_{3/2}$ level.

The emissions detected from the IOG-2 microsphere, as shown in Fig. 4.2, are due to upconversion processes involving multiple pump laser photons and/or lattice phonons. There are two upconversion mechanisms which must be considered when trying to understand the origin of the fluorescence results; excited state absorption and energy transfer. These are shown in the energy level diagram in Fig. 4.1, in which we identify a number of different groups of transition processes that play a role in the generation of the emission spectra.

Transition groups ① and ② in Fig. 4.1 are associated with the ground state (GSA) and excited state absorptions respectively. As mentioned, there is a resonant energy transfer (ET) from the Yb^{3+} sensitiser ($^2F_{5/2} \rightarrow^2 F_{7/2}$) to the Er^{3+} ion ($^4I_{15/2} \rightarrow^4 I_{11/2}$) followed by 980 nm ESA from the $^4I_{11/2}$ level to the $^4F_{7/2}$ level indicated in group ①. Transition group ② deals with the radiative and non-radiative decay processes for the erbium ion. For example, rapid, non-radiative relaxation from $^4I_{11/2} \rightarrow^4 I_{13/2}$ is possible and falls within this group. In spite of a large energy mismatch of about 1450 cm^{-1} for the $^4I_{13/2} \rightarrow^4 F_{9/2}$ transition, the long lifetime of the $^4I_{13/2}$ state and associated large population ensures that the ESA mechanism is adequately efficient [97, 98]. Due to the close spacing of the $^4F_{7/2}$ and $^4S_{3/2}$ levels, the population of $^4F_{7/2}$ readily decays non-radiatively to the $^4S_{3/2}$ level, whereby the thermal mechanism described previously populates the $^2H_{11/2}$ level. Finally, a second ESA from the $^4S_{3/2}$ level up to the $^2G_{7/2}$ level is followed by non-radiative relaxation down to the $^2H_{9/2}$ level, and the subsequent radiative decay to the ground state generates a photon at 410 nm (violet).

At the high concentrations of Er^{3+} and Yb^{3+} in this work the inter-ion separation reaches a critically small radius of ~ 3 nm for Er^{3+} ions and ~ 2 nm for Yb^{3+} ions.

This is close to the value of 2.12 nm for Yb^{3+}-Yb^{3+} ET's and an estimated 1.5 to 2.0 nm for Yb^{3+}-Er^{3+} ET's as determined from Förster-Dexter theory [99], thereby dramatically enhancing the probability of Yb^{3+}-Yb^{3+}, Yb^{3+}-Er^{3+} and, possibly, Er^{3+}-Er^{3+} energy transfers. The critical radius, R_{sx}, is determined by the overlap of the emission and absorption cross-sections and is given by

$$R_{sx}^6 = \frac{3c\tau_s}{8\pi^4 n_s^2} \int \sigma_{ems}^s(\lambda)\sigma_{abs}^x(\lambda)d\lambda, \tag{4.3}$$

where $\tau_s = 1.4$ ms is the fluorescence decay time of the unperturbed sensitiser, n_s is the refractive index, the script s stands for the sensitiser, i.e. the Yb^{3+} ions, the script x stands for either the sensitiser or the Er^{3+} acceptor ions, σ_{ems} is the emission cross-section, and σ_{abs} is the absorption cross-section. The emission and absorption cross-sections for this material are shown in Fig. 4.3, and are determined from absorption measurements with a bulk sample of IOG-2 (c.f. Section 3.4 for details of the calculation).[3] For non-radiative dipole-dipole interactions the energy transfer rate rapidly increases according to the inverse of the ion separation to the sixth power.

Figure 4.4 shows the observed IR lasing spectrum around 1.5 μm in a 50 μm diameter microsphere pumped with 10 mW of launched pump power at 980 nm. Two lasing peaks are excited, presumably due to excitation of polar modes. The inset shows fluorescing whispering gallery modes in a different 50 μm diameter microsphere. The more intense lasing line has a peak power of 45 μW which, when taken into account with the approximately 1 mW of absorbed power, translates to a quantum efficiency (QE) of 4.5%. This value is far greater than for singly doped glasses where the QE is normally $< 0.1\%$. Analysis of the whispering gallery modes

[3]The absorption measurements were provided by P. Féron in ENSSAT, Lanion, France.

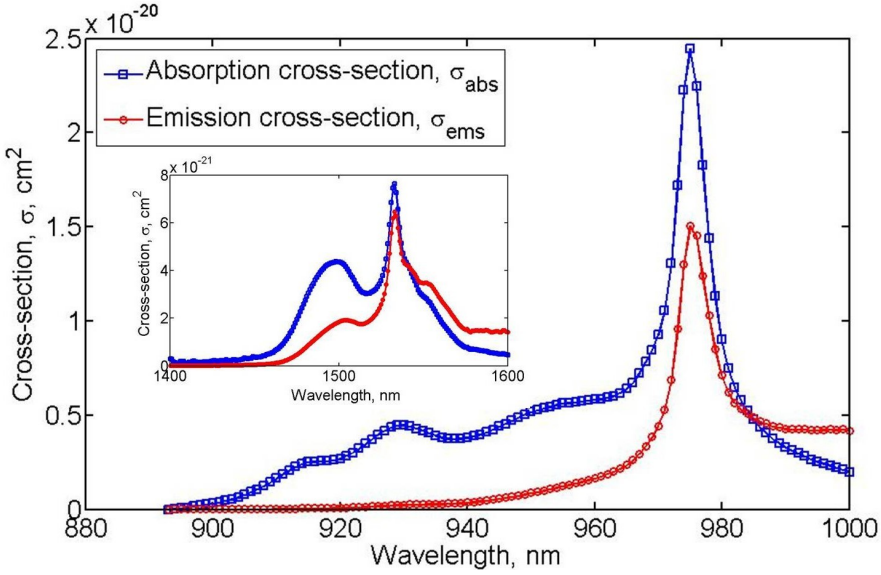

Figure 4.3: Absorption and emission cross-sections for Er^{3+}:Yb^{3+} co-doped IOG-2 bulk glass.

in the fluorescence spectrum enables us to measure the FSR of the sphere modes to be 1.32 THz ($\equiv$ 10.4 nm), indicating a microsphere diameter, $D = c/(\pi n_s \nu_{FSR})$, of 48 μm, where ν_{FSR} is the FSR from the data. This agrees reasonably well with an optical microscope measurement of $50 \pm 2\mu$m. The refractive index of IOG-2 at room temperature is 1.508 at 1540 nm. The measured spacing between TE and TM modes of 9.0 nm around 1550 nm agrees well with the calculated value of 8.50 nm. Eccentricity in the microsphere results in splitting of the azimuthal modes by about 15 GHz, corresponding to an eccentricity of around 2.7%.

4.3.2 Intensity Switching

The usual power law dependence, $I_{signal} \propto I_{pump}^{q}$, as described in Section 3.8, fails in the presence of OB. In order to study the bistability of the microspheres, we measured

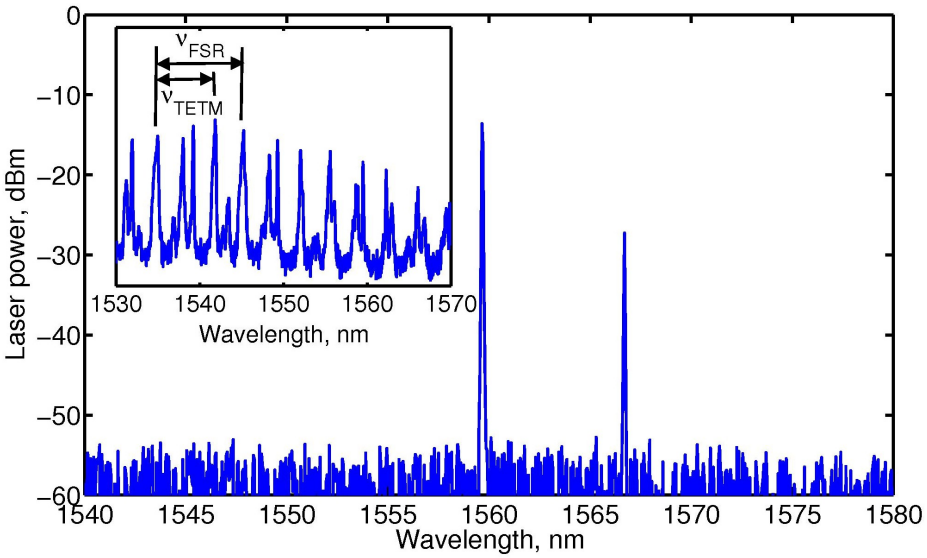

Figure 4.4: Lasing spectrum for a 50 μm diameter IOG-2 microsphere for 10 mW pump power. The inset shows whispering gallery mode structure for a different 50 μm diameter microsphere.

the emission intensity as a function of launched pump power for the same sphere as in section 4.3.1 at the lasing wavelength of 1.5 μm. Similarly, we studied the intensity of fluorescence emissions for a different sphere at three emission wavelengths: 520 nm, 567 nm, and 660 nm. (Note: we used a different sphere simply because the first sphere fell off the mount and was lost). The launched pump power was increased from 0 mW to about 22 mW and back to 0 mW while recording the spectra. The results for 1.5 μm are shown in Fig. 4.5. As the pump power was increased, the emission intensities remained almost constant until a critical power (17 mW for the IR lasing in Fig. 4.5) was reached, beyond which a sudden and dramatic rise in emission intensity was observed. Increasing the pump power beyond the critical point caused the emission to level out once more. A subsequent reduction in pump power clearly demonstrates

hysteretic behaviour and a wide bistable region, where the emission can have two intensity values depending on the history of the input power. The sudden jumps (or intensity switching) between the higher and lower branches of the hysteresis loops are characteristic of the optical bistability of the spheres. A bistable response was also observed in the fluorescence emissions shown in Fig. 4.6. The critical switching power depends on the taper-sphere coupling efficiency and sphere size, and differs for the two different spheres in Figs. 4.5 and 4.6. Possible reasons for the presence of the large peak at about 9 mW for the IR figure and its absence in the fluorescence figures will be discussed in Section 4.6.

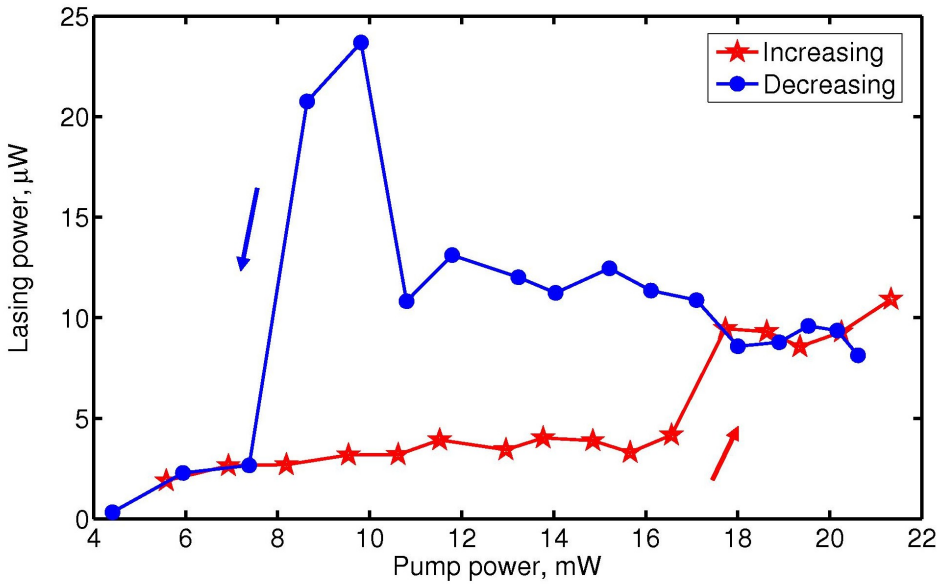

Figure 4.5: Intensity bistability for the C-band in a 50 μm diameter sphere.

A very promising feature of these microcavity resonators is the high contrast intensity switching observed; the ratio of the relative change in emission powers before and after the bistable region is 2.9 for the $^4S_{3/2}$ green, 4.6 for the $^2H_{11/2}$ green, 3.14 for

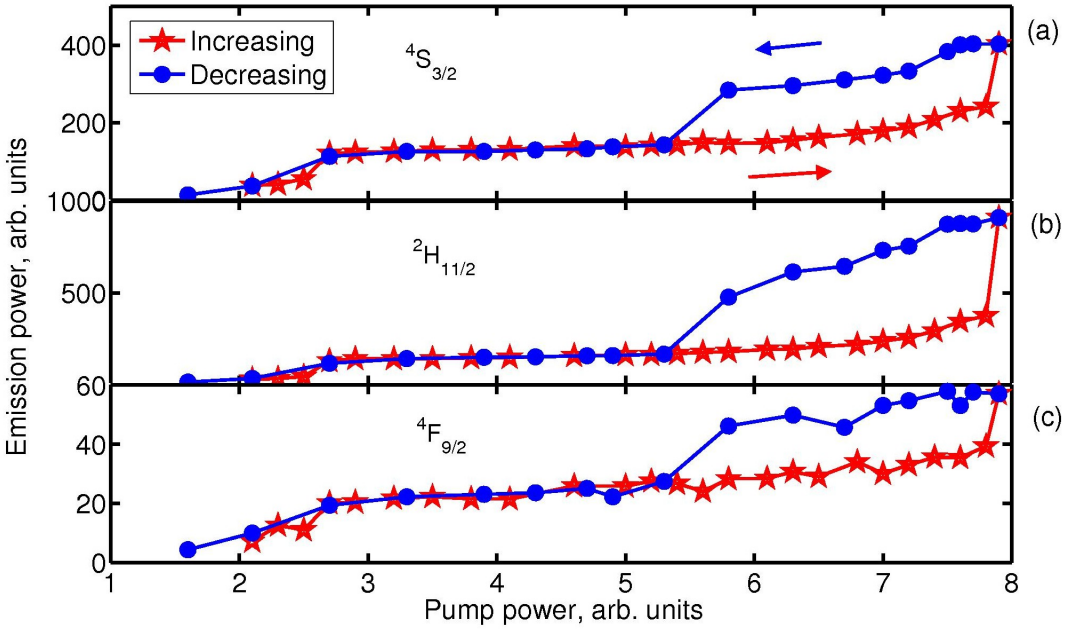

Figure 4.6: Intensity bistability for the two green states $^2H_{11/2}$ and $^4S_{3/2}$, and the red $^4F_{9/2}$ state, for a 60 μm diameter, non-lasing sphere. The launched pump power is varied from 0 to about 10 mW. The switching positions for the green and red emissions in this figure differ from the 1.5 μm lasing emission in Fig. 4.5 due to spheres of different sizes being used. The corresponding spectra for the visible fluorescence are shown in Fig. 4.2(a).

the $^4F_{9/2}$ red, and 4.7 for the $^4I_{13/2}$ IR. These contrast ratios could be further increased by selecting higher quality microspheres and improving the coupling efficiency.

4.3.3 Green Chromatic Switching

As referred to earlier, the strong temperature dependence in IOG-2 is due to the loss of about 40% of the laser power as heat in the glass, in conjunction with its low thermal conductivity. There is a sudden increased pump absorption in the microsphere associated with the sudden increase in heat generation, and visa versa. The increased absorption occurs simultaneously with the sudden rise in the 520 nm ($^2H_{11/2}$) emission intensity as compared to the 550 nm ($^4S_{3/2}$) intensity that was observed when the pump power was increased above the upper switching position of 7.8, as shown in Figs. 4.6 and 4.7. As the pump power was reduced below the lower switching position of 5.3 units, there was a sudden decrease in intensity ratio due to the drop in pump absorption (and heat generation). One of the fortunate properties of erbium is the very close spacing between the $^2H_{11/2}$ and $^4S_{3/2}$ levels. This, combined with the efficient population of the $^4S_{3/2}$ level by 976 nm pumping, and the subsequent population of the $^2H_{11/2}$ level by thermal coupling with $^4S_{3/2}$, provides an indirect measure of the internal temperature of the microsphere. Figure 4.7 reveals this connection between intensity ratio and internal microsphere temperature.

Using the methods outlined by Qiao *et al.* [100], Boltzmann statistics can be used to describe the strong thermal coupling and the population redistribution between the two green levels. The intensity ratio is a function of the internal cavity temperature and is described by

$$\frac{I(^2H_{11/2})}{I(^4S_{3/2})} = \frac{r_H g_H \hbar\omega_H}{r_S g_S \hbar\omega_S} \exp\left(\frac{\Delta E}{k_B T}\right), \tag{4.4}$$

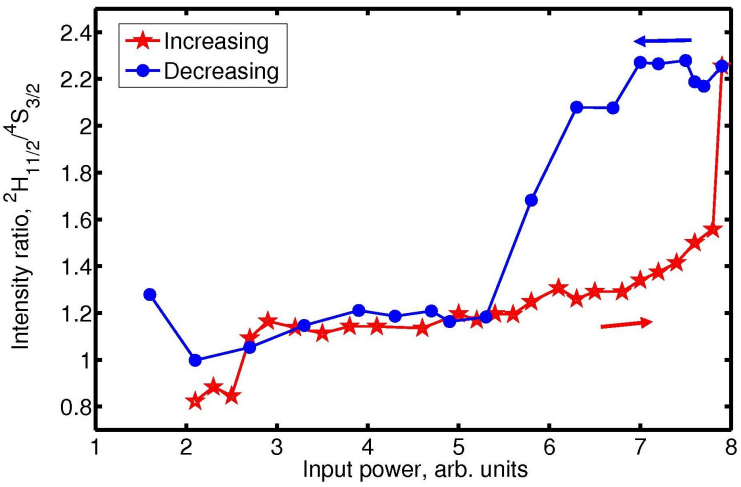

Figure 4.7: Chromatic switching for the green fluorescence emissions at $^2H_{11/2}$ (520 nm) and $^4S_{3/2}$ (550 nm). The inversion ratio is proportional to the temperature of the mode volume. The jump in intensity ratio from 1.1 to 2.3 indicates a temperature increase of 178 K. The corresponding spectra for the visible fluorescence are shown in Fig. 4.2(a).

where I is the integrated emission intensity for a particular level, r is the total spontaneous emission rate, g is the $(2J+1)$ multiplicity (or degeneracy) of each manifold, $\hbar\omega_H$ ($\hbar\omega_S$) is the energy of level $^2H_{11/2}$ ($^4S_{3/2}$), and ΔE is the energy separation between the levels. According to Eqn. 4.4, as the temperature is increased, the $^2H_{11/2}$ level is more efficiently populated, and an increasingly larger fraction of the $^4S_{3/2}$ population is rapidly promoted to this upper level, and, consequently, the ratio of the emissions from the two states inverts so that the 520 nm emission becomes stronger. For a ratio of 2.3 on the y-axis in Fig. 4.7, the corresponding temperature is 575 K. The chromatic switching can yield intensity ratios of up to 2.8 (data not shown). From Eqn. 4.4, this indicates a temperature of 642 K, just below the glass transition value of 648 K [92]. This temperature seems exceptionally high, although there was no evidence of thermal stresses, fracturing of the glass or other defects in the microsphere. However, it is important to emphasise that the temperature calculated using this method does not represent the temperature of the entire sphere, but rather just the temperature of the mode volume. Heat dissipation from this region through the remainder of the material would account for no thermal stress on the sphere itself, which is likely to be at a much lower temperature.

4.3.4 IR Wavelength Switching

In a cold cavity, with no heating, the resonance at a wavelength λ obeys the stationary wave condition $l\lambda = 2n_s(2\pi a)$, where l defines the equatorial mode number, n_s is the refractive index of the glass, and a is the microsphere radius. This resonance condition must change when there is pump-induced heating. Both the cavity dimensions and refractive index are temperature dependent and must be included in the modified

equation, given by

$$l\lambda = 2n_s d\left(1 + \frac{1}{n_s}\frac{\partial n_s}{\partial T}\right)\left(1 + \frac{1}{d}\frac{\partial d}{\partial T}\right), \tag{4.5}$$

where we define $d = 2\pi a$ [93]. The first term in the brackets gives the fraction by which the refractive index must change, and the term in the second brackets gives the fraction by which the cavity length must change. From this definition we can write the wavelength shift as a function of temperature as

$$\frac{\Delta\lambda}{\Delta T} = \lambda\left(\frac{1}{n_s}\frac{\partial n_s}{\partial T} + \frac{1}{d}\frac{\partial d}{\partial T}\right). \tag{4.6}$$

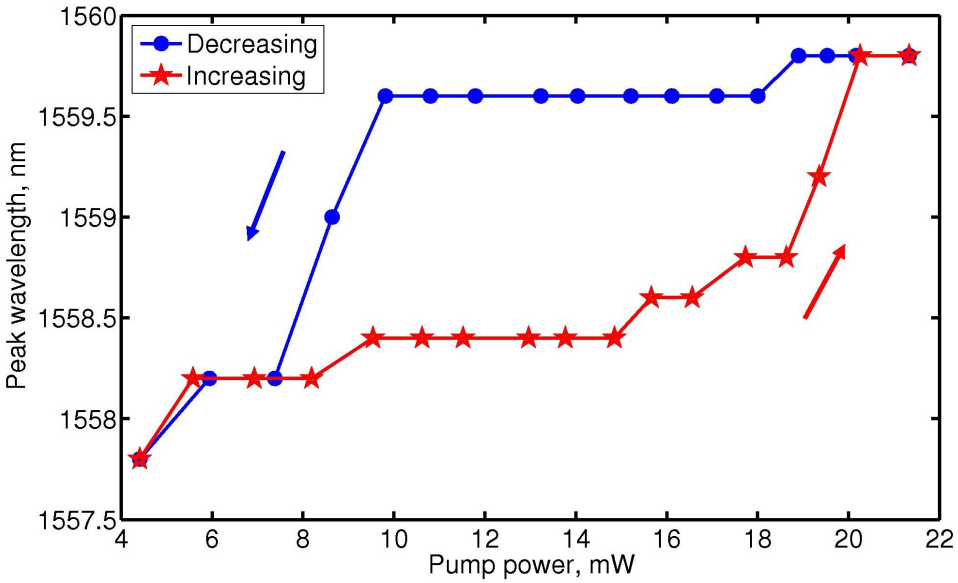

Figure 4.8: Wavelength switching in the C-band lasing at 1.5 μm. The figure corresponds with the intensity bistability measurements in Fig. 4.5. The switching positions are the same for both.

From this discussion we can reach the conclusion that the temperature and size of the mode volume are also bistable. By extension, the wavelength of the lasing

emission has a bistable response. Figure 4.8 shows a difference of 1.2 nm between upper and lower wavelength values, measured in the middle of the bistable region, corresponding to a temperature difference of 94 K. Here, we have taken the cavity expansion coefficient to be 145×10^{-7}/K from the manufacturer's specifications [92] and the thermo-optic variation coefficient is taken to be -63×10^{-7}/K from a similar glass, QE-7S [101]. A more accurate model of the wavelength shift would have to include the complex behaviour of stress-induced refractive index changes (photoelastic effect), especially since the mode volume of the 980 nm pump is more than 1.5 times smaller than in the 1.5 μm lasing mode as shown in Fig. 1.5.

4.4 Power-law Upconversions

Our microspheres tend to exhibit bistability only when the current to the pump laser, and, hence, the pump frequency, are adjusted to a precise setting for each sphere. We have plotted the emission power for three wavelengths as a function of pump power in Fig. 4.9. Unlike the previous data, Fig. 4.9(a) shows linear slopes for a 30 μm diameter, nonlasing microsphere. Lasing action is always absent for microspheres of this size, presumably due to the expected lower Q factor (c.f. the microsphere size dependence of Q in Fig. 1.4(b)). The slopes of the three plots indicate that two pump photons produce each fluorescence photon emitted, as predicted by the power law dependence. A notable feature in the spectrum in Fig. 4.9(b) is the poorer thermalisation of the $^2H_{11/2}$ level compared to other, larger, microspheres discussed in this chapter. This implies there is a relatively low amount of heating in this particular microsphere.

We expect the reason for the quadratic response to be a combination of poorer

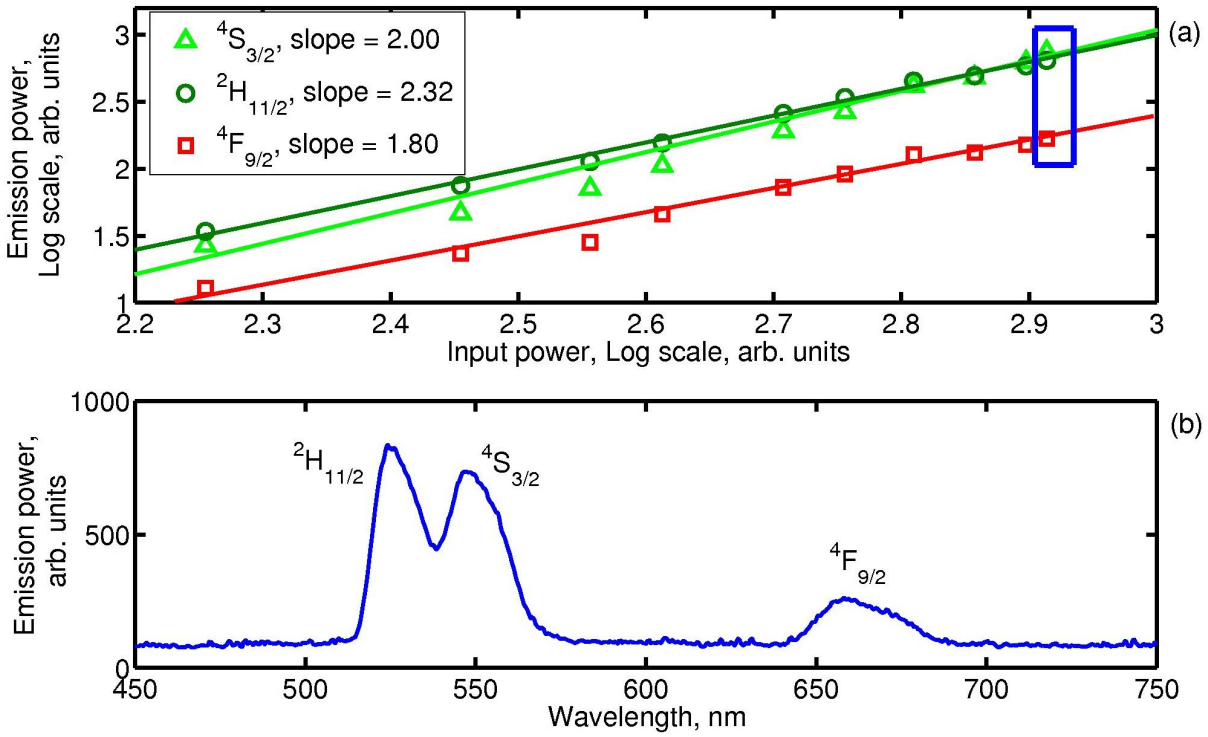

Figure 4.9: Fluorescence slopes and spectrum for the two green levels and the red level for a 30 μm diameter nonlasing sphere. The slopes in (a) follow a power law dependence and indicate two pump photons produce a photon at either of the three wavelengths. The spectrum in (b) corresponds to the last data point in (a).

phase matching between the 1 μm diameter taper coupler and the 30 μm diameter microsphere, greater cavity losses due to a lower Q value, greater heat dissipation rate due to the smaller cavity size compared to the size of the supporting post holding the microsphere, and a larger FSR. The culmination of these factors impacts dramatically on the microsphere's ability to demonstrate self-induced thermal bistability. This observation may set a lower limit on the range of microsphere diameters that can exhibit bistability, if the wavelength of the pump laser is not adjusted appropriately. It is expected that phase matching with a fibre taper will set an upper limit of roughly 100 μm on the microsphere diameter for a useful device.

4.5 Discussion

Optical bistability previously demonstrated in passive silica [10, 102] was attributed to nonlinearities arising from the Kerr effect of the resonance line, together with high Q factors ($Q > 10^8$) and a tunable, narrow linewidth laser. OB, due to the large thermo-optic effect in Silicon (a factor of 30 bigger in magnitude than in IOG-2 glass), was also observed in a 5 μm diameter ring resonator with a Q factor of only 10^4 [22]. The results presented here clearly show that IOG-2 microspheres exhibit bistable switching behaviour under vastly different conditions; we use co-doped phosphate glass microspheres, and the pump laser has a linewidth of 1 nm and is not locked to a specific cavity resonance.

In principle, a number of processes may be responsible for the observation of optical bistability, depending on whether the observed effect is temperature dependent or independent. Experiments performed in our lab have shown that the switching positions depend on the ambient temperature, thereby excluding photon avalanche

and the Kerr effect immediately, both of which are temperature independent. Temperature dependent mechanisms that may be responsible include material effects like (i) strong Yb^{3+}-Yb^{3+} coupling, i.e. non-linear energy transfer [103], (ii) nonlinear upconversion rates [104], and (iii) thermal avalanche [16], and cavity effects, such as (iv) dispersive bistability mediated by the thermo-optic effect and cavity expansion [22, 105].

Guillot-Nöel *et al.* [103] have described a mechanism that could be responsible for bistability in the regime of strong Yb^{3+}-Yb^{3+} coupling, in which case cooperative luminescence would be expected. In order to be appreciable, the distance between the ions would need to be of the order of several Å, i.e. significantly smaller than for IOG-2 (21 Å) assuming there is no clustering, and, therefore, this effect is unlikely to play a key role. However, if it is present, the luminescence would likely be very weak compared to the single ion Er^{3+} transitions. It is reasonable to assume that the back transfer rate is negligible due to the high phonon energy of the host lattice, and is, therefore, unlikely to be the source of nonlinearity in our measurements.

Another possible explanation includes a nonlinear upconversion rate either for Yb^{3+}-Yb^{3+}, Yb^{3+}-Er^{3+} or Er^{3+}-Er^{3+} energy transfers [104]. This has been observed in high concentration Er^{3+} doped fibres, where the nonlinearity is dependent on population inversion of the lasing levels, and the signal and emission rates. Temperature dependent effects in the upconversion fluorescence in Er^{3+}:Yb^{3+} Ga_2S_3:La_2O_3 chalcogenide glass and germanosilicate optical fibres have been attributed to an exponential increase in the Yb^{3+} absorption cross-section elsewhere [106]. However, there have been no reports of bistability relying on these mechanisms.

Thermal avalanche was used to explain bistability in Yb^{3+}-doped bromide lattices

by Gamelin *et al.* [16] at cryogenic temperatures. This theory relies on nonlinear absorption in the Yb^{3+} ions with increasing temperature and predicts bistable power absorbance in the microsphere as a function of pump power in the taper. As phonons are released into the lattice from Yb^{3+} excited and ground states, the temperature increases, thereby increasing absorbance and leading to a further increase in temperature. This cyclic process causes a thermal avalanche for high enough pump power. In order to determine whether thermal avalanche is truly responsible, it would be necessary to perform measurements of the dependence of the Yb^{3+} absorption coefficient and to ascertain whether it is a nonlinear function of internal microsphere temperature above 295 K. However, the results presented in Lei *et al.* [107] for different Yb^{3+}-doped phosphate glasses do not show a suitable nonlinear absorption coefficient necessary for thermal avalanche. This suggests that thermal avalanche theory is also unsuitable to describe the behaviour of IOG-2.

We suggest that dispersive bistability [105] - a mechanism commonly used to explain bistability in Fabry-Pérot etalons - can predict our results. The general theory states that as the pump laser frequency is scanned across a high-Q cavity resonance the cavity intensity rapidly rises, and when the pump frequency moves away from the cavity resonance the cavity intensity rapidly falls. In addition, this description is complicated by the fact that the frequency of the cavity resonance scales approximately linearly with the cavity intensity, leading to a bistable response. In our case, the cavity resonance could be shifted by a temperature-dependent refractive index - the thermo-optic effect - and thermal expansion of the cavity [93]. As already mentioned in the previous section, we find that in order to observe bistability the current to the pump laser, and, hence, the pump frequency, need to be adjusted to

a precise setting for each sphere. The corollary of this adjustment is the positioning of the laser frequency near a cavity resonance. For the experimental conditions here, a threshold power of about 100 μW in the cavity mode is enough to cause switching - a value which is well below our estimated 10-15% of pump power coupled into the sphere ($<$ 1mW). Firm evidence of this effect would be possible by probing individual cavity resonances with a narrow linewidth, 980 nm external cavity diode laser, while recording the power transmitted past the taper-sphere coupling junction as described by Rokhsari *et al.* [102].

4.6 Dispersive Optical Bistability

Thermal nonlinearities will affect the resonance condition in a high-Q cavity. In phosphate glass, the combined effect of the thermo-optic effect and cavity expansion red-shifts the resonance frequency. The direction in which the resonance frequency scans across the pump laser frequency, or visa versa, produces two distinct responses governed by the thermal properties of the cavity.

Two time constants describe the cavity dynamics: the fast mode volume response and the slow microsphere response. The mode volume quickly dissipates heat into the microsphere volume with a time constant $\tau_{Mode} = (2b)^2/\kappa$, where b is the half-width of the mode volume given by $b = 0.84al^{-2/3}$, and $\kappa = 0.57$ W/mK is the thermal conductivity [92]. This time constant for the mode volume is about 2 μs for our microspheres, while the time constant for the whole sphere volume is on the order of a few milliseconds [108]. A picture of the heat generation and loss mechanisms in a microsphere is shown in Fig. 4.10. Conduction is viewed as the primary mechanism affecting the thermal diffusion [109].

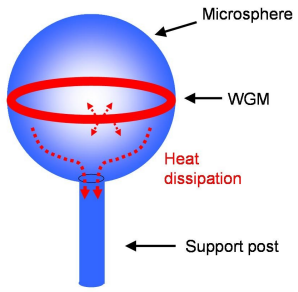

Figure 4.10: Schematic of the heat conduction from the mode volume to the rest of the microsphere and the tapered fibre (not shown). The microsphere dissipates its heat primarily through the supporting stem/post.

It was shown in [109] and [110] that cavities with thermal nonlinearity are described by a nonlinear differential equation for the internal field amplitude, e,

$$\begin{aligned} \dot{e} + e\left[\Delta x + i(\omega + \delta)\right] &= I_{inc}(t) \\ \dot{\delta} + \Gamma\delta &= \Gamma\xi|e|^2, \end{aligned} \tag{4.7}$$

where Δx is the linewidth of the mode, ω is the resonance frequency of the mode, δ is the shift in resonance frequency giving the amount of detuning, $I_{inc}(t)$ is the pump field, Γ is the relaxation rate, and ξ is the thermal nonlinearity coefficient which comes from the part in the brackets in Eqn. 4.6. Fig. 4.11 describes how the cavity resonance is scanned across the laser frequency from two different perspectives; (a) frequency detuning, and (b,c) input pump power.

The plot in Fig. 4.11(a) is the internal cavity field given by the Lorentzian [105],

$$|c_\nu|^2 = \frac{|c_\nu^0|^2}{1 + 4\left(\frac{x - x_\nu^0}{\Delta x}\right)^2}, \tag{4.8}$$

where $|c_\nu|^2$ is the shifted cavity field coefficient, $|c_\nu^0|^2$ is the unshifted cavity field, and x_ν^0 is the unshifted resonance position. Since our bistability is self-induced, the

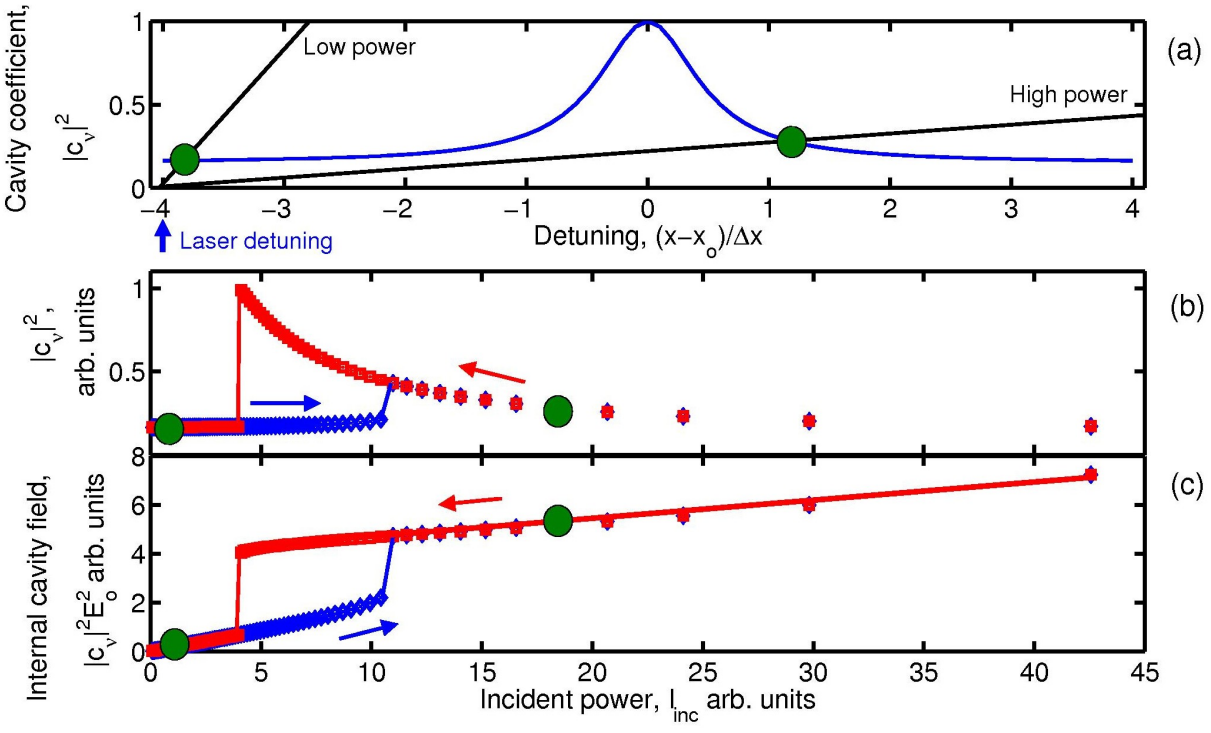

Figure 4.11: Graphical description of dispersive optical bistability due to thermal nonlinearities in a cavity. The green circles mark out corresponding points on each of the three plots. Figure (a) shows the Lorentzian of the 980 nm pump, Fig. (b) shows the cavity coefficient, i.e. the region over which the cavity resonance scans over the pump Lorentzian, as a function of input power, and Fig. (c) shows the internal cavity field as a function of input power.

detuning can be written as a function of the input pump intensity,

$$\left(\frac{x - x_\nu^0}{\Delta x}\right)^2 = \delta + K I_{inc} |c_\nu|^2, \tag{4.9}$$

where K is a constant defining the amount of spatial overlap between the perturbation and the energy distribution of the mode. This equation produces the black line in the figure which scans across $|c_\nu|^2$ with increasing values of incident pump I_{inc}. The intersection points between the line and $|c_\nu|^2$ are solutions to the cubic equation in Eqn. 4.7. The cubic equation in Eqn. 4.7 produces a response similar to that shown in Fig. 4.11(b). In reality, these intersections describe the positioning of the cavity resonance relative to the pump frequency (c.f. the movie linked in Fig. 4.11). In cases where the line intersects at three points for increasing I_{inc}, the most stable position is that with minimum detuning. Alternatively, for decreasing I_{inc}, the most stable position is that with maximum detuning. There are no stable solutions where the line intersects two points. The internal microsphere intensity amplitude is $|c_\nu|^2 E_o^2$ where $I_{inc} \propto E_o^2$. A theoretical bistable plot of the internal sphere field is plotted in Fig. 4.11(c) and clearly mimics the results in Fig. 4.6.

Comparison of the bistability plots for IR lasing in Fig. 4.5 and fluorescence in Fig. 4.6 indicates somewhat unusual behaviour around the switch-low position. The IR lasing suddenly peaks at 10 mW launched power before switching to the lower state. All spheres have demonstrated this behaviour to a greater or lesser degree. Despite this, the fluorescence never shows a sudden jump before switching to the lower state. In particular, a sudden increase in absorption (as determined from the ratio of the two green emissions discussed in Section 4.3.3) in the sphere at this point, is never observed. There seems to be no similar effect observed in Fabry-Pérot cavities and other resonators, which might have shed some insight onto the problem. A possible

explanation for the peak in the IR lasing bistability plots, and its notable absence in fluorescence plots, may be related to thermal lensing (c.f. Section 1.10) and the two different methods used to detect the light, i.e. a tapered fibre is used for the lasing emissions and a high NA fibre is used to collect scattered fluorescence. In order to fully understand this behaviour it needs to be investigated further by analysing the effect of thermal lensing in microspheres, and by imaging the mode propagation path in the microsphere.

4.7 Conclusions

In conclusion, a multi-wavelength, microsphere light source with optical bistability has been demonstrated in an Er^{3+}:Yb^{3+} co-doped IOG-2 sphere, and the Er^{3+} transitions and fluorescence mechanisms involved have been identified. Factors affecting the dynamics of visible fluorescence and C-band lasing emission have been examined and show that the thermal properties of IOG-2 glass play an important role in the microsphere performance. In particular, the high loss of pump power to the glass as heat, in conjunction with the low thermal conductivity have a pronounced effect on the green emissions from levels $^2H_{11/2}$ and $^4S_{3/2}$. Our calculations show that the close proximity of the ions in our glass greatly enhances the probability of sensitiser-sensitiser and sensitiser-acceptor energy transfers.

We have also reported on the simultaneous observation of chromatic and intensity OB in IOG-2 glass at room temperature. These results show that there are two possible temperatures in the bistable region and that it is also possible to have two emission intensities for the same excitation power. Chromatic bistability is dependent on the presence of intensity bistability due to the energy coupling between the green

emitting levels $^2H_{11/2}$ and $^4S_{3/2}$. Therefore, the switching positions are the same for both types of bistability. The OB shows high contrast switching ratios. The intensity switching shows ratios of 2.9 and 4.6 for the two green emissions, 3.1 for the red fluorescence emissions, and 4.7 for the IR lasing, while the chromatic switching ratios are as high as 2.8.

Our observations may be tentatively explained in terms of dispersive bistability, where the temperature dependent refractive index and thermal expansion of phosphate glass causes the resonant cavity mode and the laser mode to behave nonlinearly, yielding a bistable response. Several other possible mechanisms (strong Yb^{3+}-Yb^{3+} coupling, nonlinear upconversion rates, and thermal avalanche) were examined; however, all are considered unfavourable under our experimental conditions or else require further measurements to study their influence on the observed behaviour.

Microcavity resonators offer substantial miniaturisation, greatly reduced power for switching, and allow for all emissions to be easily fibre coupled [111]. In addition, the improved optomechanical properties of IOG-2 compared to other glasses used for OB, such as $CsCdBr_3$, makes this glass appealing for all-optical logic elements in optical engineering applications. The expected low operating speed of a few hundred Hz is likely to make this type of bistability unfavourable for all-optical computing applications.

There are, however, numerous engineering situations where this device will have superior performance. The advantage of using a non-electrical, fibred device for industrial applications is promising. Such applications might include a miniature temperature limit switch and/or a pressure limit switch where electrical noise limits traditional electrical devices. For example, it may not be possible to use a piezo-strain gauge -

and the associated wheatstone bridge - near large, noisy switch gears or generators. A similar limitation exists with electrical resistance thermometers, which also require a wheatstone bridge, when placed in noisy environments. In addition to electrical noise immunity, the switching thresholds can be controlled to give the desired performance. The upper temperature operating limit is only limited by the glass transition temperature of 649 K. Nanometre variations in the cavity radius are enough to exploit the switching mechanism in the microsphere. Furthermore, recent work in our laboratory has demonstrated the mechanical robustness of such a system by thermally fusing the fibre taper to the microsphere at a specific point, thereby minimising drift in the switching positions arising from changes in the coupling efficiency [112], and, as a result, the pump intensity.

The functionality offered by the wavelength switching could be exploited for 1×2 ADD-DROP filtering. Details of a similar passive device have already been proposed in [113]. In our case, the 980 nm pump would serve as a control beam for either adding and/or dropping a wavelength by causing the cavity resonance frequency to shift. The device would be largely independent of wavelength, except for those frequencies falling within the material absorption bands.

Chapter 5

Homemade External Cavity Diode Laser

5.1 Introduction

The work in this thesis has focussed primarily on the exploitation of the material properties of different glasses and their dopants. Chapter 4 revealed the profound importance of the cavity modes in gain media. Future work in the group will depart from the material science emphasis and will study novel cavity effects, such as coupled resonator induced transparency using Fano resonances in passive microspheres, and the effect of mutually coupled resonators on the lasing threshold or Q factor in either active or passive microspheres respectively. The study of such phenomena requires a narrow linewidth laser in order to controllably probe individual cavity resonances. For this purpose an external cavity diode laser (ECDL) with a Littrow configuration grating was constructed using the Sussex and Melbourne designs [114, 115]. This chapter describes the design, construction, and testing of the ECDL.

Homemade ECDLs have been a mainstay of atomic physics and microcavity physics for a number of decades [4, 116]. Their low cost and yet long term, high

performance have made them an indispensable tool for studying specific resonances. The basic principle of the ECDL relies on the frequency selective feedback of part of the optical signal into the diode laser. This is achieved using a diffraction grating to create an external cavity and can yield linewidths of a couple hundred kHz [115].

5.2 Design and Construction

In our design we use a Littrow configuration for the grating that reflects about 40% of the first order diffracted beam back into the laser diode cavity as shown in Fig. 5.1. The Littrow configuration is shown in the zoomed image. The output beam from the ECDL is the zeroth order reflection from the diffraction grating. The angle of reflection from the grating, θ, is wavelength dependent according to the grating formula $m\lambda = 2d\sin(\theta)$, where m is the order of diffraction and d is the groove spacing on the grating. This formula dictates the necessary grating to purchase for the chosen wavelength range. It also shows that one can selectively feedback a specific wavelength by simply adjusting the angle of the grating, θ. Unlike other ECDL designs [114, 116], the Melbourne design has an added mirror that exactly counteracts any transverse displacements of the beam over the full range of θ adjustments. This is vitally important for fibre coupling into a single mode fibre.

The construction follows the designs by Hawthorn *et al.* [115] and the associated website [117], where technical drawings and a parts list are available. The laser diode is a 50 mW 980 nm Fabry-Pérot cavity with no anti-reflection (AR) coating, supplied by Roithner Lasertechnik Gmbh (S9850MG). These diodes were found to operate very well and are reasonably priced at 12 euro each. The lens in the collimation tube has an AR coating. A small, replicated holographic grating with 1200 lines/mm from

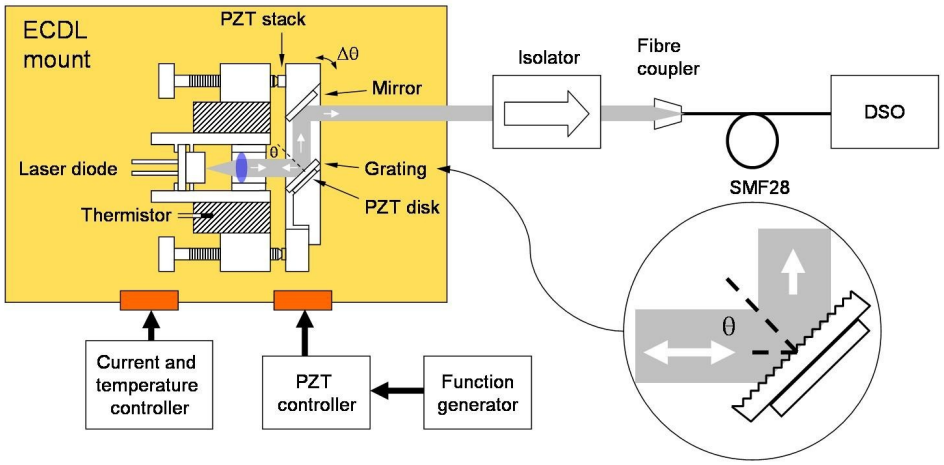

Figure 5.1: Schematic of the external cavity diode laser and the supporting hardware. The angle θ in the zoomed imaged is defined as the angle between the normal to the grating and the optical axis of the beam from the laser diode. DSO: Digital storage oscilloscope, PZT: piezo-electric element, SMF28: single mode fibre, angular displacements, $\Delta\theta$, are done with the upper adjustment screw in the main figure.

PTR Optics is the main feature of the ECDL. A PZT stack scans the grating angle at 50-100 Hz, and a 1 mm thick PZT disk beneath the grating provides ultra-fine scans. All other design details, and electrical wiring are described in Appendix F.

Alignment of the laser cavity is a two-step process. First, the beam is collimated over a distance of about 3 m by adjusting the collimation lens. The second step is to precisely align the first order beam sent back into the Fabry-Pérot cavity by noting the threshold current for every adjustment of (i) the grating angle and (ii) the collimation lens. A reduction in threshold corresponds to improved alignment. Reference [114] suggests that the current to the laser should be set just below the threshold while making the adjustments, however, it can be more convenient to operate the

laser slightly above threshold. The advantage is that any degradation or improvement can be immediately noticed in the output power measurement. Figure 5.2(a) shows a spectrum with a single 1.65 mW lasing peak after fibre-coupling to an OSA. Figure 5.2(b) shows a plot of the lasing threshold, as the alignment is improved. The collimation lens should only be adjusted a few degrees of rotation in the threaded mount until the threshold is minimised. Very slight movements in the lens persist for about one minute after each adjustment and this tends to affect the alignment and must be taken into consideration also.

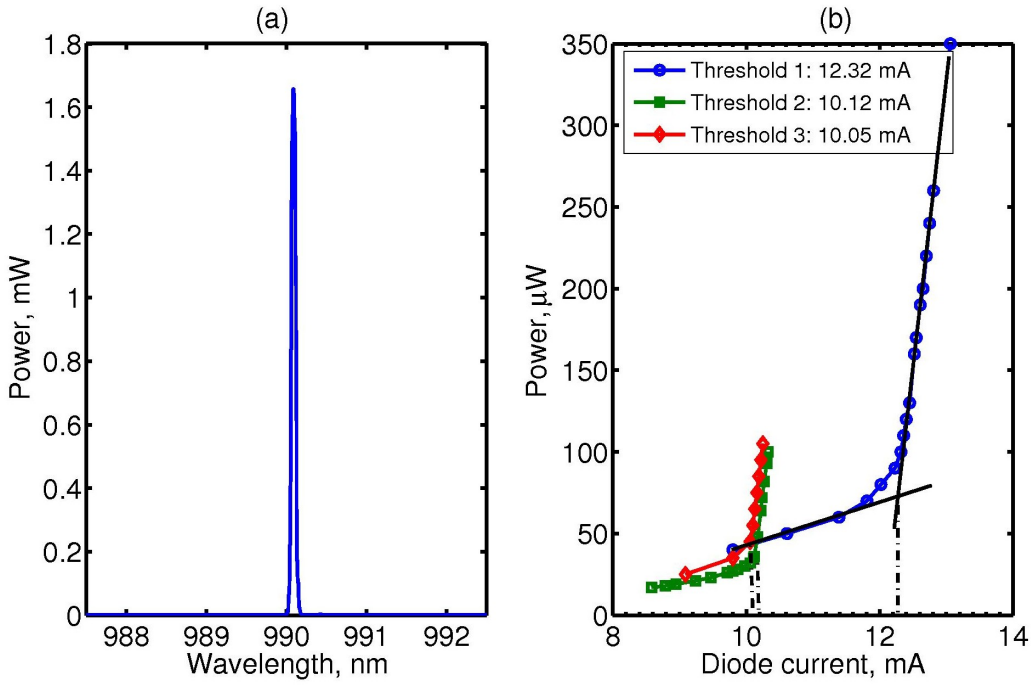

Figure 5.2: (a) Fibre coupled lasing peak as measured on the OSA, and (b) threshold currents. The threshold currents were recorded at different stages of the collimation tube alignment.

The ECDL is mounted on a heavy 5 kg steel block to provide vibration isolation and a large thermal sink. A layer of Sorbothane beneath the block damps the transmission of vibrations from the optical table through to the ECDL. Thermal paste is applied to each of the joints between the laser cavity and block to improve conductivity. In addition, an aluminium enclosure surrounds the ECDL, combined with a further clear plastic enclosure, adding two layers of thermal buffering from air currents as well as acoustic noise, thereby improving the stability of the laser (c.f. Appendix A).

5.3 Performance

The ECDL must meet several requirements; fixed direction output of the laser beam for fibre coupling compatibility, wide tunability over a range of one FSR for a typical microsphere, i.e. about 10 nm, and narrow linewidth.

As stated, the design is inherently optimised for fixed direction output. The ability to tune the laser over 30 nm, using the angular adjustment screw shown in Fig. 5.1, while maintaining at least 60 % laser power shows the advantage of the design. Such a wide tuning range, from 965 - 995 nm, is of great benefit when scanning across a microsphere's FSR.

As the angular adjustment screw is turned, the lasing mode is shifted from one spectral mode to the adjacent spectral mode, typically 0.5 nm apart, while always maintaining single mode output over the 30 nm range. Unfortunately, this wavelength tuning requires the two enclosures to be removed and direct manual adjustment of the screw. The wavelength of the lasing peak can be shifted over this 0.5 nm range by varying the laser diode current from 15 - 75 mA. A LL curve for the full current

range is shown in Fig. 5.3(a). Several mode hops start appearing for currents greater than 45 mA. Juxtaposed with these mode hops are those appearing when the piezo stack is scanned. The piezo stack provides fine scans over a range of around 6 GHz, which is wider than a typical resonance width, i.e. < 1 GHz, and is shown in Fig. 5.3(b). Ultra-fine scans over a range of around 0.4 GHz are possible by scanning the piezo disk beneath the diffraction grating. AR coated LDs, while considerably more expensive, can improve the continuous tuning range to several hundred GHz up to a few THz. These measurements were performed by connecting the fibre-coupled laser output into a wavemeter (Burleigh Instruments, WA 1100), which has a resolution of 0.001 nm.

Homemade ECDLs compare favourably with commercial counterparts, and typically have linewidths ranging from 100 kHz to around 5 MHz. Hawthorn *et al.* [115] quote a linewidth of 370 kHz over 100 s for their 780 nm ECDL, measured by looking at the beat signal of two identical lasers locked to atomic resonances in rubidium using a fast photodiode. Initial attempts to find a resonance in an Er^{3+}:ZBLALiP microsphere with the ECDL built here have been unsuccessful. This may be because the linewidth is several tens of MHz, i.e. greater than the width of a microsphere resonance. The identification of resonances is compounded by the appearance of many narrow mode hops over piezo-stack tuning range. These mode hops are often misleading due to their narrow width, giving the false impression of a microsphere resonance. Nevertheless, these misleading mode hops can be eliminated from the identification process with some experience. An actual linewidth measurement using the self-homodyne technique may be necessary to confirm the laser performance in future work.

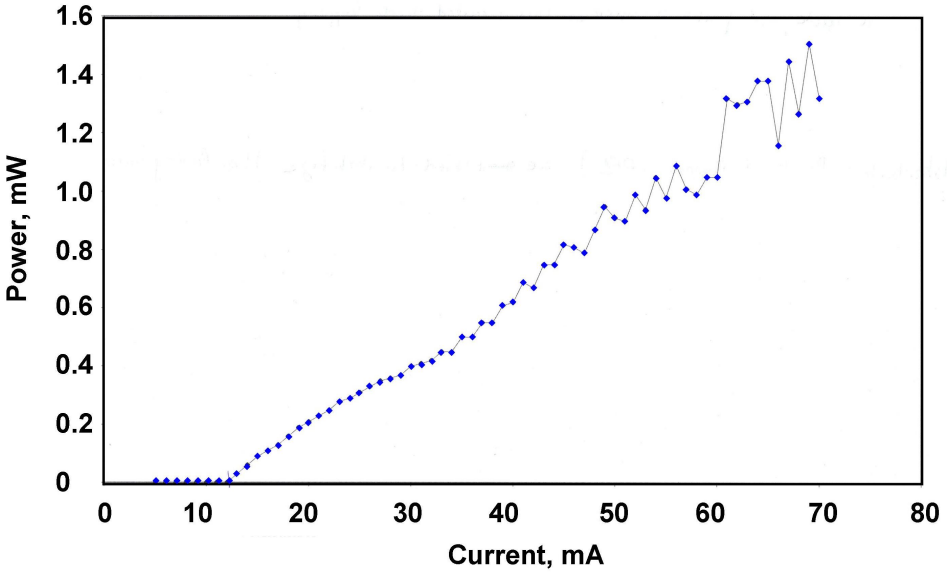

(a) Light-in light-out curve for the ECDL.

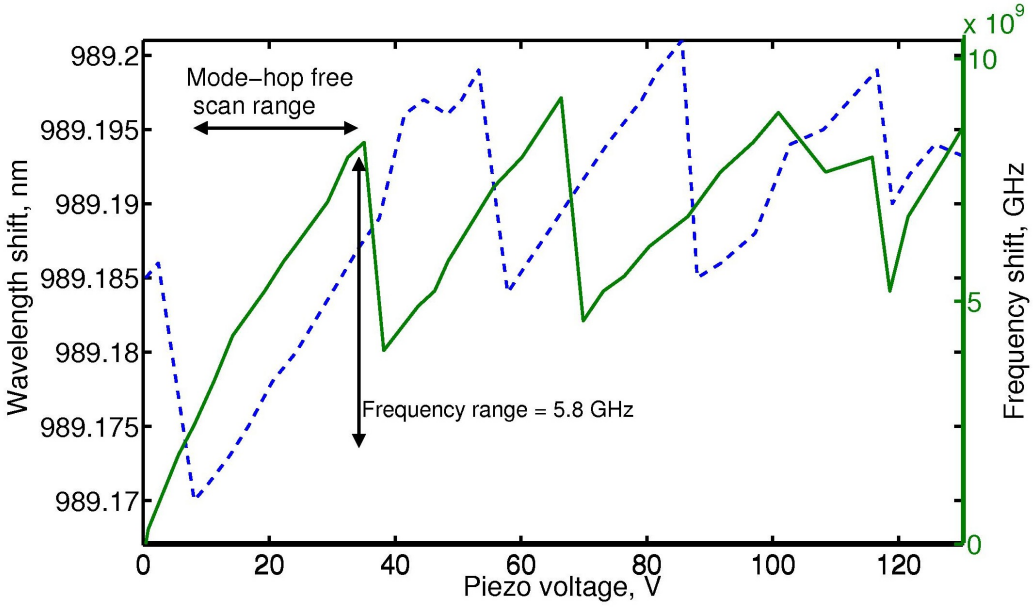

(b) ECDL wavelength as a function of PZT scanning of the grating angle.

Figure 5.3: Mode hopping with both (a) laser diode current tuning and (b) PZT scanning. The wavelength in (a) is 990 nm and the laser diode temperature is 23 °C. The solid green line in (b) represents increasing voltage across the piezo stack and the dashed blue line represents decreasing voltage.

Chapter 6

Conclusions

This project has investigated the emission characteristics of an Er^{3+} doped fluorozirconate glass and an Er^{3+}:Yb^{3+} co-doped phosphate glass microspheres resonators. A method for fabricating and characterising adiabatic fibre tapers as coupling devices into microsphere resonators was presented. The tapers used for this thesis normally excite more than one cavity mode, resulting in multimode lasing at 1.5 μm, however, single mode lasing is sometimes observed when the taper and microsphere are optimally aligned.

Our results on the erbium-doped fluorozirconate glass, ZBLALiP, build on earlier work by Mortier *et al.* [24] and show very efficient upconversions over a broad range. Thirteen discrete emissions ranging from 320 to 850 nm have been observed in the upconversion spectrum. The absorption and fluorescence properties are studied, and the processes responsible for the generation of the observed wavelengths are outlined. To the best of our knowledge, no other singly doped glass has been shown to generate such a range of emissions from the UV to the near-IR, including Er^{3+} doped ZBLAN microspheres [118].

Scorching or blackening of the microspheres during fabrication in the plasma chamber is a problem. In order to exploit ZBLALiP's very low absorption in the mid-IR, the fabrication process would need to be improved so as not to degrade the material quality. Mid-IR lasing has been observed at 2.7 μm from the $^4I_{11/2} \rightarrow ^4 I_{13/2}$ transition in bulk samples of ZBLALiP by Mortier [119]. Mid-IR lasing in a ZBLALiP microsphere would be a very exciting development since other glass hosts, such as silica, typically do not transmit at this wavelength. Unfortunately, we do not have a spectrum analyser for these wavelengths in our laboratory. A profound implication of the attenuation graph presented in Fig. 3.1, is the suggestion that if fluorozirconate glasses can become an affordable, practical, and ultra-low-loss alternative to silica optical fibres, there will be a race to develop lasers at 2.6 μm. An erbium doped ZBLALiP microsphere would serve as a laser source around this wavelength. Furthermore, it has been suggested [24] that optical fibre fabrication issues such as re-crystallisation defects may be partially remedied by using ZBLALiP rather than the more conventional glass, ZBLAN.

Fluorozirconate glasses such as ZBLALiP are ideal for upconversion lasing due to their lower phonon energy (600 cm^{-1} max.) compared with silica (1190 cm^{-1} max.), for example. Green upconversion lasing with a very low threshold of 30 μW absorbed power at 801 nm pumping was observed in Er^{3+} doped ZBLAN microspheres [118]. Green lasing was also observed in an Er^{3+} doped ZBLAN microsphere following three ESAs when pumped at 800 nm [120]. All these experiments were performed with the outdated techniques of free beam coupling and prism coupling using microspheres of unstated Q values. Upconversion lasing in ZBLALiP microspheres, when pumped at 800 nm, seems very probable given the high upconversion rates observed in the present

work. The reason for choosing 800 nm rather than 980 nm is that the metastable $^4I_{13/2}$ level can be readily depopulated via an ESA to the green level at $^4S_{3/2}$. A further ESA from this long-lived level could then populate the $^2P_{3/2}$ level, and the resulting violet and UV emissions would follow.

To the best of our knowledge, the work in this thesis presented the first systematic study of optical bistability in a glass microspherical laser. Dispersive optical bistability in an Er^{3+}:Yb^{3+} co-doped IOG-2 microspherical cavity has been studied. The thermal properties of IOG-2 glass play an important role in the microsphere performance. In particular, the high loss of pump power to the glass as heat, in conjunction with the low thermal conductivity, have a pronounced effect on the cavity resonance. As such, we have seen self-induced switching in the intensity at C-band lasing and visible fluorescence wavelengths, and chromatic/wavelength switching at green and C-band lasing wavelengths. The dispersive bistability model seems to correctly predict our results. It cannot, however, explain the spike observed in the lasing bistable plots while decreasing the pump power; thermal lensing was suggested as a contributing factor affecting the mode propagation path and, thus, causing variable light collection efficiency. Lifetime measurements of the excited states are needed to confirm or reject the influence of ETU. Switching speeds are expected to be limited by the energy level lifetimes in the Er^{3+} ions; however, measurements are needed to confirm this.

In comparison to other bistable glasses and crystals, IOG-2 microspheres have large contrasts between the two bistable states and require very low switching powers. In addition, their size and room temperature operation make them interesting for miniature devices. These results are of immediate importance for applications

requiring co-doped laser glasses and crystals, such as all-optical processing. A compact laser source would be ideal for microchip integration, especially if it can be mounted with a waveguide such as a stripline pedestal anti-resonant reflecting optical waveguide (SPARROW) [85]. A microdisk or microtoroid geometry would be even more appealing due to their smaller dimensions and tighter mode confinement. It is, perhaps, industrial applications that may benefit most from the unique properties of a bistable microsphere. Non-electrical solutions are often sought for noisy applications. An all-optical, miniature, high sensitivity temperature limit switch and/or a pressure limit switch, such as a co-doped microcavity, has particular advantages over other commercial systems. There is also the option of choosing from either intensity or wavelength switching, both of which occur simultaneously.

All in all, the two glasses investigated in this thesis work offer new and interesting avenues of research for a wide variety of applications. Our group will, no doubt, continue to study these glasses in the future.

Appendix A

Spectral Characterisation of Erbium-Doped Microspherical Lasers

Spectral characterisation of erbium doped microspherical lasers

Brian J. Shortt♦, Jonathan Ward, Danny O'Shea and Síle Nic Chormaic
Department of Applied Physics and Instrumentation, Cork Institute of Technology
and Tyndall National Institute, Prospect Row, Cork, Ireland.

ABSTRACT

We present continuing theoretical and experimental investigations into the characterisation of fibre taper coupled microspherical lasers. We investigate the spectral emissions of these micro resonators as a function of the wavelength and power of the pump radiation. We also consider various means of efficiently coupling radiation into and out of these devices. We are particularly interested in studying emissions about 1.55 μm with the aim of exploiting potential telecommunications applications of these devices. We study microspheres with diameters in the range 40-150 μm. Pump light about 980 nm or 1480 nm is coupled into the microsphere through evanescent wave coupling between microsphere and optical fibre. The resulting spatial and spectral distribution of radiation within the spheres is described by whispering gallery modes. Half and full-taper optical fibres are used to both couple the pump light into the sphere and to out couple the resulting infra red lasing. The physics of whispering gallery modes and the challenges of coupling to such modes is discussed. Experimental techniques and results will be presented and future directions indicated.

Keywords: Lasers, microspheres, erbium doped glass, whispering gallery modes, evanescent coupling, fibre taper

1. INTRODUCTION

The first demonstration of a spherically symmetric rare earth doped solid microcavity undergoing laser action was presented over forty years ago.[1] Samarium doped CaF_2 glass spheres with diameters of a few millimetres were pumped by xenon flashtube. Upon exceeding a threshold pump power the output power grew quickly indicating the presence of stimulated emission. Interest in the study and application of these microcavities as potential laser sources developed from this point. The first continuous wave laser oscillation in a solid state medium was demonstrated in Nd:YAG spheres with a diameter of 5 mm and lasing threshold of 100 mW.[2] Current lasing thresholds stand at the microwatt level, while, simultaneously, the size of the spheres has decreased dramatically. A more complete introduction to microcavity laser devices has been presented in an earlier paper and the interested reader is directed to it and the references contained therein.[3]

The capture and propagation of radiation in circular microlasers is based on multiple total internal reflections (TIR) of light within the resonant cavity structure. The resulting spatial and spectral electromagnetic field distributions have been termed whispering gallery modes (WGMs) or morphology dependent resonances (MDRs). WGMs in micro resonators have attracted much attention in recent years due to the intrinsic high *Q*-factors and the very low mode volumes of typically a few hundred μm^3 that can be achieved.[4] *Q*-factors as high as 10^{11} have been reported.[5] This coupling of low mode volume with high *Q*-factor can lead to sufficiently high light intensities within the sphere such that non linear effects come into play.[6] The development of such microresonators is of interest for both fundamental (e.g. cavity quantum electrodynamics[7,8]) and applied studies (e.g. the development of optical networks[5]). Recent work[9] has reported on the coupling between quantum dots and microspheres with the result being lasing at wavelengths between 1240 and 1780 nm at sub microwatt threshold. Applications have also been identified in chemical and biological sensing whereby the evanescent portion of the electromagnetic field interacting with target species on or near the microsphere surface gives rise to a shift in the resonant wavelength of a sphere mode.[10,11] This shift can be calibrated to yield the concentration of the target analyte. The high *Q*-factor of the passive microspheres used in these studies leads to a cavity enhancement effect equating to effective interaction path lengths of up to tens of metres.

♦ Tel: +353 21 490 4897, fax: +353 21 490 4880, email: brian.shortt@cit.ie

Photon Management II, edited by John T. Sheridan, Frank Wyrowski, Proc. of SPIE Vol. 6187,
618708, (2006) · 0277-786X/06/$15 · doi: 10.1117/12.662831

In this paper we will give an overview of the whispering gallery mode depiction of the electromagnetic field within a dielectric microsphere. Particular attention will be drawn to the description of the spatial distribution of the electromagnetic energy including the evanescent portion of the field. We will describe how we use a suitably sized silica fibre taper to efficiently couple light into and out of the microsphere via evanescent wave coupling and the potential of using angle polished fibres to achieve similar coupling results. The fabrication of the spheres used in this work will be briefly discussed. We are working with microspheres fabricated from two different erbium doped glasses. The first material is a novel heavy metal fluoride glass, ZBNA, optimised for its ability to act as a host for erbium. The second material is a commercial Schott glass IOG-2, a potassium-barium-alumino phosphate glass with doping levels of 2 % Er_2O_3 and 3 % Yb_2O_3 by weight. We have constructed a fibre taper production rig based on a scanning mirror and a CO_2 laser heat source. Practical considerations and techniques involved in the production of low loss adiabatic fibre tapers by this method will be discussed. Finally results from our investigations into microspherical lasers fabricated from the two doped glass materials will be presented and future avenues of investigation discussed.

2. THEORETICAL CONSIDERATIONS

In this paper we will provide some insight into electromagnetic resonances existing in a microsphere. Efficient coupling to a microsphere requires that the propagation modes of light in the coupling element match the WGMs within the sphere. The use of quantum tunnelling via an evanescent wave component of the light field is used for this purpose and we present how one can ensure that the coupling technique satisfies the mode-matching requirements when a half-taper fibre is used as the coupling component. Finally, we examine a second coupling technique based on angle-polished fibres.

2.1 Whispering gallery modes

In the geometrical-optic model, if a ray strikes the microsphere glass-air interface at an angle of incidence greater than the critical angle, TIR will occur. The ray is reflected and due to the symmetry of the cavity strikes the glass-air interface again at the same angle. In the case of large microspheres i.e. radius >> wavelength of trapped light ($a >> \lambda$), the light ray will be trapped by this mechanism and can propagate continuously around the inside wall giving rise to a standing wave, hence the concept of resonant modes. The integer number of these wavelengths around a single revolution can be denoted by the equatorial mode number, l.

Fig. 1. WGM in a microsphere. (a) Ray propagation around the sphere by TIR; (b) Spherical coordinate system.

The momentum p of a photon is $p = \hbar k = 2\pi\hbar/\lambda$ where $\hbar$ is Planck's constant divided by 2π and k is the wavenumber inside the sphere. The angular momentum, $\hbar l$, of the photon when it strikes the surface with near glancing incidence is $\hbar l = 2\pi r\hbar n/\lambda$ where n is the refractive index of the sphere. We see that the integer l is the angular momentum of the photon of unit $\hbar$ and is going into the page in Fig. 1 (a). An important variable describing the resonance condition is the size parameter, $x_l^{(n)} = 2\pi a/\lambda$.

A realistic mathematical description of the electromagnetic field patterns in a microsphere begins with the solution of the Helmholtz equation in spherical coordinates.[12] The solution is obtainable from the scalar wave equation

$$\nabla^2\psi(r) + n^2k^2\psi(r) = 0 \tag{1}$$

by assuming the polarization is constant. There are four solutions to Eqn. (1) corresponding to the transverse electric (TE) and transverse magnetic (TM) components of the sphere electric and magnetic fields. Spherical Bessel (Hankel) functions describe the radial field inside (outside) the sphere which are given by

$$\vec{E}^{TE}(r,\theta,\phi) = \begin{cases} j_l(nkr)\vec{X}_{lm}(\theta,\phi) & r \le a \\ j_l(nkr)h_l^{(1)}(kr)/h_l^{(1)}(ka)\vec{X}_{lm}(\theta,\phi) & r > a \end{cases}$$

$$\vec{B}^{TE}(r,\theta,\phi) = -\frac{1}{k}\nabla\times\vec{E}(r,\theta,\phi)$$

$$\vec{B}^{TM}(r,\theta,\phi) = \begin{cases} j_l(nkr)\vec{X}_{lm}(\theta,\phi) & r \le a \\ j_l(nkr)h_l^{(1)}(kr)/h_l^{(1)}(ka)\vec{X}_{lm}(\theta,\phi) & r > a \end{cases} \qquad (2)$$

$$\vec{E}^{TM}(r,\theta,\phi) = -\frac{1}{\varepsilon(\vec{r})k}\nabla\times\vec{B}(r,\theta,\phi)$$

where j_l ($h_l^{(1)}$) are spherical Bessel functions (Hankel functions of the first kind) of order l and X_{lm} and Y_{lm} are vector spherical harmonic functions. These latter two functions describe the sinusoidal nature of the field corresponding to reflections of the ray off the sphere surface.

Three mode numbers n, l, and m are used to characterise the radial, equatorial and polar components of the electromagnetic field. Mode number n (n = 1, 2, 3,…) gives the number of maxima in the radial electromagnetic field distribution. The fundamental (n = 1) TM radial mode is depicted in Fig. 2 (a). The second mode number, m ($m = -l, -l + 1,\ldots, 0,\ldots, l-1, l$), describes the number of maxima in the sinusoidal variation in field intensity in the equatorial or latitudinal direction. Finally the mode number, l, describes the field intensity distribution in the polar or longitudinal direction and can take values l = 0, 1, 2,… with the number of maxima present in the polar field distribution been given by $l - |m| + 1$.

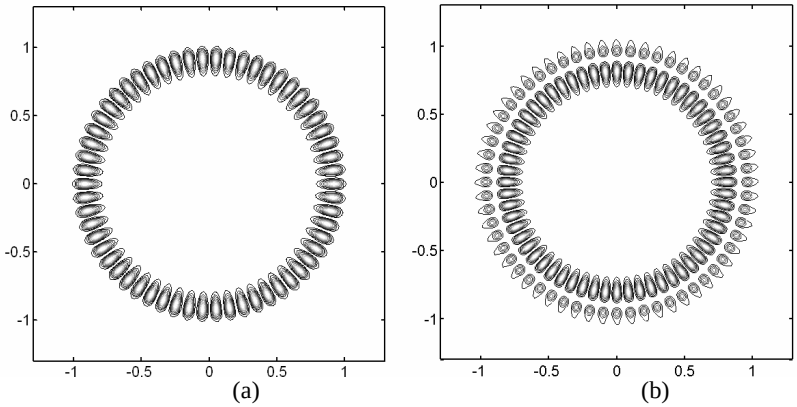

Fig. 2. Calculated intensity distribution of the TM mode in the equatorial plane (a) for n = 1 and l = 30 with x =24.623 (b) and for n = 2 and l = 30 with x = 27.978. The wavelength is 1.55 μm and the sphere radius is normalized to unity in both cases.

For a perfect sphere (zero ellipticity), modes with the same l but different m values have a $2l+1$ degeneracy and so the mode numbers n and l are sufficient to describe the WGM. In reality some ellipticity exists in the sphere which removes this degeneracy. For minimal mode volumes one wants n to be small and $m \approx l$ as seen in Fig. 3. The spheres used in the present studies have radii in the range 50-250 μm with <5 % ellipticity. Fig. 3 shows a cross-section of the field for different values of m and l. We can see that the mode volume is lowest for the fundamental mode and increases for more complicated mode structures. In the ray optics picture, the fundamental mode represents a ray with the smallest reflection angle, the lowest diffraction losses, the lowest mode volume and the highest Q-factor.

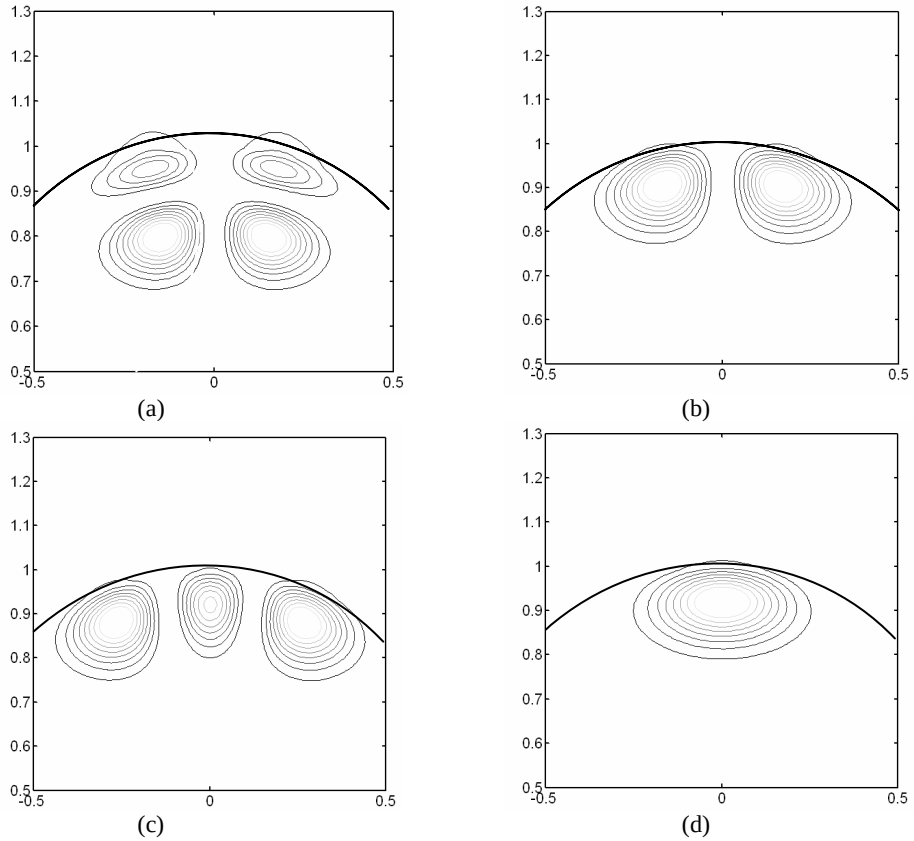

Fig. 3. Azimuthal intensity distribution for TM modes with (a) $n = 2$, l-$|m| = 1$, (b) $n = 1$, l-$|m| = 1$, (c) $n = 1$, $l - |m| = 2$, (d) $n = 1$, $l - |m| = 0$. The wavelength is 980 μm and the sphere radius is normalized to unity.

The fundamental mode in Fig. 3 (d) is located on the equatorial plane of the sphere. Although modes with $l - |m| > 0$ travel with greater inclinations with respect to the equator, they still have the same resonant wavelength as the fundamental mode since the curvature of the sphere precisely compensates. The path length for $l - |m| > 0$ modes in (a) to (d) are all equal i.e. they are degenerate. Therefore the equatorial mode number, m, is superfluous when describing the resonance wavelength

The quantum mechanical analogy of morphology dependent resonances[13] is shown in Fig. 4 (a). An effective radial potential, comprising of the well potential and centrifugal potential at the surface, ensures that the propagating photons remain confined to the well near the sphere surface. Classically, as long as the energy of the bound state photon is below the level of the potential barrier the photon cannot leak out of the potential well and into the forbidden regions. However, the wave function has a non-zero probability outside the potential well, thus giving rise to whispering gallery mode losses. The radial Schrödinger equation is of the form

$$-\frac{d^2\psi(r)}{dr^2}+\left[V(r)+\frac{l(l+1)}{r^2}-E\right]\psi(r)=0 \tag{3}$$

where $V(r)$ is the total effective potential, l is the equatorial mode number and E is the total energy (equal to k^2). The effective potential is a function of the radial position and is governed by the local refractive index and the wavelength. The effective potential in Fig. 4 (a) is given by

$$V_l(r)=\begin{cases}k^2(1-n^2)+l(l+1)/r^2 & r\le a\\ l(l+1)/r^2 & r>a\end{cases} \tag{4}$$

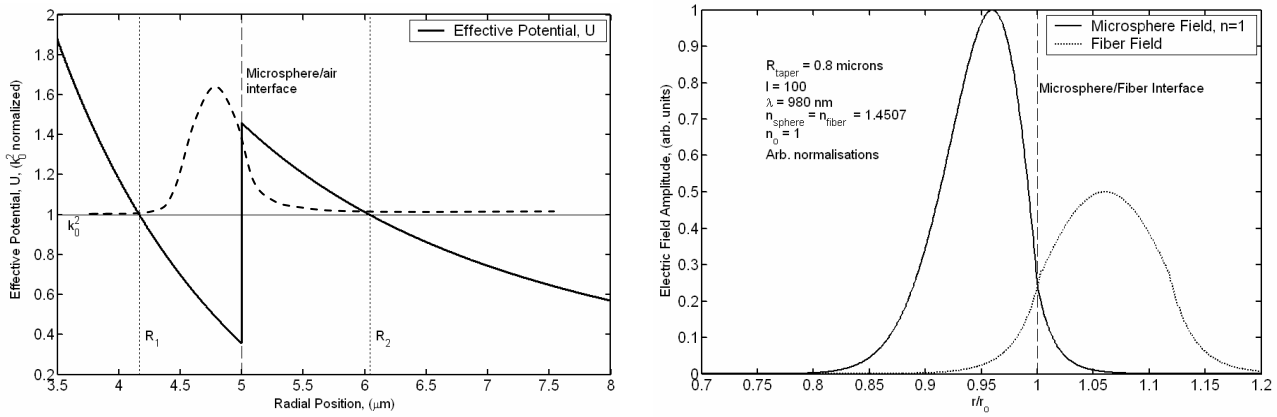

(a) (b)

Fig. 4. (a) Effective potential for a silica microsphere with $l = 24$. The wavefunction (dashed) is only representative. (b) Overlap of the microsphere TM mode and fibre taper evanescent fields (fibre diameter, $2a = 1.6\ \mu$m, $l = 100$).

Turning points are defined where the difference between the total energy and effective potential is zero. These are defined as

$$R_1 = (l + 1/2)/kn \tag{5}$$

$$R_2 = (l + 1/2)/k \tag{6}$$

Photons between R_1 and the sphere-air interface are the classically predicted bound photons, while those photons outside the sphere, between R_2 and the sphere-air interface, are evanescent.

The continuity of the tangential components of the electric and magnetic fields at the sphere surface (see Eqn. (2)) must satisfy a characteristic equation.[14] The position and width of the resonances are obtained by numerically solving this characteristic equation.

$$n^{-2b}\frac{\left[nkaj_l(nka)\right]'}{j_l(nka)} = \frac{\left[kah_l^{(1)}(ka)\right]'}{h_l^{(1)}(ka)} \tag{7}$$

where b is the polarization (equal to 1 for TM modes and 0 for TE modes). The prime denotes differentiation with respect to the argument. The solution yields discrete values of frequency at which resonances are possible. In practice, the locations of these resonances are found by scanning a tuneable diode laser over the free spectral range of the sphere.

The solution to Eqn. (7) requires a significant amount of computational time as the resonances have sharp Lorentzian line-shapes. Schiller[15] has used asymptotic formulas to yield an approximation for the resonance frequency in terms of the size parameter, $x_l^{(n)}$, up to order $\alpha = 8$

$$x_l^{(n)} = \frac{\nu}{m} - \frac{\zeta_n}{m}\left(\frac{\nu}{2}\right)^{1/3} + \sum_{\alpha=0}^{8}\frac{d_\alpha(m,\zeta_n)}{\nu^{\alpha/3}(m^2-1)^{(\alpha+1)/2}} \tag{8}$$

where $\nu = l + ½$, $m = n_s/n_a$, where n_s is the refractive index of the sphere and n_a is the refractive index of the surrounding medium, ζ_n is the nth zero of the Airy function. The coefficients of the expansion are given by the polarization dependant term $d_\alpha(m, \zeta_n)$. Identification of these resonances is achieved by measuring the separations of the resonance frequencies $x_l^{(n)} - x_{l-1}^{(n)}$. The widths of the resonances, $\Gamma_l^{(n)}$, are given at FWHM by Lam[16] as

$$\Gamma_l^{(n)} = 2\left[Nx^2 n_l(x)^2\right]^{-1} \tag{9}$$

where n_l is the spherical Neumann function, and

$$N = \begin{cases} n^2 - 1 & TE \\ (n^2-1)[\mu^2 + (\mu^2/n^2 - 1)] & TM \end{cases} \tag{10}$$

where $\mu = \nu/x$ with x evaluated at $x_l^{(n)}$.

2.2 Mode matching between a microsphere and fibre taper

In order to effectively couple light into a microsphere, the angular momentum and propagation constant of the pump beam must match that of the WGMs within the sphere such that there is phase matching at the point of closest contact. We achieve this by using a suitably sized silica fibre taper to couple light into and out of the microsphere via evanescent wave coupling.

The eigenvalue equations of the Helmholtz equation for the fibre are[17]

$$\left[\frac{J_n'(ha)}{haJ_n(ha)}+\frac{K_n'(qa)}{qaK_n(qa)}\right]\left[\frac{n_{core}^2 J_n'(ha)}{haJ_n(ha)}\right]=\left[\frac{n\beta}{k}\right]^2\left[(qa)^{-2}+(ha)^{-2}\right]^2 \tag{11}$$

for HE_{nm} and EH_{nm} modes where J_n (K_n) is a Bessel function (modified Hankel function of the second kind) of order n, β is the propagation constant, n_{core} is the index of the core, n_{clad} is the index of the cladding, $h^2=n^2_{core}k^2-\beta^2$ is the radial propagation constant in the core, $q^2=n^2_{clad}k^2-\beta^2$ is the radial propagation constant in the cladding, and the prime denotes differentiation with respect to the argument. We use the Sellmeier dispersion formula to determine refractive indices at room temperature. The transcendental equation in Eqn. (11) is solved numerically for the fundamental HE_{11} fibre mode for specific taper diameters. The propagation constant of the sphere is $\beta=kl/x_{nlm}$ where x_{nlm} is the size parameter determined from Eqn. (6). The taper and sphere are phase matched when the difference between propagation constants is zero.

If efficient coupling is to be achieved using tapers or half-tapers, it is imperative that the taper be only a few microns in diameter. Taper coupling provides a simple and potentially compact method of exciting the sphere. We fabricate low-loss 3 to 4 μm diameter tapers using a 25 W CO_2 Synrad laser. Fibre taper coupling efficiencies of more than 99 % have been reported[18] which depends on the refractive index of the sphere, sphere dimensions, taper fibre dimensions and the relative position of the components.

2.3 End-polished fibres

We have recently begun investigating how end-polished fibres can be used to excite resonant modes in microspheres. This device is a hybrid of the more traditional prism and taper couplers.[19] The fabrication consists of polishing the end of a single mode fibre to an angle sufficient to obtain efficient coupling into the sphere. By placing the sphere at the polished surface TIR conditions will be met, just as in the case of prism coupling. Therefore the phase matching condition is controlled by the polish angle, $\theta=sin^{-1}(n_{sphere}/n_{fibre})$. The effective index of the resonant mode in the sphere is found from $n_{sphere}=ln_s/x_l^{(n)}$ where n_s is the refractive index of the sphere material, for example silica, as determined from the Sellmeier dispersion formula. The effective index of the fibre is assumed to be β/k where β is evaluated from Eqn. (11) for the fundamental HE_{11} mode. Fig. 5 shows the required polish angle as a function of sphere radius for n = 1 and n = 2 modes at wavelengths of 980 nm and 1480 nm.

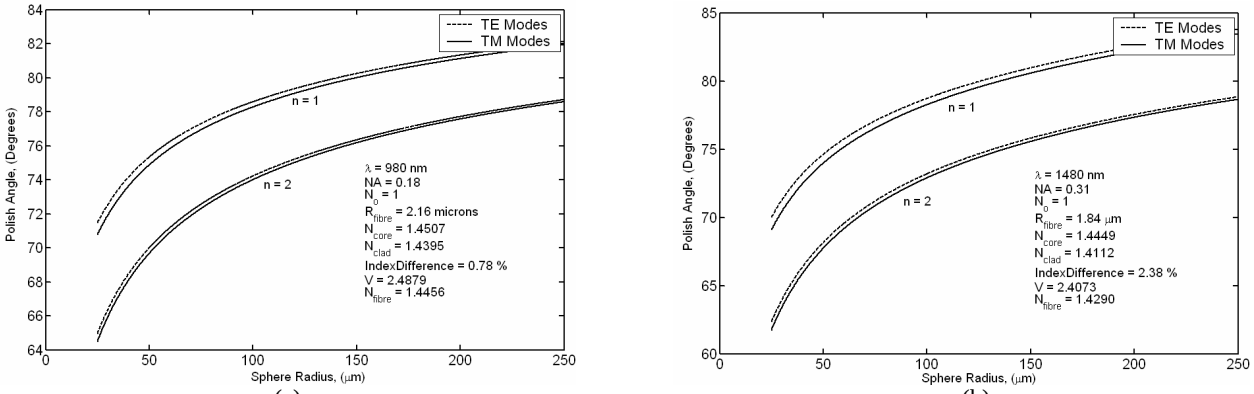

Fig. 5. Calculated polish angle for wavelengths of (a) 980 nm, and (b) 1480 nm in silica.

Among the advantages of end-polished fibres are their robustness and small package size. One disadvantage of using fibre tapers is the competing requirement of small diameter to maximise the evanescent field against a suitably large

diameter for good phase matching. For example, a silica fibre diameter of 6 μm is required to phase match an Er:ZBLAN sphere of diameter 100 μm.[20] The fraction of the field in the core of the fibre is almost 100 % for this diameter taper. Further advantages of end-polished fibres are in ease of alignment of the sphere and fibre as the interaction region is larger and good coupling efficiencies of up to 60 %.[19]

3. EXPERIMENT

3.1 Experimental setup

We are working towards the characterisation of microspherical lasers fabricated from two different erbium doped glasses. The first material is a novel heavy metal fluoride glass, ZBNA[21] with 0.1% Er^{3+} doping. The second material is a commercial Schott glass IOG-2, a potassium-barium-alumino phosphate glass[22] with doping levels of 2 % Er_2O_3 and 3 % Yb_2O_3 by weight. Microspheres with diameters between 10 μm and 200 μm are formed using a 2 kW microwave plasma torch.[23] The system can be optimised for different glass materials by changing the plasma gas feed ratio and discharge power.

The experimental arrangement is presented schematically in Fig. 6. Excitation of the erbium active medium within the microspheres is achieved using tuneable diode lasers operating at 980 and 1480 nm. The pump light is sent through an optical isolator to prevent back reflections into the laser. It then passes through a manual variable attenuator, which enables us to study the lasing characteristics of the microsphere as a function of the pump beam power.

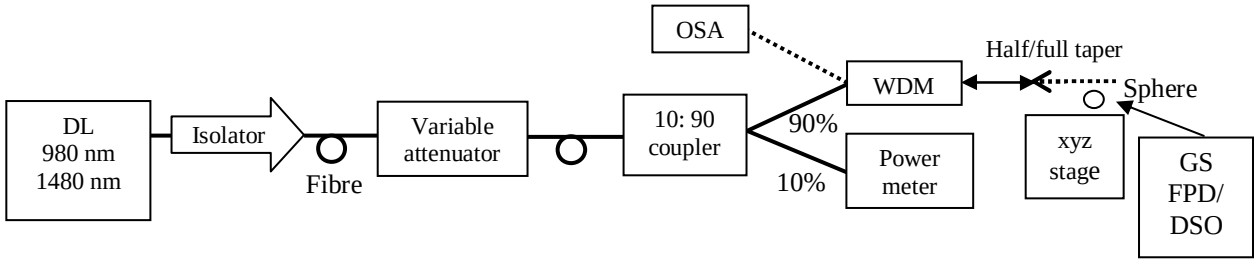

Fig. 6. Experimental set-up. Full line indicates 980/1480 nm. Dashed line indicates 1.55 μm. DL: Diode laser, WDM: Wavelength division multiplexer, OSA: Optical spectrum analyser, GS: Grating spectrometer, FPD: Fast photo diode, DSO: Digital storage oscilloscope.

An IDIL 10:90 coupler is used to split the light into a 10% channel for monitoring the pump power and a 90% channel which is used as the source of WGM excitation in the microsphere. This is coupled into the fibre taper via a wavelength division multiplexer (WDM). Efficient coupling between sphere and taper is achieved by aligning the microsphere equator precisely with the taper via the use of piezo controlled precision translation stages. Cooperative upconversion in the microsphere is evident from visible green light strong enough to be observed with the naked eye. A Zeiss microscope connected to a monitor via a CCD camera is used for general imaging in the experiment and also for monitoring the alignment position of the taper and microsphere. Experiments as a function of sphere-taper gap are underway but the results presented in this paper are for the case of sphere and taper in physical contact.

The 1.55 μm radiation within the microsphere is evanescently coupled out into the exciting fibre or a separate second taper aligned at the sphere equator but on the opposite side of the sphere. The light passes through the WDM, which separates out the reflected pump component at 980/1480 nm from the lasing component at 1.55 μm. The 1.55 μm laser signal is sent to an Anritsu optical spectrum analyser (OSA) for analysis of its spectral properties. A grating spectrometer (Horiba Jobin Yvon Triax 190, resolution 0.3 nm or Ocean Optics USB 4000, resolution 0.5 nm) with either free space or fibre coupling is used to measure the microsphere visible emission spectrum.

3.2 Low cost fibre taper production

The three most widely exploited means of achieving micron-sized tapers are by flame,[18,24] CO_2 laser,[25] and to a lesser extent by fusion splicer.[20] CO_2 lasers present a largely stable and easily controllable method of heating a fibre. Air

currents or other deleterious environmental effects bear no consequence on the power output or the ability to scan the beam across the fibre with a galvanometer mirror. The benefit of precise control of the hot-zone on a fibre yields the option of producing any desired taper profile.[26] The physical process of heating a fibre with a laser beam involves the fibre absorbing the radiation and heating from the inside, while for a flame, the process involves heating the surface of the fibre. This ultimately places a stricter limit on the minimum taper diameter attainable for a given CO_2 laser power as compared with a flame.[27] Previous attempts of producing tapers using the CO_2 technique have achieved a diameter of 4.6 μm with a CO_2 laser power of 13 W and FWHM spot size of 820 μm using a galvanometer-scanning mirror.[25]

3.2.1 Method

We have developed a low cost method for fabricating fibre tapers which offers good reproducibility. This method relies on a geared stepper motor rather than a galvanometer to scan the laser beam across the fibre taper with a mirror. A future publication[28] will describe in detail the procedure and requirements for pulling adiabatic tapers[17,26] with losses typically in the range of 0.1 to 0.3 dB. A 12.5 cm focal length Zn-Se lens focuses the laser beam onto the fibre with a spot size ($1/e^2$) of approximately 500 μm that is 5.5 cm in front of the scanning mirror. The stepper motor has a resolution of 1.8×10^{-3} degrees/step, which corresponds to a length of ~1.7 μm/step on the fibre. The discrete nature of the step size is smeared-out by the size of the beam at the focus. Two motorised translation stages pull the fibre with a resolution of 1 μm. As the taper is being drawn, the transmission loss through the fibre is monitored with a photodiode and oscilloscope. In tandem with the taper pull, the laser power is ramped in a manner which follows a fourth-order polynomial optimised to produce 3 and 4 μm diameter tapers.

3.2.2 Results

Fig. 7 shows the power transmission through a length of fibre as a taper is drawn. In Fig. 7(a) there are oscillations during the middle section of the pull. These oscillations are thought to be mode coupling between the core and cladding modes. Fig. 7(b) shows that is it possible to eliminate this modal coupling with a sight decrease in laser power during the pull. There is no significant difference in the final transmission loss with values of 0.15 dB and 0.21 dB for Fig. 7(a) and (b) respectively. Examination of these tapers reveals that the taper angle is well below that required to meet the adiabatic criteria as depicted by the delineation curve.[17] A typical measured taper profile is shown in Fig 7(c) with final diameter of 3 μm.

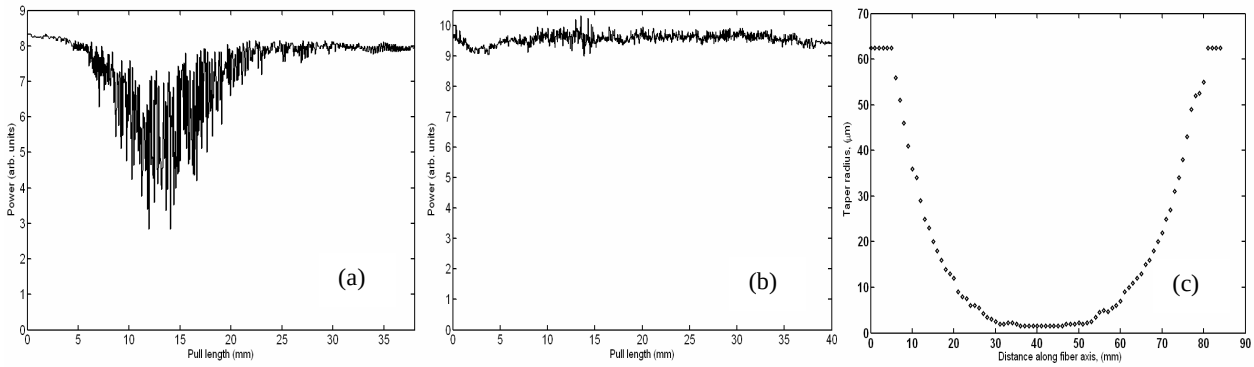

Fig. 7. Transmission loss measurements: (a) with and (b) without multi-mode coupling during the middle portion of the pull. (c) typical taper profile, 3μm diameter, pull length 40mm, scan length 7mm and initial taper diameter 125 μm.

3.3 ZBNA microsphere results

This section presents results obtained through the pumping of a 0.1% erbium doped ZBNA microsphere of diameter 60 μm. Pump light about 980 nm was coupled in to the sphere via a half tapered optical fibre of diameter ~ 2 μm at the point of contact. The sphere and taper were in physical contact. The same taper was used to probe for 1.55 μm radiation by evanescent outcoupling, through a WDM and into an optical spectrum analyser. Despite the study of several different sphere-taper combinations we failed to observe any infra-red emissions from this heavy metal fluoride glass sample.

During all experiments the microsphere was observed to fluoresce in the green with sufficient intensity as to be visible to the naked eye. This is the well known two-photon process of cooperative upconversion[4,29] Absorption of a laser photon at 980 nm pumps the erbium atom from the ground state $^4I_{15/2}$ to the $^4I_{11/2}$ excited state (lifetime < 1 μs). From this excited state the atom can either a) undergo non-radiative relaxation to the metastable $^4I_{13/2}$ state (lifetime ~10 ms) or b) absorb a second pump laser photon to enter the $^4F_{7/2}$ excited state – excited state absorption. In the case of a) the atom can return to the ground state after ~10 ms via the spontaneous emission of an infra-red photon at 1.55 μm. Alternatively the atom can relax to the ground state via stimulated emission and this forms the basis for 1.55 μm lasing in the microsphere. The multiphoton process described in b) is a source of possible quenching of the lasing at 1.55 μm. If the 980 nm pump intensity is too high the two photon absorption rate will lead to efficient population of the $^4F_{7/2}$ state. This state can relax to either the $^2H_{11/2}$ or $^4S_{3/2}$ states and these states further decay to the ground state with photon emission at 520 and 540 nm respectively.

Evidence of the efficient population of these two states is provided in Fig. 8. Fig. 8(a) presents wavelength scans of the microsphere fluorescence from 475 to 625 nm as a function of pump power launched in to the taper. As a half taper was used, no measure of the coupling efficiency between taper and sphere was possible. The peak at 520 nm is attributed to erbium relaxations to the ground state from the $^2H_{11/2}$ excited state and the peak at 540 nm corresponds to the $^4S_{3/2}$ state. Confirmation of the multiphoton nature of the cooperative upconversion process in found in Fig. 8(b) where the integrated green intensity for the $^2H_{11/2}$ state as a function of launched pump power is presented. The linear fit has slope of two as expected from the power law dependence of n-photon processes.

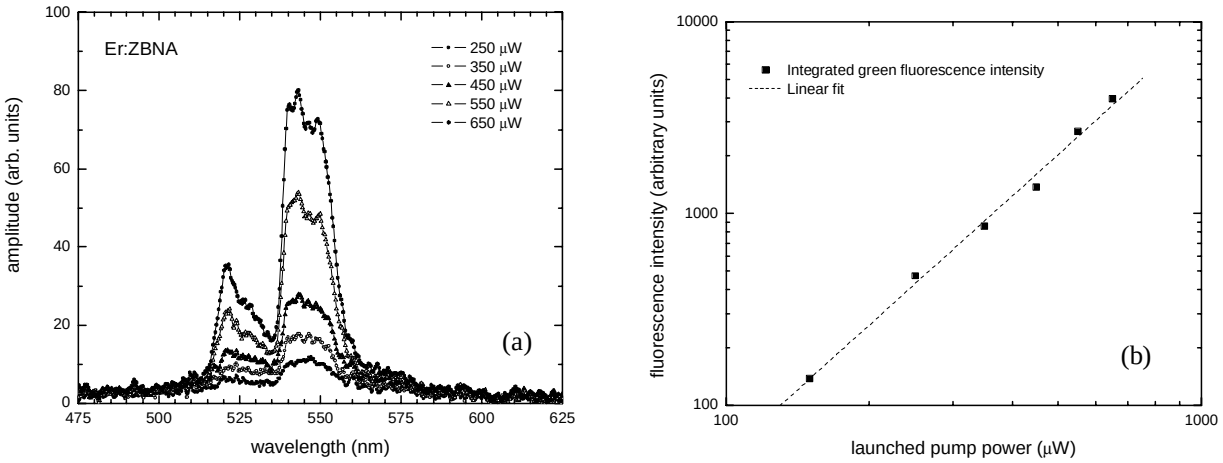

Fig. 8. (a) Upconversion green fluorescence spectrum as a function of power launched into half-taper fibre. (b) Integrated green fluorescence intensity as a function of launched pump power.

3.4 IOG-2 microsphere results

A second commercial phosphate glass (Schott IOG-2) with doping levels of 2 % Er_2O_3 and 3 % Yb_2O_3 by weight was also studied. A previous report[30] has shown this material to be suitable for sustaining continuous-wave oscillation in a microsphere laser. Again half-taper coupling was employed to couple pump light about 980 nm into a 130 μm diameter IOG-2 microsphere. Fig. 9 shows a laser emission spectrum from the microsphere as detected by the exciting taper.

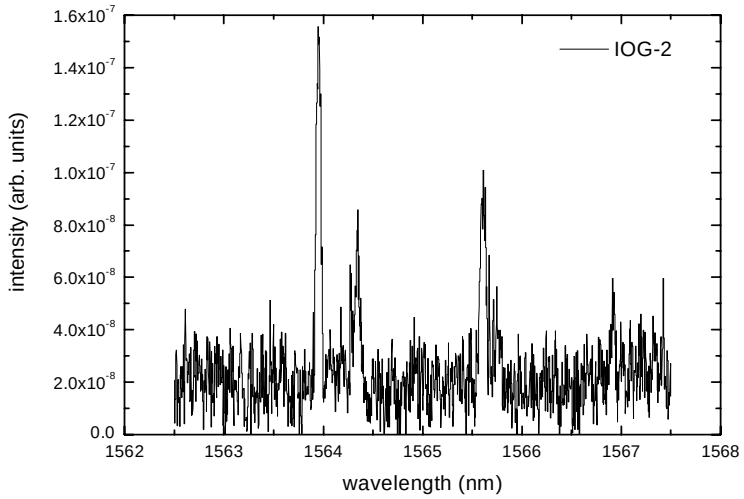

Fig. 9. IOG-2 spectrum showing infra-red laser emission about 1.56 μm.

Three distinctive lasing modes can be seen in Fig. 9. Similar multimode lasing has been reported previously.[20] Work is continuing to determine the lasing threshold power for a microspherical laser fabricated from IOG-2 glass. These measurements require adiabatic full tapers and a single mode narrow linewidth pump source which are currently been integrated in to our experimental setup.

4. CONCLUSIONS

Some subtleties of evanescent wave coupling between optical fibre components and microcavities have been presented. A low cost CO_2 laser based fibre taper production method which we believe will be of interest to other researchers has been described. We have observed infrared radiation in IOG-2 phosphate glass microspheres pumped at 980 nm. The competition between cooperative upconversion leading to green emissions and infrared generation in a ZBNA microsphere has been discussed. Future plans include the study of the interaction of a microspherical laser array and the interaction between the evanescent field of a microsphere with a cloud of cold atoms. In studying a laser array, we intend to study coupled oscillators including synchronisation and coherence[31] and enforced chaotic behaviour.[32]

ACKNOWLEDGEMENTS

We wish to acknowledge Patrice Féron for the supply of bulk glass and the subsequent fabrication of microspheres. This work is supported by Science Foundation Ireland project number 02/IN1/I28. DOS acknowledges support from IRCSET through the Embark Initiative.

REFRENCES

1. C. G. B. Garrett, W. Kaiser and W. L. Bond, “Stimulated emission into optical whispering modes of spheres”, Phys. Rev. **124**, 1807-1809, 1961.
2. T. Baer, “Continuous-wave laser oscillation in a Nd:YAG sphere”, Opt. Lett. **12**, 392-394, 1987.
3. B. Shortt, R. Carey and S. Nic Chormaic, “Characterisation of Er:ZBNA microsphere lasers”, Proc. SPIE **5827**, 47-57, Dublin, 2005.
4. W. von Klitzing, E. Jahier, R. Long, F. Lissillour, V. Lefèvre-Seguin, J. Hare, J-M. Raimond and S. Haroche, “Very low threshold green lasing in microspheres by up-conversion of IR photons”, J. Opt. B: Quantum Semiclass. Opt. **2**, 204-206, 2000.
5. T. Bilici, S. Isci, A. Kurt and A. Serpengüzel, “Microsphere based channel dropping filter with an integrated photodetector”, IEEE Photon. Technol. Lett., **16**, 476-478, 2004.

6. T. J. Kippenberg, S. M. Spillane, B. Min and K. J. Vahala, “Theoretical and experimental study of stimulated and cascaded Raman scattering in ultra-high *Q* optical microcavities”, IEEE J. of Selected Topics in Quant. Electron. **10**, 1219-1228, 2004.
7. J. Campillo, J. D. Eversole and H-B Lin, “Cavity quantum electrodynamics enhancement of stimulated emission in microdroplets”, Phys. Rev. Lett. **67**, 437-440, 1991.
8. F. Treussart, J. Hare, L. Collot, V. Lefèvre, D. S. Weiss, V. Sandoghdar, J. M. Raimond and S. Haroche, “Quantized atom-field force at the surface of a microsphere”, Opt. Lett. **19**, 1651-1653, 1994.
9. S. I. Shopova, G. Farca, A. T. Rosenberger, W. M. S. Wickramanayake and N. A. Kotov, “Microsphere whispering-gallery-mode laser using HgTe quantum dots”, Applied Physics Letters **85**, 6101-6103, 2004.
10. I. White, N. Hanumegowda and X. Fan, “Subfemtomole detection of small molecules with microsphere sensors”, Optics Letters **30**, 3189-3191, 2005.
11. F. Vollmer, D. Braun, A. Libchaber, M. Khoshsima, I. Teraoka and S. Arnold, “Protein Detection by Optical shift of a Resonant Microcavity”, Applied Physics Letters **80**, 4057-4059, 2002.
12. T. Mashide, “Study of spherical microlasers levitated in an ion trap”, Ph.D. Thesis, Kochi University of Technology, 2002.
13. B.R. Johnson, “Theory of morphology-dependent resonances: shape resonances and width formulas”, J. Opt. Soc. Am. A **10**, 343-352, 1993.
14. S.M. Spillane, “Fibre-coupled ultra-high-Q microresonators for nonlinear and quantum optics”, Ph.D. Thesis, California Institute of Technology, 2004.
15. S. Schiller, "Asymptotic expansion of morphological resonance frequencies in Mie scattering", Appl. Opt. **32**, 2181-2185, 1993.
16. C.C. Lam, P.T. Leung and K. Young, “Explicit asymptotic formulas for the positions, widths, and strengths of resonances in Mie scattering”, J. Opt. Soc. Am. B **9**, 1585-1592, 1992.
17. A.W. Snyder and J.D. Love, *Optical Waveguide Theory*, Kluwer Academic Publishers, 2000.
18. S.M. Spillane, T.J. Kippenberg, O.J. Painter and K.J. Vahala, “Ideality in a fibre-faper-coupled microresonator system for application to cavity quantum electrodynamics”, Phys. Lett. Rev**. 91**, 043902, 2003.
19. V. S. Ilchenko, X. S. Yao and L. Maleki, “Pigtailing the high-*Q* microsphere cavity: a simple fibre coupler for optical whispering gallery modes”, Opt. Lett. 24, 723-725, 1999.
20. F. Lissillour, D. Messager, G. Stéphan and P. Féron, “Whispering-gallery-mode laser at 1.56 µm excited by a fibre taper”, Opt. Lett. **26**, 1051-1053, 2001.
21. M. Mortier, M. Génotelle, G. Patriarche, "Rare earth doped transparent glass-ceramics", presented at Journée Nanoparticule, Paris, 2000.
22. G.C. Righini, C. Arnaud, S. Berneschi, M. Bettinelli, M. Brenci, A. Chiasera, P. Feron, M. Ferrari, M. Montagna, G. Nunzi Conti, S. Pelli, H. Portales, C. Siligardi, A. Speghini, L. Zampedri, “Integrated optical amplifiers and microspherical lasers based on erbium-doped oxide glasses”, Optical Materials **27**, 1711-1717, 2005.
23. P. Féron, "Whispering gallery modes as laser sources- a short review", in *Quaderni di optica e fotonica, special issue: Photonics & Optoelectronics*, Winter School, Trento, 2001.
24. L Tong, R.R. Gattass, J.B. Ashcom, S. He, J. Lou, M. Shen, I. Maxwell, and E. Mazur, “Subwavelength silica wires for lowloss optical wave guiding”, Nature **426**, 816, 2003.
25. T.E. Dimmick, G. Kakarantzas, T.A. Birks, and P.St.J. Russel, “Carbon dioxide laser fabrication of fused-fibre couplers and tapers”, Appl. Opt. **38**, 6845, 1999.
26. T.A. Birks and Y.W. Li, “The Shape of Fibre Tapers”, J. Lightwave Technol. **10**, 432, 1992.
27. A. Grellier, N.K. Zayer, and C.N. Pannell, “Heat transfer modelling in CO laser processing of optical fibres”, Opt. Comm. **324**, 152, 1998.
28. J. Ward, D. O’Shea, B. J. Shortt and S. Nic Chormaic, “CO_2 laser based fabrication of tapered fibre devices”, (*in preparation for submission to Rev. Sci. Inst.*).
29. P. A. Krugh, M. G. Sceats, G. R. Atkins, S. C. Guy and S. B. Poole, “Intermediate excited-state absorption in erbium doped fibre strongly pumped at 980 mn”, Opt. Lett. **24**, 1976-1978, 1991.
30. C. Arnaud, M. Boustimi, M. Brenci, P. Féron, M. Ferrari, G. Nunzi Conti, S. Pelli amd G. Righini, “Microsphere laser in Er^{3+} doped oxide glasses ”, Proc. SPIE **5622**, 315-320, Venezuela, 2004.
31. J. R. Terry, K. S. Thornburg, D. de Shazer, G. D. van Wiggeren, S. Zhu, P. Ashwin and R. Roy, “Synchronization of chaos in three lasers”, Phys. Rev. E **59**, 4036-4043, 1999.
32. K. S. Thornburg, M. Moller, R. Roy, T. W. Carr, R.-D. Li and T. Erneux, “Chaos and coherence in coupled lasers”, Phys. Rev. E **55**, 3865-3869, 1997.

Appendix B

A Heat-and-Pull Rig for Fiber Taper Fabrication

Heat-and-pull rig for fiber taper fabrication

Jonathan M. Ward, Danny G. O'Shea, Brian J. Shortt, Michael J. Morrissey, Kieran Deasy, and Síle G. Nic Chormaic
Department of Applied Physics and Instrumentation, Cork Institute of Technology, Bishopstown, Cork, Ireland and Tyndall National Institute, Prospect Row, Cork, Ireland

(Received 6 April 2006; accepted 2 July 2006; published online 18 August 2006)

We describe a reproducible method of fabricating adiabatic tapers with 3–4 μm diameter. The method is based on a heat-and-pull rig, whereby a CO_2 laser is continuously scanned across a length of fiber that is being pulled synchronously. Our system relies on a CO_2 mirror mounted on a geared stepper motor in order to scan the laser beam across the taper region. We show that this system offers a reliable alternative to more traditional rigs incorporating galvanometer scanners. We have routinely obtained transmission losses between 0.1 and 0.3 dB indicating the satisfactory production of adiabatic tapers. The operation of the rig is described in detail and an analysis on the produced tapers is provided. The flexibility of the rig is demonstrated by fabricating prolate dielectric microresonators using a microtapering technique. Such a rig is of interest to a range of fields that require tapered fiber fabrication such as microcavity-taper coupling, atom guiding along a tapered fiber, optical fiber sensing, and the fabrication of fused biconical tapered couplers. © *2006 American Institute of Physics.* [DOI: 10.1063/1.2239033]

I. INTRODUCTION

Techniques for evanescent coupling of light into microspherical cavities include prism couplers,[1] optical fiber half-block couplers,[2] end-polished fibers,[3] and fiber tapers.[4] Fiber tapers have proven to be the most attractive device for achieving near lossless coupling of light into microspherical cavities and exciting the fundamental resonant mode.[4,5] The overlap of the taper and microsphere evanescent fields defines the strength of this coupling.[6] The attainment of taper diameters typically in the range of 1–4 μm is critical to maximize this coupling. For a 2 μm diameter taper at a wavelength of 1550 nm, the fraction of power in the core is nearly 96%.[7] Recent discussions on the form of the evanescent field have shown the spatial extent of the radial component of the field to greatly increase for diameters less than 3 μm.[7,8] It has also been reported that efficient coupling of light into submillimeter sized silica microspheres is possible for taper diameters up to 4.5 μm.[9]

The four most widely exploited means of achieving micron-sized tapers are by flame,[5,10,11] CO_2 laser heating,[12] microfurnace,[13,14] and, to a lesser extent, fusion splicer.[4] While subwavelength diameters have been shown to be achievable with the flame method, it presents significant technical challenges.[11] Firstly, the gas flow rate must be precisely regulated in order to maintain a suitable temperature. The purity of the gas supply becomes increasingly important for smaller taper diameters due to contamination concerns. Air currents in the vicinity of the flame also pose a problem, thereby limiting the option of scanning the flame across a length of fiber and causing areas of uneven heating. Despite being able to produce submicron tapers with the microfurnace method, the fibers cannot be controllably structured to produce different taper profiles.

As an alternative, CO_2 lasers present a largely stable and easily controllable method of heating a fiber. Air currents or other deleterious environmental effects bear no consequence on the power output or the ability to scan the beam across the fiber with a mirror scanner. It is possible to precisely control the length of fiber to be heated (i.e., the hot zone), thereby yielding any desired taper profile.[15] The physical process of heating a fiber with a laser beam involves the fiber absorbing radiation and heating from the inside, whereas for a flame the process involves heating the surface of the fiber. There is an inverse square relationship between radius and heating for a CO_2 laser heat source, while for a flame heat source there is simply an inverse relationship between heating and radius. This ultimately places a stricter limit on the minimum taper diameter attainable for a given CO_2 laser power as compared with a flame heat source.[16] Previous reported attempts of producing tapers using the CO_2 laser technique have achieved a diameter of 4.6 μm with a CO_2 laser power of 13 W and full width at half maximum (FWHM) spot size of 820 μm using a galvanometer mirror scanner.[12] In this article we describe a reliable method of fabricating low loss 3–4 μm diameter tapers as well as the possibility of fabricating bottle resonators using a 25 W CO_2 laser.

In recent years, interest in the use of microspherical resonators in cavity QED experiments has increased.[17] The use of such microcavities in these experiments requires the possibility of tuning the resonance frequency of the microcavity to an atomic line. In principle, there are two main methods of achieving this: strain tuning and temperature tuning. Strain tuning can be used to sweep the resonant frequency through the cavity free spectral range (FSR), whereas temperature tuning is limited to a fraction of the FSR.[18] Temperature tuning is unsuitable as a stand-alone method and the fabrication of microspheres suitable for the strain tuning apparatus is difficult. A new type of prolate microcavity that

 © 2006 American Institute of Physics

Downloaded 13 Nov 2007 to 134.93.129.164. Redistribution subject to AIP license or copyright, see http://rsi.aip.org/rsi/copyright.jsp

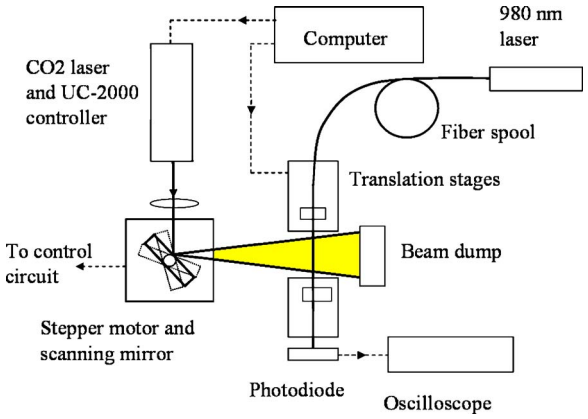

FIG. 1. Schematic of the taper fabrication rig. The dashed lines indicate control lines or data transfer.

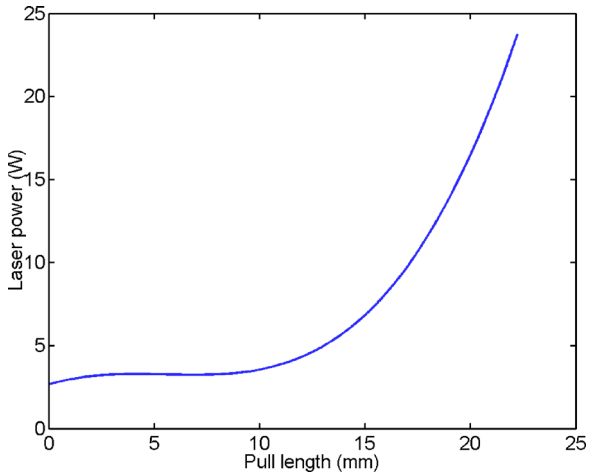

FIG. 2. Power curve for the CO_2 laser for a pull length of 22 mm.

offers potentially greater flexibility in tuning the microcavity resonance frequency has recently been described theoretically in the literature.[19,20] Such cavities are termed *bottle resonators*. Strain tuning of these devices may tune the frequency over several FSR, while temperature tuning over a single FSR may only require a few tens of Kelvin. Another appealing feature compared with typical spherical microcavities is the stronger evanescent field at the bottle resonator surface due to the smaller resonator dimensions.

Our fabrication method relies on the use of a geared stepper motor to scan the laser beam rather than the more traditional galvanometer. Implementation of our rig is trivial, requiring only interconnection of the stepper motor with the controller circuit. In contrast, galvanometer scanners require proportional-derivative (PD) or proportional-integral-derivative (PID) control, which can be tedious to tune correctly. From a mechanical perspective, the stepper motor has a more robust design and better torque which negates any effects induced by the inertia of the mirror attached to the shaft of the motor and the overall scanning angle achievable is larger than that for a galvanometer scanner (typically limited to ±40°). Additionally, the stepper motor represents a significant cost saving since the cost of a scanning galvanometer system is typically in excess of US$1990,[21] while the cost of a Radionics hybrid stepper motor, gear box, and controller circuit is approximately US$210.[22] By choosing the stepper motor scanner rather than a galvanometer scanner we saved 15% on the total laser rig cost.

The technique described is not only of interest for applications involving microresonator coupling; areas requiring the fabrication of fused biconical tapered couplers will also find this inexpensive apparatus of use. This article describes the procedure and requirements for pulling adiabatic fiber tapers[15,23] with typical losses in the range of 0.1–0.3 dB at 980 nm. We also report on successful attempts at fabricating bottle resonators to suitable dimensions using a microtapering technique.

II. EXPERIMENT

A schematic of the laser scanning rig is shown in Fig. 1. Custom designed software automates the instrument control and data acquisition through serial and universal serial bus (USB) interfaces, thereby ensuring ease of parameter adjustment and reproducibility. A 12.5 cm focal length ZnSe lens focuses the laser beam onto the fiber with a FWHM spot size of approximately 500 μm, 5.5 cm in front of the scanning mirror. The stepper motor used in conjunction with a 500:1 gear box in half-step mode has a resolution of 1.8×10^{-3} deg/half-step, which corresponds to a hot-spot translation of around 1.7 μm/ half-step on the fiber. The *hot spot* refers to the point on the fiber which is being heated by the laser beam at any instant. A 1 in. gold mirror and holder are vertically mounted on the shaft of the gear box. The CO_2 laser beam is incident on the center of the mirror at an angle of 45° and is directed onto the fiber. A Thurlby Thander TG250 function generator connected to the stepper motor controller circuit cyclically scans the mirror through a sweep angle of approximately 10°, thereby scanning the laser beam across the fiber. Alternatively, we can use customized limit switches to control the sweep angle of the mirror. Another function generator connected to the stepper motor controller circuit provides the clocking pulses, which dictate the speed at which the mirror scans the laser beam. The discrete nature of the stepper motor step size is smeared out by the size of the beam at the focus. Two motorized translation stages (Standa Ltd., Lithuania) pull the ends of the fiber taper (SM980 single mode fiber from Fibercore) with a resolution of 1 μm. As the taper is being drawn, the transmission loss of a 980 nm diode laser through the fiber is monitored with a Thorlabs Si photodiode (DET series) connected to a digital storage oscilloscope.

The computer provides an analog voltage signal to the UC-2000 laser controller based on the power curve shown in Fig. 2. Although the power curve is an oversimplification,[16] we find that it serves the application quite well. To determine the initial settings for our software, we manually increased the power of the laser while observing the incandescent light produced at the hot spot. The laser power was recorded as a function of pull length. A fourth-order polynomial fit to these data provides the laser power curve. An exponential fit was also attempted but the slope of the curve increased too rapidly towards the end of the taper pull causing premature breaking of the fiber and limiting the minimum taper diam-

Downloaded 13 Nov 2007 to 134.93.129.164. Redistribution subject to AIP license or copyright, see http://rsi.aip.org/rsi/copyright.jsp

eter to 4 μm. On the other hand, the polynomial power curve readily produced 3 and 4 μm diameter tapers.

Since the taper profile closely follows an exponential profile, we use this relationship to predict suitable scan lengths, L, and pull lengths, z, for any desired taper waist radius $r(z)$,

$$r(z) = r_0 e^{-z/L}, \tag{1}$$

where r_0 is the initial fiber radius before tapering.[15] There is some flexibility in choosing z and L. Scan lengths ranging from 5 to 15 mm and pull lengths ranging from 12 to 40 mm were examined and all yielded low transmission losses and taper diameters of 3–4 μm. We found that Eq. (1) always gives an accurate prediction of the waist diameter. The pull speed is less flexible and a value of 80–110 μm/s provided the best results.

Several preparatory steps are essential in ensuring that the finished taper is of satisfactory quality. Firstly, the fiber is liberally cleaned with acetone to remove inorganic substances. It is imperative that the laser beam and fiber be horizontal to within a few tens of microns so that the focus of the beam covers the fiber precisely throughout the scan. The fiber must also be slightly taut before attempting this alignment. Failure to optimize the alignment before starting fabrication results in sagging and possible vibrations of the fiber, which tends to distort taper profiles leading to high transmission losses. The polarization of the laser beam is set vertical to the fiber so that the absorption coefficient is maximized.[16]

III. RESULTS AND DISCUSSION

As a rule, tapers can only be produced with low losses if their profile follows the adiabaticity criterion.[23] This criterion requires the taper profile to be such that the change in taper angle is small enough to prevent light propagation being either coupled from the fundamental mode, HE_{11}, to higher order parasitic modes in the fiber or being lost as radiation. The criterion can be stated as $|dr/dz| \leqslant \rho(z)[\beta_1(z) - \beta_2(z)]/2\pi$, where dr/dz defines the local taper angle, $\Omega(z)$, by the trigonometric expression $\Omega(z) = \tan^{-1}|dr/dz|$, $\rho(z)$ is the local core radius, $\beta_1(z)$ and $\beta_2(z)$ are the local propagation constants of the fundamental mode and the next closest mode, respectively, and z is along the fiber axis.[15,23] The transcendental equation for the propagation constants has been solved numerically as a function of local taper diameter. Figure 3 shows a plot of this criterion and the core taper angle of a typical adiabatic taper as produced by the above-described method. The taper curve is based on an optimum exponential fit of the measurements in Fig. 4 and has the form as described by Eq. (1).

When the angle of the delineation curve is less than approximately ten times the taper angle, the light in the propagating mode will be lost to parasitic modes. While the fiber has only a single propagating mode in the untapered region, the taper itself contains multiple modes since the light is cladding-air guided. For a taper waist radius, a, of 1.5 μm, the core guidance parameter $V \equiv ka\sqrt{n_{\text{core}}^2 - n_{\text{clad}}^2} \approx 9.669 > 2.405$ at a wavelength of 980 nm, indicating the taper is

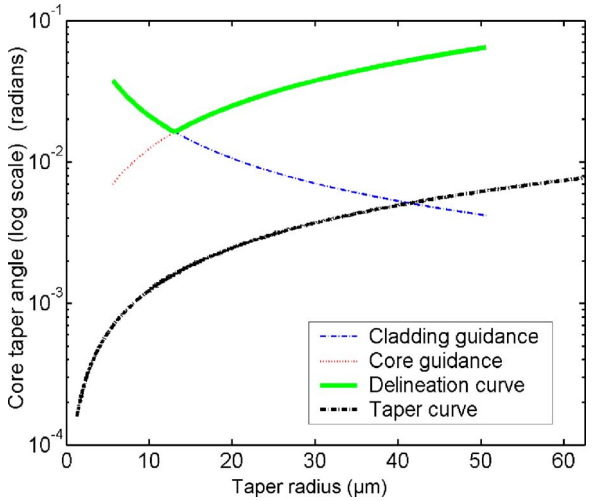

FIG. 3. Approximated length-scale delineation curve.

multimoded.[8] The refractive index of the core, n_{core}, is actually the effective index of the fundamental mode determined from $\beta_1(z)/k$ where k is the free space wave number and the refractive index of the air cladding, n_{clad}, is 1. However, once the taper is adiabatic, light only propagates in the fundamental mode. A single-mode tapered fiber is only possible when the diameter is less than about 1 μm.

The delineation curve in Fig. 3 is read from right to left when considering a decreasing taper diameter. Starting from the untapered region on the right, the initial taper transition consists of a core where the light propagates and a cladding where the refractive index difference is $\Delta = (n_{\text{core}} - n_{\text{clad}})/n_{\text{clad}} \approx 7.8 \times 10^{-3}$. An approximation for the core guidance curve is given in Ref. 23 and is based on the assumption of an infinite cladding diameter. Gradually, the diameter and core guidance parameter decrease until the core effectively disappears and the propagating light becomes cladding-air guided. At the taper waist, there is a large index difference of about 0.42 between the cladding and surrounding air causing the core guidance parameter to gradually increase; this is shown as an increase in the angle of the delin-

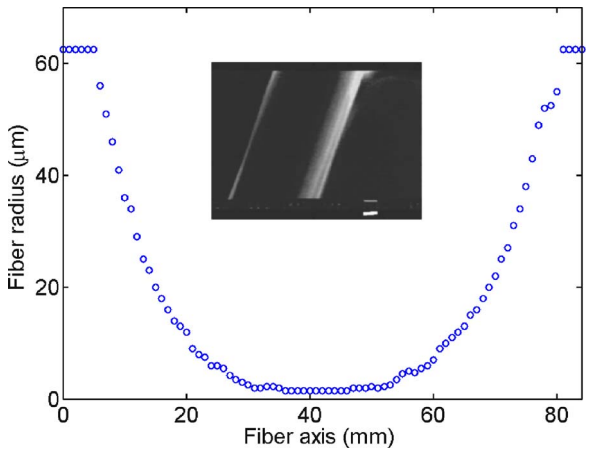

FIG. 4. Taper profile for a 3 μm diameter taper. The pull length is 40 mm, scan length is 7 mm, and the initial taper diameter is 125 μm. The inset shows a SEM image of a section of the taper with a diameter of 5.9 μm. The bar is 1.0 μm.

Downloaded 13 Nov 2007 to 134.93.129.164. Redistribution subject to AIP license or copyright, see http://rsi.aip.org/rsi/copyright.jsp

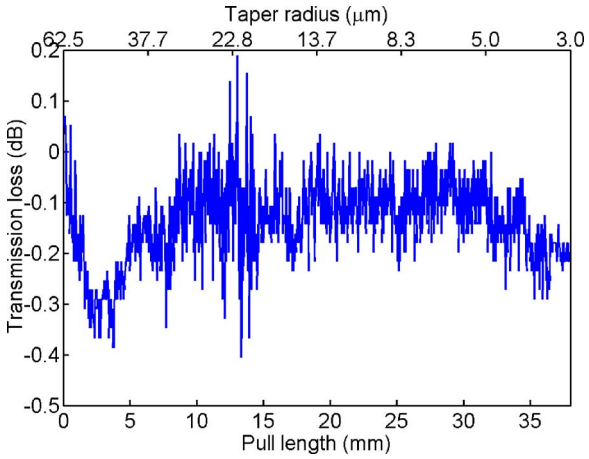

FIG. 5. Transmission loss measurements for a 3 μm diameter taper with 0.20 dB loss.

eation curve. For the cladding guidance curve, an approximation is also given in Ref. 23 and is based on the assumption that the core diameter is vanishing. Figure 4 shows a typical taper angle decreasing when approaching the taper waist. Both core and cladding contribute to distinct regions in the delineation curve. The taper clearly meets the adiabaticity criterion since the angle of the taper transitions is sufficiently below the delineation curve.

Figure 5 shows power transmission loss for a taper with a 3 μm diameter as a function of pull length. The power remains constant except for minute oscillations that do not influence the final taper transmission. A final transmission loss of 0.20 dB was measured and is quite acceptable for applications involving microsphere coupling. For a set of 11 taper pulls, the loss was 0.3 ± 0.2 dB with some of the tapers having losses as low as 0.04 dB. Losses lower than 0.04 dB were not routinely observed, which is thought to be primarily due to the fact that the taper curve is not strictly a factor of 10 below the delineation curve for the whole taper profile. Using a shorter wavelength diode laser would proportionately shift the delineation curve to the left and this would increase the taper-delineation curve separation in Fig. 3, consequently giving lower losses.[23] Surface roughness on the taper is negligible as evidenced by the scanning electron microscopy (SEM) image in the inset of Fig. 4.

The bottle resonator in Fig. 6 is produced with similar dimensions to that described in the theoretical work of Louyer *et al.*[19] and Sumetsky.[20] The resonator has a midsection diameter of 12 μm and length of approximately 300 μm. Shorter bottle resonators are limited by the size of the hot spot. Kakarantzas *et al.*[24] describe a bottle resonator 160 μm long with a diameter of 16 μm. The fabrication begins with tapering of the fiber down to a waist diameter of 10–20 μm, as described already. Each microtapered section on either side of the resonator is produced by pulling the taper at a speed of 10 μm/s for a length of about 0.2 mm

FIG. 6. Optical micrograph of a bottle resonator with a diameter of 12 μm and length of 300 μm. The bar is 10 μm.

while keeping the hot spot stationary. The discrete rotation of the stepper motor shaft allows the scanning mirror to direct the beam onto exact locations where microtapering is to take place.

Subwavelength diameters of below 100 nm have been achieved with the microfurnace method.[14] A 20 W CO_2 laser heats a small sapphire tube that surrounds the fiber rather than directly heating the fiber with the laser. Alignment of the beam focus with the taper is not as stringent as compared to the direct laser heating method. A limitation of this method is that microstructuring of the fiber profile cannot be achieved. Different taper shapes[15] may not be easily produced since the hot zone cannot be precisely varied and is typically several millimeters in length. A very short hot zone is vital for the microtapering step when producing bottle resonators. Furthermore, high losses of several decibels have, until now, been observed with the microfurnace method because the taper transitions are nonadiabatic.[13] This is likely to be detrimental when coupling to the fundamental mode of a microresonator.

We have described a simple and reproducible method of fabricating 3–4 μm diameter tapers using commercial single-mode SM980 fiber. A stepper motor and gear box can be used to scan the laser beam across the fiber with sufficient precision as a simpler and inexpensive alternative to the more traditional galvanometer scanners reported for flame systems. Transmission losses of 0.3 ± 0.2 dB at a wavelength of 980 nm are within acceptable limits of other tapering rigs described in the literature.[25] We verify our optical microscope measurements of the taper diameter with SEM imaging. This rig is of interest for applications involving microresonator coupling and it can also be used to produce long period gratings[24] and fused biconical taper couplers.[25]

Apart from the simplicity and cost savings of such a laser scanning rig, we have shown its flexibility for producing bottle resonators. This technique involves microtapering a fiber over a distance of about 0.2 mm and at a very slow speed. The dimensions of this new type of resonator can be precisely controlled. The discrete step size of the stepper motor can be used to control the length of the resonator with a resolution of approximately 1.7 μm half-step given the current rig configuration. The diameter of the bottle resonators can be as small as 3–4 μm. Installation and operation of our laser scanning rig require a minimum amount of skill compared with most other tapering methods.

Smaller diameter tapers and shorter bottle resonators would, no doubt, be possible by first expanding the CO_2 beam before focusing it through the 12.5 cm lens, thereby yielding a higher power density by virtue of the smaller size of the laser beam at the focus. This will be the subject of future investigations. Even though the microfurnace tapering method can achieve any reasonable diameter required for microcavity coupling, the technique we have described is still required for bottle resonator fabrication. We intend to use these tapers to couple light into active microspheres made from doped phosphate and ZBNA glass.[26] We are also interested in studying the interactions between cold, rubidium atoms and the evanescent field at the taper region for atom manipulation and guiding purposes.[27]

Downloaded 13 Nov 2007 to 134.93.129.164. Redistribution subject to AIP license or copyright, see http://rsi.aip.org/rsi/copyright.jsp

ACKNOWLEDGMENTS

This work is supported by Science Foundation Ireland Project No. 02/IN1/128. The authors thank Dr. Anthony Grant of Cork Institute of Technology for his help with the SEM measurements. One of the authors (D.G.O.S.) acknowledges support from IRCSET through the Embark Initiative. Another author (K.D.) is supported by Cork Institute of Technology and one of the authors (M.J.M.) acknowledges support from the Council of Directors of the Institutes of Technology.

[1] S. Götzinger, O. Benson, and V. Sandoghdar, Appl. Phys. B: Lasers Opt. **73**, 825 (2001).
[2] G. Griffel, S. Arnold, D. Taskent, A. Serpengüzel, J. Connolly, and N. Morris, Opt. Lett. **21**, 695 (1996).
[3] V. S. Ilchenko, X. S. Yao, and L. Maleki, Opt. Lett. **24**, 723 (1999).
[4] F. Lissillour, D. Messager, G. Stéphan, and P. Féron, Opt. Lett. **26**, 1051 (2001).
[5] S. M. Spillane, T. J. Kippenberg, O. J. Painter, and K. J. Vahala, Phys. Rev. Lett. **91**, 043902 (2003).
[6] B. E. Little, J.-P. Laine, and H. A. Haus, J. Lightwave Technol. **17**, 704 (1999).
[7] L. Tong, J. Lou, and E. Mazur, Opt. Lett. **12**, 1025 (2004).
[8] F. Le Kien, J. Q. Liang, K. Hakuta, and V. I. Balykin, Opt. Commun. **242**, 445 (2004).
[9] J. C. Knight, G. Cheung, F. Jacques, and T. A. Birks, Opt. Lett. **22**, 1129 (1997).
[10] L. Tong, R. R. Gattass, J. B. Ashcom, S. He, J. Lou, M. Shen, I. Maxwell, and E. Mazur, Nature (London) **426**, 816 (2003).
[11] G. Brambilla, V. Finazzi, and D. J. Richardson, Opt. Express **12**, 2258 (2004).
[12] T. E. Dimmick, G. Kakarantzas, T. A. Birks, and P. St. J. Russel, Appl. Opt. **38**, 6845 (1999).
[13] M. Summetsky, Y. Dulashko, and A. Hale, Opt. Express **12**, 3521 (2004).
[14] M. Sumetsky, Y. Dulashko, J. M. Fini, A. Hale, and D. J. DiGiovanni, J. Lightwave Technol. **24**, 242 (2006).
[15] T. A. Birks and Y. W. Li, J. Lightwave Technol. **10**, 432 (1992).
[16] A. Grellier, N. K. Zayer, and C. N. Pannell, Opt. Commun. **152**, 324 (1998).
[17] F. Treussart, J. Hare, L. Collot, V. Lefèvre, D. S. Weiss, V. Sandoghdar, J. M. Raimond, and S. Haroche, Opt. Lett. **19**, 1651 (1994).
[18] W. von Klitzing, R. Long, V. S. Ilchenko, J. Hare, and V. Lefèvre-Seguin, New J. Phys. **3**, 14.1 (2001).
[19] Y. Louyer, D. Meshede, and A. Rauschenbeutel, Phys. Rev. A **72**, 031801(R) (2005).
[20] M. Sumetsky, Opt. Lett. **29**, 8 (2004).
[21] Laser 2000 UK Ltd., Britannia House, Denford Road, Ringstead, Northants NN14 4DF, United Kingdom. 671XX series drive card and 6210H series moving magnet galvanometer scanner.
[22] Radionics Ltd., Glenview Industrial Estate, Herberton Road, Rialto, Dublin 12, Ireland. Hybrid stepper motor, stock No. 440-436; 500:1 gear box, stock No. 718-925; and controller circuit, stock No. 217-3611.
[23] J. D. Love, W. M. Henry, W. J. Stewart, R. J. Black, S. Lacroix, and F. Gonthier, IEE Proc.-J: Optoelectron. **138**, 343 (1991).
[24] G. Kakarantzas, T. E. Dimmick, T. A. Birks, R. Le Roux, and P. St. J. Russel, Opt. Lett. **26**, 1137 (2001).
[25] C. McAtamney, A. Cronin, R. Sherlock, G. M. O'Connor, and T. J. Glynn, Proceedings of the Third International WLT Conference on Lasers in Manufacturing, Munich, (2005), p. 673.
[26] B. J. Shortt, J. Ward, D. O'Shea, and S. Nic Chormaic, Proc. SPIE **6187**, 618708 (2006).
[27] F. Le Kien, V. I. Balykin, and K. Hakuta, Phys. Rev. A **70**, 063403 (2004).

Downloaded 13 Nov 2007 to 134.93.129.164. Redistribution subject to AIP license or copyright, see http://rsi.aip.org/rsi/copyright.jsp

Appendix C

Upconversion Channels in Er:ZBLALiP: a Multi-Color Microspherical Light Source

EPJ Applied Physics proofs
(will be inserted by the editor)

Upconversion channels in Er^{3+}:ZBLALiP fluoride glass microspheres

D.G. O'Shea[1,2], J.M. Ward[2,3], B.J. Shortt[2,3], M. Mortier[4], P. Féron[5], and S. Nic Chormaic[1,2,a]

[1] Physics Department, University College Cork, Cork, Ireland
[2] Photonics Centre, Tyndall National Institute, Prospect Row, Cork, Ireland
[3] Department of Applied Physics and Instrumentation, Cork Institute of Technology, Bishopstown, Cork, Ireland
[4] Laboratoire de Chimie de la Matière Condensée de Paris, ENSCP, 11 rue Pierre et Marie Curie, 75005 Paris, France
[5] ENSSAT-FOTON (CNRS-UMR 6082) Université de Rennes 1, 6 rue de Kerampont, BP 80518, 22305 Lannion Cedex, France

Received: 29 May 2007 / Received in final form: 21 August 2007 / Accepted: 28 August 2007
Published online (Inserted Later) – © EDP Sciences

Abstract. We present results on the realization of a multicolour microspherical glass light source fabricated from the erbium doped fluoride glass ZBLALiP. Whispering gallery mode lasing and upconversion processes give rise to laser and fluorescent emissions at multiple wavelengths from the ultraviolet to the infrared. Thirteen discrete emissions ranging from 320 to 849 nm have been observed in the upconversion spectrum. A Judd-Ofelt analysis was performed to calculate the radiative properties of Er^{3+}:ZBLALiP microspheres, including the radiative transition probabilities, the electric dipole strengths, the branching ratios and the radiative lifetimes of the transitions involved. We have also identified the primary processes responsible for the generation of the observed wavelengths and have shown that this material has an improved range of emissions over other erbium doped fluoride glasses.

PACS. 42.55.Sa Microcavity and microdisk lasers – 42.70.Hj Laser materials – 42.70.Ce Glasses, quartz

1 Introduction

Microspherical resonators have attracted significant attention in recent years due to their interesting optical properties and the range of applications for which they can be used including quantum optics [1–3] and optical communications [4,5]. In particular, microspheres fabricated from rare-earth ion doped materials have been shown to operate as miniature laser devices [6,7]. Recently, there have been significant breakthroughs in the exploitation of upconversion mechanisms in rare-earth ion doped materials to yield wavelengths from the near infrared to the near ultraviolet. The spectral properties of the emissions from the materials depend on (i) the choice of dopant (e.g. Er^{3+}, Yb^{3+}) and (ii) the host matrix (e.g. fluoride or phosphate glass) in which the dopant is embedded. The close proximity of numerous energy levels in triply-ionized rare earth ions is advantageous for obtaining fluorescent and lasing emissions through various upconversion mechanisms such as excited state absorption (ESA), energy transfer upconversion (ETU) and photon avalanche (PA) [8].

Three-photon upconversion lasing yielding red and blue emissions about 480 nm and 800 nm in thulium-doped fluorozirconate (ZBLAN) glass microspheres has been reported [9]. The same authors also observed red and green upconversion lasing in erbium doped ZBLAN glass microspheres [10]. In both cases, 1064 nm free-space laser pulses focused on the microsphere surface acted as the pump source. The first microspherical laser pumped using a fibre taper was demonstrated when an Yb:Er-doped phosphate glass microsphere was pumped at 980 nm [11]. The microsphere lased in the infrared about 1550 nm with a threshold power of 60 μW, and emitted green fluorescence attributed to a two-photon ESA process. Several groups [6,7,12,13] have also made considerable progress in the development of microspherical lasers operating in the infrared region, in particular with emission wavelengths falling in the C- and L-bands.

The suitability of fluoride glasses as rare-earth host materials has been known for some time [14] due to their low phonon energies which determine multiphonon relaxation rates and, subsequently, the efficiency of any upconversion processes present. In this paper, we report on a number of upconversion processes identified in an erbium-doped fluoride glass (Er^{3+}:ZBLALiP) microsphere, using a 980 nm pump laser coupled via a fibre taper. Preliminary work on Er^{3+}:ZBLALiP was presented in [7], including evidence of 1550 nm lasing in 1480 nm pumped microspheres. In this paper, we provide a more systematic study of the upconversion processes involved in 980 nm pumping of Er^{3+}:ZBLALiP microspheres. We identify the

[a] e-mail: s.nicchormaic@ucc.ie

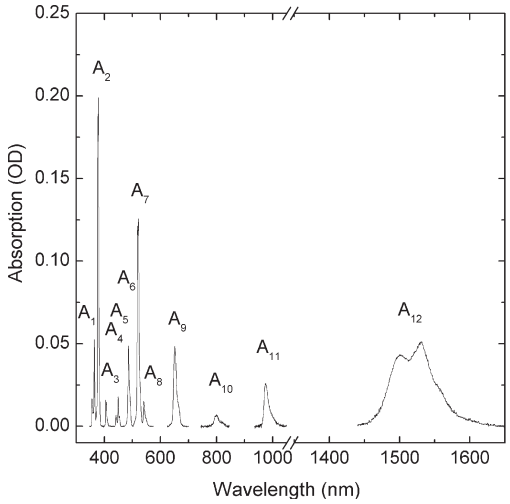

Fig. 1. Absorption spectrum of 0.2 mol% Er^{3+}:ZBLALiP bulk glass.

transitions involved and analyse the dominant processes that give rise to the observed emissions. In addition, we calculate associated material properties through McCumber and Judd-Ofelt theories. We have observed upconversion emissions from the ultraviolet to the infrared and we identify several new emissions including the first observation of a 320 nm upconversion following 980 nm pumping of Er^{3+}. This arises due to the exceptionally long lifetimes of the $^4F_{3,5/2}$ levels within Er^{3+}:ZBLALiP compared to other glasses [15]. The identification and analysis of the numerous upconversions enable us to attribute the emissions to particular erbium transitions and suggest the processes responsible. In addition, the efficiency of the ultraviolet upconversion processes and the stability of erbium doped ZBLALiP microspheres (permitting high optical quality to be achieved during fabrication) make this material suitable for information storage applications where short wavelengths are desirable [16].

2 Experiment

An initial study of some fundamental material properties of Er^{3+} doped ZBLALiP (ZrF_4-BaF_2-LaF_3-AlF_3-LiF-PbF_2) glass was reported earlier [7], where the improved stability of ZBLALiP with respect to similar fluorozirconate glasses and its suitability as a host for rare-earth ions was discussed. Here, we present additional material properties and extend the range of functionality of Er^{3+}:ZBLALiP as a material suitable for optical communications and optical sensing. Figure 1 shows the measured absorption spectrum for a 5.8 mm thick bulk sample of 0.2 mol% Er^{3+}:ZBLALiP in which twelve absorption bands can be identified. These represent the transitions from the ground state $^4I_{15/2} \rightarrow A_N$ with $A_1 = {}^2G_{9/2} + {}^2K_{15/2} + {}^2G_{7/2}$, $A_2 = {}^4G_{11/2}$, $A_3 = {}^2H_{9/2}$, $A_4 = {}^4F_{3/2}$, $A_5 = {}^4F_{5/2}$, $A_6 = {}^4F_{7/2}$, $A_7 = {}^2H_{11/2}$, $A_8 = {}^4S_{3/2}$, $A_9 = {}^4F_{9/2}$, $A_{10} = {}^4I_{9/2}$, $A_{11} = {}^4I_{11/2}$ and $A_{12} = {}^4I_{13/2}$.

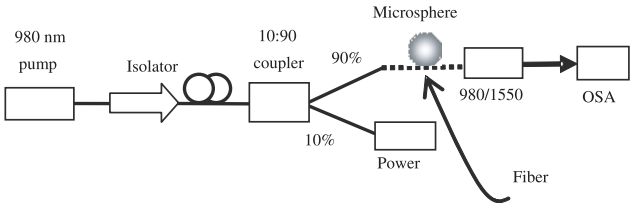

Fig. 2. Experimental setup. OSA – optical spectrum analyser.

The absorption spectra were recorded using a double-beam Cary 17 spectrometer (Varian) with a resolution better than 0.1 nm.

The fabrication techniques for the Er^{3+}:ZBLALiP microspheres was described elsewhere [17]. We use glass with an erbium concentration of 0.2 mol%, which equates to 4×10^{19} Er^{3+} ions/cm^3. Note that, at this concentration, energy transfer (ET) should not play a major role in the upconversion processes and, therefore, excited state absorption (ESA) is the dominant mechanism [18]. Nevertheless, due to the non-trivial problem of distinguishing the two mechanisms, some authors have suggested that ET may play a role even when the dopant concentration is below the critical value of about 1 mol% [19–21].

In our work, the C-band lasing characteristics and upconversion spectra are investigated at room temperature using a single mode, 980 nm laser diode pump with a spectral width of about 1 nm and under CW pumping conditions. The experimental setup is depicted in Figure 2. A fibre-optical isolator is placed immediately after the 980 nm pump laser in order to avoid optical feedback. The pump light then passes through a 10:90 coupler, whereby 10% is monitored using a power meter and the larger fraction is sent through a fibre taper and coupled into the microsphere via evanescent wave coupling. The 980 nm light transmitted through the fibre taper is separated from the C-band emissions using a WDM and an optical spectrum analyser is used to detect the lasing around 1550 nm. The UV to IR emissions are detected by free-space coupling of the scattered radiation from the microsphere into an optical spectrometer. To achieve efficient coupling of the pump into the microsphere and efficient collection of the infrared lasing spectrum, the fibre taper is manufactured using 1550 nm SMF-28 fibre that is adiabatically tapered to 1 μm diameter using a direct heating technique [22]. The transmission loss of these tapers is typically less than 0.1 dB/cm. Optimum mechanical alignment of the taper and microsphere is achieved by translating the microsphere to different locations along the taper until the lasing about 1550 nm is maximized. The transmission through the pump fibre is also monitored during the alignment and around 10–15% of the pump light is coupled into the microsphere. This relatively low coupling efficiency is, in part, due to the broad spectral nature of the pump laser relative to the whispering gallery mode resonances of the microsphere and can be improved by the use of a narrow linewidth pump source [23].

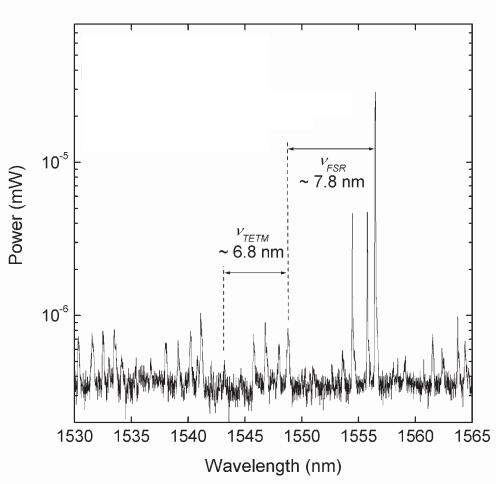

Fig. 3. 70 μm diameter microsphere lasing spectrum (intense peaks) about 1550 nm showing whispering gallery mode structure.

3 Results

Figure 3 shows a typical lasing spectrum obtained for a 70 μm sphere pumped under the aforementioned conditions. Characteristic whispering gallery mode bands about the sphere equator are also observed. The intense peaks represent multimode lasing and the smaller signals indicate fluorescence emissions. The microsphere eccentricity is determined from $\varepsilon = (\Delta\omega_{ecc}/\omega_{nml})\left(l^2/|m| - 1/2\right)$, where l and m are the angular mode numbers, ω_{nml} is the angular frequency of the mode and $\Delta\omega_{ecc}$ is the azimuthal mode splitting. The eccentricity is calculated to be ~2.1% for $l = |m|$ with corresponding azimuthal mode splitting, $\Delta\omega_{ecc}$, of ~11 GHz. Analysis of the lasing peaks enables us to measure the free spectral range, ν_{FSR}, between successive mode groups with a difference in angular mode number l of 1, to be ~7.8 nm (0.97 THz). Theoretically, we can determine the diameter of the sphere from $D = c/\pi p \nu_{VSR}$, where c is the speed of light and p is the refractive index of the material. Using $p = 1.49$ at 1550 nm, we find that $\nu_{FSR} = 7.8$ nm indicates a microsphere diameter of 66 μm, which is reasonably close to the (70 ± 2) μm determined using an optical microscope.

It can be seen from Figure 3 that each group of modes contains four distinct lasing peaks due to the excitation of multiple modes in the sphere. The peak power of the lasing peaks presented here is ~30 nW, although we have also observed lasing in a single mode with a peak value of ~500 nW. The spacing between TE and TM modes (ν_{TETM}) of 6.8 nm in Figure 3 agrees well with the calculated value of 6.4 nm. An estimate of the loaded cavity Q for this system yields a value in the region of 1×10^7.

The Er^{3+}:ZBLALiP upconversion spectrum recorded coincidently to the C-band lasing spectrum (cf. Fig. 3) is shown in Figure 4. Approximately 700 μW of 980 nm pump light was coupled into the microsphere. The spectrum is detected by monitoring the free-space scattering from the microsphere into a high numerical aperture fibre coupled spectrometer (Ocean Optics USB2000). Due to the limited dynamic linear range of the spectrometer the fluorescence spectrum is produced by splicing two separate spectra together. This also enables us to maximize the signal-to-noise ratio of the lower intensity transitions. The spectra about the green were recorded for a detector integration time reduced by a factor of 40. Thirteen discrete peaks have been noted in the spectrum and are numbered from T1–T13. The spectra have also been corrected for the responsivity of the spectrometer detector as a function of wavelength. The total power outcoupled and detected is 0.5 nW for the green transitions (T6 and T7) and 0.1 nW for T13. The limited resolution of the spectrometer used, combined with the smaller microsphere free spectral range at shorter wavelengths, means that the whispering gallery mode structure is only visible for emissions at wavelengths above 800 nm. The mode structure for the 849 nm (T13) emission is distinguishable in the inset of Figure 4.

3.1 Emission and absorption cross-sections of Er^{3+}:ZBLALiP

The emission cross-section, σ_{ems}, for Er^{3+}:ZBLALiP around 1550 nm can be determined from the absorption spectrum (Fig. 1). Using McCumber theory, under the assumption of a strongly phonon coupled system [24], the emission cross-section is given by

$$\sigma_{ems}(\lambda) = \sigma_{abs}(\lambda)\frac{Z_L}{Z_U}\exp\left(\frac{E_{UL}}{k_B T}\right)\exp\left(-\frac{hc}{\lambda k_B T}\right), \quad (1)$$

where Z_L (Z_U) is the partition function of the lower (upper) state given by a summation of continuous levels $\sum_i \exp(\Delta E_i/k_B T)$, where ΔE_i is the energy difference between the Stark split sublevels and the lowest energy level in the lower (upper) manifold, E_{UL} is the energy difference between the lowest sublevels in the upper and lower manifolds, h is Planck's constant, c is the speed of light, k_B is Boltzmann's constant, and T is temperature in Kelvin. From equation (1), the bulk sample of Er^{3+}:ZBLALiP has a peak emission cross-section of 4.6×10^{-21} cm^2 in the C-band, which compares well with values of 4.9×10^{-21} cm^2 measured for fluoroindate glasses [15] and 4.6×10^{-21} cm^2 measured in other fluorozirconate glass bulk samples [25].

Using the absorption data presented in Figure 1, it is also possible to determine the absorption cross-section using the expression [20]

$$\sigma_{abs} = \frac{-\log A}{l\, N'} \quad (2)$$

where A is the absorbance, l is the sample thickness, and N' is the Er^{3+} concentration of 3.76×10^{19} cm^{-3}. Figure 5 presents the absorption and emission cross-sections for 0.2 mol% Er^{3+}:ZBLALiP in the C-band. Emission spectra for both bulk and powder ZBLALiP samples are shown.

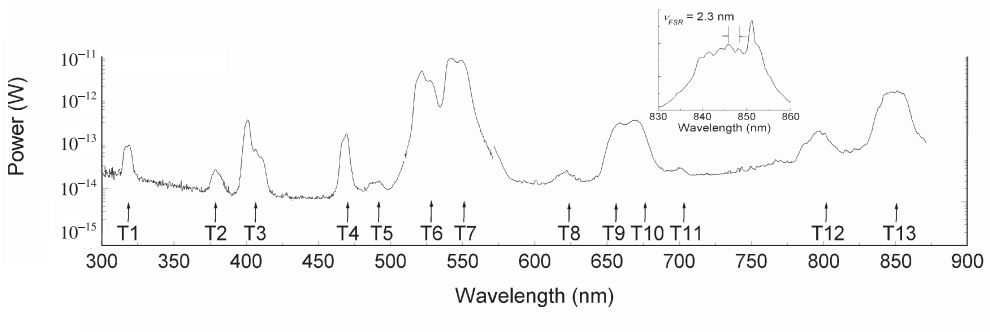

Fig. 4. Er^{3+}:ZBLALiP microsphere upconversion spectrum. The spectrometer integration time was reduced by a factor of forty about the green transitions T6 and T7. Inset: whispering gallery mode structure about T13.

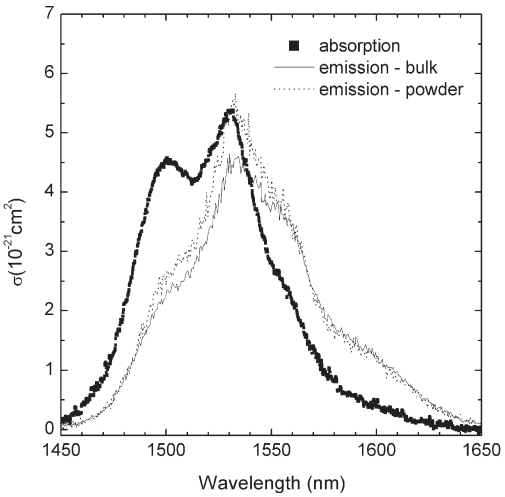

Fig. 5. Absorption (bulk) and emission (bulk and powder) cross-section measurements for 0.2 mol% Er^{3+}:ZBLALiP.

3.2 Radiative properties of Er^{3+}:ZBLALiP

In order to gain a thorough understanding of the emission processes within Er^{3+}:ZBLALiP its radiative properties can be determined through Judd-Ofelt (JO) analysis of the absorption data presented in Figure 1. The JO intensity parameters Ω_t (t = 2, 4, 6) are derived from the electric-dipole contributions of the measured line strengths by a least-squares-fitting approach to minimize the root mean square deviation with the calculated line strength. Values of $\Omega_2 = 3.12 \times 10^{-20}$ cm^2, $\Omega_4 = 1.49 \times 10^{-20}$ cm^2, and $\Omega_6 = 1.15 \times 10^{-20}$ cm^2 [7] are used throughout our calculations. A spectroscopic quality factor can be defined as Ω_4/Ω_6, which gives 1.30 for the quoted intensity parameters. Note that the JO parameters for Er^{3+}:ZBLALiP are slightly higher than those for Er^{3+}:ZBLAN ($\Omega_2 = 2.37 \times 10^{-20}$ cm^2, $\Omega_4 = 1.24 \times 10^{-20}$ cm^2, and $\Omega_6 = 0.73 \times 10^{-20}$ cm^2) [26]. A higher Ω_2 indicates greater asymmetry of the host glass, while a higher Ω_6 has a dominant influence on the electric dipole line strength, S^{ed}, of the lasing transition $^4I_{13/2} \rightarrow {}^4I_{15/2}$ [27].

Determination of the electric dipole line strength, S^{ed}, and the magnetic dipole line strength, S^{md}, combined with the JO intensity parameters for our material, can be used to predict significant radiative properties for Er^{3+}:ZBLALiP such as the spontaneous radiative transition rates, electric dipole line strengths, branching ratios and radiative lifetimes. S^{ed} depends on the double reduced matrix elements of the unit tensor operator, U, and these are assumed to be independent of the host material [27]. Following this argument we have taken average published matrix elements [27,28] for our calculations and these are reproduced in Table 1 for convenience. S^{md} depends on the double reduced matrix elements of the $L + 2S$ operator, where L is the total orbital angular momentum and S is the total spin.

The total spontaneous radiative transition rate between two levels J and J', is given by

$$A_{JJ'} = A^{ed}_{JJ'} + A^{md}_{JJ'} = \frac{64\pi^4}{3h\lambda^3(2J+1)} \left(\chi_{ed} S^{ed} + \chi_{md} S^{md}\right), \tag{3}$$

where λ is the mean wavelength of the absorption, $\chi_{ed} = p(p^2+2)^2/9$ is the local field correction factor for electric dipole transitions, and $\chi_{md} = p^3$ is the local field correction factor for magnetic dipole transitions. We calculate the magnetic dipole emission probabalities, $A^{md}_{JJ'}$, using published values [27] for LaF_3 ($A'^{md}_{JJ'}$) and corrected for the refractive index difference using the relation $A^{md}_{JJ'} = (p/p')^3 A^{md}_{JJ'}$, where p' (p) is the refractive index of LaF_3 (ZBLALiP). The refractive index for ZBLALiP is 1.49 at 1550 nm, while that for LaF_3 is 1.57, hence $A^{md}_{JJ'} = 0.86 A'^{md}_{JJ'}$.

The radiative lifetime, τ_R, of transitions between levels J and J' is related to the inverse of $A_{JJ'}$ by

$$\tau_R = \frac{1}{\sum_{J'} A_{JJ'}}, \tag{4}$$

and the branching ratio, β, between J and J' is simply the ratio of $A_{JJ'}$ for the initial level to the sum of $A_{JJ'}$ for all the lower levels given by

$$\beta = A_{JJ'} \tau_R. \tag{5}$$

Table 1 shows our values for the radiative probabilities, electric dipole line strengths, branching ratios, and radiative lifetimes for the transitions involved in 980 nm pumped Er^{3+}:ZBLALiP. Several levels have high branching ratios for transitions to the ground level and intermediate levels, many of which have been observed in the emission spectrum in Figure 4. Where possible we have identified the transition associated with the emissions observed in Figure 3 and have indicated this correspondence in the average wavelength column. Note that the radiative properties for the observed 667 nm emission (T10) have not been calculated due to limited data availability and, therefore, it does not appear in Table 1.

4 Discussions

In Figure 6 we present an energy level diagram for erbium indicating the radiative and non-radiative transitions that are responsible for the thirteen emissions identified in Figure 4. Even though it is energetically possible for several emissions to originate from the same level, the branching ratios, β, predicted in the JO theory can help determine the most likely emissions from a particular level. For example, it is energetically possible for both the 383 nm (T2) and 618 nm (T8) emissions to originate from the radiative decay of $^4G_{11/2}$ to lower levels. However, the ratio of the measured emission intensities (1:3) disagrees substantially from the calculated ratios (1:21), thereby indicating that both emissions cannot arise from the $^4G_{11/2}$ level. In fact, only the 383 nm emission is from $^4G_{11/2}$ and the 618 nm emission is due to the $^2P_{3/2} \rightarrow ^4F_{9/2}$ decay. In this way, we can use a combination of the energy gaps between the energy levels and the calculated branching ratios to determine the energy levels involved in the radiative emissions.

Four emissions in Figure 4 are attributed to the decay of the $^2P_{3/2}$ level. These are the 618 nm (T8) decay to $^4F_{9/2}$ ($\beta = 0.05$), the 479 nm (T4) decay to $^4I_{11/2}$ ($\beta = 0.29$), the 403 nm (T3) decay to $^4I_{13/2}$ ($\beta = 0.39$), and the 320 nm (T1) decay to $^4I_{15/2}$ ($\beta = 0.12$). The branching ratio calculations predict the ratio of emission intensities for each of the levels to be 1 (618 nm):5.8 (470 nm):7.8 (403 nm), which is in reasonable agreement with the measured ratios of 1:5.3:6.6. We have excluded the intensity of the 320 nm emission from this comparison because fluorozirconate glasses have very substantial absorption losses in the UV region [29].

Further understanding of the transition(s) responsible for a particular wavelength can be obtained by the intensity dependence behaviour of the fluorescence at a particular wavelength. The centre wavelength associated with each transition is also shown in Figure 6. In the case of ESA, the dependence of the fluorescence intensity upon pump power often exhibits a simple power law dependence with a slope, n, equal to the number of photons absorbed. Measurements of this dependence for the case of the observed green transitions $^2H_{11/2} \rightarrow ^4I_{15/2}$ (T6) and $^4S_{3/2} \rightarrow ^4I_{15/2}$ (T7) are presented in Figure 7, where we plot the intensity as a function of the absorbed pump power in the fibre taper. From the energy diagram (cf. Fig. 6) both T6 and T7 are attributed to 2-photon absorption. Slopes corresponding to $n = 1.58$ for T6 and $n = 1.66$ for T7 have been recorded, whereas a slope of two would be expected. This discrepancy from the expected result can be understood as depletion of the $^4I_{15/2}$ ground state [9].

Based on our analysis we predict that the $^4F_{3,5/2}$ levels of Er^{3+}:ZBLALiP have unusually long radiative lifetimes of 1.44 ms and 1.15 ms compared to other glasses, such as Er^{3+}-doped fluoroindate glass which has a lifetime of 0.50 ms [15]. As can be seen from the energy level diagram (cf. Fig. 6), this is critically important for the generation and observation of UV and violet emissions from the $^2P_{3/2}$ level since it facilitates the third ESA, $^4F_{3,5/2} \rightarrow ^2K_{13/2}$, by maintaining a large $^4F_{3,5/2}$ population. In Er^{3+}-doped fluoroindate glass, nonradiative decay rapidly depletes the $^4F_{3,5/2}$ population, effectively preventing any further ESA and prohibiting UV emissions.

Our measurements demonstrate a broad range of emission from 320 nm to 849 nm in Er^{3+}:ZBLALiP, in addition to the IR lasing around 1550 nm. We suggest that the combination of high cavity quality factor and low whispering gallery mode volume (approximately 2000 μm^3) significantly enhances the probability of excited state absorption by enhancing the pump field strength ($\sim 10^3$ V/m per photon) within the microsphere. This is reflected in the fact that a significant number of the observed transitions are attributed to 3-photon and 4-photon absorption events for what is a relatively modest pump power (sub mW) coupled into the microsphere.

The emission line centred at 320 nm (T1) is, most likely, due to a 4-photon process populating the $^2P_{3/2}$ state, which in turn radiatively relaxes to the $^4I_{15/2}$ ground state. Three pump photons populate the $^2G_{7/2}$ state. The $^2G_{7/2}$–$^2P_{3/2}$ energy gap of $\sim$3600 cm^{-1} combined with a phonon energy of 650 cm^{-1} is such that the $^2P_{3/2}$ state is unlikely to be populated by thermalisation and, as such, we suggest that the absorption of a fourth pump photon is necessary to explain T1. This 320 nm transition has previously been reported in Er^{3+}-doped glass, but was identified as a 3-photon process following pumping at 637 nm [16]. The same authors also reported emissions corresponding to the transitions T3, T4, T7 and T9. Transition T1 has been reported [30] in an Yb^{3+}:Er^{3+} co-doped material although in that case the excitation process involved successive energy transfers from Yb^{3+}. It should be noted that this is very different from our work which involves a single dopant i.e. erbium and, therefore, does not rely on a sensitizer ion. Additionally, ETU does not play a major role in our experiments due to the low dopant concentration.

We believe that the transitions $^2P_{3/2} \rightarrow ^4I_{13/2}$ (T3), $^2P_{3/2} \rightarrow ^4I_{11/2}$ (T4) and $^2P_{3/2} \rightarrow ^4F_{9/2}$ (T8) also arise due to 4-photon excitation. Transitions T1, T3 and T4 have been observed following pumping at 545 nm [31]. Transitions T6, T7, T12 and T13 have been reported following 980 nm pumping [32]. The ultraviolet line

Table 1. Predicted radiative transition probabilities electric dipole line strengths (S^{ed}) ($A^{ed}_{JJ'}$and$A^{md}_{JJ'}$), branching ratios (β), and radiative lifetimes (τ_R) for Er^{3+}:ZBLALiP. Note that the number in brackets (T1, T2, ...) listed under the average wavelength corresponds to the observed transitions in Figure 3.

Transition	Average wavelength (nm)	$\left[U^{(2)}\right]^2$	$\left[U^{(4)}\right]^2$	$\left[U^{(6)}\right]^2$	S^{ed} ($\times 10^{-20}$cm^3)	$A^{ed}_{JJ'}$ (s^{-1})	$A^{md}_{JJ'}$ (s^{-1})	β	τ_R (ms)
$^4I_{13/2} \rightarrow$ $^4I_{15/2}$	1542	0.0195	0.1173	1.4316	1.88	78	32.2	1.00	9.10
$^4I_{11/2} \rightarrow$ $^4I_{15/2}$	975	0.0282	0.0003	0.3953	0.54	98	7.2	0.84	8.53
$\rightarrow$ $^4I_{13/2}$	2727	0.0210	0.1100	1.0400	1.43	12		0.16	
$^4I_{9/2} \rightarrow$ $^4I_{15/2}$	793 (T12)	0.0000	0.1733	0.0099	0.27	106	1.0	0.76	7.14
$\rightarrow$ $^4I_{13/2}$	1668	0.0003	0.0081	0.6400	0.75	32		0.23	
$\rightarrow$ $^4I_{11/2}$	4663	0.0030	0.0674	0.1271	0.26	1		0.01	
$^4F_{9/2} \rightarrow$ $^4I_{15/2}$	656 (T9)	0.0000	0.5354	0.4618	1.33	947	5.1	0.89	0.938
$\rightarrow$ $^4I_{13/2}$	1025	0.0096	0.1576	0.0870	0.36	67	2.2	0.06	
$\rightarrow$ $^4I_{11/2}$	1966	0.0671	0.0088	1.2611	1.67	44		0.05	
$\rightarrow$ $^4I_{9/2}$	3623	0.0960	0.0061	0.0120	0.32	1		0.00	
$^4S_{3/2} \rightarrow$ $^4I_{15/2}$	540 (T7)	0.0000	0.0000	0.2211	0.25	700		0.66	0.949
$\rightarrow$ $^4I_{13/2}$	849 (T13)	0.0000	0.0000	0.3481	0.40	294		0.28	
$\rightarrow$ $^4I_{11/2}$	1212	0.0000	0.0037	0.0789	0.10	24		0.02	
$\rightarrow$ $^4I_{9/2}$	1688	0.0000	0.0729	0.2560	0.40	36		0.03	
$^2H_{11/2} \rightarrow$ $^4I_{15/2}$	520 (T6)	0.7056	0.4109	0.0870	2.91	3453	54.5	0.92	0.265
$\rightarrow$ $^4I_{13/2}$	792	0.0230	0.0611	0.0527	0.22	75	81.5	0.03	
$\rightarrow$ $^4I_{11/2}$	1115	0.0357	0.1382	0.0371	0.36	43	0	0.03	
$\rightarrow$ $^4I_{9/2}$	1507	0.2077	0.0662	0.2858	1.08	53	0.2	0.01	
$\rightarrow$ $^4F_{9/2}$	2579	0.3629	0.0224	0.0022	1.17	11		0.00	
$^4F_{7/2} \rightarrow$ $^4I_{15/2}$	492 (T5)	0.0000	0.1467	0.6273	0.94	1964		0.78	0.397
$\rightarrow$ $^4I_{13/2}$	727	0.0000	0.3371	0.0001	0.50	316		0.13	
$\rightarrow$ $^4I_{11/2}$	983	0.0035	0.2648	0.1515	0.58	147		0.06	
$\rightarrow$ $^4I_{9/2}$	1245	0.0163	0.0954	0.4277	0.68	86		0.03	
$\rightarrow$ $^4F_{9/2}$	1947	0.0121	0.0342	0.0151	0.11	4		0.00	
$^4F_{5/2} \rightarrow$ $^4I_{15/2}$	450	0.0000	0.0000	0.2237	0.26	873		1.00	1.15
$^4F_{3/2} \rightarrow$ $^4I_{15/2}$	443	0.0000	0.0000	0.1204	0.14	690		1.00	1.44
$^2H_{9/2} \rightarrow$ $^4I_{15/2}$	409	0.0000	0.0190	0.2255	0.29	831	31.1	0.33	0.400
$\rightarrow$ $^4I_{13/2}$	556	0.0780	0.1194	0.3535	0.83	953	0.9	0.38	
$\rightarrow$ $^4I_{11/2}$	697 (T11)	0.0428	0.0824	0.1128	0.39	226	36.5	0.10	
$\rightarrow$ $^4I_{9/2}$	823	0.0147	0.0062	0.0043	0.06	21	0.9	0.01	
$\rightarrow$ $^4F_{9/2}$	1079	0.0055	0.0314	0.0369	0.11	184	0.7	0.09	
$\rightarrow$ $^2H_{11/2}$	1854	0.0308	0.1828	0.0671	0.45	152		0.06	
$\rightarrow$ $^4F_{7/2}$	2485	0.1058	0.0488	0.0240	0.43	61		0.02	
$^4G_{11/2} \rightarrow$ $^4I_{15/2}$	383 (T2)	0.9178	0.5271	0.1197	3.79	11620	37.9	0.84	0.072
$\rightarrow$ $^4I_{13/2}$	505	0.1011	0.2642	0.2550	1.00	1300	0.1	0.10	
$\rightarrow$ $^4I_{11/2}$	618	0.0002	0.4930	0.0144	0.75	527	0.6	0.04	
$\rightarrow$ $^4I_{9/2}$	724	0.0645	0.0117	0.0467	0.27	120	2.6	0.01	
$\rightarrow$ $^4F_{9/2}$	905	0.4436	0.0388	0.0104	1.45	328	10.2	0.02	
$\rightarrow$ $^2H_{11/2}$	1394	0.0006	0.1600	0.1100	0.37			0.00	
$^4G_{9/2} \rightarrow$ $^4I_{15/2}$	365	0.0000	0.2416	0.1235	0.50	2034		1.00	0.492
$^2G_{7/2} \rightarrow$ $^4I_{15/2}$	358	0.0000	0.0174	0.1163	0.16	839		1.00	1.192
$^2P_{3/2} \rightarrow$ $^4I_{15/2}$	320 (T1)	0.0000	0.0000	0.0260	0.03	403	19.5	0.12	0.310
$\rightarrow$ $^4I_{13/2}$	403 (T3)	0.0000	0.0000	0.1600	0.18	1242		0.39	
$\rightarrow$ $^4I_{11/2}$	470 (T4)	0.0000	0.1300	0.0250	0.22	936		0.29	
$\rightarrow$ $^4I_{9/2}$	524	0.0000	0.0440	0.0092	0.08	230		0.07	
$\rightarrow$ $^4F_{9/2}$	618 (T8)	0.0000	0.0560	0.0045	0.09	164		0.05	
$\rightarrow$ $^4S_{3/2}$	763	0.0847	0.0000	0.0000	0.26	259		0.09	
$^2K_{13/2} \rightarrow$ $^4I_{15/2}$	302	0.0032	0.0029	0.0152	0.03	167		1.00	5.99

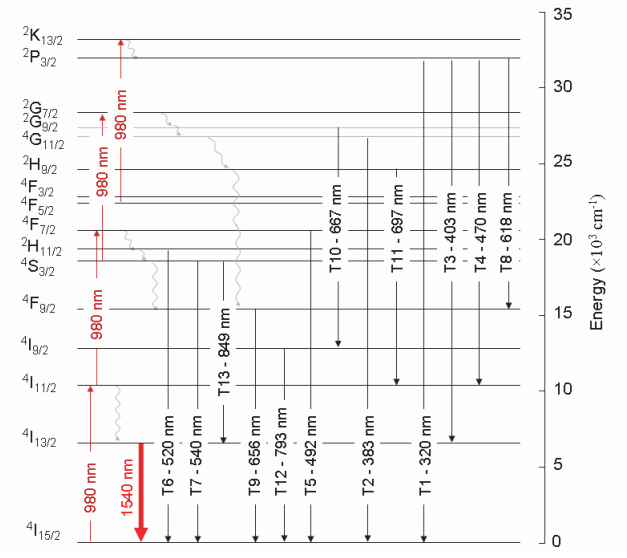

Fig. 6. Erbium energy level diagram with radiative (solid lines) and non-radiative transitions. The thick, red line at 1540 nm indicates the C-band lasing transition.

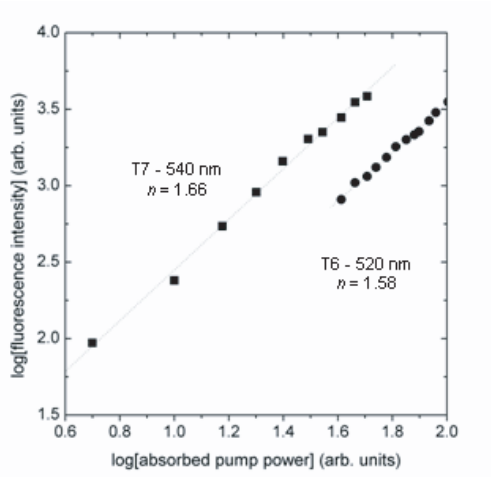

Fig. 7. Intensity dependence of 70 μm diameter Er^{3+}:ZBLALiP microsphere green emissions T6 and T7.

at 383 nm (T2) and the 492 nm emission (T5) have been reported under 973 nm excitation [33].

Notably, we have also observed emissions about 700 nm (T11). Previous Er^{3+} emission at 700 nm has been attributed to the transition $^4F_{7/2} \rightarrow {}^4I_{13/2}$ following absorption of three pump photons at 1480 nm [34]. This seems unlikely in our case, since the JO theory suggests that a 492 nm emission would be more probable than a 700 nm emission from $^4F_{7/2}$. We presume this assignment was on the basis of the 3-photon resonance $^4F_{7/2} \rightarrow {}^4I_{15/2}$. As an alternative, we propose this emission follows the transition $^2H_{9/2} \rightarrow {}^4I_{11/2}$, which is in better agreement with the energy gap between the levels and the JO theory. Finally, we have observed emissions centred at 618 nm (T8) and 667 nm (T10) that have not been observed elsewhere for 980 nm pumping of Er.

5 Conclusions

In conclusion, we have demonstrated a multiwavelength microsphere light source for microphotonic applications [35] fabricated using Er^{3+}:ZBLALiP and we have identified the Er^{3+} transitions involved in the material through a combination of Judd-Ofelt analysis, the erbium energy level diagram and the published centre wavelengths. Upconversion emissions from 320 nm to 849 nm and 1550 nm lasing have been observed. We propose that a number of the upconversion transitions are attributable to 3- and 4-photon processes, in contrast to previous observations for erbium-doped glasses. This is due to the long erbium lifetimes within Er^{3+}:ZBLALiP that favour higher order photon absorptions and, consequently, emissions in the UV at 320 nm have been observed. These results indicate that Er^{3+}:ZBLALiP is an attractive alternative to Er^{3+}:ZBLAN for information-storage applications where even very small powers are sufficient for data retrieval operations [16] and its improved stability [7] promises easier fabrication of devices using ZBLALiP such as erbium doped fibres, microspheres and optical switches. Future work will focus on using integrated optics for the device based on waveguide technology [36] that will enable us to improve the detection efficiency for the upconversion spectrum.

This work is funded by Science Foundation Ireland under grant 02/IN1/128. D. O'Shea acknowledges generous support from IRCSET through the Embark Initiative.

References

1. L. Collot, V. Lefèvre-Sequin, M. Brune, J.M. Raimond, S. Haroche, Europhys. Lett. **23**, 327 (1993)
2. H. Mabuchi, H.J. Kimble, Opt. Lett. **19**, 749 (1994)
3. W. von Klitzing, E. Jahier, R. Long, F. Lissillour, V. Lefèvre-Seguin, J. Hare, J.-M. Raimond, S. Haroche, J. Opt. B **2**, 204 (2000)
4. M. Cai, G. Hunziker, K.J. Vahala, IEEE Photon. Technol. Lett. **6**, 686 (1999)
5. T. Bilici, S. Isci, A. Kurt, A. Serpengüzel, IEEE Photon. Technol. Lett. **16**, 476 (2004)
6. F. Lissillour, D. Messager, G. Stéphan G.P. Féron, Opt. Lett. **26**, 1051 (2001)
7. M. Mortier, P. Goldner, P. Féron, G.M. Stephan, H. Xu, Z. Cai, J. Non-Cryst. Sol. **326**&**327**, 505 (2003)
8. M.-F. Joubert, Opt. Mat. **11**, 181 (1999)
9. H. Fujiwara H.K. Sasaki, J. Appl. Phys. **86**, 2385 (1999)
10. H. Fujiwara, K. Sasaki, Jpn. J. Appl. Phys. **41**, L46 (2002)
11. M. Cai, O. Painter, K.J. Vahala, Opt. Lett. **25**, 1430 (2000)
12. X. Peng, F. Song, S. Jiang, N. Peyghambarian, M. Kuwata-Gonokami, L. Xu, Appl. Phys. Lett. **82**, 1497 (2003)
13. J. Wu, S. Jiang, T. Qua, M. Kuwata-Gonokami, N. Peyghambarian, Appl. Phys. Lett. **87**, 211118 (2005)

14. D.S. Funk, J.G. Eden, IEEE J. Sel. Top. Quant. Elec. **1**, 784 (1995)
15. A. Florez, Y. Messaddeq, O.L. Malta, M.A. Aegerter, J. Alloys Comp. **227**, 135 (1995)
16. C.L. Pope, B.R. Reddy, S.K. Nash-Stevenson, Opt. Lett. **22**, 295 (1997)
17. F. Lissilour, P. Féron, N. Dubreuil, P. Dupriez, G.M. Stéphan, M. Poulain, Proc. SPIE **3611**, 199 (1999)
18. J.P. van der Ziel, F.W. Ostermayer, L.G. van Uitert, Phys. Rev. B **2**, 4432 (1970)
19. R. Rolli, M. Montagna, A. Chiasera, G.C. Righini, S. Pelli, A. Jha, V.K. Tikhomirov, S.A. Tikhomirova, A. Monteil, S. Chaussedent, M. Ferrari, Phil. Mag. B **82**, 573 (2002)
20. T. Catunda, L.A.O. Nunes, A. Florez, Y. Messaddeq, M.A. Aegerter, Phys. Rev. B **53**, 6065 (1996)
21. M.D. Shinn, W.A. Sibley, M.G. Drexhage, R.N. Brown, Phys. Rev. B **27**, 6635 (1983)
22. J.M. Ward, D.G. O'Shea, B.J. Shortt, M.J. Morrissey, K. Deasy, S.G. Nic Chormaic, Rev. Sci. Instrum. **77**, 083105 (2006)
23. J.C. Knight, G. Cheung, F. Jacques, T.A. Birks, Opt. Lett. **22**, 1129 (1997)
24. C. Florea, K.A. Winick, J. Lightwave, Technol. **17**, 1593 (1999)
25. R.M. Martin, R.S. Quimby, J. Opt. Soc. B **23**, 1770 (2006)
26. S.R. Bullock, B.R. Reddy, P. Venkateswarlu, S.K. Nash-Stevenson, J.C. Fajardo, Opt. Quant. Electron. **29**, 83 (1997)
27. M.J. Weber, Phys. Rev. **157**, 262 (1967)
28. W.T. Carnall, P.R. Fields, K. Rajnak, J. Chem. Phys. **49**, 4424 (1968)
29. P.W. France, M.G. Drexhage, J.M. Parker, M.W. Moore, S.F. Carter, J.V. Wright, *Fluoride Glass Optical Fibres* (CRC Press Inc., Florida, 1990)
30. L.F. Johnson, J.E. Geusic, H.J. Guggenheim, T. Kushida, S. Singh, L.G. van Uitert, Appl. Phys. Lett. **15**, 48 (1969)
31. H. Xu, Z. Jiang, Phys. Rev. B **66**, 035103-1 (2002)
32. F. Vetrone, J.-C. Boyer, J.A. Capobianco, A. Speghini, M. Bettinelli, Appl. Phys. Lett. **80**, 1752 (2002)
33. A. Biswas, G.S. Maciel, C.S. Friend, P.N. Prasad, J. Non-Cryst. Sol. **316**, 393 (2003)
34. S. Arahira, K. Watanabe, K. Shinozaki K.Y. Ogawa, Opt. Lett. **17**, 1679 (1992)
35. B.E. Little, J.-P. Laine, D.R. Lim, H.A. Haus, Opt. Lett. **25**, 73 (2000)
36. S. Kobayashi, Proc. SPIE **2997**, 264 (1997)

To access this journal online:
www.edpsciences.org

Appendix D

An All Fibre-Coupled Multicolor Microspherical Light Source

An All-Fiber Coupled Multicolor Microspherical Light Source

Danny G. O'Shea, Jonathan M. Ward, Brian J. Shortt, and Síle Nic Chormaic

Abstract—**We present results on the realization of an all-taper coupled, multicolor microspherical light source fabricated from the erbium doped fluoride glass ZBLALiP. Whispering gallery mode lasing and fluorescent emissions at multiple wavelengths from the ultraviolet to the infrared have been observed. A tapered fiber is used to both launch 980 nm pump light into the microresonator cavity and to collect the resulting infrared lasing. A separate half-taper fiber is used to outcouple the upconversion spectrum over several hundred nanometers. A number of discrete emissions from 400 nm to 850 nm have been observed in the upconversion spectrum, indicating the suitability of this scheme as a miniature device with a 450 nm wide band and reasonable output coupling efficiency.**

Index Terms—**Microsphere resonator, whispering gallery modes, erbium doped fluoride glass, upconversion processes.**

I. Introduction

In recent years, much effort has been devoted to the exploitation of upconversion mechanisms in rare-earth doped materials to yield a range of wavelengths from the near infrared to the ultraviolet. The spectral properties of the resulting fluorescence and/or lasing depends on the choice of dopant and the host matrix in which it is embedded. The vast majority of work on activated glass deals with bulk samples, waveguides and - to a lesser extent - microcavities. One class of microcavity which displays very interesting optical properties is the microspherical resonator. These miniature resonators exhibit whispering gallery modes (WGMs) and are appealing for applications such as laser engineering [1], [2], bio-sensors [3] and optical switches [4] due to their small size of several tens of microns in diameter, ultrahigh quality factors ($Q \sim 10^{10}$) and small mode volumes.

Several methods have been demonstrated for coupling pump light into microcavities, including adiabatic single-mode tapered fibers [5] and prisms [6]. Traditionally, the fluorescence from rare-earth doped microcavities has been collected by free-space coupling of the scattered radiation into an optical spectrometer. While the pump taper can also be used to outcouple lasing emissions from the microcavity, it has been known for some time that it is not possible to use it to simultaneously outcouple the lasing *and* UV to near-IR fluorescence emissions over a broad range of wavelengths because phase matching cannot be maintained [7]. Furthermore, the fabrication of adiabatic, multimode fiber tapers is not possible [8], making pumping and light collection over hundreds of nm using a single taper fiber unrealistic.

In this letter, we report on a new scheme for the realization of an all-taper coupled, multiwavelength light source fabricated from the fluoride glass, ZBLALiP, doped with 0.2 mol% erbium [9]. The suitability of fluoride glass as a rare-earth host material has long been known, [10] as the low phonon energies determine multiphonon relaxation rates and, ultimately, the efficiency of upconversion processes. We have observed upconversion emissions from the near ultraviolet to the infrared using this scheme. We compare these results to those obtained using the traditional approach, whereby the scattered emissions from the microsphere are detected using a spectrometer [11]. We believe that the use of a multimode fiber taper to outcouple the upconversion spectrum over several hundred nanometers will offer improved functionality for these devices and the range of colors emitted will render these devices suitable for evanescent wave sensing.

II. Experimental Setup and Results

Our microspheres are made using a microwave plasma torch [12], which uses a mixture of argon and oxygen or nitrogen. The Er:ZBLALiP glass is crushed into a powder and is axially injected through the plasma flame. The glass melts on passing through the flame and surface tension gives the spheres their spherical shape. Free spheres are formed and collected several tens of cm beneath the torch. The diameter of the spheres produced varies between 10 μm and 200 μm and is largely dependent on powder size.

The basic experimental setup is shown in Fig. 1. We use a single mode, 980 nm laser diode pump with a spectral width of 1 nm in continuous operating mode. A fiber-optic isolator is inserted after the pump laser in order to avoid feedback from reflections. An adiabatic taper fiber, fabricated from 1550 nm SMF28, is used to couple the 980 nm pump light into and out of the microsphere. The same fiber is used to collect the 1550

Manuscript received May 4, 2007. This work was funded in part by Science Foundation Ireland under grant 02/IN1/128 and IRCSET through the Embark Initiative RS/2005/156.

D. G. O'Shea, J. M. Ward, and B. J. Shortt are with the Dept. of Applied Physics and Instrumentation, Cork Institute of Technology, Cork, Ireland and Tyndall National Institute, Prospect Row, Cork, Ireland (e-mail: jonathan.ward@cit.ie).

S. Nic Chormaic is with the Physics Dept., University College Cork and Tyndall National Institute, Cork, Ireland (e-mail: s.nicchormaic@ucc.ie).

nm lasing signal. The taper has a diameter of 1 μm and a transmission loss of less than 0.1 dB/cm. The lasing signal is separated from the pump using a 980/1550 WDM. The separation between the microsphere and the taper is controlled using a piezoelectric precision stage and the alignment is optimized by moving the microsphere to different locations along the taper until the microsphere emission spectrum at 1550 nm is maximized on an optical spectrum analyzer (OSA). The transmission through the pump fiber is also monitored during alignment and, typically, 10-15% of the pump light is coupled into the microsphere. This relatively low coupling efficiency is, in part, due to the broad spectral nature of the pump laser relative to the WGM resonances of the microsphere and could be improved by the use of a narrow linewidth pump source [5].

Characteristic whispering gallery mode bands about the sphere equator are routinely observed by the eye with the aid of a CCD camera attached to a TV monitor. Fig. 2 shows the recorded lasing spectrum of a single microsphere with a diameter of 70 μm. It can be seen that each group of modes contains four distinct lasing peaks, due to the probable excitation of multiple polar modes in the sphere. The peak power of the lasing peaks is ~ 30 nW, although we have observed lasing in a single mode with a peak value of ~ 500 nW. The spacing between the TE and TM modes is about 6.8 nm. The loaded cavity Q-factor for this system is determined to be 1 x 10^7 and is measured as the width of a resonance at a pump wavelength of 780 nm.

In our work we have devised a new scheme for detecting the upconversion spectrum emitted from the microspheres. For this we use a half-taper fiber, located on the microsphere equator diametrically opposed to the pump fiber taper, as depicted in Fig. 3, and coupled into the optical spectrometer. This second fiber is non-adiabatic and fabricated from multimode fiber (Thorlabs AFS50/125Y), with a taper waist of 2 μm at the point of contact with the microsphere. The advantage of the two-taper system over other schemes is that we have a method of simultaneously monitoring the lasing emissions at 1550 nm via the pump taper and the upconversion emissions via the half-taper. This technique allows us to study the competition between these two processes and provides a miniature device for ease of integration into optical setups.

The Er:ZBLALiP upconversion spectrum for a 980 nm pumped, 65 μm microsphere, measured using the standard scattering technique and the half-taper scheme is shown in Fig. 4. Note that Fig. 4 is obtained by joining two separate spectra together. This is necessary due to the limited dynamic linear range of the optical spectrometer used and in order to maximize the signal-to-noise ratio of the lower intensity transitions. The scattered spectrum (Fig. 4(a)) is collected by placing a probe with a 500 μm diameter core about 100 μm from the microsphere. On the other hand, a 2 μm diameter tapered fiber with an initial core diameter of 50 μm is used to collect the spectrum in Fig. 4(b). Most transitions observable using the standard procedure (Fig. 4(a)) are reproduced using our half-taper approach (Fig. 4(b)), thereby indicating its suitability for such measurements. We also reduced the integration time for the spectra around the green by a factor of 40 and this enabled us to observe an additional emission in the ultraviolet at 320 nm for an erbium-doped material [11].

In total, thirteen discrete peaks, labeled T1-T13, have been identified in Fig. 4(a), for approximately 700 μW of 980 nm pump light coupled into the microsphere. There is some loss in the outcoupling detection efficiency using the half-taper technique due to a lower ideality [13] and this results in the weak emissions T1 and T5 not being resolved in Fig. 4(b). Both spectra in Fig. 4 have been corrected for the responsivity of the spectrometer detector as a function of wavelength. The total power outcoupled and detected in the taper spectrum is 27 pW for the green transitions (T6 and T7) and 7 pW for T13, with corresponding values for the scattering spectrum of 0.5 nW and 0.1 nW respectively. The limited resolution of the spectrometer combined with the smaller FSR of the microsphere at shorter wavelengths means that the WGM structure is only visible for emissions at wavelengths longer than about 800 nm. The mode structure for the 849 nm (T13) emission is distinguishable and shown in the inset to Fig. 4.

Our results demonstrate a broad range of emission from 320 nm to 849 nm and illustrate the suitability of using a half-taper, multimode fiber for detecting the majority of these emissions. The cavity Q-factor for our system is reasonably high and, combined with the low WGM mode volume of approximately 2000 μm^3, serves to enhance the probability of excited state absorption occurring within the erbium ions. This is reflected by the fact that a large number of the observed transitions are likely the result of 3-photon and 4-photon absorption events for a relatively modest pump power (sub mW) coupled into the microsphere [11]. It is important to note that the upconversion emissions cannot be detected using the pump taper, since the 980 nm signal overwhelms the weak fluorescence emissions. This problem is overcome by the use of the second taper, since any 980 nm signal coupled into the cavity is completely absorbed by the Er^{3+} ions and, therefore, no pump signal is coupled into the second taper.

III. Conclusion

We have demonstrated a new scheme for detecting broad spectrum emissions from an erbium-doped microsphere resonator. The use of a half-taper, multimode fiber to collect the emission spectrum over a 450 nm span has been compared to the more traditional approach of observing the scattered emissions directly using an optical spectrometer. The advantage of our scheme is the ease of integration of the all-fiber coupled device and will increase the range of applications for these microresonators. We have also extended the range and increased the number of observable transitions for erbium-doped microresonators, having observed thirteen discrete fluorescence emissions from the ultraviolet to the near infrared, in addition to the infrared lasing around 1550 nm. The trade-off of lower outcoupling efficiency is an acceptable

compromise for the simplicity of this technique to outcouple a broad range of wavelengths. This device could find many uses as a miniature all-fiber-coupled, multicolor light source with, for example, application to evanescent wave sensing based on the excitation of transitions in target molecules adsorbed on the microsphere surface and other microphotonic applications [14]. Our results for the violet emissions in Er:ZBLALiP indicate an attractive alternative to Er:ZBLAN for information storage applications, where shorter wavelengths are desirable and even very small powers are sufficient for data retrieval operations [15]. This all-fiber coupling scheme should also be applicable to other types of WGM resonators such as microrings, microdisks and microtoroids.

ACKNOWLEDGMENT

The authors wish to acknowledge generous assistance from P. Féron and L. Ghisa, ENSSAT, France for providing the microspheres.

REFERENCES

[1] V. Sandoghdar, F. Treussart, J. Hare, V. Lefevre-Seguin, J. M. Raimond, and S. Haroch, "Very low threshold whispering-gallery-mode microsphere laser," *Phys. Rev. A*, vol. 54, pp. 1777-1780, Sep. 1996.

[2] K. Kieu and M. Mansuripur, "Self-locked excitation scheme for microsphere resonators, " *IEEE Photon. Technol. Lett.*, vol. 19, pp. 100-102, Jan. 2007.

[3] F. Vollmer, S. Arnold, D. Braun, I. Teraoka, and A. Libchaber, "Multiplexed DNA quantification by spectroscopic shift of two microsphere cavities," *Biophys. J.*, vol. 85, pp. 1974-1979, Sep. 2003.

[4] H. C. Tapalian, J.-P. Laine, and P. A. Lane, "Thermooptical switches using coated microsphere resonators," *IEEE Photon, Technol. Lett.*, vol. 14, pp. 1118-1120, Aug. 2002.

[5] J. C. Knight, G. Cheung, F. Jacques, and T. A. Birks, "Phase-matched excitation of whispering-gallery-mode resonances by a fiber taper," *Opt. Lett.*, vol. 22, pp. 1129-1131, Aug. 1997.

[6] M. L. Gorodetsky and V. S. Ilchenko, "High-Q optical whispering-gallery microresonators: precession approach for spherical mode analysis and emission patterns with prism couplers," *Opt. Commun.*, vol. 113, pp. 133-143, Dec. 1994.

[7] T. Carmon, S. Y. Wang, E. P. Ostby, and K. J. Vahala, "Wavelength-independent coupler from fiber to an on-chip cavity, emonstrated over an 850 nm span", *Opt. Express*, vol. 15, 7677-7681, Jun, 2007.

[8] T. Pagnot and C. Pierali, "Fabrication of multimode fiber tapers with a high reproducibility of the subwavelength extremity size: application to scanning near-field optical microscope probes," *Opt. Comm.*, vol. 132, pp. 161-169, Nov. 1996.

[9] M. Mortier, P. Goldner, P. Féron, G. M. Stephan, H. Xu, and Z. Cai, "New fluoride glasses for laser applicatons," *J. Non-Crys. Sol.*, vols. 326&327, pp. 505-509, Oct. 2003.

[10] D. S. Funk and J. G. Eden, "Glass-fiber lasers in the ultraviolet and visible," *IEEE J. Sel. Topics Quantum Electron.*, vol. 1, pp. 784-791, Sep. 1995.

[11] D. G. O'Shea, J. M. Ward, B. J. Shortt, M. Mortier, P. Féron, and S. Nic Chormaic, "Upconversion channels in Er3+:ZBLALiP fluoride glass microspheres", *Eur. Phys. J. Appl. Phys.*, submitted for publication.

[12] P. Féron "Whispering gallery modes as laser sources- a short review," in *Quaderni di optica e fotonica, special issue: Photonics & Optoelectronics*, Winter School, Trento, 2001.

[13] S. M. Spillane, T. J. Kippenberg, O. J. Painter, and K. J. Vahala, "Ideality in a fiber-taper-coupled microresonator system for application to cavity quantum electrodynamics", *Phys. Rev. Lett.*, vol. 91, pp. 043902-1-4, Jul. 2003.

[14] B. E. Little, J.-P. Laine, D. R. Lim, H. A. Haus, L. C. Kimerling, and S. T. Chu, "Pedestal antiresonant reflecting waveguides for robust coupling to microsphere resonators and for microphotonic circuits," *Opt. Lett.* vol. 25, pp. 73-75, Jan. 2000.

[15] C. L. Pope, B. R. Reddy, and S. K. Nash-Stevenson, "Efficient violet upconversion signal from a fluoride fiber doped with erbium," *Opt. Lett.* vol. 22, pp. 295-297, Mar. 1997.

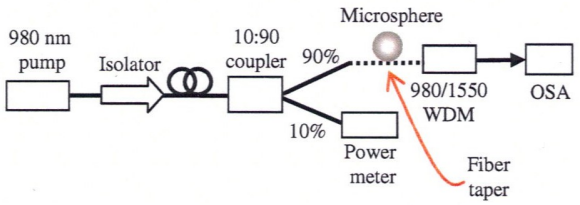

Fig. 1. Experimental setup showing a single fiber taper used for incoupling and outcoupling the 980 nm pump. This fiber is also used to outcouple the lasing emissions around 1550 nm.

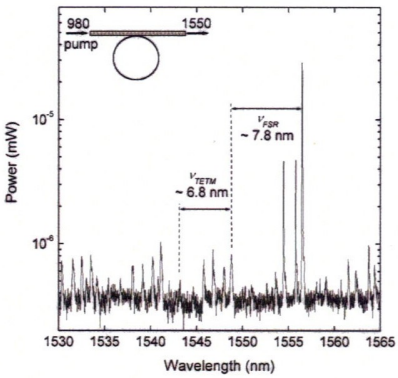

Fig. 2. Lasing spectrum for a 70 μm diameter microsphere, pumped using a 980 nm diode laser. The inset shows the fiber taper arrangement used to outcouple the lasing emissions around 1550 nm.

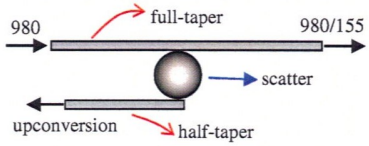

Fig. 3. The all-taper outcoupling scheme. A half-taper fiber is used to outcouple the upconversion spectrum simultaneously with the lasing emissions at 1550 nm. The scattered light from the microsphere can also be detected using an optical spectrometer.

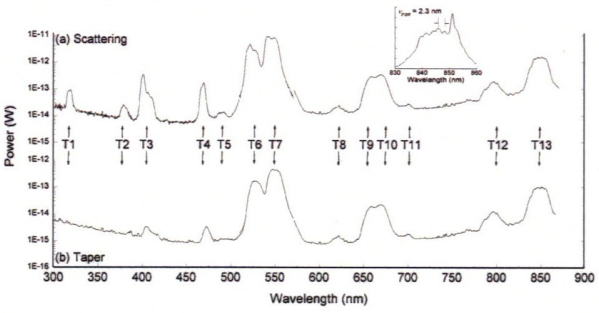

Fig. 4. Er:ZBLALiP microsphere upconversion spectrum using (a) scattering into an optical spectrometer and (b) the half-fiber taper coupling into an optical spectrometer. The spectrometer integration time is reduced by a factor of 40 for the green transitions, T6 and T7. Inset: whispering gallery mode structure about T13.

Appendix E

Optical Bistability in Er-Yb co-doped phosphate glass microspheres at room temperature

Optical bistability in Er-Yb codoped phosphate glass microspheres at room temperature

Jonathan M. Ward[a)]
Department of Applied Physics and Instrumentation, Cork Institute of Technology, Bishopstown, Cork, Ireland
and Photonics Centre, Tyndall National Institute, Prospect Row, Cork, Ireland

Danny G. O'Shea
Physics Department, University College Cork, Ireland
and Photonics Centre, Tyndall National Institute, Prospect Row, Cork, Ireland

Brian J. Shortt
Department of Applied Physics and Instrumentation, Cork Institute of Technology, Bishopstown, Cork, Ireland
and Photonics Centre, Tyndall National Institute, Prospect Row, Cork, Ireland

Síle Nic Chormaic
Physics Department, University College Cork, Ireland
and Photonics Centre, Tyndall National Institute, Prospect Row, Cork, Ireland

(Received 15 February 2007; accepted 31 May 2007; published online 20 July 2007)

We experimentally demonstrate optical bistability in Er^{3+}-Yb^{3+} phosphate glass microspheres at 295 K. Bistability is associated with both Er^{3+} fluorescence and lasing behavior, and chromatic switching. The chromatic switching results from an intrinsic mechanism exploiting the thermal coupling of closely spaced energy levels, and occurs simultaneously with the intensity switching. A contrast ratio of 2.8 has been obtained for chromatic switching. The intensity switching shows ratios of 21 for 520 nm and 11 for 660 nm fluorescence emissions, and 11 for IR lasing at 1.5 μm. Concurrent with these observations, we investigate a temperature-dependent absorption of pump power, which exhibits bistable behavior. The influences of the host matrix on lasing and fluorescence mechanisms are highlighted. © *2007 American Institute of Physics*.
[DOI: 10.1063/1.2753591]

I. INTRODUCTION

Optical bistability (OB) in a sodium vapor was reported by Gibbs in 1976[1] and, since then, numerous other materials exhibiting the phenomenon have been studied, including Yb^{3+} doped glasses and crystals, and semiconductors.[2–8] The mechanisms responsible for nonlinearity in glasses and crystals are varied, with many requiring cryogenic temperatures (typically <40 K) to maintain the necessary low atomic decay rates in Yb^{3+} dimer and monomer systems.[3] Alternative and more easily achievable mechanisms include photon avalanche and thermal avalanche,[2,5] suggesting that a wider range of materials can exhibit OB at room temperature and above. However, no evidence of OB through these mechanisms in this temperature range has yet been observed. Bistable sensitized luminescence in Er-Yb:$CsCdBr_3$ was shown by Redmond and Rand,[3] and, subsequently, by Ródenas *et al.*[4] in a Nd-Yb codoped crystal. They also described *chromatic switching* in addition to the more traditional *intensity switching*, though both mechanisms required temperatures well below room temperature. In chromatic switching, the wavelengths of light emitted from an optically pumped sample change abruptly as a function of pump power. In contrast, for intensity switching, the output intensity at any particular wavelength changes abruptly as a function of pump power. To date, OB has also been predicted and observed in Yb^{3+} doped oxide crystals, Cr-doped $LiSrGaF_6$ and $LiSrAlF_6$ crystals,[5] Sm^{3+} doped glass microspheres,[6] and Tm^{3+}-Yb^{3+} codoped glass.[7] The later system exhibited multiple hysteresis loops in the fluorescence intensity at room temperature.

The interest in studying micron-sized spherical cavities stems from the potential they offer as components for experiments ranging from the very applied realization of all-optical networks to fundamental quantum optics experiments, whereby the microspheres can be used as ultrahigh Q cavities for measurements based on the principles of cavity quantum electrodynamics.[9] Such microcavities can be either active or passive depending on the material used. For example, a sphere doped with the triply ionized rare-earth ions Er^{3+} can yield fluorescence emissions ranging from UV to IR through various upconversion mechanisms,[10,11] due to the close proximity of the numerous energy levels in the ion. Microcavities that exhibit optical bistability are interesting for generating optical switches for all-optical computing, and miniature C-band laser sources are important for telecommunications applications.[12] These factors have resulted in significant research focusing on the characterization of microcavities in recent years.

The concept of an Er^{3+}-Yb^{3+} codoped glass laser was demonstrated[13] in 1965 as a means of optimizing the Er^{3+}

[a)]Electronic mail: Jonathan.ward@cit.ie

 © 2007 American Institute of Physics

Downloaded 13 Nov 2007 to 134.93.129.164. Redistribution subject to AIP license or copyright, see http://jap.aip.org/jap/copyright.jsp

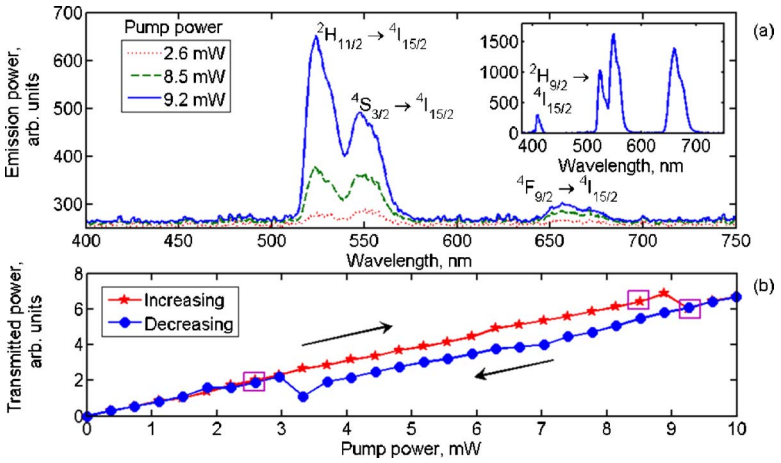

FIG. 1. (Color online) (a) Upconversion fluorescence spectrum for three different pump powers in a 50-μm-diam IOG-2 microsphere. The inset shows an additional weak violet emission from a 35-μm-diam microsphere, observable when no lasing emission at 1.5 μm is present and for a pump power of 8 mW. The violet emission has been scaled up by a factor of 5 for clarity. The ratio of the emission powers from the $^2H_{11/2}$ to $^4S_{3/2}$ levels for a pump power of 9.2 mW is 1.34. (b) Transmitted power past the taper-sphere junction for the 50 μm sphere as shown in (a). The three spectra in (a) correspond with the three highlighted data points (□) in (b).

emission cross section while simultaneously ensuring an optimum Yb^{3+} absorption cross section.[14] This overlap alleviates the difficulty of trying to directly pump the narrow Er^{3+} absorption band. Phosphate glass has been investigated as a host matrix for rare-earth ions due to its favorable properties, such as (i) the possibility of obtaining large dopant concentrations (up to 1.8×10^{21} ions/cm^3 for Yb^{3+}, and $\sim10^{19}$ ions/cm^3 for Er^{3+}) compared to silicate, borate, and fluoride glasses, (ii) its large absorption band in the near-infrared region, (iii) its large emission cross section at 1.5 μm, and (iv) the low back energy transfer from Er^{3+} ions to Yb^{3+} ions.[15–17] The spectral characteristics are also especially beneficial for C-band lasing; the intermediate lasing level $^4I_{11/2}$ has a high nonradiative relaxation rate (<1 μs lifetime, maximum phonon energy of 1300 cm^{-1}) to the $^4I_{13/2}$ level compared with silica (maximum phonon energy of 1190 cm^{-1}), and the long lifetime of the $^4I_{13/2}$ level of about 8.45 ms facilitates population inversion and high gain.[12] The larger phonon energy of phosphate glass has a negative effect on the upconversion efficiency compared to fluoride glass (with a maximum phonon energy of 600 cm^{-1}). This, however, is counterbalanced by the large dopant concentrations and wide absorption cross section of the Yb^{3+} sensitizer. In addition, phosphate glass has better optomechanical properties compared to other glasses used for OB, such as $CsCdBr_3$.

Here, we report on the simultaneous observation of chromatic and intensity OB in phosphate glass (Schott IOG-2) at room temperature. We present experimental results on lasing around 1550 nm and propose suitable upconversion mechanisms for the observed three color emission bands. Optical bistability previously demonstrated in passive silica[9,18] and silicon[8] resonators was attributed to nonlinearities arising from the Kerr effect or thermo-optic effect of the resonance line, together with high Q factors ($Q>10^8$) and a tunable, narrow linewidth laser. The results presented here clearly show that IOG-2 microspheres exhibit bistable switching behavior under vastly different conditions; we use microspheres with relatively high loaded cavity Q's typically 1×10^7, and the pump laser has a linewidth of 1 nm and is not locked to individual cavity resonances. For clarity, our results are organized in two sections: fluorescence and lasing emissions are discussed in Sec. III, and the results of the OB measurements are discussed in Sec. IV.

II. EXPERIMENT

The IOG-2 glass used is doped with 2 wt % Er_2O_3 (1.7×10^{20} ions/cm^3) and codoped with 3 wt % Yb_2O_3 (2.5×10^{20} ions/cm^3). We study lasing and upconversion fluorescent emissions following CW pumping with a tunable 980 nm laser diode (spectral width ~1 nm). IOG-2 glass, with a low glass transition temperature of around 648 K,[19] is ideal for producing microspheres with diameters of between 30 and 70–μm using a microwave plasma torch.[20] A detailed description of our experimental approach has been published elsewhere.[21] Efficient coupling of the pump into the microsphere is attained by using adiabatically tapered fibers fabricated using a direct heating technique.[22] We use a 1-μm-diam, 1550 nm SMF-28 fiber with a typical transmission loss of 0.1 dB/cm. The alignment of taper and microsphere is optimized by adjusting the relative positions of the two, while maximizing the 1550 nm emissions. These lasing emissions are monitored by connecting one end of the fiber taper to an optical spectrum analyzer. During alignment we also monitor the transmission through the fiber and, typically, 10%–15% of the pump light is coupled into the microsphere. All upconversion fluorescence spectra were acquired by free space coupling into an Ocean Optics 2000 spectrometer.

III. LASING AND FLUORESCENCE IN IOG- 2

In our first experiments, we changed the 980 nm pump power from 0 to 10 mW and observed a clear change in the visible emission spectra obtained, as shown in Fig. 1(a) for powers of 2.6 mW, 8.5 mW, and 9.2 mW. These results were obtained for a 50-μm-diam sphere and the chromatic switching behavior is clearly evident at room temperature, by the change in the ratio of the emissions at different wavelengths for the different pump powers. We note three distinct emission bands corresponding to erbium transitions at 520 nm ($^2H_{11/2}\rightarrow{}^4I_{15/2}$), 550 nm ($^4S_{3/2}\rightarrow{}^4I_{15/2}$), and 660 nm ($^4F_{9/2}\rightarrow{}^4I_{15/2}$). The red emission is stronger than red emissions produced in other singly doped glasses investigated in our laboratory, such as Er:ZBLALiP and Er:ZBNA, due to the much larger Yb^{3+} absorption cross section compared to Er^{3+}. One would expect the slope of the fluorescence to exhibit a simple power law dependence, $I_{\text{emission}}\propto I^a_{\text{excitation}}$, where a is the number of pump photons required to produce each emit-

Downloaded 13 Nov 2007 to 134.93.129.164. Redistribution subject to AIP license or copyright, see http://jap.aip.org/jap/copyright.jsp

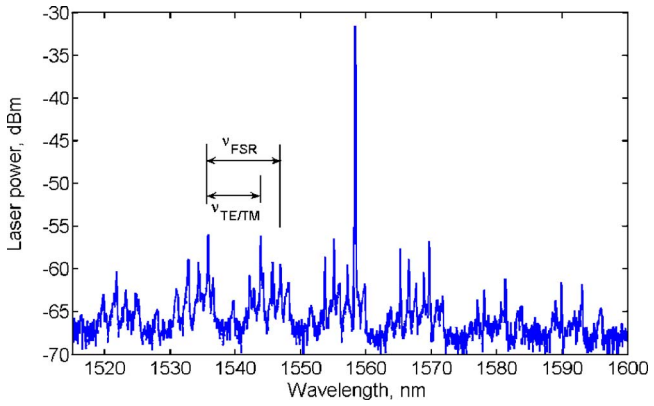

FIG. 2. (Color online) Lasing spectrum and whispering gallery mode structure for a 50-μm-diam IOG-2 microsphere (same as for Fig. 1).

ted photon, thus reflecting the multiphoton nature of the upconversion process. However, this law fails in the presence of OB, as will be shown in Sec. IV. Note that, on occasion, we have also observed a very weak, but distinct, fourth emission band in the UV corresponding to an erbium transition at 405 nm ($^2H_{9/2} \rightarrow {}^4I_{15/2}$). The inset in Fig. 1(a) shows a fluorescence spectrum representing the UV to IR upconversions for a fixed pump power of 8 mW and a 35 μm sphere. Such UV emissions are only observed in spheres that do not lase around 1550 nm, due to a competition between processes involved. We have also monitored the power transmitted past the taper-sphere junction as a function of launched pump power into the fiber taper. This dependency is presented in Fig. 1(b) as the pump power is varied from 0 to 10 mW and back to 0. These measurements allow us to estimate the coupling efficiency of light into the sphere as a function of pump power.

Figure 2 shows the observed IR lasing spectrum around 1550 nm, for the same 50-μm-diam IOG-2 sphere as in Fig. 1, and 10 mW of pump power launched into the fiber taper. A single lasing peak and fluorescing whispering gallery modes are evident. Analysis of the whispering gallery modes in the fluorescence spectrum enables us to measure the free spectral range ν_{FSR} of the sphere modes to be 1.40 THz ($\equiv$11.1 nm). Hence, we can calculate the microsphere diameter using $D=c/(\pi N \nu_{FSR})$, where c is the speed of light in vacuum and N is the refractive index of the material. The refractive index of IOG-2 at room temperature is 1.508 at 1540 nm, yielding a sphere diameter of 45 μm. This agrees reasonably well with an optical microscope measurement of 50±2 μm. The measured spacing between TE and TM modes of 8.05 nm around 1540 nm agrees well with the calculated value of 8.40 nm. This microsphere has a peak lasing emission of 700 nW for a launched pump power of ~10 mW and, in general, we record lasing thresholds of less than 1 mW.

For ions excited to the $^2F_{5/2}$ level in Yb^{3+}, IOG-2 has a quantum efficiency, $\eta=\lambda_{pump}/\lambda_{laser}$, of about 60%–80%, resulting in the remaining 20%–40% being dissipated in the host matrix as heat. The $^2H_{11/2}$ level and the $^4S_{3/2}$ level can be considered to be in quasithermal equilibrium since the energy gap is ~740 cm^{-1},[23] comparable to the maximum phonon energy of 1300 cm^{-1} for phosphate glass.[12] As such,

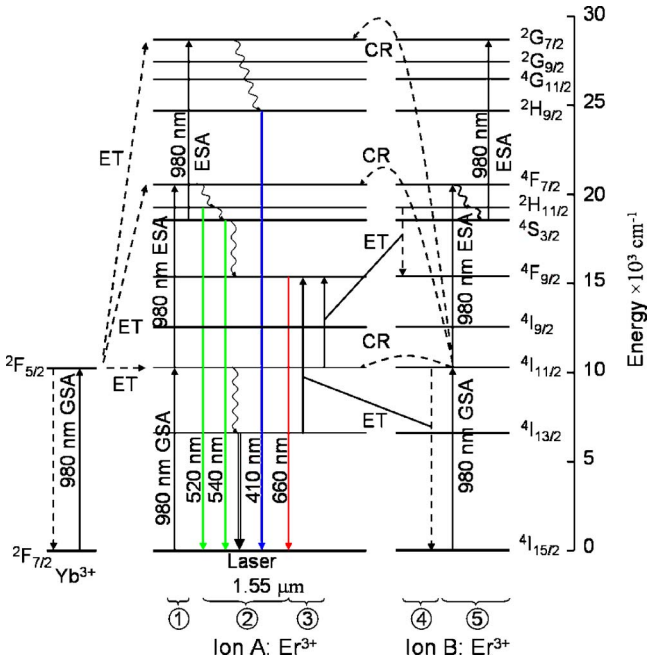

FIG. 3. (Color online) Energy level diagram and fluorescence mechanisms with radiative (solid lines) and nonradiative transitions (wiggly lines). (①) Upconversion based on GSA and ESA in ion A only; (②) radiative and nonradiative decays; (③ and ④) energy transfer processes from ion A to ion B populating the $^4F_{9/2}$ level in ion A; (⑤) GSA and ESA in ion B; (CR) cross relaxation; (ET) energy Transfer; (GSA) ground state absorption; (ESA) excited state absorption.

only one phonon is required to bridge the energy difference between the two green levels, thereby populating the $^2H_{11/2}$ level at room temperature. The thermalization of the $^2H_{11/2}$ level by the $^4S_{3/2}$ level has a temperature-dependent effect on the ratio of the radiative emissions from these two levels as well as the excited state lifetimes.[23] The multiphonon stimulated emission rate between these levels at a temperature T is[24]

$$K_{mp}(T) = K_{mp}(0)\left[1 - \exp\left(-\frac{\hbar\omega}{k_B T}\right)\right]^{-p}, \quad (1)$$

where k_B is Boltzmann's constant, ω is the phonon frequency, and p is the number of phonons required to bridge the energy gap ΔE between the levels and is given by $\Delta E/\hbar\omega$, where $\hbar\omega$ is the phonon energy. For Er-Yb codoped glasses, K_{mp}(295 K) is typically of the order of 10^{11} s^{-1}, which is significantly higher than the value of 10^3 s^{-1} reported for radiative emissions,[24] indicating that the multiphonon decay is dominant. The energy difference between the $^4S_{3/2}$ level and the next lowest level $^4F_{9/2}$, requires three phonons, therefore making this level far less likely to be populated from the $^4S_{3/2}$ level.

The emissions detected from the IOG-2 microsphere, as shown in Figs. 1 and 2, are due to upconversion processes involving multiple pump laser photons and/or lattice phonons. Two upconversion mechanisms which must be considered when trying to understand the origin of the fluorescence results are excited state absorption (ESA) and energy transfer upconversion (ETU).[23,25] These are shown in the energy level diagram in Fig. 3, in which we identify a number of different groups of transition processes, ①–⑤, that play a

Downloaded 13 Nov 2007 to 134.93.129.164. Redistribution subject to AIP license or copyright, see http://jap.aip.org/jap/copyright.jsp

role in the generation of the emission spectra. The combination of relatively high cavity quality factor (typically 1×10^7) and strongly localized electromagnetic field in the form of a whispering gallery mode (mode volume $\sim3000\ \mu m^3$) serves to significantly enhance the probability that an excited ion will absorb further pump photons.

Transition groups ① and ⑤ in Fig. 3 are associated with the ground state (GSA) and excited state absorptions in a single erbium ion. As mentioned, there is a resonant energy transfer (ET) from the Yb^{3+} sensitizer ($^2F_{5/2}\rightarrow{}^2F_{7/2}$) to the Er^{3+} ion ($^4I_{15/2}\rightarrow{}^4I_{11/2}$) followed by 980 nm ESA from the $^4I_{11/2}$ level to the $^4F_{7/2}$ level indicated in group ①. Transition group ② deals with the radiative and nonradiative decay processes for a single erbium ion. For example, rapid, nonradiative relaxation from $^4I_{11/2}$ to $^4I_{13/2}$ is possible and falls within this group. In spite of a large energy mismatch of about 1450 cm^{-1} for the $^4I_{13/2}\rightarrow{}^4F_{9/2}$ transition, the long lifetime of the $^4I_{13/2}$ state and associated large population ensures that the ETU mechanism is adequately efficient.[23,26] Due to the close spacing of the $^4F_{7/2}$ and $^4S_{3/2}$ levels, the population of $^4F_{7/2}$ readily decays nonradiatively to the $^4S_{3/2}$ level, whereby the thermal mechanism described previously populates the $^2H_{11/2}$ level. Finally, a second ESA from the $^4S_{3/2}$ level up to the $^2G_{7/2}$ level is followed by nonradiative relaxation down to the $^2H_{9/2}$ level and the subsequent radiative decay to the ground state generates a photon at 410 nm (violet).

At the high concentrations of Er^{3+} and Yb^{3+} in this work the inter ion separation reaches a critically small radius of ~3 nm for Er^{3+} ions and ~2 nm for Yb^{3+} ions. This is close to the value of 2.12 nm for Yb^{3+}-Yb^{3+} ET's and an estimated 1.5–2.0 nm for Yb^{3+}-Er^{3+} ET's as determined from the Förster-Dexter theory,[27,28] dramatically enhancing the probability of Yb^{3+}-Yb^{3+}, Yb^{3+}-Er^{3+} and, presumably, Er^{3+}-Er^{3+} energy transfers. The critical radius R_{sx} is determined by the overlap of the emission and absorption cross sections and is given by

$$R_{sx}^6=\frac{3c\tau_s}{8\pi^4n^2}\int\sigma_{ems}^s(\lambda)\sigma_{abs}^x(\lambda)d\lambda, \tag{2}$$

where c is the velocity of the photons, $\tau_s=1.4$ ms is the fluorescence decay time of the unperturbed sensitizer, n is the refractive index, σ_{ems} is the emission cross section, and σ_{abs} is the absorption cross section. The emission and absorption cross sections are shown in Fig. 4, and are determined from measurements with a bulk sample of IOG-2. The ion s stands for the sensitizer, i.e., the Yb^{3+} ions, and the ion x stands for either the sensitizer or the Er^{3+} acceptor ions. For nonradiative dipole-dipole interactions the energy transfer rate rapidly increases according to the inverse of the ion separation to the sixth power.

A further group ② transition deals with red emissions from a single erbium ion. However, the strength of the observed red emission cannot be wholly explained by multiphonon relaxation from the $^4S_{3/2}$ level to the $^4F_{9/2}$ level, due to the low relaxation rate. Notwithstanding the ESA process already mentioned, two ETU cross-relaxation channels can explain the strength of the red emission relative to the green emissions and the associated processes are indicated by transition groups ③ and ④ in Fig. 3. The first ETU is via $^4I_{11/2}(B)+{}^4I_{13/2}(A)\rightarrow{}^4I_{15/2}(B)+{}^4F_{9/2}(A)$ and the second channel is via $^2H_{11/2}(B)+{}^4I_{11/2}(A)\rightarrow{}^4F_{9/2}(B)+{}^4F_{9/2}(A)$, where A and B denote the two erbium ions involved. Therefore, ions are removed from the green levels and transferred to the red $^4F_{9/2}$ level. The two possible cross-relaxation processes feeding the $^4F_{9/2}$ level deplete the intermediate $^4I_{11/2}$ level and the metastable $^4I_{13/2}$ level, thereby placing the 1.5 μm emission in competition with the red emission and the other upconversion processes. We find that the power of the red emission is, typically, twice as high in microspheres that exhibit no lasing (due to excessive inhomogeneities in the cavity) compared to those that exhibit lasing.

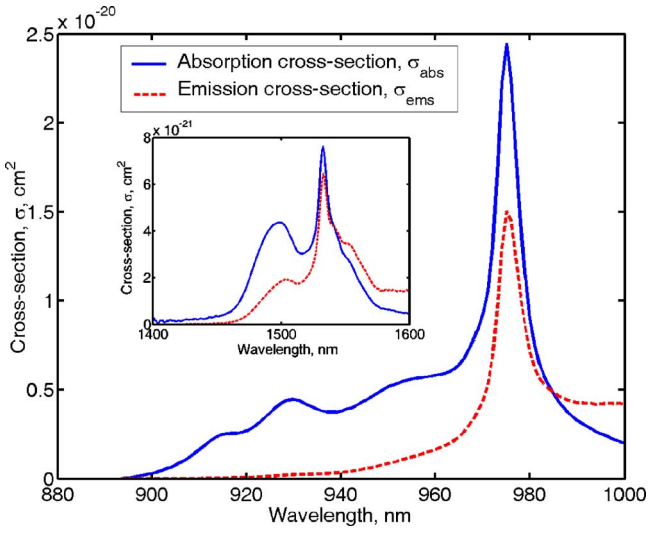

FIG. 4. (Color online) Absorption and emission cross sections for Er^{3+}-Yb^{3+} codoped IOG-2 bulk glass.

IV. RESULTS AND DISCUSSION

A. Intensity switching

In order to study the optical bistability of the microspheres we measured the emission intensity as a function of launched pump power for a single sphere at three different emission wavelengths: 520 nm (green), 660 nm (red), and 1550 nm (IR). The pump power was increased from 0 to 10 mW and back to 0, while recording the fluorescence emission intensities [Fig. 5(a)]. These measurements were taken simultaneously to the transmitted pump power shown in Fig. 1(b). As the launched pump power was increased the emission intensities remained almost constant until a critical power of 8.5 mW was reached [cf. Fig. 5(a)], beyond which a sudden and dramatic rise in emission intensity was observed. Increasing the pump power beyond the critical point caused the emission to level out once more. A subsequent reduction in pump power clearly demonstrates hysteretic behavior and a wide bistable region, where the emission can have two intensity values depending on the history of the input power. The sudden jumps (or intensity switching) between the higher and lower branches of the hysteresis loops are characteristic of the optical bistability of the spheres. A bistable response was also observed for the lasing emission in Fig. 5(b) for the same sphere, but in a slightly different

Downloaded 13 Nov 2007 to 134.93.129.164. Redistribution subject to AIP license or copyright, see http://jap.aip.org/jap/copyright.jsp

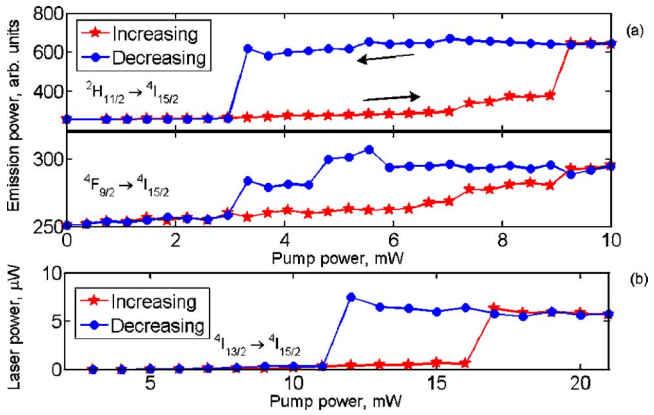

FIG. 5. (Color online) Intensity bistability for green $^2H_{11/2}$ state, red $^4F_{9/2}$ state, and 1.5 μm lasing from the $^4I_{13/2}$ state for a 50-μm-diam sphere. The switching positions for the green and red emissions in (a) differ from the 1.5 μm lasing emission in (b) due to a different setup with a poorer taper-sphere coupling. The corresponding spectra for the visible fluorescence are shown in Fig. 1(a).

experimental setup with the sphere positioned on a different position of the taper. The critical power depends on the taper-sphere coupling efficiency and, hence, differs for the two experiments presented in Fig. 5.

A very promising feature of these microcavity resonators is the high contrast intensity switching observed; the ratio of the relative change in emission powers (defined as the difference between the maximum and minimum powers, divided by the minimum power) is 21 for the green, 11 for the red, and 11 for the IR as determined from Fig. 5. The violet emission is too weak to be considered in these measurements.

B. Chromatic switching

As referred to earlier, the strong temperature dependence in IOG-2 is due to the loss of 20%–40% of the laser power as heat in the glass, in conjunction with its low thermal conductivity. With reference to Fig. 1(b), the sudden dip in transmitted power implies increased pump absorption with an associated increase in the heat generation. In contrast, the sudden increase in transmitted power results in a decrease in heat generation. The increased absorption occurs simultaneously with the sudden rise in the 520 nm ($^2H_{11/2}$) emission intensity as compared to the 550 nm ($^4S_{3/2}$) intensity that was observed when the pump power was increased above the upper switching position of 8.9 mW, as shown in Fig. 1(b). As the pump power was reduced below the lower switching position of 3.3 mW, there was a sudden decrease in intensity ratio due to the drop in pump absorption. Using the methods outlined by Qiao *et al.*,[29] Boltzmann statistics can be used to describe the strong thermal coupling and the population redistribution between the two green levels. The intensity ratio is a function of the internal cavity temperature and is described as[29]

$$\frac{I(^2H_{11/2})}{I(^4S_{3/2})} = \frac{r_H g_H \hbar\omega_H}{r_S g_S \hbar\omega_S} \exp\left(\frac{\Delta E}{k_b T}\right), \tag{3}$$

where I is the integrated emission intensity for a particular level, r is the total spontaneous emission rate, g is the $(2J+1)$ multiplicity (or degeneracy) of each manifold, $\hbar\omega_H(\hbar\omega_S)$ is the energy of level $^4H_{11/2}(^4S_{3/2})$, and ΔE is the energy separation between the levels. According to Eq. (3), as the temperature is increased the $^2H_{11/2}$ level is more efficiently populated and an increasingly larger fraction of the $^4S_{3/2}$ population is rapidly promoted to this upper level and, consequently, the ratio of the emissions from the two states inverts so that the $^2H_{11/2}$ emission becomes stronger. This chromatic switching can yield intensity ratios of up to 2.8 for the integrated power from the 520 nm ($^2H_{11/2}$) and 550 nm ($^4S_{3/2}$) emissions (data not shown). From Eq. (3) this indicates a temperature of 642 K, just below the glass transition value of 648 K.[19] This temperature seems exceptionally high, although there was no evidence of thermal stresses, fracturing of the glass or other defects in the microsphere during these measurements. However, it is important to emphasize that the temperature calculated using this method does not represent the temperature of the entire sphere, but rather the temperature of the mode volume. Heat dissipation from this region through the remainder of the material would account for no evident thermal stress on the sphere itself, which is likely to be at a much lower temperature.

C. Temperature dependence of optical bistability

Previously reported mechanisms for OB in Tm-Yb-doped BaY_2F_8 crystals have suggested that photon avalanche may be a possible mediator, while for silica microspheres the Kerr effect led to OB at 2 K.[30,31] Both these mechanisms are temperature independent. However, other mechanisms such as the thermo-optic effect,[8,18] nonlinear upconversion and energy transfer rates,[32,33] and thermal avalanche[2] are temperature dependent. In order to gain a further understanding on the mechanisms involved, the temperature dependence of the OB was examined by placing a platinum heater and thermocouple close to the microsphere and heating it to around 345 K. The pump power transmitted past the taper-sphere junction was recorded at the same time as the microsphere emissions, while cycling the pump power from low to high and back again as shown in Fig. 6. Comparison of the plots taken at room temperature and at 345 K shows that an increase in external temperature causes the upper knee at 17 mW input power to shift down to 13 mW, while the lower knee at 7 mW only shifts slightly to the right, thereby shortening the bistable region. The pump power was cycled at a slow rate of $\sim$1 mW/min due to the thermal response time of the microsphere. The bistable microsphere emissions are essentially the same as those shown in Fig. 5 except for the different switching positions, and the results shown in Fig. 6 imply that the bistable behavior is a function of temperature.

D. Possible optical bistability mechanisms

In principle, a number of processes may be responsible for the observation of optical bistability, depending on whether the observed effect is temperature dependent or independent. The measurements shown in Fig. 6 indicate clearly that the bistable behavior exhibited by our microspheres is temperature dependent, thereby permitting us to exclude temperature independent processes. Temperature-

Downloaded 13 Nov 2007 to 134.93.129.164. Redistribution subject to AIP license or copyright, see http://jap.aip.org/jap/copyright.jsp

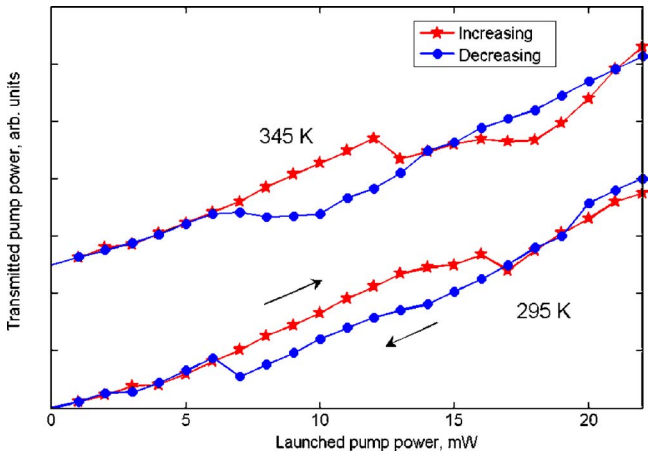

FIG. 6. (Color online) Bistable absorption of pump power at 295 and 345 K for a 50-μm-diam sphere. The data at 345 K has been offset for clarity. As the sphere temperature was increased from 295 K to 345 K, the knee at 17 mW input power shifted to the left, while the lower knee at 7 mW only shifted slightly to the right, thereby shortening the bistable region.

dependent mechanisms that may be responsible include material effects such as (i) strong Yb^{3+}-Yb^{3+} coupling, i.e., nonlinear energy transfer,[32] (ii) nonlinear upconversion rates,[33] and (iii) thermal avalanche,[2] in addition to cavity effects such as (iv) dispersive bistability mediated by the thermo-optic effect.[8,34]

Guillot-Nöel *et al.*[32] have described a mechanism that could be responsible for bistability in the regime of strong Yb^{3+}-Yb^{3+} coupling, in which case cooperative luminescence would be expected. In order to be appreciable, the distance between the ions would need to be of the order of several Å, i.e., significantly smaller than for IOG-2 (21 Å) and, therefore, this effect is unlikely to play a key role. However, if it is present, the luminescence would likely be very weak compared to the single ion Er^{3+} transitions. It is reasonable to assume the back transfer rate is negligible due to the high phonon energy of the host lattice, and is, therefore, unlikely to be the source of nonlinearity in our measurements.

Another possible explanation includes a nonlinear upconversion rate either for Yb^{3+}-Yb^{3+}, Yb^{3+}-Er^{3+}, or Er^{3+}-Er^{3+} energy transfers.[33] This has been observed in high concentration Er^{3+} doped fibers, where the nonlinearity is dependent on population inversion of the lasing levels, and the signal and emission rates. Temperature-dependent effects in the upconversion fluorescence in Er-$YbGa_2S_3$:La_2O_3 chalcogenide glass and germanosilicate optical fibers have been attributed to an exponential increase in the Yb^{3+} absorption cross section elsewhere.[35] However, there have been no reports of bistability relying on these mechanisms.

Thermal avalanche was used to explain bistability in Yb^{3+}-doped bromide lattices by Gamelin *et al.*[2] at cryogenic temperatures. This theory relies on nonlinear absorption in the Yb^{3+} ions with increasing temperature and predicts bistable power absorbance in the microsphere as a function of pump power in the taper, similar to that shown in Fig. 6. As phonons are released into the lattice from Yb^{3+} excited and ground states the temperature increases, thereby increasing absorbance and leading to a further increase in temperature. This cyclic process causes a thermal avalanche for high enough pump power. In order to determine whether thermal avalanche is truly responsible, it would be necessary to perform measurements of the dependence of the Yb^{3+} absorption coefficient and to ascertain whether it is a nonlinear function of internal microsphere temperature above 295 K. However, the results presented in Lei *et al.*[36] for different Yb^{3+}-doped phosphate glasses do not show a suitable nonlinear absorption coefficient necessary for thermal avalanche. This suggests that thermal avalanche theory is also unsuitable to describe the behavior of IOG-2.

We suggest that dispersive bistability[34]—a mechanism commonly used to explain bistability in Fabry-Pérot etalons—can predict our results. The general theory states that as the pump laser frequency is scanned across a high-Q cavity resonance, the cavity intensity rapidly rises, and when the pump frequency moves away from the cavity resonance the cavity intensity rapidly falls. In addition, this description is complicated by the fact that the frequency of the cavity resonance scales approximately linearly with the cavity intensity, leading to a bistable response. In our case, the cavity resonance could be shifted by a temperature-dependent refractive index—the thermo-optic effect—which has a value of $\sim 10^{-6}$/K in phosphate glass.[20] We find that in order to observe bistability the current to the pump laser, and, hence, the pump frequency, need to be adjusted to a precise setting for each sphere. The corollary of this adjustment is the positioning of the laser frequency near a cavity resonance. For the experimental conditions here, a threshold power of about 100 μW in the cavity mode is enough to cause switching—a value which is well below our estimated 10%–15% of pump power coupled into the sphere. Firm evidence of this effect would be possible by probing individual cavity resonances with a narrow linewidth, 980 nm external cavity diode laser, while recording the power transmitted past the taper-sphere coupling junction as described by Rokhsari *et al.*[18]

V. CONCLUSIONS

In conclusion, we have demonstrated a multiwavelength, upconversion, microsphere light source exhibiting optical bistability and we have identified the Er^{3+} transitions and fluorescence mechanisms involved. Factors affecting the dynamics of visible fluorescence and C-band lasing emission have been examined and show that the thermal properties of IOG-2 glass play an important role in the microsphere performance. In particular, the high loss of pump power to the glass as heat, in conjunction with the low thermal conductivity, has a pronounced effect on the green emission from levels $^2H_{11/2}$ and $^4S_{3/2}$. Our calculations show that the close proximity of the ions in our glass greatly enhances the probability of sensitizer-sensitizer and sensitizer-acceptor energy transfers.

We have also reported on the simultaneous observation of chromatic and intensity OB in phosphate glass (Schott IOG-2) at room temperature. These results show that there are two possible temperatures in the bistable region and it is also possible to have two emission intensities for the same excitation power. Chromatic bistability is dependent on the

Downloaded 13 Nov 2007 to 134.93.129.164. Redistribution subject to AIP license or copyright, see http://jap.aip.org/jap/copyright.jsp

presence of intensity bistability due to the energy coupling between the green emitting levels $^2H_{11/2}$ and $^4S_{3/2}$. Therefore the switching positions are the same for both types of bistability. The OB shows high contrast switching ratios. The intensity switching shows ratios of 21 for the green, 11 for the red fluorescence emissions, and 11 for the IR lasing, while the chromatic switching ratios $I(^2H_{11/2})/I(^4S_{3/2})$ are as high as 2.8.

We have found that the switching position is dependent on the microsphere temperature, thereby eliminating intensity-dependent mechanisms such as photon avalanche and the Kerr effect. Our observations may be tentatively explained in terms of dispersive bistability, where the temperature-dependent refractive index of phosphate glass causes the resonant cavity mode and the laser mode to behave nonlinearly, yielding a bistable response. Several other possible mechanisms (strong Yb^{3+}-Yb^{3+} coupling, nonlinear upconversion rates, and thermal avalanche) were examined; however, all are considered unfavorable under our experimental conditions.

Microcavity resonators offer substantial miniaturization, greatly reduced power for switching, and allow for all emissions to be easily fiber coupled. In addition, the improved optomechanical properties of IOG-2 compared to other glasses used for OB, such as $CsCdBr_3$, makes this glass appealing for all-optical logic elements in optical engineering applications.

ACKNOWLEDGMENTS

This work was funded by Science Foundation Ireland under Grant No. 02/IN1/128. The authors gratefully acknowledge P. Féron and L. Ghisa from ENSSAT for providing the IOG-2 microspheres. D.O. S. acknowledges support from the Irish Research Council for Science, Engineering and Technology through the Embark Initiative RS/2005/156.

[1] H. M. Gibbs, S. L. McCall, and T. N. C. Venkatesan, Phys. Rev. Lett. **36**, 1135 (1976).
[2] D. R. Gamelin, S. R. Lüthi, and H. U. Güdel, J. Phys. Chem. B **104**, 11045 (2000).
[3] S. M. Redmond and S. C. Rand, Opt. Lett. **28**, 173 (2003).
[4] A. Ródenas, D. Jaque, and J. García Solé, Phys. Rev. B **74**, 035106 (2006).
[5] M. A. Noginov, M. Vondrova, and B. D. Lucas, Phys. Rev. B **65**, 035112 (2001).
[6] T. Hayakawa, H. Ooishi, and M. Nogami, Opt. Lett. **26**, 84 (2001).
[7] A. Kuditcher, M. P. Hehlen, C. M. Florea, K. W. Winick, and S. C. Rand, Phys. Rev. Lett. **84**, 1898 (2000).
[8] V. R. Almeida and M. Lipson, Opt. Lett. **29**, 2387 (2004).
[9] F. Treussart, J. Hare, L. Collot, V. Lefèvre, D. S. Weiss, V. Sandoghdar, J. M. Raimond, and S. Haroche, Opt. Lett. **19**, 1651 (1994).
[10] G. H. Dieke and H. M. Crosswhite, Appl. Opt. **2**, 675 (1963).
[11] M.-F. Joubert, Opt. Mater. **11**, 181 (1999).
[12] P. Laporta, S. Taccheo, S. Longhi, O. Svelto, and C. Svelto, Opt. Mater. **11**, 269 (1999).
[13] E. Snitzer and R. Woodcock, Appl. Phys. Lett. **6**, 45 (1965).
[14] X. Zou and H. Toratani, Phys. Rev. B **52**, 15889 (1995).
[15] S. Jiang, M. Myers, and N. Peyghambarian, J. Non-Cryst. Solids **239**, 143 (1998).
[16] R. Wu, J. D. Myers, M. J. Myers, and C. Rapp, Proc. SPIE **4968**, 11 (2003).
[17] Z. Yang, Z. Feng, and Z. Jiang, J. Phys. D **38**, 1629 (2005).
[18] H. Rokhsari, S. M. Spillane, and K. J. Vahala, Appl. Phys. Lett. **85**, 3029 (2004).
[19] IOG-2 phosphate laser glass specification sheet, Schott Glass Technologies, 400 York Ave., Duryea, PA 18642, USA.
[20] Z. Cai, A. Chardon, H. Xu, P. Féron, and G. M. Stéphan, Opt. Commun. **203**, 301 (2002).
[21] B. J. Shortt, J. Ward, D. O'Shea, and S. Nic Chormaic, Proc. SPIE **6187**, 618708 (2006).
[22] J. C. Knight, G. Cheung, F. Jacques, and T. A. Birks, Opt. Lett. **22**, 1129 (1997).
[23] J. F. Phillips, T. Töpfer, H. Ebendorff-Heiderpriem, D. Ehrt, and R. Sauerbrey, Appl. Phys. B **72**, 399 (2001).
[24] M. P. Hehlen, N. J. Cockroft, T. R. Gosnell, and A. J. Bruce, Phys. Rev. B **56**, 9302 (1997).
[25] M. J. Weber, Phys. Rev. B **8**, 54 (1973).
[26] M. Ajroud, M. Haouari, H. Ben Ouada, H. Mâaref, A. Brenier, and B. Champagnon, Phys. Status Solidi A **202**, 316 (2005).
[27] T. Förster, Ann. Phys. **437**, 55 (1948).
[28] D. L. Dexter, J. Chem. Phys. **21**, 836 (1953).
[29] X. Qiao, X. Fan, M. Wang, J.-Luc Adam, and X. Zhang, J. Phys.: Condens. Matter **18**, 6937 (2006).
[30] M. A. Noginov, M. Vondrova, and D. Casimir, Phys. Rev. B **68**, 195119 (2003).
[31] F. Treussart, V. S. Ilchenko, J.-F. Roch, J. Hare, V. Lefevre-Seguin, J.-M. Raimond, and S. Haroche, Eur. Phys. J. D **1**, 235 (1998).
[32] O. Guillot-Nöel, L. Binet, and D. Gourier, Phys. Rev. B **65**, 245101 (2002).
[33] B. Jaskorzyńska, S. Sergeyev, M. Świllo, and D. Khoptyar, Acta Phys. Pol. A **99**, 147 (2000).
[34] M. M. Mazumder, S. C. Hill, D. Q. Chowdhury, and R. K. Chang, J. Opt. Soc. Am. B **12**, 297 (1995).
[35] E. A. Gouveia, M. T. de Araujo, and A. S. Gouveia-Neto, Braz. J. Phys. **31**, 89 (2001).
[36] G. Lei, J. E. Anderson, M. I. Buchwald, B. C. Edwards, R. I. Epstein, M. T. Murtagh, and G. H. Seigel, IEEE J. Quantum Electron. **34**, 1839 (1998).

Downloaded 13 Nov 2007 to 134.93.129.164. Redistribution subject to AIP license or copyright, see http://jap.aip.org/jap/copyright.jsp

Appendix F

External Cavity Diode Laser Design Files

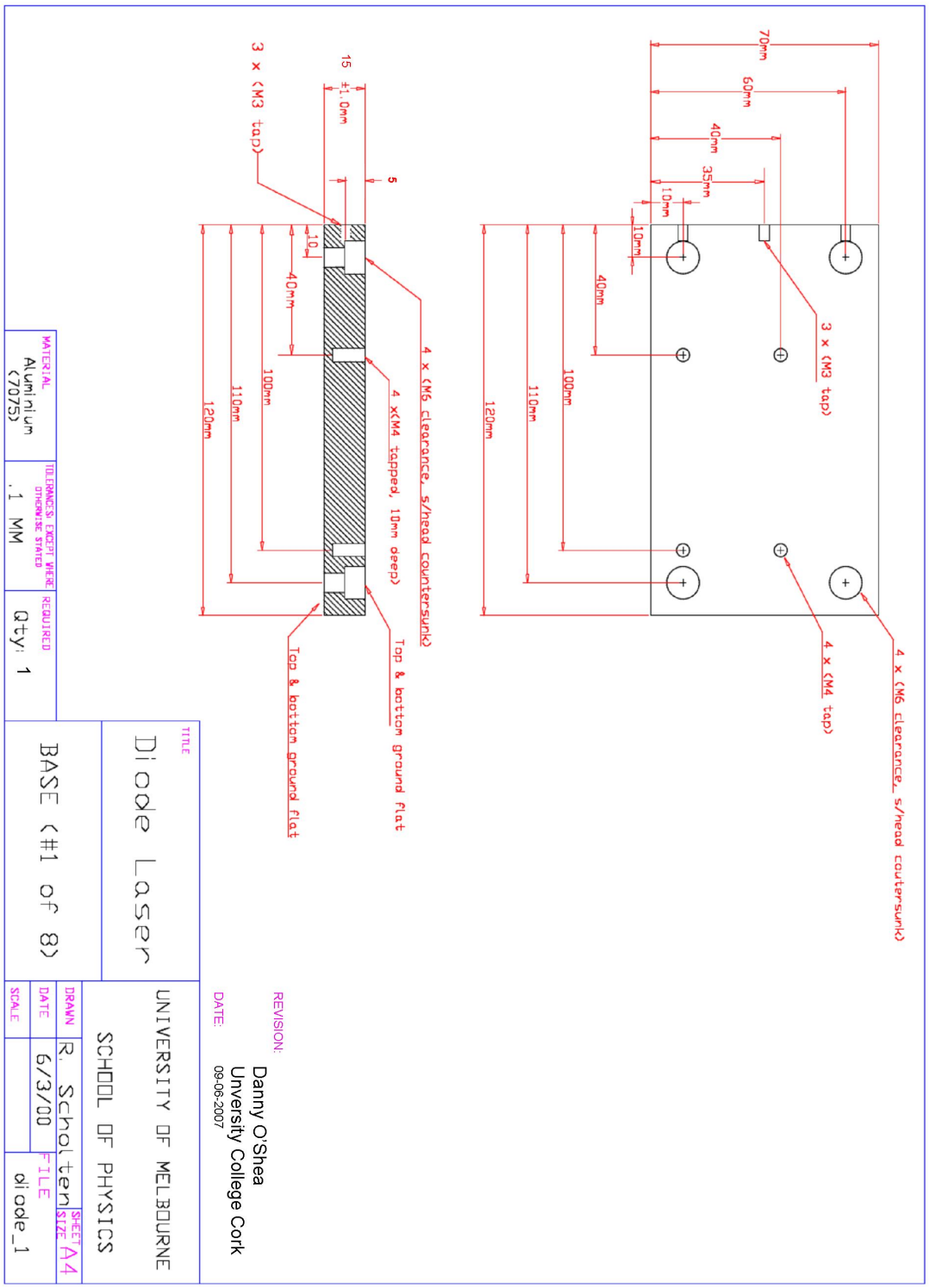
4 x (M6 clearance, s/head countersunk)
4 x (M4 tap)
3 x (M3 tap)
70mm
60mm
40mm
35mm
10mm
10mm
40mm
100mm
110mm
120mm
4 x (M6 clearance, s/head countersunk)
4 x(M4 tapped, 10mm deep)
Top & bottom ground flat
Top & bottom ground flat
3 x (M3 tap)
15 ±1.0mm
5
10
40mm
100mm
110mm
120mm
MATERIAL
Aluminium (7075)
TOLERANCES EXCEPT WHERE OTHERWISE STATED
.1 MM
REQUIRED
Qty: 1
TITLE
Diode Laser
BASE (#1 of 8)
UNIVERSITY OF MELBOURNE
SCHOOL OF PHYSICS
DRAWN
R. Scholten
DATE
6/3/00
SCALE
SHEET SIZE A4
FILE
diode_1
REVISION:
DATE:
Danny O'Shea
University College Cork
09-06-2007

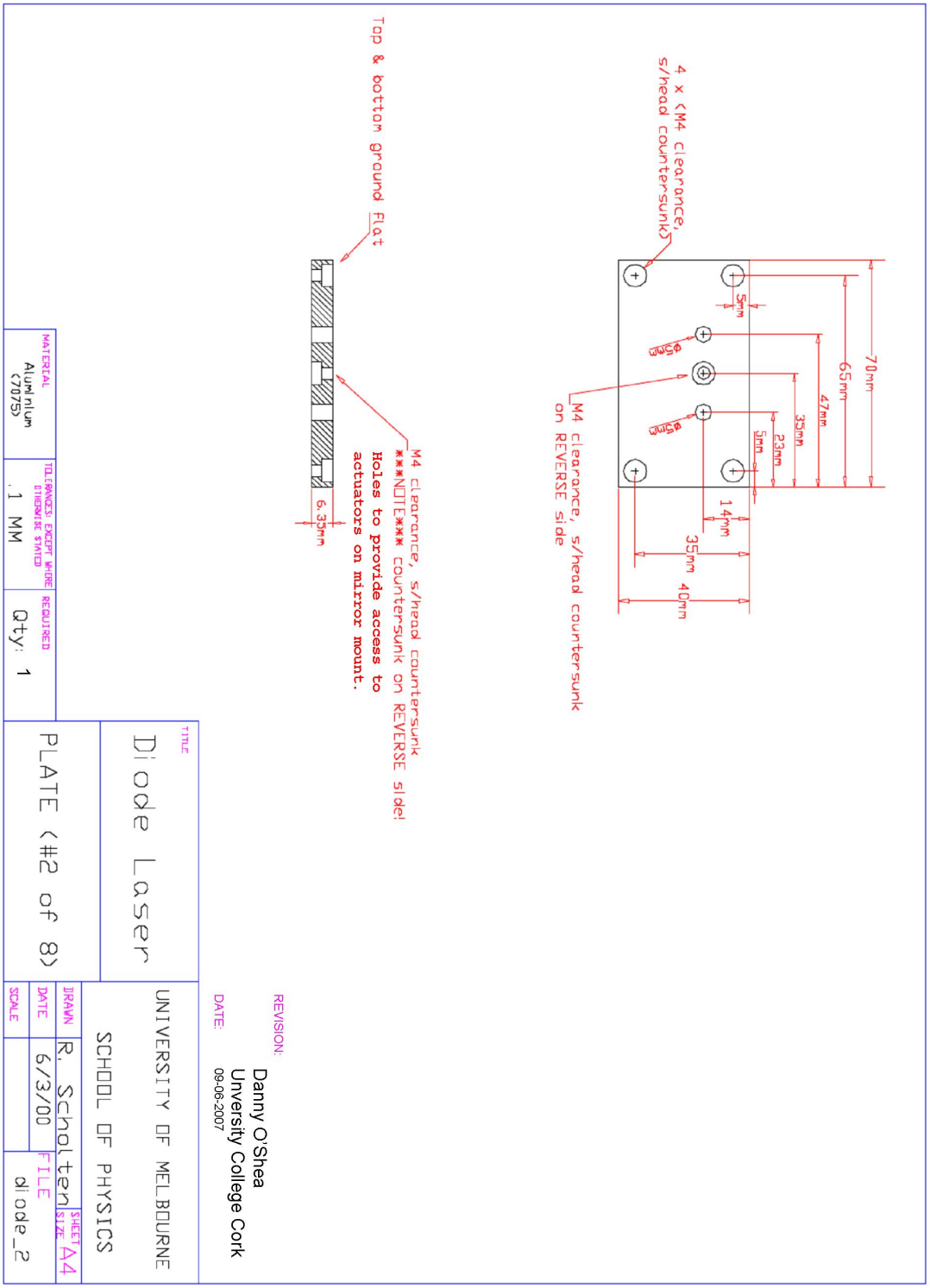
4 x (M4 clearance, s/head countersunk)
M4 clearance, s/head countersunk on REVERSE side
70mm
65mm
47mm
35mm
23mm
5mm
5mm
14mm
35mm
40mm
Top & bottom ground flat
M4 clearance, s/head countersunk
NOTE countersunk on REVERSE side!
Holes to provide access to actuators on mirror mount.
6.35mm
REVISION:
Danny O'Shea
University College Cork
DATE: 09-06-2007
TITLE
Diode Laser
UNIVERSITY OF MELBOURNE
SCHOOL OF PHYSICS
PLATE (#2 of 8)
MATERIAL
Aluminum (7075)
TOLERANCES: EXCEPT WHERE OTHERWISE STATED
.1 MM
REQUIRED
Qty: 1
DRAWN
R. Scholten
DATE
6/3/00
SCALE
SHEET SIZE
A4
FILE
diode_2

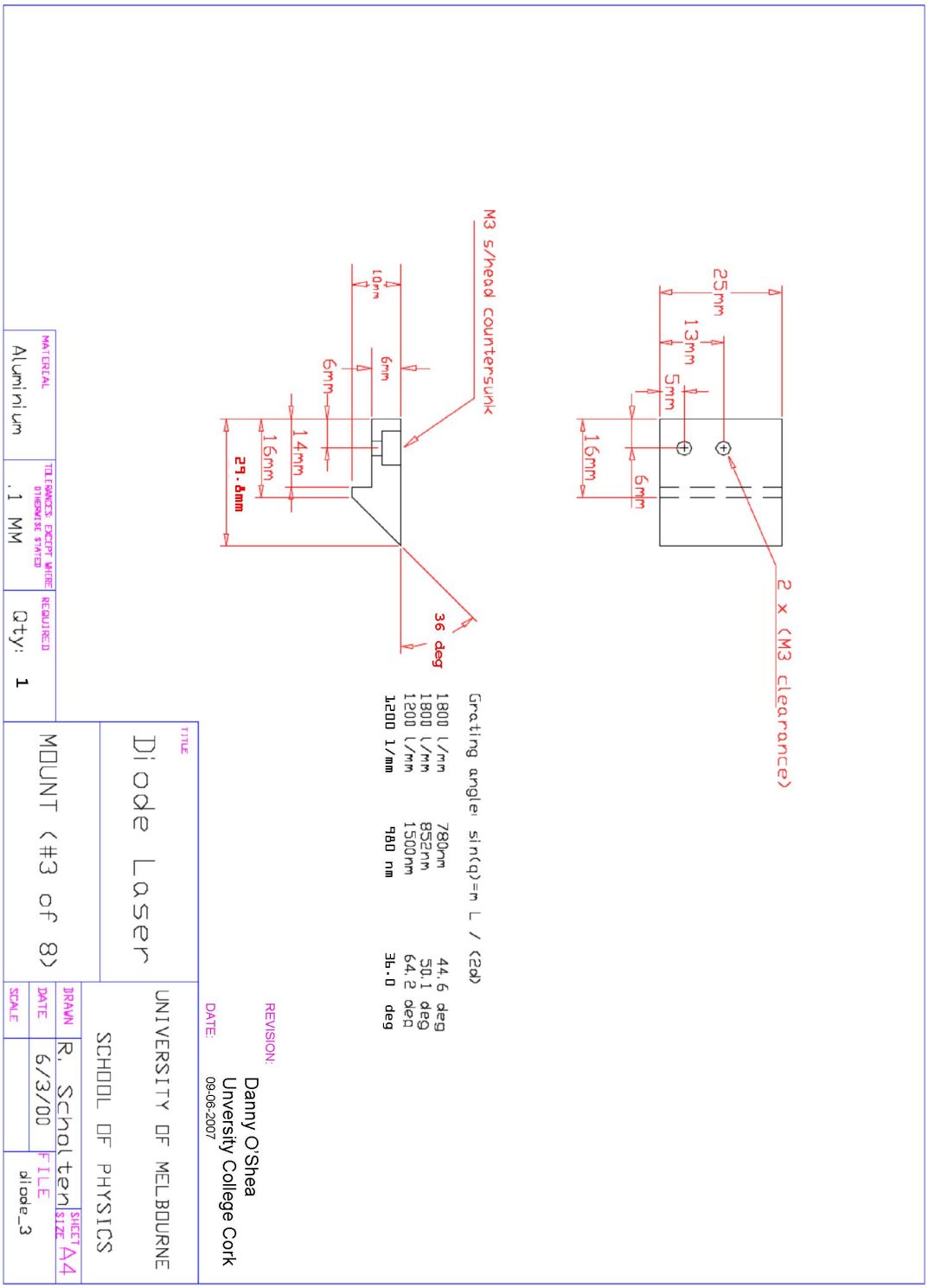
2 x (M3 clearance)
25mm
13mm
5mm
6mm
16mm
M3 s/head countersunk
10mm
6mm
6mm
14mm
16mm
29.8mm
36 deg
Grating angle: sin(a)=m L / (2d)
1800 l/mm 780nm 44.6 deg
1800 l/mm 852nm 50.1 deg
1200 l/mm 1500nm 64.2 deg
1200 l/mm 980 nm 36.0 deg
REVISION:
Danny O'Shea
University College Cork
DATE: 09-06-2007
TITLE
Diode Laser
UNIVERSITY OF MELBOURNE
SCHOOL OF PHYSICS
MOUNT (#3 of 8)
MATERIAL
Aluminium
TOLERANCES: EXCEPT WHERE DIMENSIONS OTHERWISE STATED
.1 MM
REQUIRED
Qty: 1
DRAWN
R. Scholten
DATE
6/3/00
SCALE
SHEET SIZE A4
FILE
diode_3

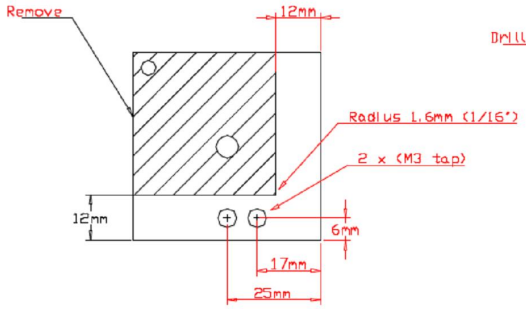

U100-P
Front
Plate
(top view)

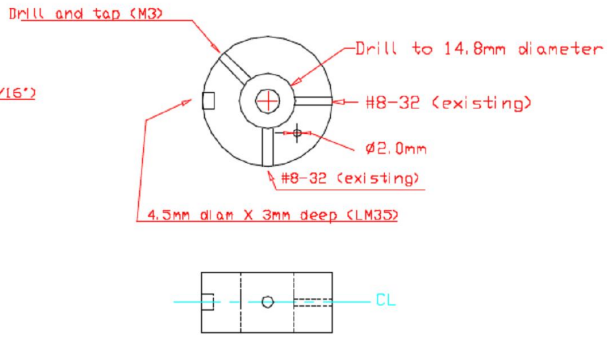

UPA-PA1
Adaptor
(top view)

REVISION:

Danny O'Shea
Unversity College Cork

DATE: 09-06-2007

TITLE: Diode Laser			UNIVERSITY OF MELBOURNE SCHOOL OF PHYSICS
MODS (#4 of 8)		DRAWN: R. Scholten	SHEET SIZE: A4
		DATE: 6/3/00	FILE: diode_4
		SCALE:	
MATERIAL: Provided	TOLERANCES: EXCEPT WHERE OTHERWISE STATED: .1 MM	REQUIRED: Qty: 1	

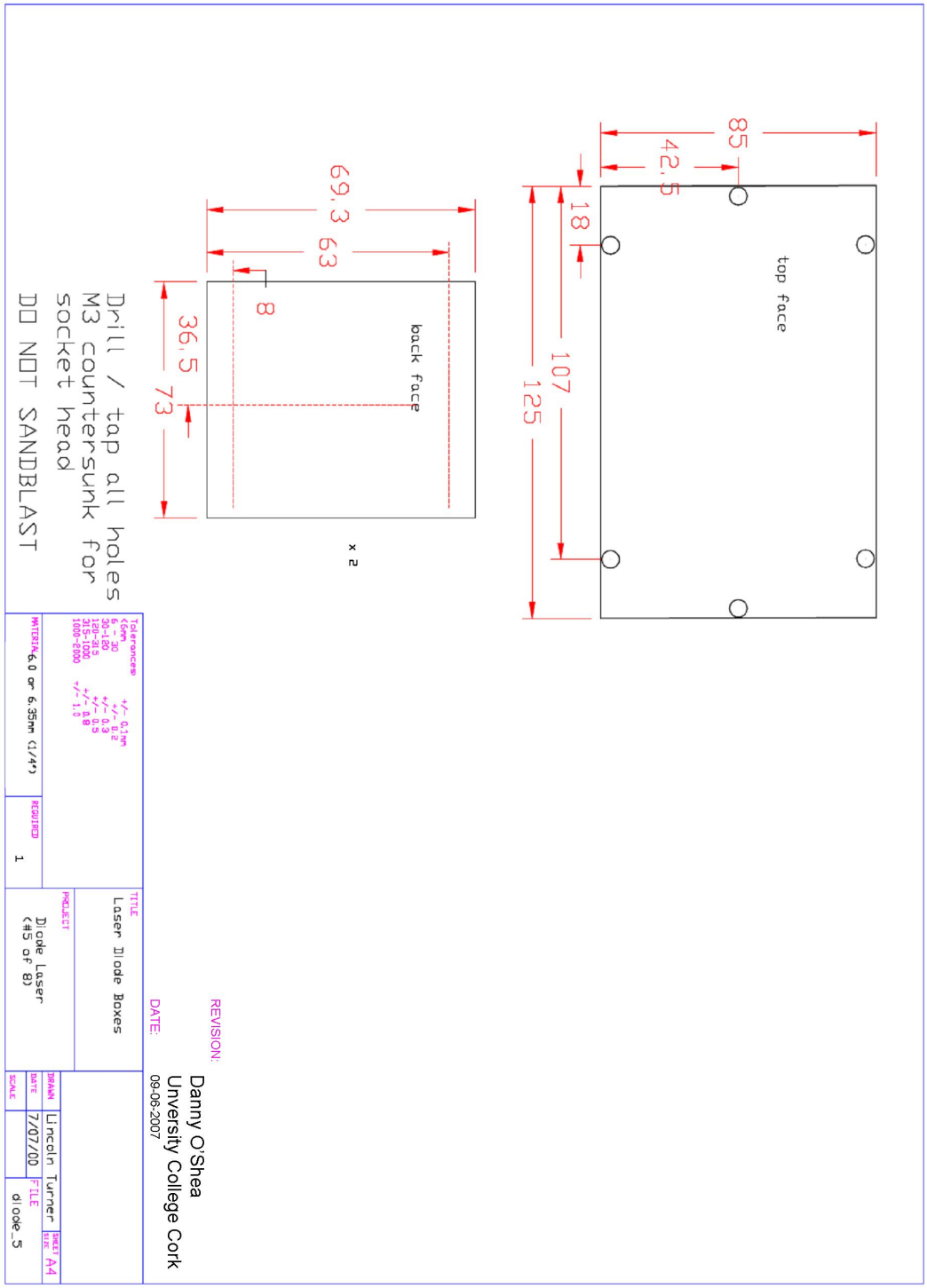
top face
85
42.5
18
107
125
back face
69.3
63
8
36.5
73
x 2
Drill / tap all holes
M3 countersunk for
socket head
DO NOT SANDBLAST
Tolerances
<6mm +/- 0.1mm
6-30 +/- 0.2
30-120 +/- 0.3
120-315 +/- 0.5
315-1000 +/- 0.8
1000-2000 +/- 1.0
MATERIAL 6.0 or 6.35mm (1/4")
REQUIRED 1
TITLE Laser Diode Boxes
PROJECT Diode Laser (#5 of 8)
DRAWN Lincoln Turner
DATE 7/07/00
SCALE
SHEET SIZE A4
FILE diode_5
REVISION:
DATE:
Danny O'Shea
University College Cork
09-06-2007

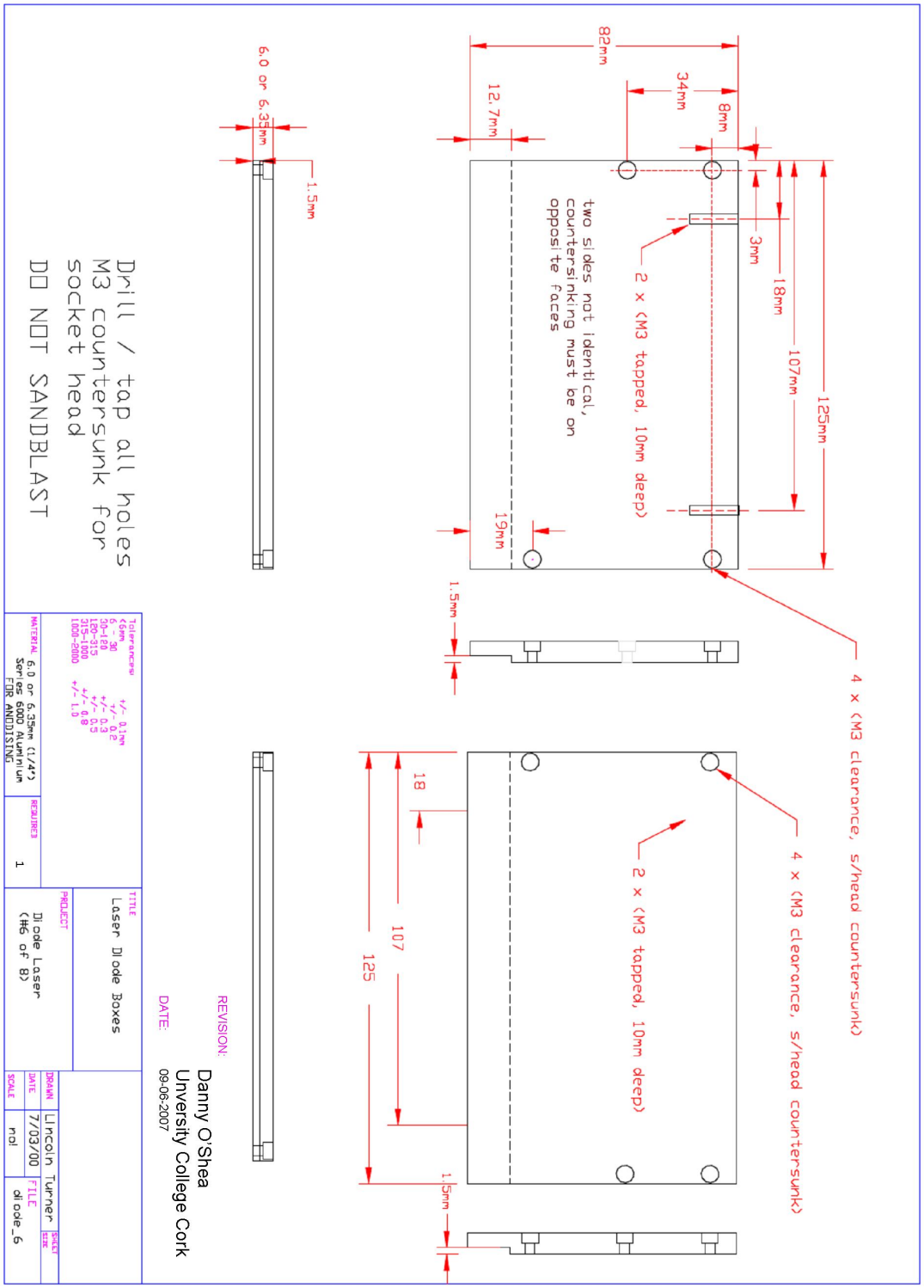
4 x (M3 clearance, s/head countersunk)
4 x (M3 clearance, s/head countersunk)
2 x (M3 tapped, 10mm deep)
2 x (M3 tapped, 10mm deep)
two sides not identical, countersinking must be on opposite faces
125mm
107mm
18mm
3mm
8mm
34mm
82mm
12.7mm
19mm
1.5mm
6.0 or 6.35mm
1.5mm
125
107
18
1.5mm
Drill / tap all holes M3 countersunk for socket head
DO NOT SANDBLAST
Tolerances
0-6mm +/- 0.1mm
6-30 +/- 0.2
30-120 +/- 0.3
120-315 +/- 0.5
315-1000 +/- 0.8
1000-2000 +/- 1.0
MATERIAL 6.0 or 6.35mm (1/4") Series 6000 Aluminium FOR ANODISING
REQUIRED 1
TITLE Laser Diode Boxes
PROJECT Diode Laser (#6 of 8)
DRAWN Lincoln Turner
DATE 7/03/00
SCALE nol
FILE diode_6
REVISION:
DATE: 09-06-2007
Danny O'Shea
University College Cork

Tokin AE0203D04
4mm piezo stack

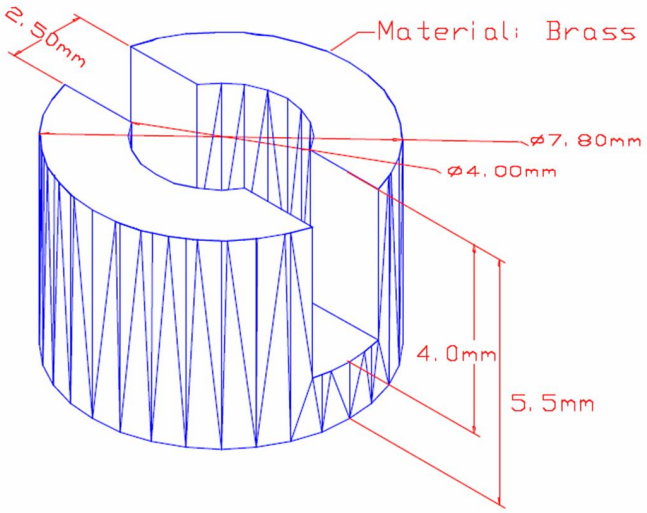

Note: only one (4mm or 8mm) per laser

Tokin AE0203D08
8mm piezo stack

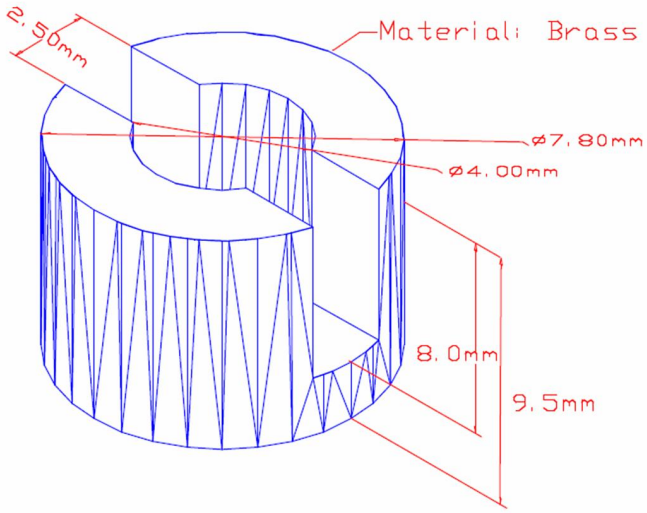

Note: Inside bottom surface must be smooth and flat

MATERIAL: Brass	TOLERANCES: EXCEPT WHERE OTHERWISE STATED: .01 mm	REQUIRED: Qty: 1	TITLE: Diode Laser Piezo support (#7 of 8)

REVISION:
Danny O'Shea
Unversity College Cork
DATE: 09-06-2007

DRAWN	R. Scholten	SHEET SIZE	A4
DATE	6/3/00	FILE	diode_7
SCALE			

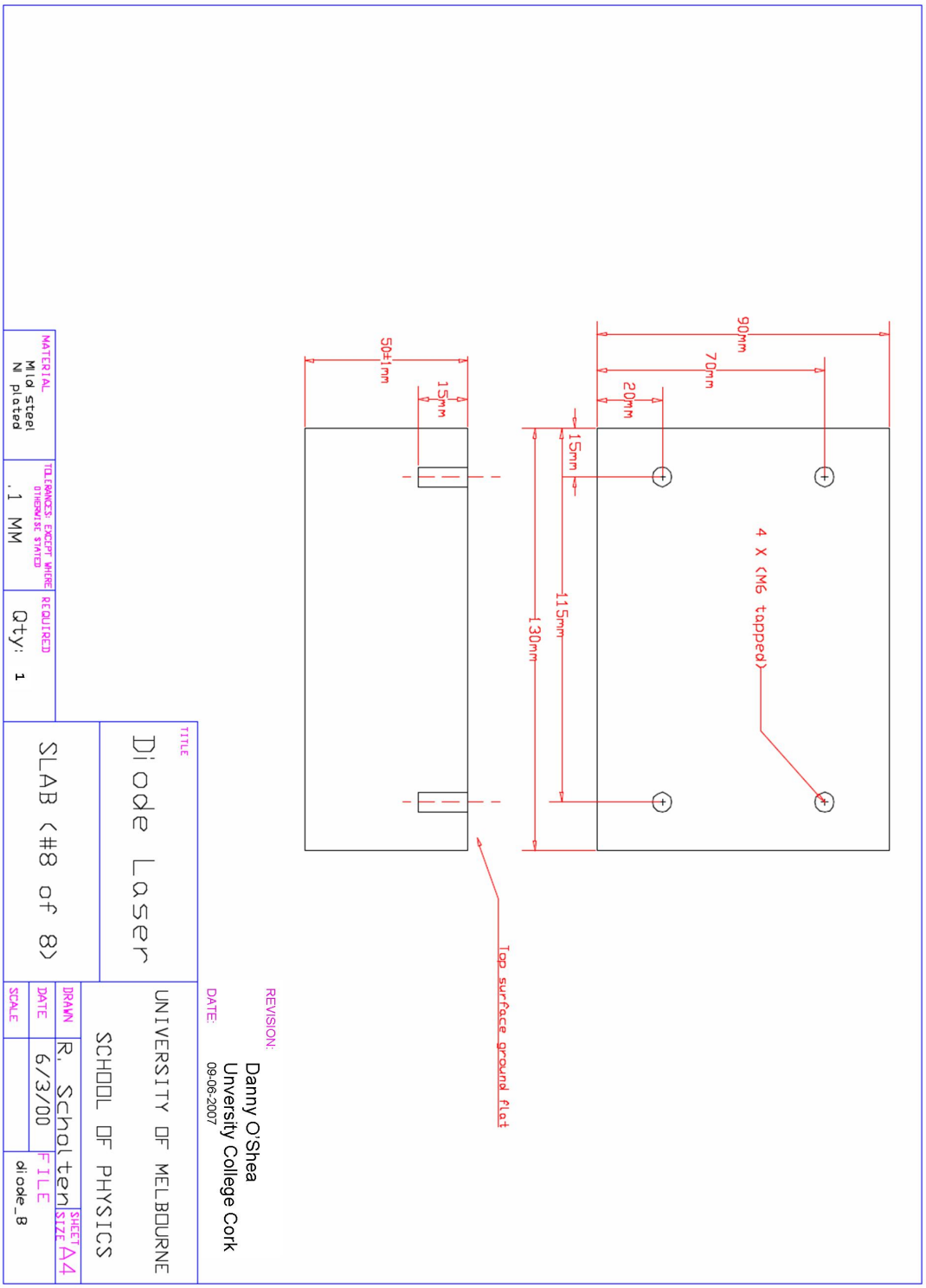
90mm
70mm
20mm
15mm
115mm
130mm
4 X (M6 tapped)
50±1mm
15mm
Top surface ground flat
REVISION:
Danny O'Shea
University College Cork
DATE: 09-06-2007
TITLE
Diode Laser
SLAB (#8 of 8)
MATERIAL
Mild steel
N plated
TOLERANCES: EXCEPT WHERE OTHERWISE STATED
.1 MM
REQUIRED
Qty: 1
UNIVERSITY OF MELBOURNE
SCHOOL OF PHYSICS
DRAWN
R. Scholten
DATE
6/3/00
SCALE
FILE
diode_B
SHEET SIZE A4

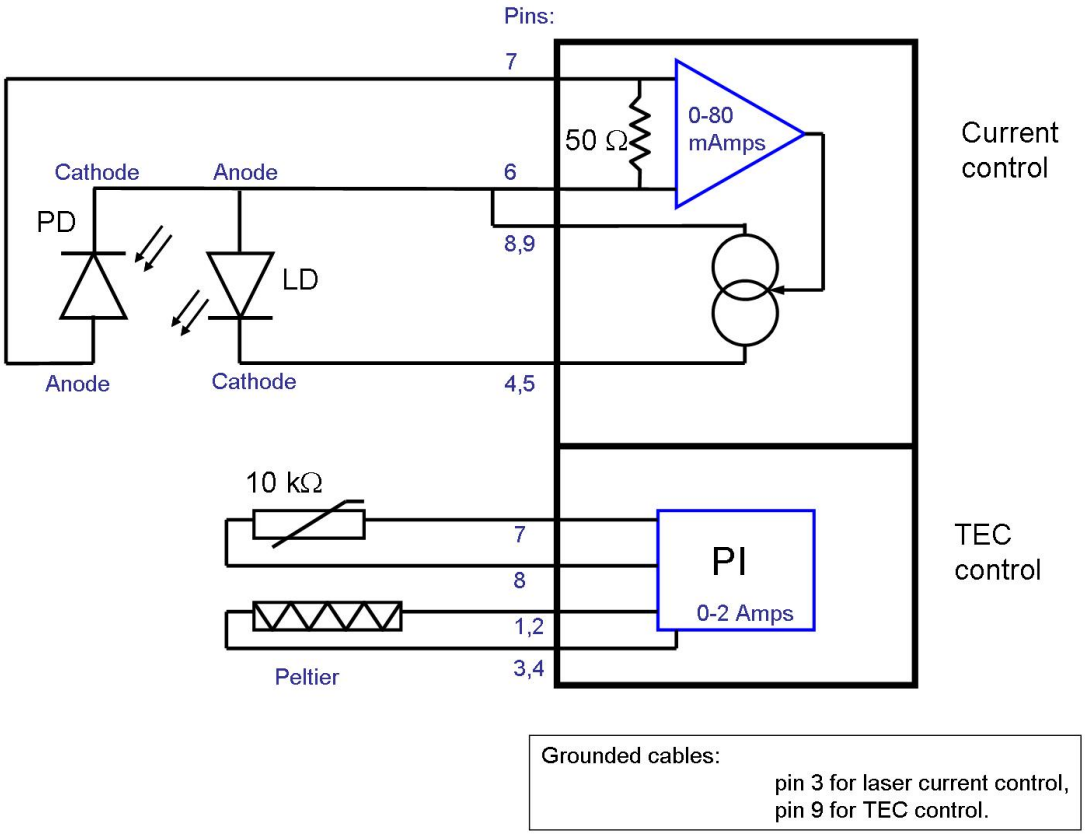

Figure F.1: Electrical wiring diagram for the ECDL and laser diode controller.

Bibliography

[1] E. J. Burkes, J. Hoke, E. Gomes and M. Wolbarsht. "Wet versus dry enamel ablation by Er:YAG laser." *J. Prosthet. Dent.*, **67**, 847, 1992.

[2] K. J. Vahala. "Optical microcavities." *Nature*, **424**, 2003, 1987.

[3] J. C. Knight. "Photonic crystal fibers." *Nature*, **424**, 847, 2003.

[4] V. B. Braginsky and V. S. Ilchenko. "Properties of optical dielectric microresonators." *Sov. Phys. Dokl.*, **32**, 36, 1987.

[5] C. G. B. Garrett, W. Kaiser, and W. L. Bond. "Stimulated emission into optical whispering modes of spheres." *Phys. Rev.*, **124**, 1807, 1961.

[6] T. Baer. "Continuous-wave laser oscillation in a Nd:YAG sphere." *Opt. Lett.*, **12**, 392, 1987.

[7] A. A. Savchenkov, A. B. Matsko, V. S. Ilchenko, and L. Maleki. "Optical resonators with ten million finesse." *Opt. Express*, **15**, 6768, 2007.

[8] H. B. Lin, A. L. Huston, J. D. Eversol, and A. J. Campillo. "Double-resonance stimulated Raman scattering in micrometer-sized droplets." *J. Opt. Soc. Am. B.*, **7**, 2079, 1990.

[9] J. Z. Zhang and R. K. Chang. "Generation and suppression of stimulated brillouin-scattering in single liquid droplets." *J. Opt. Soc. Am. B.*, **6**, 151, 1989.

[10] F. Treussart, V. S. Ilchenko, J.-F. Roch, J. Hare, V. Leferve-Seguin, J.-M. Raimond, and S. Haroche. "Evidence for intrinsic Kerr bistability of high-Q microsphere resonators in super liquid helium." *Eur. Phys. J. D*, **1**, 235, 1998.

[11] S. M. Spillane, T. J. Kippenberg, and K. J. Vahala. "Ultralow-threshold Raman laser using a spherical dielectric microcavity." *Nature*, **415**, 621, 2002.

[12] T. J. Kippenberg, S. M. Spillane, B. Min, and K. J. Vahala. "Theoretical and experimental analysis of stimulated and cascaded Raman scattering in ultra-high-Q optical microcavities." *IEEE J. Select. Top. Quant. Electron.*, **10**, 1219, 2004.

[13] T. J. Kippenberg, S. M. Spillane, and K. J. Vahala. "Kerr nonlinearity induced optical parametric oscillation in a toroid microcavity." *Phys. Rev. Lett.*, **93**, 083904, 2004.

[14] H. Rokshari, and K. J. Vahala. "Observation of Kerr nonlinearity in microcavities at room temperature." *Opt. Lett.*, **30**, 427, 2005.

[15] H. M. Gibbs, S. L. McCall, and T. N. C. Venkatesan. "Differential gain and bistability using a sodium filled Fabry Pérot interferometer." *Phys. Rev. Lett.*, **36**, 1135, 1976.

[16] D. R. Gamelin, S. R. Lüthi, and H. U. Güdel. "The Role of Laser Heating in the Intrinsic Optical Bistability of $Yb3^{+}$-Doped Bromide Lattices." *J. Phys. Chem. B*, **104**, 11045, 2000.

[17] S. M. Redmond and S. C. Rand. "Intrinsic chromatic switching of visible luminescence in Yb^{3+}, Er^{3+}:$CsCdBr_3$." *Opt. Lett.*, **28**, 173, 2003.

[18] A. Ródenas, D. Jaque, and J. García Solé. "Bistable chromatic switching in Yb^{3+}-doped $NdPO_4$ crystals." *Phys. Rev. B*, **74**, 035106, 2006.

[19] M. A. Noginov, M. Vondrova, and B. D. Lucas. "Thermally induced optical bistability in Cr-doped Colquiriite crystals." *Phys. Rev. B*, **65**, 035112, 2001.

[20] T. Hayakawa, H. Ooishi, and M. Nogami. "Optical bistability of stimulated-emission lines in Sm^{3+}-doped glass microspheres." *Opt. Lett.*, **26**, 84, 2001.

[21] A. Kuditcher, M. P. Hehlen, C. M. Florea, K. W. Winick, and S. C. Rand. "Intrinsic bistability of luminescence and stimulated emission in Yb- and Tm-doped glass." *Phys. Rev. Lett.*, **84**, 1898, 2000.

[22] V. R. Almedia and M. Lipson. "Optical bistability on a silicon chip." *Opt. Lett.*, **29**, 2387, 2004.

[23] M. Saad and J.-S. Tassé. "MID-IR OPTICS: Fluoride glasses draw fiber into the mid-infrared." *Laser Focus World*, **43**, 2007.

[24] M. Mortier, P. Goldner, P. Féron, G. M. Stephan, H. Xu, Z. Cai. "New fluoride glasses for laser applications." *J. Non-Crys. Sol.*, **326-327**, 505, 2003.

[25] S. M. Spillane, T. J. Kippenberg, O. J. Painter, and K. J. Vahala. "Ideality in a fiber-taper-coupled micro-resonator system for application to cavity quantum electrodynamics." *Phys. Rev. Lett.*, **91**, 043902, 2003.

[26] T. Mashide. "Study of spherical microlasers levitated in an ion trap." Ph.D. thesis, Kochi University of Technology, 2002.

[27] S. Schiller. "Asymptotic expansion of morphological resonance frequencies in Mie scattering." *Appl. Opt.*, **32**, 2181, 1993.

[28] C. C. Lam, P. T. Leung and K. Young. "Explicit asymptotic formulas for the positions, widths, and strengths of resonances in mie scattering." *J. Opt. Soc. Am. B*, **9**, 1585, 1992.

[29] J. R. Buck and H. J. Kimble. "Optimal sizes of dielectric microspheres for cavity QED with strong coupling." *Phys. Rev. A*, **67**, 033806, 2003.

[30] B. Little. J.-P. Laine, and H. A. Haus. "Analytic theory of coupling from tapered fibers and half-blocks into microsphere resonators." *J. Lightwave Technol.*, **17**, 704, 1999.

[31] M. L. Gorodetsky, A. A. Savchenkov, and V. S. Ilchenko. "Ultimate Q of optical microsphere resonators." *Opt. Lett.*, **21**, 453, 1996.

[32] D. W. Vernooy, V. S. Ilchenko, H. Mabuchi, E. W. Streed, and H. J. Kimble. "High-Q measurements of fused-silica microspheres in the infrared." *Opt. Lett.*, **23**, 247, 1998.

[33] M. L. Gorodetsky, A. D. Pryamikov, and V. S. Ilchenko, V. Lefèvre-Seguin, L.-M. Raimond, and S. Haroche. "Rayleigh scattering in high-Q microspheres." *J. Opt. Soc. Am. B*, **17**, 1051, 2000.

[34] D. S. Weiss, V. Sandoghdar, J. Hare, V. Lefèvre-Seguin, L.-M. Raimond, and S. Haroche. "Splitting of high-Q modes induced by backscattering in silica microspheres." *Opt. Lett.*, **20**, 1835, 1995.

[35] D. W. Vernooy and H. J. Kimble. "Quantum structure and dynamics for atom galleries." *Phys. Rev. A*, **55**, 1239, 1997.

[36] S. M. Spillane. "Fiber-coupled ultra-high-Q microresonators for nonlinear and quantum optics." Ph.D. thesis, California Institute of Technology, 2004.

[37] V. B. Braginsky, M. L. Gorodetsky, and V. S. Ilchenko. "Quality-factor and nonlinear properties of optical whispering-gallery-modes." *Phys. Lett. A*, **137**, 393, 1989.

[38] R. Casprary. "Applied rare-earth spectroscopy for fiber laser optimization." Ph.D. thesis, Von der Gemeinsamen Fakultät für Maschinenbau und Elektrotechnik der Technischen Universität Carolo-Wilhelmina zu Braunschweig, 2002.

[39] F. Auzel. "Upconversion and anti-Stokes processes with f and d ions in solids." *Chem. Rev.*, **104**, 139, 2004.

[40] F. Lissillour, D. Messager, G. Stéphan and P. Féron. "Whispering-gallery-mode laser at 1.56 μm excited by a fiber taper." *Opt. Lett.*, **26**, 1051, 2001.

[41] S. Götzinger, O. Benson, and V. Sandoghdar. "Towards controlled coupling between a high-Q whispering-gallery mode and a single nanoparticle." *Appl. Phys. B*, **73**, 825, 2001.

[42] G. Griffel, S. Arnold, D. Taskent, A. Serpengüzel, J. Connolly, and N. Morris. "Morphology-dependent resonances of a microsphere-optical fiber system." *Opt. Lett.*, **21**, 695, 1996.

[43] V. S. Ilchenko, X. S. Yao and L. Maleki. "Pigtailing the high-Q microsphere cavity: a simple fiber coupler for optical whispering gallery modes." *Opt. Lett.*, **24**, 723, 1999.

[44] L. Tong, J. Lou, and E. Mazur. "Single-mode guiding properties of subwavelength-diameter silica and silicon wire waveguides." *Opt. Express*, **12**, 1025, 2004.

[45] F. Le Kien, J. Q. Liang, K. Hakuta, and V. I. Balykin. "Field intensity distributions and polarization orientations in a vacuum-clad subwavelength-diameter optical fiber." *Opt. Commun.*, **242**, 445, 2004.

[46] J. C. Knight, G. Cheung, F. Jacques, and T. A. Birks. "Phase-matched excitation of whispering-gallery-mode resonances by a fiber taper." *Opt. Lett.*, **22**, 1129, 1997.

[47] A. W. Snyder and J. D. Love. *Optical Waveguide Theory.* Kluwer Academic Publishers, 2000.

[48] L. Tong, R. R. Gattass, J. B. Ashcom, S. He, J. Lou, M. Shen, I. Maxwell, and E. Mazur. "Subwavelength-diameter silica wires for low-loss optical wave guiding." *Nature*, **426**, 816, 2003.

[49] G. Brambilla, V. Finazzi, and D. J. Richardson. "Ultra-low-loss optical fiber nanotapers." *Opt. Express*, **12**, 2258, 2004.

[50] T. E. Dimmick, G. Kakarantzas, T. A. Birks, and P. St. J. Russel. "Carbon dioxide laser fabrication of fused-fiber couplers and tapers." *Appl. Opt.*, **38**, 6845, 1999.

[51] M. Summetsky, Y. Dulashko, and A. Hale. "Fabrication and study of bent and coiled free silica nanowires: Self-coupling microloop optical interferometer." *Opt. Express*, **12**, 3521, 2004.

[52] M. Sumetsky. "Whispering-gallery-bottle microcavities: the three-dimensional etalon." *Opt. Lett.*, **29**, 8, 2004.

[53] T. A. Birks and Y. W. Li. "The shape of fiber tapers." *J. Lightwave Technol.*, **10**, 432, 1992.

[54] A. Grellier, N. K. Zayer, and C. N. Pannell. "Heat transfer modelling in CO_2 laser processing of optical fibres." *Opt. Commun.*, **152**, 324, 1998.

[55] Laser 2000 UK Ltd. *671XX series drive card, and 6210H series moving magnet galvanometer scanner specifaication sheet.*

[56] Radionics Ltd. *Hybrid stepper motor, stock number 440-436, 500:1 gear box, stock number 718-925, and controller circuit, stock number 217-3611.*

[57] J. D. Love, W. M. Henry, W. J. Stewart, R. J. Black, S. Lacroix, and F. Gonthier. "Tapered single-mode fibres and devices. I. Adiabaticity criteria." *IEEE Proc. J*, **138**, 343, 1991.

[58] M. Sumetsky, Y. Dulashko, J. M. Fini, A. Hale, and D. J. DiGiovanni. "The microfiber loop resonator: Theory, experiment, and application." *J. Lightwave Technol.*, **24**, 242, 2006.

[59] W. von Klitzing, R. Long, V. S. Ilchenko, J. Hare, and V. Lefèvre-Seguin. "Tunable whispering gallery modes for spectroscopy and CQED experiments." *New J. Phys.*, **3**, 141, 2001.

[60] Y. Louyer, D. Meshede, and A. Rauschenbeutel. "Tunable whispering-gallery-mode resonators for cavity quantum electrodynamics." *Phys. Rev. A*, **72**, 031801, 2005.

[61] G. Kakarantzas, T. E. Dimmick, T. A. Birks, R. Le Roux, and P. St. J. Russel. "Miniature all-fiber devices based on CO2 laser microstructuring of tapered fibers." *Opt. Lett.*, **26**, 1137, 2001.

[62] C. McAtamney, A. Cronin, R. Sherlock, G. M. OConnor, and T. J. Glynn. "Reproducible method for fabricating fused biconical tapered couplers using a CO2 laser based process." *Proc. 3rd International WLT-Conference on Lasers in Manufacturing*, 2005.

[63] M.-F. Joubert. "Photon avalanche upconversion in rare earth laser materials." *Opt. Mat.*, **11**, 181, 1999.

[64] D. S. Funk and J. G. Eden. "Glass-fiber lasers in the ultraviolet and visible." *IEEE J. Sel. Top. Quant. Elec.*, **1**, 784, 1995.

[65] J. P. van der Ziel, F. W. Ostermayer, and L. G. Van Uitert. "Infrared Excitation of Visible Luminescence in $Y_{1-x}Er_xF_3$ via Resonant Energy Transfer." *Phys. Rev. B.*, **2**, 4432, 1970.

[66] R. Rolli, M. Montagna, A. Chiasera, G. C. Righini, S. Pelli, A. Jha, V. K. Tikhomirov, S. A. Tikhomirova, A. Monteil, S. Chaussedent, and M. Ferrari. "A comparative study of the spectroscopic properties at 1.5 μm of erbium-activated fluoride and tellurite glasses." *Phil. Mag. B.*, **82**, 573, 2002.

[67] T. Catunda, L. A. O. Nunes, A. Florez, Y. Messaddeq, and M. A. Aegerter. "Spectroscopic properties and upconversion mechanisms in Er^{3+}-doped fluoroindate glasses." *Phys. Rev. B.*, **53**, 6065, 1996.

[68] M. D. Shinn, W. A. Sibley, M. G. Drexhage, and R. N. Brown. "Optical transitions of Er^{3+} ions in fluorozirconate glass." *Phys. Rev. B.*, **27**, 6635, 1983.

[69] C. Florea and K. A. Winick. "Ytterbium-doped glass waveguide laser fabricated by ion exchange." *J. Lightwave Technol.*, **17**, 1593, 1999.

[70] A. Florez, Y. Messaddeq, O. L. Malta, and M. A. Aegerter. "Optical transition probabilities and compositional dependence of Judd-Ofelt parameters of Er^{3+} ions in fluoroindate glass." *J. Alloys Compounds*, **227**, 135, 1995.

[71] R. M. Martin and R. S. Quimby. "Experimental evidence of the validity of the McCumber theory relating emission and absorption for rare-earth glasses." *J. Opt. Soc. B*, **23**, 1770, 2006.

[72] S. R. Bullock, B. R. Reddy, P. Venkateswarlu, S. K. Nash-Stevenson, and J. C. Fajardo. "Energy upconversion and spectroscopic studies of ZBLAN:Er^{3+}." *Opt. Quant. Electron.*, **29**, 83, 1997.

[73] M. J. Weber. "Probabilities for radiative and nonradiative decay of Er^{3+} in LaF_3." *Phys. Rev.*, **157**, 262, 1967.

[74] W. T. Carnall, P. R. Fields, and K. Rajnak. "Electronic energy levels in the trivalent lanthanide aquo ions. I. Pr^{3+}, Nd^{3+}, Pm^{3+}, Sm^{3+}, Dy^{3+}, Ho^{3+}, Er^{3+}, and Tm^{3+}." *J. Chem. Phys.*, **49**, 4424, 1968.

[75] J. Yang, S. Dai, N. Dai, L. Wen, L. Hu, and Z. Jiang. "Investigation on nonradiative decay of $^4I_{13/2} \rightarrow^4 I_{15/2}$ transition of Er^{3+}-doped oxide glasses." *J. Lumin.*, **9**, 106, 2004.

[76] P. W. France, M. G. Drexhage, J. M. Parker, M. W. Moore, S. F. Carter, and J. V. Wright. *Fluoride Glass Optical Fibres.* Florida, 1990.

[77] C. L. Pope, B. R. Reddy, and S. K. Nash-Stevenson. "Efficient violet upconversion signal from a fluoride fiber doped with erbium." *Opt. Lett.*, **22**, 295, 1997.

[78] L. F. Johnson, J. E. Geusic, H. J. Guggenheim, T. Kushida, S. Singh, and L. G. van Uitert. "Comments on materials for efficient infrared conversion." *Appl. Phys. Lett.*, **15**, 48, 1969.

[79] H. Xu and Z. Jiang. "Ultraviolet and violet upconversion luminescence in Er^{3+}-doped yttrium aluminum garnet crystals." *Phys. Rev. B.*, **66**, 035103, 2002.

[80] F. Vetrone, J.-C. Boyer, J. A. Capobianco, A. Speghini and M. Bettinelli. "980 nm excited upconversion in an Er-doped $ZnOTeO_2$ glass." *Appl. Phys. Lett.*, **80**, 1752, 2002.

[81] A. Biswas, G. S. Maciel, C. S. Friend, and P. N. Prasad. "Upconversion properties of a transparent $Er^{3+}Yb^{3+}$ co-doped LaF_3SiO_2 glass-ceramics prepared by solgel method." *J. Non-Crys. Sol.*, **316**, 393, 2003.

[82] S. Arahira, K. Watanabe, K. Shinozaki, and Y. Ogawa. "Successive excited absorption through a multistep process in highly Er^{3+}-doped fiber pumped by a 1.48-μm laser diode." *Opt. Lett.*, **17**, 1679, 1992.

[83] M. Pollnau, D. R. Gamelin, S. R. Lüthi, and H. U. Güdel. "Power dependence of upconversion luminescence in lanthanide and transition-metal-ion systems." *Phys. Rev. B*, **61**, 3337, 2000.

[84] M. R. Poulsen, P. I. Borel, J. F.-Pedersen, J. Hübner, M. Kristensen, J. H. Povlsen, K. Rottwitt, M. Svalgaard, and W. Svendsen. "Power dependence of upconversion luminescence in lanthanide and transition-metal-ion systems." *Opt. Eng.*, **42**, 2821, 2003.

[85] J.-P. Laine, B. E. Little, D. R. Lim, H. C. Tapalian, L. C. Kimerling, and H. A. Haus. "Microsphere resonator mode characterization by pedestal anti-resonant reflecting waveguide coupler." *IEEE Photon. Technol. Lett.*, **12**, 1004, 2000.

[86] E. Snitzer and R. Woodcock. "Yb^{3+}-Er^{3+} glass laser." *Appl. Phys. Lett.*, **6**, 45, 1965.

[87] X. Zou and H. Toratani. "Evaluation of spectroscopic properties of Yb^{3+} -doped glasses." *Phys. Rev. B*, **52**, 15889, 1995.

[88] S. Jiang, M. Myers, and N. Peyghambarian. "Er^{3+} doped phosphate glasses and lasers." *J. Non-Cryst. Solids*, **239**, 143, 1998.

[89] R. Wu, J.D. Myers, M.J. Myers, and C. Rapp. "Fluorescence lifetime and 980nm pump energy transfer dynamics in erbium and ytterbium co-doped phosphate laser glasses." *Proc. SPIE*, **4968**, 11, 2003.

[90] L. Yang, T. Carmon, B. K. Min, S. M. Spillane, and K. J. Vahala. "Erbium-doped and Raman microlasers on a silicon chip fabricated by the sol-gel process." *Appl. Phys. Lett.*, **86**, 091114, 2005.

[91] P. Laporta, S. Taccheo, S. Longhi, O. Svelto, and C. Svelto. "Erbium ytterbium microlasers: optical properties and lasing characteristics." *Opt. Mat.*, **11**, 269, 1999.

[92] Schott Glass Technologies. *IOG-2 phosphate laser glass specification sheet.*

[93] Z. Cai, A. Chardon, H. Xu, P. Féron, and G. M. Stéphan. "Laser characteristics at 1535 nm and thermal effects of an Er:Yb phosphate glass microchip pumped by Ti:sapphire laser." *Opt. Commun.*, **203**, 301, 2002.

[94] M. Laroche, S. Girard, J. K. Sahu, W. A. Clarkson, and J. Nilsson. "Accurate efficiency evaluation of energy-transfer processes in phosphosilicate $Er^{3+}Yb^{3+}$-codoped fibers." *J. Opt. Soc. Am. B*, **23**, 195, 2006.

[95] K. T. V. Grattan, A. W. Palmer, and C. A. Wilson. "A miniaturised microcomputer-based neodymium 'decay-time' temperature sensor." *J. Phys. E*, **20**, 1201, 1987.

[96] M. P. Hehlen, N. J. Cockroft, and T. R. Gosnell. "Spectroscopic properties of Er^{3+}- and Yb^{3+}-doped soda-lime silicate and aluminosilicate glasses." *Phys. Rev. B*, **56**, 9302, 1997.

[97] J. F. Phillips, T. Töpfer, H. Ebendorff-Heiderpriem, D. Ehrt, and R. Sauerbrey. "Spectroscopic and lasing properties of Er^{3+}:Yb^{3+}-doped fluoride phosphate glasses." *Appl. Phys. B*, **72**, 399, 2001.

[98] M. Ajroud, M. Haouari, H. Ben Ouada, H. Mâaref, A. Brenier, and B. Champagnon. "Study of the spectroscopic properties and infrared-to-visible upconversion fluorescence of Er^{3+}-doped germanate glasses." *Phys. Status Solidi A*, **202**, 316, 2005.

[99] D. L. Dexter. "A theory of sensitized luminescence in solids." *J. Chem. Phys.*, **21**, 836, 1953.

[100] X. Qiao, X. Fan, M. Wang, J.-Luc Adam, and X. Zhang. "Spectroscopic properties of Er^{3+}/Yb^{3+} co-doped $50SiO_2$ $20Al_2$ O_3 $30CaF_2$ glass and glass ceramics." *J. Phys.: Condens. Matter*, **18**, 6937, 2006.

[101] Kigre, Inc. *QE-7S phosphate laser glass specification sheet.*

[102] H. Rokhsari, S. M. Spillane, and K. J. Vahala. "Loss characterization in microcavities using the thermal bistability effect." *Appl. Phys. Lett.*, **85**, 3029, 2004.

[103] O. Guillot-Nöel, L. Binet, and D. Gourier. "General conditions for intrinsic optical bistability at the atomic and molecular scale: An effective spin-Hamiltonian approach." *Phys. Rev. B.*, **65**, 245101, 2002.

[104] B. Jaskorzyńska, S. Sergeyev, M. Swillo, and D. Khoptyar. "Nonlinear upconversion-rate in Er-doped fibers." *Acta Phys. Pol. A*, **99**, 147, 2000.

[105] Md. M. Mazumder, S. C. Hill, D. Q. Chowdhury, R. K. Chang. "Dispersive optical bistability in a dielectric sphere." *J. Opt. Soc. Am. B*, **12**, 297, 1995.

[106] E. A. Gouveia, M. T. de Araujo, and A. S. Gouveia-Neto. "Thermal effects on light emission in Yb^{3+}-sensitized rare-earth doped optical glasses." *Braz. J. Phys.*, **37**, 89, 2001.

[107] G. Lei, J. E. Anderson, M. I. Buchwald, B. C. Edwards, R. I. Epstein, M. T. Murtagh, and G. H. Seigel. "Spectroscopic evaluation of Yb^{3+}-doped glasses for optical refrigeration." *IEEE J. Quantum Electron.*, **34**, 1839, 1998.

[108] V. B. Braginsky, M. L. Gorodetsky, and V. S. Ilchenko. "Optical whispering-gallery microresonators." *Proc. SPIE*, **2097**, 283, 1993.

[109] A. E. Fomin, M. L. Gorodetsky, I. S. Grudinin, V. S. Ilchenko. "Nonstationary nonlinear effects in optical microspheres." *J. Opt. Soc. Am. B*, **22**, 459, 2005.

[110] A. B. Matsko, A. A. Savchenkov, D. Strekalov, V. S. Ilchenko and L. Maleki. "Review of applications of whispering-gallery mode resonators in photonics and nonlinear optics." *IPN Progress Report*, 42–162, 2005.

[111] D. G. O'Shea, J. M. Ward, B. J. Shortt, and S. Nic Chormaic. "An all-fiber coupled multicolor microspherical light source." *To appear in IEEE Photon. Technol. Lett.*, **(physics/0611197)**, 2007.

[112] J. Ward and S. Nic Chormaic. "Taper-fused microspherical laser." 2007. In preparation for IEEE Photon. Technol. Lett.

[113] M. Cai, B. Hunziker, and K. J. Vahala. "Fibre-optic Add-Drop device based on a silica microsphere-whispering gallery mode system." *IEEE Photon. Technol. Lett.*, **11**, 686, 1999.

[114] A. S. Arnold, J. S. Wilson, and M. G. Boshier. "A simple extended-cavity diode laser." *Rev. Sci. Instrum.*, **69**, 1236, 1998.

[115] C. J. Hawthorn, K. P. Weber, and R. E. Scholten. "Littrow configuration tunable external cavity diode laser with fixed direction output beam." *Rev. Sci. Instrum.*, **72**, 4477, 2001.

[116] L. Ricci, M. Weidemüller, T. Esslinger, A. Hemmerich, C. Zimmermann, V. Vuletic, W. König, and T. W. Hänsch. "A compact grating-stabilized diode laser system for atomic physics." *Opt. Commun.*, **117**, 541, 1995.

[117] R. Scholten. "http://optics.ph.unimelb.edu.au/atomopt/atomopt.html."

[118] W. von Klitzing, E. Jahier, R. Long, F. Lissillour, V. Lefèvre-Seguin, J. Hare, J.-M. Raimond, and S. Haroche. "Very low threshold green lasing in microspheres by up-conversion of IR photons." *J. Opt. B*, **2**, 204, 2000.

[119] M. Mortier. "Private communication."

[120] H. Fujiwara and K. Sasaki. "Microspherical lasing of an erbium-ion-doped glass particle." *Jpn. J. Appl. Phys.*, **41**, L46, 2002.